Imperial College London

The selective and sensitive detection of protein biomarkers using aptamer-based nanosensors

Benjamin James Edwards

A thesis submitted in partial fulfilment of the requirement for the degree of

Doctor of Philosophy

Department of Chemistry

Imperial College London

2020

Abstract

A multitude of diseases are known to have specific biomarkers yet detection with high specificity and selectivity remains highly challenging. For example, single molecule-based fluorescence techniques while highly sensitive, requires labelling with expensive fluorescent tags, as well as recognition elements (e.g. antibodies) if detection is to be carried out in complex solutions. Such labelling compromises the biophysical properties of the analyte likely resulting in altered aggregation. To address these limitations, the PhD project aimed to combine the single molecule and label-free detection granted by nanopores with highly specific single stranded oligonucleotides known as aptamers in order to detect biologically relevant proteins.

The aptamer-based nanosensor was constructed in a two-step method. An initial silanisation step carried out in the vapour phase allowed the formation of a mono-silane layer with a terminal methacrylate functional group, which in turn allowed a thiol-modified aptamer to be added via click chemistry-based Michael addition. Characterisation of the developed sensor was carried out electrochemically via *in-situ* I-V curves, while further confirmation could be seen through the presence of substantial current blockades upon addition of complementary (to the aptamer) nucleotide sequences.

The primary aim of the project was to detect thrombin, a biomarker which has links to Multiple Sclerosis and cancer. Thrombin provided an excellent initial target due to its well characterised structure alongside a high affinity (kD = 0.5 nM) binding aptamer. Characterisation of the developed sensor was initially carried out via concentration and voltage-based assays, before showing that the aptamer-based nanosensor could not only be regenerated but also carried out in multi-protein solutions. In addition, highly cytotoxic alpha synuclein oligomers; the likely biomarkers of Parkinson's Disease have been detected. After a concentration-based assay, it was shown that the (anti-oligomer) aptamer specifically targeted a specific oligomer sub-type when samples were detected over a range of different aggregation timepoints.

Overall the developed aptamer-based nanosensor is able to specifically detect high-value biomarkers at ultra-low concentrations, underlying its potential to be used in the healthcare industry.

Declarations

I, the author, hereby declare that the work presented in the following thesis is original and performed by myself; otherwise it is clearly cited and acknowledged.
This work has not previously been submitted in any form to satisfy any degree requirement at this or any other university.

Ben Edwards

Copyright notice

The copyright of this thesis rests with the author and is made available under a Creative Commons Attribution Non-Commercial No Derivatives license. Researchers are free to copy, distribute or transmit the thesis on the condition that they attribute it, that they do not use it for commercial purposes and that they do not alter, transform or build upon it. For any reuse or redistribution, researchers must make clear to others the license terms of this work.

Acknowledgements

I would like to first and foremost thank my supervisors, Joshua Edel, Alex Ivanov and Tony Cass for their support and guidance over the course of my PhD studies. I would also like to take this opportunity to thank Professor Eiry Kobatake for hosting me at his lab at Tokyo tech university as part of the Global Fellows programme. It was a genuine pleasure to undertake research in another culture, while also allowing me to explore Japan during Cherry blossom season.

I of course would like to give a huge shout-out to the Edel group members both past and present. In particular, I would like to thank Binoy, Jane, Jasmine and Paulo who remained ever-lasting patient to my never-ending questions, Giulia and Mike for help with alpha synuclein experiments and Isobel for help with fluorescent experiments involving G-quadruplex dyes. Thanks to Binoy for much needed tea breaks, Alex-D-L and Micol for the most random of conversations as well as the rest of the 5th floor gang.

A PhD is certainly not without its stresses and in particular I would like to commend the societies at Imperial for much needed distraction. At the squash society, I would particularly like to thank Siego for coaching, Matyas for our constant (good-natured) battles, Alex D-L and Vanessa for the unofficial squash ski-trip, as well as Cathy and Billy. At the karate society, I would not only like to thank my fellow committee members both past (Josh, Ingrid) and present (Austin, Dalisay, Swetha, Antoine and Dalisay) but also would like to express my gratitude to the world class instruction provided by sensei Jim Lewis and Anne-Marie. I would also like to take this opportunity to thank my roommate Chris, for our impromptu tennis matches and Xbox sessions; good luck for the rest of your studies. Furthermore, I could never forget my friends from my home town; Dooley, Rutter, Tim and Barron, for much needed entertainment, especially during the write-up stage (Sweden was fun).

Finally, but by no means least I would like to thank my family. In particular, I would like to thank Uncle Phil and Auntie Kippers for letting me stay at your home during the last (and most frantic) month of my PhD, as well as the rest of my extended family for our regular meet-ups often ending up in pubs. To my supportive sister Laura who beat me at being called Dr and to my parents, I would never have made it this far without you.

This PhD thesis is dedicated to
my parents, Lesley and Robert

Table of contents

Abstract 2
Declarations 3
Acknowledgements 4
Table of contents 6
List of Figures 10
List of Tables 20
List of Equations 22
Abbreviations 23
Chapter outline 25
Chapter 1: Introduction 26
1.1. Overview 27
1.2. Protein Biomarkers 27
1.2.1. Protein aggregates as biomarkers 27
1.3. Single molecule detection 29
1.4. Nanopore 31
1.4.1. Nanopore types 32
1.4.1.1. Biological 32
1.4.1.2. Solid state 33
1.4.1.3 Hybrid nanopores 34
1.4.1.4 Nanopipettes 35
1.4.2 Nanopore properties 36
1.4.2.1 Ion blockade sensing 36
1.4.2.2 Electrical double layer 37
1.4.2.3. The driving forces of translocation 38
1.4.2.4. Ion current rectification 39
1.3.2.5 Ion blockade conductance 40
1.4.4 Limitations of protein detection using nanosensors 41
1.4.4.1. Low capture rate 41
1.4.4.2. Low signal to noise ratio (SNR) 42
1.4.4.3. Effects of electroosmosis and electrophoresis 42
1.4.4.4. Limited selectivity 44
1.5. Aptamers 46
1.5.1. Binding mechanism 47
1.5.2 G-quadruplex based aptamers 48
1.5.2.1 Structure 48
1.6. Solutions to detect protein translocation in nanopores 48
1.6.1. Receptor modified carrier 49

1.6.2. Receptor modified nanopores **51**
1.7. Thesis aim and objectives ***55***
1.8. References ***56***
Chapter 2: Materials and methods ***61***
2.1. Overview ***62***
2.2. Nanopipette fabrication ***62***
2.3. Nanopipette functionalisation ***63***
2.3.1. Nanopipette aptamer modification **64**
2.4. Experimental ***65***
2.4.1. Ag/AgCl electrode preparation **65**
2.4.2. Electrolyte solutions **65**
2.4.3. Electrochemical set-up **66**
2.4.4. Translocation studies **67**
2.4.5. Data acquisition **68**
2.5. Data analysis ***68***
2.5.1. I/V curves **68**
2.5.2. Gap-free studies **69**
2.5.3. Noise analysis **73**
2.5.3.1. Root mean square (RMS) 73
2.5.3.2. Power spectrum density (PSD) 73
2.6. Materials utilised: proteins and DNA aptamers ***73***
2.7. References ***75***
Chapter 3: Construction of an aptamer-modified nanopore sensor ***76***
3.1. Overview ***77***
3.2 Introduction ***77***
3.2.1 Silanisation **77**
3.2.2. Bioconjugation **79**
3.3. Aim ***80***
3.4. Results ***80***
3.4.1. Nanopipette functionalisation with an aptamer modified pipette. **80**
3.4.1.1 Silanisation 81
3.4.1.2. Aptamer reduction 81
3.4.1.3. Bioconjugation 81
3.5. Characterisation ***81***
3.5.1. Fabrication Characterisation **81**
3.5.1.1. I/V curves 81
3.5.1.2. Translocation studies 82

3.5.2. Noise characterisation 83
3.6. Sensor design *84*
3.7. Discussion *87*
3.8. Conclusion *92*
3.9. References *92*
Chapter 4: Detection of thrombin using an aptamer-modified nanopore sensor *94*
4.1. Overview *95*
4.2. Introduction *95*
4.2.1. Thrombin structure **95**
4.2.2. Thrombin's role in the coagulation cascade **96**
4.2.3. Thrombin as a biomarker **97**
4.2.4. Current detection of thrombin **100**
4.3. Aim *102*
4.4. Challenges *103*
4.4.1. Experimental **103**
4.4.2. Data analysis **103**
4.5. Results *108*
4.5.1. Concentration dependence **108**
4.5.2. Voltage dependence **111**
4.5.3. Electrolyte concentration dependence **112**
4.5.4. Detection in a multi-protein analyte **113**
4.5.5. Noise analysis **115**
4.5.5.1. RMS 115
4.5.5.2. Power spectrum density 116
4.5.6. Low-pass filter effects **117**
4.5.7. Sensor regeneration **118**
4.6. Discussion *119*
4.7. Conclusion *124*
4.8. References *124*
Chapter 5: Detection of alpha synuclein oligomers using an aptamer-modified nanopore sensor *126*
5.1. Overview **127**
5.2. Introduction *127*
5.2.1. Parkinson's Disease **127**
5.2.2.Oligomer structure **129**

5.2.3. Physiological function of alpha synuclein monomers and pathological mechanisms of alpha synuclein oligomers 129

5.2.4. Oligomer detection 131

5.3. Aim and challenges 135

5.4. Results 135

5.4.1. Concentration dependence 135

5.4.2. Oligomer AFM images 140

5.5. Discussion 141

5.6. Conclusion 143

5.7. References 144

Chapter 6: Conclusion 147

6.1. References 153

Appendices 155

List of Figures

Chapter 1

Figure 1. 1. Aggregation of protein occurs via a nucleated polymerisation process, an initial lag phase is followed by an exponential elongation before culminating in a steady state plateau. THF fluorescence, a ß-sheet binding dye is used to characterise the aggregation process. 28

Figure 1. 2. A schematic showing the aggregation process 29

Figure 1. 3. Single molecule fluorescent-based detection of alpha synuclein oligomers. (a) Instrumental set-up. A microfluidic device (used for sample delivery) is mounted onto a confocal microscope. Fluorescence from Alexa Fluor 488 and Alexa 594 (indirectly via FRET) are collected via separate Avalanche photodiode detectors (APD). (b) Examples of intensity traces involving donor fluorophore alexa 488 (blue) and acceptor fluorophore alexa 594 (red). Monomeric bursts are donor bursts only while oligomeric species have bursts in the donor and acceptor channel. (c) Number of donor burst as a function of time during the aggregation of alpha synuclein. The donor burst decreases as monomers incorporate into oligomers and fibrils due to the lower concentration (d) A 2D contour plot of size and FRET efficiency of alpha synuclein at various aggregation timepoints. Both the size and FRET efficiency increases with aggregation time. Figure adapted from reference 27. 31

Figure 1. 4. Ribbon representations of the αlpha-hemolysin pore. A) View perpendicular to the sevenfold axis and parallel to the membrane plane. The height is approximately 100 Å, while the stem domain measures 52 Å. Also shown are the locations of the cap, stem and rim regions. B) View from the top of the structure and parallel to the sevenfold axis highlighting the diameter of alpha-hemolysin (100 Å at parts) as well as the inner diameter of the stem region (26 Å). Figure adapted from reference 40. 33

Figure 1. 5. TEM images of solid state nanopores. Figure 1.5a shows a nanopore formed via electron beam lithography. Figures (b-d) shows pore shrinkage accomplished by subsequent application of a high energy electron beam. Figure adapted from reference 41. 34

Figure 1. 6. (a) An alpha hemolysin is mutated to contain a cysteine allowing the covalent attachment of a thiol modified 12 nucleotide. Hybridisation of the sticky end allows incorporation of a 3 kbp dsDNA 'guide' strand. (b) Insertion of the hybrid nanopore into the narrow solid state nanopore is carried out electrophoretically. Figure adapted from reference 37. 35

Figure 1. 7. A glass nanopipette tip (left) alongside the zoomed in tip of the nanopore (right). Figure adapted from reference 43. 35

Figure 1. 8. The basic principles of ion-blockade sensing. (a) A schematic showing a typical nanopore set-up. (b) Application of a voltage bias lead to production of an ionic current (b), which is momentarily disrupted upon passage of an analyte (c) otherwise known as translocation. (d) A schematic showing the characteristics of a typical translocation event. The dwell time (t_{off}) is the width of the peak and is related to the size of the molecule, the peak amplitude (ΔI) is related to the analyte charge and inter-event time (t_{on}) is related to the analyte concentration. 37

Figure 1. 9. The EDL formed in nanochannels consist of an inner stern layer and a diffuse layer. The size of the EDL layer depends on the surface charge, as well as the electrolyte concentration.....37

Figure 1. 10. A model showing the mechanism of biomolecule translocation through nanopores (a) The effects of electroosmosis and electrophoresis on the movement of an analyte (e.g protein) in a nanopore. The negatively charged protein is attracted by electrophoretic effects (black solid arrow) and also by electroosmotic effects (dashed arrow). (b) A balance between a driving Force ($F_{driving}$) that pulls the DNA through the pore and a drag Force (F_{drag}) related to the viscosity of the solvent which is in opposition. Figure adapted from reference 48. 39

Figure 1. 11. A schematic showing that the rectification of glass nanopipettes results in a non-linear I/V profile. 40

Figure 1. 12. Detection of proteins using unmodified solid state nanopores. (a) Event rate as a function of pore diameter. ß -galactosidase is measured at two different applied voltages (b) Event rate as a function of protein concentration. hCG is measured in pores with different diameters. Figures adapted from reference 51.....42

Figure 1. 13. The distortion of rectangular pulses of 10−200 μs duration by a 10 kHz Gaussian filter. For a 100 μs pulse duration the dashed red line shows an ideal pulse (delayed 40 μs for visual clarity), before filtering, while the solid red line shows the same 100 μs pulse after filtering. All pulses have the same amplitude before filtering. Due to the limited rise time of the filter, any pulse with a duration less than twice the filter rise time (2Tr =66 μs) is distorted. Figure adapted from reference 51. 42

Figure 1. 14. The effects of electroosmosis and electrophoresis on protein translocation through a nanopore. Depending on the relative charges of the nanopore wall and protein, electrophoresis and electroosmosis can oppose each other (left) or work alongside each other (right). 43

Figure 1. 15. The effects of electroosmosis and electrophoresis on actin translocation through a nanopore as a function of solution pH. Current traces are shown at both positive and negative applied potentials while the schematic underneath show the relative velocities of electroosmosis and electrophoresis allowing determination of the direction of overall movement. Figure adapted from reference 52 44

Figure 1. 16. (a) Modification agents are composed of a headgroup which binds to the surface and a tail which leads to incorporation of a functional group. (b) A schematic of a self-assembled monolayer, formed through a thiol head binding to the gold surface and stabilised by Van Der Waal forces present between hydrocarbon chains.....45

Figure 1. 17. Examples of 3D structures formed by aptamers. (a) hairpin loop structure occurs through complementary binding in the stem region. (b) G-quadruplex is formed vis Hoogsteen hydrogen bonding between guanine bases 46

Figure 1. 18. The SELEX process is used to generate oligonucleotide sequences known as aptamers that bind a specific analyte. A library of oligonucleotides is incubated with a specific target prior to a series of washing steps used to remove any unbound sequences. The bound sequences can now be

eluted and subsequently amplified with further variations for additional SELEX cycles until necessary. 47

Figure 1. 19. Binding modes of aptamer. (1) In an induced fit mechanism, the aptamer changes its shape in response to the target analyte only. (2) In a pre-formed binding model the aptamer requires prior organisation before it can bind the target analyte. 47

Figure 1. 20. (a) A schematic showing a G-tetrad. (b(i) A unimolecular parallel formation (ii) A Unimolecular anti-parallel formation. G4 quadruplexes are typically made up of three tetrads stabilised with metal ions (red spheres). 48

Figure 1. 21. An example of a typical peak seen utilising a carrier system. A large blockade peak corresponds to the translocation of a dsDNA while the sub-peak can be attributed to the bound analyte. Figure adapted form reference 69. 49

Figure 1. 22. The formation of DNA carriers through cutting and hybridising with complementary sequences. (b) The detection of streptavidin using DNA carriers with 3 biotin receptors (i) Biotin groups in close proximity lead to one sub-peak while (ii) spatial separation of biotin groups lead to three distinct sub-peaks. (c) Selective detection of streptavidin using the carrier based system. Mix 1 contains streptavidin among 3 other proteins while in mix 2 streptavidin is replace by BSA. 3B refers to a carrier system with 3 biotin groups while 0B refers to a carrier system with no biotin groups. Figures adapted from reference 69.....50

Figure 1. 23. The detection of thrombin using a DNA carrier system. (a) An unmodified carrier (b) hybridisation with nucleotide sequences containing the complementary sequence and TBA at both ends results in a 2 carrier system (c) The 2 carrier system is incubated with proteins (d) A three carrier system formed by extension of the 2nd binding site is incubated with three protein analytes. A schematic of the carrier system (i) is shown alongside representative traces (ii) and representative peaks (iii). Data analysis can be shown via dwell time vs current scatter plots (iv). Figures adapted from reference 70. 51

Figure 1. 24. (a) An illustration showing the binding and subsequent translocation of streptavidin (large red) to specific lipid anchored biotin (blue circles). (b) Current versus time traces for streptavidin (6 pM) translocation through lipid bilayer coated nanopores without (top) and with (bottom) biotin lipids. Figures adapted from reference 71.....52

Figure 1. 25. The detection of His-tagged protein using solid state nanopores modified with Nickel-NTA receptors. (a) A schematic showing the modified nanosensor. (b) A typical trace showing binding events. (c) Dwell time (pulse width) vs peak amplitude (pulse height) scatter plots for His tagged protein translocated through nanopores with no NTA i) as well as nanopores with 1 (ii) and 2 NTA (ii) modifications. Figures adapted from reference 72. 53

Figure 1. 26. The detection of thrombin using alpha hemolysin externally modified with TBA. Traces before (a) and after (b) the addition of 350 nM thrombin. (c) A mechanistic overview of the different type of events encountered. Figures adapted from reference 73. 54

Figure 1. 27. The detection of thrombin using aptamer (15 mer TBA) modified nanopipettes. (i) The rectification ratio at each stage of the modification process. (ii) Thrombin detection is based on the

reduction in current upon addition of thrombin to the modified nanopipette. Figures adapted from reference 74. (b) Traces show the detection of immunoglobin using a nanopipette modified with the corresponding aptamer. Traces before (i) and after (ii) the addition of 5nM immunoglobin. Figures adapted from reference 75. 54

Chapter 2

Figure 2. 1. (a) The process of nanopipette fabrication. An initial plasma cleaning step removes contaminants and hydrolyses the surface. The nanopipette is then placed in a pipette puller where it is heated by a laser and subsequently pulled. The nanopipette dimensions (taper length, pore diameter) can be adjusted by varying the laser power, glass capillary width and pull time/strength. (b) The Sutter P-2000 pipette puller. (c) SEM images of a single barrelled nanopipette. (c) An SEM image of a nanopipette (left) alongside the nanopore (right). Figure adapted from reference 1. 63

Figure 2. 2. The set-up used to vapour silanise nanopipettes. Pre-heated glass beakers were filled with the silanising agent with nanopipettes suspended above. The beakers were then placed in a desiccator and a vacuum applied for 2 hours. 64

Figure 2. 3. The set-up used to fabricate AgCl electrodes 65

Figure 2. 4. The axopatch set-up used in electrochemical experiments is shown above. The analyte dissolved in filled nanopipette with an inserted Ag/AgCl electrode was placed into the well containing the same electrolyte concentration and electrode.Reference electrode 66

Figure 2. 5. The experimental set-up used in electrochemical based nanopipette experiments. Nanopipettes filled with electrolyte is lowered into a bath filled with the same electrolyte. The application of a voltage bias leads to the generation of ionic current. 67

Figure 2. 6. A schematic showing an I-V curve. The rectification ratio (right) is determined by the current at a given voltage (+V) over the current at its negative equivalent (-V).....69

Figure 2. 7. The effects of low-pass filters on 10 pM thrombin translocation through TBA-modified pipettes. The trace (left) is filtered with a 10 kHz low-pass filter, before filtering with a 1 kHz low-pass filter. 69

Figure 2. 8. (a) The baseline is fitted using Poisson distribution (b) The trace is oversampled with translocation peaks counted as part of the baseline. (c) The trace is undersampled with fitting not following the baseline as closely as required. 70

Figure 2. 9. A threshold (red dotted lines) based on standard deviation is used to discriminate between translocation peaks and background noise.....71

Figure 2. 10. Peaks selected by the software are typically done at full width at half maximum 71

Figure 2. 11. Histogram analysis of the translocation peak dwell time. Correct bin width provides a far more accurate value of the average dwell time. 72

Figure 2. 12. A dwell time vs peak current scatter plot 72

Figure 2. 13. An exponential decay plot of inter-event time (t_{on}) allows determination of the capture rate. 72

Chapter 3

Figure 3. 1. A silanising agent includes hydrolysable groups alongside a functional group.....78

Figure 3. 2. The process of silanisation. An initial hydrolysis reaction (i) leads to silanol cross-linking via hydrogen bonding (ii) and subsequently a condensation reaction (iii). The cross-linked silanol can now react with silanol surface groups through hydrogen bonds (iv) and a final condensation reaction (v). 78

Figure 3. 3. A scheme highlighting the commonly used bioconjugation strategy; copper catalysed azide alkyne cycloaddition (CuAAC). An azide couples with an alkyne under copper catalysis in a Diers-Alder type reaction. 79

Figure 3. 4. An overview of the bioconjugation strategy used to construct our aptamer based nanosensor. 80

Figure 3. 5. I/V curves at each stage of the modification process recorded in 100 mM KCl. Shown in the legend is the rectification ratio ± SD (n = 8). 82

Figure 3. 6. TBA modified nanopipettes in (i) 100mM KCl electrolyte only, (ii) 10 pM control sequence and (iii) 10 pM complementary sequence. Traces have a sampling frequency of 100 kHz and had a low-pass filter of 10 kHz. 83

Figure 3. 7. Traces recorded at 0 mV for each stage of the modification process; unmodified (i), silanised (ii) and TBA-modified (iii) nanopipettes. Traces were low-pass filtered at 10 kHz with a scanning rate of 250 kHz. 83

Figure 3. 8. PSD of the fabrication process; unmodified (blue), silanised (red) and TBA modified (green). The top PSD was recorded at 0 mV while the bottom PSD was recorded at 500mV. Traces have a scanning rate of 250 kHz and were filtered at 10 kHz. 84

Figure 3. 9. The length of the silanising agent is estimated via bond lengths and bond angle calculations with the use of the program ChemBio3D. The purple sphere is a silicon atom, the red sphere is an oxygen atom, the grey sphere is a carbon atom while the white sphere is a hydrogen atom. 85

Figure 3. 10. The length of the 6 carbon linker is estimated via bond length and angles calculations via use of the program ChemBio3D. The grey spheres are carbon atoms while the white spheres are hydrogen atoms. 86

Figure 3. 11. The predicted structure of the 29mer TBA was estimated through its related structure; HD 22 missing nucleotides A_1 and T_{29}). The G-quadruplex is assumed to be a rigid structure allowing a length calculation based on dsDNA measurements. Figure adapted from reference 20.....86

Figure 3. 12. A schematic of the aptamer functionalised nanosensor with an estimated diameter of 17 nm. The zoomed in section (top-left) provides a layer by layer overview of the modified nanopipette while showing differing conformations of the aptamer. The unmodified glass layer is shown in blue, the silane layer is shown in red while the aptamer sequences are shown either in their linear form or as G-quadruplex when stabilised by potassium ions. 87

Figure 3. 13. Mechanistic overview of thiol Michael addition. Step 1: TCEP (R_3P) acts as a nucleophilic catalyst through conjugate addition on the methacrylate functional group resulting in the formation of an adduct intermediate. Regeneration of the carbonyl through abstraction of a proton from a nearby thiol results in formation of the more reactive thiolate ion. Step 2: The thiolate ion undergoes nucleophilic attack on the methacrylate system. The α,β system is regenerated through abstraction of a proton from a nearby thiol. 88

Figure 3. 14. The thiol methacrylate reaction (top) and the thiol maleimide reaction (bottom). 89

Figure 3. 15. ESI-MS of oligo($PEGMEMA_{475}$). S = Starting material, P = Phosphine conjugated species, C = thiol oligomer conjugate species. Adapted from reference 15 89

Figure 3. 16. Possible side reaction of the phosphine catalyst attacking the vinyl group alongside proton abstraction results in the formation of a phosphine conjugate. 90

Figure 3. 17. ssDNA aptamers are highly flexible allowing free movement in solution. Upon the addition of a complementary sequence, rigid dsDNA structures are formed resulting in a large decrease in ionic current. Peaks can be attributed to unzipping off the complementary sequence... 91

Figure 3. 18. ssDNA are favoured at high voltages although G-quadruplexes are expected to dominate at higher electrolyte concentrations. 91

Figure 3. 19. A likely binding mechanism of aptamer modified nanopipette 92

Chapter 4

Figure 4. 1. (a) A 3D schematic structure (left) of thrombin. Figure adapted from reference 2. (b) A schematic structure (right) showing the 29-mer aptamer (red) bound to exosite I of thrombin (blue). Figures adaoted from reference 3. 96

Figure 4. 2. A simplified version of the coagulation cascade. 96

Figure 4. 3. A schematic showing a summary of the effects of thrombin on pulmonary metastasis. Figure adapted from reference 5 98

Figure 4. 4. The passage of thrombin, its substrate fibrinogen and product fibrin through the BBB, whereby it can lead to neuroinflammation. For example, fibrinogen can induce growth factor pathway activation in astrocyte, oligodendrocytes and pericytes, whereby it can regulate scar formation, cell differentiation and inhibition of neurite growth respectively. Upon conversion of fibrinogen to fibrin, a cryptic epitope (e.g. y377-395) is revealed which is the binding site for the

CD11b/CD18 integrin receptor. Furthermore, the immobilisation of fibrinogen and fibrin can lead to the activation of microglia and macrophages. Figure adapted from reference 6.....99

Figure 4. 5. (a) A schematic of the biosensor. In the unbound state (left), the aptamer is free to interact with the electrode surface with its molecular beacon (MB) redox tag in turn allowing electron transfer (eT) to occur. Upon the addition of thrombin (right), aptamer binding prevents close contact of the MB to the electrode preventing eT from occurring. (b) A concentration profile of thrombin alongside the signal decrease. (c) The biosensor (compared with buffered saline) is carried out in 50% fetal calf serum (left) and 50% fetal calf serum when spiked with 64 nM thrombin (right). Figures adapted from reference 8.....101

Figure 4. 6. (a) A schematic showing the mechanism of the probe. The probe consisting of ACPP conjugated with Cy5 is linked to a non-penetratable anion. Upon introduction of thrombin, the linker is cleaved allowing ACPP to penetrate through cells. (c) Fluorescent signal in whole spinal cord scans from mice injected with PPRSFL-ACPP at different timepoints of EAE. Figures adapted from reference 7.....101

Figure 4. 7. Figure showing methods used to simplify traces for subsequent analysis. (a) A trace showing 10 pM thrombin translocation through TBA-modified pipettes with a low-pass filter of 10 kHz. (b) The same trace with a 1 kHz low-pass filter. (c) The trace in (b) has noisy sections with non-analysable translocation peaks removed to simply the trace. 104

Figure 4. 8. Baseline and threshold fitting for the same trace when conducted in pipettes modified with TBA-29mer. (a) Baseline fitting alongside zoomed in subsections utilising a tight fit (left) and loose fit (right). (b) Threshold analysis corresponding to the fitted baseline of (a). 105

Figure 4. 9. Peak selection alongside deterimination of dwell times. (a) Peak selection is fitted correctly allowing dwell tme to be selected carefully, while in (b) dwell times are incorrectly picked resulting in overestimation (left) and underestimation (right). 106

Figure 4. 10. Histogram analysis of dwell time with correct bin width (top) and incorrect bin width (bottom). 107

Figure 4. 11. A trace alongside a zoomed in subsection showng the effects of peak clustering. 107

Figure 4. 12. Representative traces of current (pA) vs time (s) at each stage of modification (glass, silanised and TBA) alongside controls (random DNA sequence and TBA without protein over a concentration range (1 pM – 5nM) of thrombin. Additionally, representative peaks are shown for TBA-modified peaks. Thrombin concentrations (1-10 pM) are recorded at 10 kHz and low-pass filtered at 1 kHz, while concentrations (500 pM and above) are recorded at 50 kHz and low-pass filtered at 5 kHz. 108

Figure 4. 13. Histogram analysis of dwell time and peak amplitudes alongside dwell time vs peak amplitude scatter plots for a concentration range (1 pM – 5 nM) of thrombin in aptamer-modified pipettes. Number of events (N) at each concentration are as follows. N = 491 for 1 pM thrombin, N = 527 for 10 pM thrombin, N = 270 for 500 pM thrombin, N = 158 for 1 nM thrombin and N = 756 for 5nM thrombin. 109

Figure 4. 14. The dependence of concentration shown on a logarithmic scale as a function of dwell time (left) and dissociation constant (right).....110

Figure 4. 15. A graph showing voltage plotted against dissociation rate for 10 pM and 500 pM thrombin in aptamer-based nanopipettes.....112

Figure 4. 16. The dependence of molar electrolyte concentration on TBA-modified pipettes. (a) I/V traces of TBA-modified pipettes measured in 100 mM KCl (red) and 1 M KCl (blue), with the rectification ratio shown in brackets. (b) The dependence of molar concentration on thrombin translocation through TBA-modified pipettes. Traces show the translocation of 500 pM thrombin in 100mM KCl (left) alongside the translocation of 1pM thrombin in 1M KCl (right).....113

Figure 4. 17. Traces of current (pA) vs time (s) alongside representative peaks for (i) 1:50 human serum/100 mM KCl 1 x TE electrolyte mix, (ii) 10 pM thrombin in 100 mM KCl 1 x TE electrolyte (ii) and 10 pM thrombin in 1:50 human serum:100 mM KCl in 1 x TE electrolyte mix. All traces were filtered at 1 kHz and recorded at 10 kHz.....114

Figure 4. 18. Histogram analysis of dwell time (top row), peak amplitude (middle row) alongside dwell time vs peak amplitude scatter plots (bottom row) for three repeats of 10 pM thrombin in 1:50 human serum:100mM KCl in 1 x TE. Number of events for each repeat are as follows. N = 175 for repeat 1, N = 503 for repeat 2 and N = 154 for repeat 3.....114

Figure 4. 19. PSD of TBA-modified nanopipettes. (a) TBA-modified pipettes conducted in 100mM KCl without (blue) and with (red) 10 pM thrombin. (b) TBA-modified pipettes conducted in a 1:50 HS:100mM KCl without (blue) and with (red) 10 pM thrombn.....116

Figure 4. 20. The effects of low-pass filters on thrombin translocation through TBA-modified pipettes. (a) 500 pM thrombin translocation using a low-pass 10 kHz filter (i) as well as a low-pass 5 kHz filter (ii). (b) 10 pM thrombin using a low-pass 10 kHz filter as well as a low-pass 1 kHz filter (ii). (c) 10 pM thrombin translocation conducted in 1:50 HS:100mM KCl using a low-pass 10 kHz filter (i) and a low-pass filter 1 kHz filter (ii).....117

Figure 4. 21. Regeneration experiments conducted using TBA-modified nanopipettes. TBA-modified pipettes could be measured in solutions containing KCl only and 10pM thrombin with washing in TE buffer used to remove any thrombin. (a) The graph shows the rectification ratio plotted with each experiment corresponding to whether the TBA-modified pipettes is filled with thrombin or KCl. Traces corresponding to the above experiment were recorded with a sampling frequency of 50 kHz with a low-pass filter of 5 kHz. 118

Figure 4. 22. Traces showing the regeneration of the TBA-modified pipette using 1 pM thrombin as the substrate with TE washings were used to remove any residual thrombin. Trcaces were recorded at 10 kHz with a low-pass filter of 1 kHz. 119

Figure 4. 23. A likely mechanism of protein transport in aptamer modified pipettes alongside representative peaks. At low thrombin concentrations aptamer binding occurs (long dwell times) while at higher thrombin concentrations protein translocation dominates (short dwell times).....121

Figure 4. 24. The detection of ß-lactoglobin and ovalbumin using glass nanopipettes. 1 second traces (top) are shown at + 500 mV (red) and – 500 mV (blue) alongside dwell time vs amplitude scatter plots (bottom), with N = 1059 (ß-lactoglobin) and N = 1820 (ovalbumin). ß-lactoglobin was filtered with a low-pass filter 10 kHz and sampled at 100 kHz sampling rate, while ovalbumin was filtered with a 50 kHz low-pass filter and sampled at 500 kHz sampling rate. Figures adapted from reference 20.....123

Chapter 5

Figure 5. 1. (a) An overview of the causes of alpha synuclein monomer aggregation. (b) A schematic showing the primary structure of alpha synuclein monomers. The amphipathic region contains three mutants (A30P, E46K and A53T), while the non-amyloid component (NAC) region is responsible for aggregation. 128

Figure 5. 2. Commonly encountered alpha synuclein oligomer structures. 129

Figure 5. 3. Native function of alpha synuclein monomers. Alpha synuclein monomers are believed to have roles in the refilling and trafficking of synaptic vesicles from the reserve pool to the site of synaptic release. Figure adapted from reference 6. 130

Figure 5. 4. The various pathological disruptive mechanisms of toxic oligomers in neurons. Figure adapted from reference 5. 130

Figure 5. 5. The principles of sandwich based ELISA, an indirect yet highly sensitive based detection method. A 'capture' antibody localised on a well plate and 'detection' antibody linked to an enzyme (e.g Horseradish Peroxidase) are both selective to a specific antigen. Upon antigen binding and subsequent washing steps the introduction of enzyme based activity on a specific product leads to detection of a measurable product.....132

Figure 5. 6. Representative traces arising from alpha synuclein oligomer translocation through solid state nanopores at 100 mV in a 0.5M NaCl solution at pH 8.0. (a-c) WT oligomer detection after 6, 12 and 15 days. (d-f) E46K oligomer detection after 6, 12 and 15 days. (g-i) A30P oligomer detection after 6, 12 and 15 days. Figure adapted from reference 13.....133

Figure 5. 7. Colour contour plots of $\Delta I/I_o$ vs log td (µs)(i) and $\Delta I/I_o$ histogram plots for E46K mutant oligomer aggregates at (a) 6 days, (b) 12 days and (c) 15 days. Figure adapted from reference 13. 133

Figure 5. 8. (a) A schematic showing the movement of alpha synuclein through the alpha-hemolysin pore. Unfolded alpha synuclein monomer (left) is allowed to freely translocate through the pore while a partially folded intermediate (right) is captured. (b) A characteristic event (left) alongside mechanism of capture for an alpha synuclein monomer within the vestibule of alpha-hemolysin. (1) Upon application of voltage (100 mV), a drop in the open pore current (L_o) is observed due to translocation of the unfolded alpha synuclein monomer. (2) The applied field can induce folding allowing capture (L_c). (3) Elongation/ordering of the alpha synuclein can result in a further current decrease (L_b). Capture can be reversed by reducing the applied voltage to 40 mV. (c) A dwell time vs peak current scatter plot shows two different event types. The translocation events (TE) corresponding to the L_o to L_c (blue scatter) are generally short-lived (ms to s) and have greater

amplitudes (20-80 pA). Capture events (CE) corresponding to the Lc to Lb transition generally have small amplitude (18pA) and longer dwell times (up to minutes). Figure adapted from reference 14. 134

Figure 5. 9. Traces (current (pA) over time (s)) alongside representative peaks at each stage of the modification process (unmodified, silanised and TS-0530 modified) alongside controls (random 24mer control sequence and TS-0530 before protein addition) over a concentration range (500 pM – 5 nM) for 8 h oligomers aggregates. A low pass filter of 5 kHz was used alongside a scanning rate of 50 kHz. 136

Figure 5. 10. Histogram analysis of dwell time (top row), peak amplitude (middle row) alongside dwell time vs peak amplitude scatter plots (bottom row) for a concentration range (500 pM – 5 nM) of 8h oligomer aggregates. Number of events (N): N = 151 for 500 pM, N = 457 for 1 nM and N = 442 for 5 nM. 136

Figure 5. 11. Traces (current (pA) over time (s)) alongside representative peaks at each stage of the modification process (unmodified, silanised and TS-0530 modified) alongside controls (random 24mer control sequence and TS-0530 before protein addition) over an aggregation timepoint range (0h – 16h). The oligomer concentration was 1 nM while a low-pass filter of 5 kHz was used alongside a scanning rate of 50 kHz. 138

Figure 5. 12. (a) Histogram analysis of dwell time (top row), peak amplitude (middle row) alongside dwell time vs peak amplitude scatter plots (bottom row) across an oligomer (1 nM) aggregate timepoint range (2 – 16 h). Number of events (N) are as follows. N = 739 for 2 hours, N = 814 for 4 hours, N = 348 for 6 hours, N = 457 for 8 hours, N = 88 for 10 hours and N = 681 for 16 hours. (b) A plot showing the dwell time of binding events as a function of the oligomer aggregation timepoint. 139

Figure 5. 13. AFM images allowing determination of the oligomer radius at different stages of the aggregation process. Images courtesy of Imperial PhD student Giulia Campolo. 141

Figure 5. 14. A schematic showing the dwell time magnitude as a response to the aggregation timepoint. 142

Chapter 6

Figure 6. 1. The dissociation constant as a function of voltage at different distances away from the nanopore tip. Inset z_1 = 5.5 nm (black circles), z_2 = 25.5 nm (red circles), z_3 = 45.5 nm (green triangles) and z_4 = 65.5 nm (inverted blue triangles). 152

List of Tables

Chapter 1

Table 1. 1. A comparison of the different types of nanopores 32

Chapter 2

Table 2. 1. The pulling programme parameters used in the construction of nanopipettes utilising the Sutter P-2000 instrument. Heat' refers to the magnitude of laser power used while 'Filament' refers to the longitudinal length of the capillary heated. 'Velocity' is related to the speed of the pull while 'Delay' refers to the time between the laser being switched off and the subsequent pull and finally 'Pull' is related to the force of the pulling motion. 63

Chapter 3

Table 3. 1. The rectification ratio (V = ± 430) at each stage of the modification process (n =8) 82

Table 3. 2. The RMS value of KCl electrolyte only alongside translocation of 10 pM 29 mer control sequence and a 10 pM 29 mer complementary sequence. 83

Table 3. 3. The RMS value of KCl electrolyte only alongside translocation of 10 pM 29 mer control sequence and a 10 pM 29 mer complementary sequence. 84

Table 3. 4. An overview of the length of the modification as well as the resulting diameter of the functionalised pipette. 87

Table 3. 5. The experimentally calculated rectification ratio and theoretical pKa values for each stage of the modification process.....90

Chapter 4

Table 4. 1. Normalised peak amplitudes of events for a thrombin concentration range. Values represent mean ± standard deviation (n = 3).....110

Table 4. 2. Capture rates of events for thrombin (1 pM – 5 nM). Values represent mean ± standard deviation (n = 3). Values in red showcases examples of the capture rate being over-estimated when calculated via inter-event (t_{on}) measurements. 110

Table 4. 3. Polarity of binding events for thrombin (1 pM – 5 nM) used in the concentration assay for each repeat (n = 3). 111

Table 4. 4. A voltage-based (300-500 mV) assay at 10 pM and 500 pM including peak amplitude, dwell time and capture rate analysis for aptamer-based nanopipettes. 111

Table 4. 5. Average values of normalised peak amplitudes, dwell times and capture rates for three repeats of 10 pM thrombin translocation conducted using 1:50 human serum:100mM KCl in 1 x TE in TBA-modified pipettes. 115

Table 4. 6. RMS values at different stages of the modification process when recorded in 100 mM KCl 1 x TE only and 10 pM thrombin in 100 mM KCl in 1 x TE. (b) RMS values of different solutions in TBA-modified pipettes include 100mM KCl, 1 x TE, with and without 10 pM thrombin as well as 1:50 human serum to 100 mM KCl with and without 10 pM thrombin. 115

Chapter 5

Table 5. 1. Average values of normalised peak amplitude, dwell time and capture rate (n = 1).....137

Table 5. 2. The normalised peak amplitude and capture rate across the oligomer aggregation timepoint. 139

Chapter 6

Table 6. 1. An overview of protein biomarkers and their associated aptamers. 151

List of Equations

Chapter 1

Equation 1. 1. The Smoluchowski equation, where J is the rate of free diffusion ($mols^{-1}$), c is the bulk analyte concentration ($moldm^{-3}$), D is the diffusion constant (m^2s^{-1}) and r_p is the pore radius (nm)...38

Equation 1. 2. The rectification ratio (r) provides a numerical value of the phenomenon. I refers to the current (pA) at voltage (mV). 40

Equation 1. 3. The polarity of translocation peaks. ΔG refers to the polarity of peaks while – G_{resist} refers to the loss of ionic conductance (S) and $G_{conduct}$ refers to the gain in ionic conductance (S).....40

Equation 1. 4. A simplified model used to estimate the polarity *of peaks as a measure of change in conductance* ($\Delta G, S$) of DNA translocations in KCl solution, where d is the diameter of the molecule (nm), L is the length of the pore (nm), μ_K and μ_{Cl} are electrophoretic mobilities of K^+ and Cl^- ions ($m^2V^{-1}s^{-1}$) respectively, n_{KCl} is the number density of potassium or chloride ions (Mm^{-3}), e is the elementary charge (C), μ_K* is the effective electrophoretic mobility of K^+ moving along the DNA ($m^2V^{-1}s^{-1}$) and q_{DNA}* is the effective charge on the DNA per unit length (Cm^{-1}).....41

Equation 1. 5. An expression showing effective velocity (v, ms^{-1}) of protein movement through a nanopore, where ζ is the zeta potential (mV), η is the viscosity (Nsm^{-2}), E is the external electric field (Vm^{-1}) and ε is the permittivity (Fm^{-1}). 43

Equation 1. 6. The kinetic rate constants for analyte dissociation (K_{off}, s^{-1}) and analyte association (K_{on}, $mol^{-1}dm^3s$) where t_{off} is dwell time (s), t_{on} is inter-event time (s) and c is the concentration ($moldm^{-3}$).....46

Chapter 2

Equation 2. 1. Calculation of the root-mean-square (RMS) for the total number of samples (n) over a set of values (x_n). 73

Chapter 3

Equation 3. 1. Estimation of the nanopore tip diameter through conductance measurements where d_i = nanopore diameter (nm), D_i = internal glass capillary diameter (mm), σ = electrolyte conductivity (Sm^{-1}), G = conductance (S) and l = taper length (mm). 85

Abbreviations

A	Ampere
pA	Picoampere
Ag	Silver
AgCl	Silver Chloride
ACPC	Activatable cell-penetrating peptides
AD	Alzheimer's Disease
AFM	Atomic force microscopy
AMPA	α-amino-3-hydroxy-5-methylis-oxazole-4-propionic acid
AU	Analytical ultracentrifugation
BBB	Blood brain barrier
CD	Circular dichroism
CNS	Central nervous system
CSF	Cerebral spinal fluid
Cu(I)	Copper 1+ ions
CuAAC	Copper-catalysed azide alkyne cycloaddition
CSF	Cerebral Spinal fluid
DNA	Deoxyribonucleic acid
ssDNA	Single stranded DNA
dsDNA	Double stranded DNA
EAE	Experimental autoimmune encephalomyelitis
EDL	Electrical double layer
EDTA	Ethylenediaminetetraacetic acid
ELISA	Enzyme-Linked ImmunoSorbent Assay
ELONA	Enzyme-linked oligonucleotide assay
Fwhm	Full width half maximum
FRET	Fluorescence resonance energy transfer
G4	G tetrad
hCG	Human chorionic Gonadotropin
HRP	Horseradish Peroxidase
HS	Human serum
Hz	Hertz
kHz	Kilohertz
MHz	Megahertz
Ig	Immunoglobin
ICR	Ion current rectification
I/V	Current-Voltage
KCl	Potassium Chloride
KOH	Potassium Hydroxide
KCl	Potassium chloride
L	Litre
µL	Microlitre
M	Molar
nM	Nanomolar
pM	Picomolar
µM	Micromolar
mab	Monoclonal antibody
MS	Multiple Sclerosis
NaCl	Sodium chloride
NaN3	Sodium azide
NHS	N-Hydroxysuccinimide
NTA	Nitrilotriacetic acid
pKA	Acid dissociation constant
PD	Parkinson's Disease
PSD	Power spectrum density
RMS	Root mean square
RNA	Ribonucleic acid
Rpm	Revolutions per minute
s	Second
µs	Microsecond
S/N	Signal to noise ratio
SAM	Self-assembled monolayers
SELEX	Systematic evolution of ligands by exponential enrichment
SEM	Scanning electron microscope
SERS	Surface enhanced Raman scattering
SiN	Silicon nitride
SiO2	Silicon dioxide
SNpc	*Substantia nigra pars compacta*
SNARE	SNAP Receptor
SNAP	Soluble NSF attachment proteins
TBA	Thrombin binding aptamer

TCEP	Tris(2-carboxyethyl)phosphine
TE	Tris-EDTA
TEM	Transmitting Electron Microscope
THF	Thioflavin
TMSPM	3-(trimethoxysilyl)propyl methacrylate
TS-0530	Anti-oligomer binding aptamer
TNF-α	Tumour necrosis factor alpha
V	Voltage
VAMP	Vesicle associated membrane protein
VEGF	Vascular endothelial growth factor
VWF	Von Willebrand factor
WT	Wild type
ß-sheet	Beta sheet
io	Open pore current
kD	Dissociation constant
K_{off}	Kinetic rate for dissociation
K_{on}	Kinetic rate for association
Kb	Kilobase
ΔI	Peak amplitude
t_{off}	Dwell time
t_{on}	Inter-event time

Chapter outline

Chapter 1 provides an overview of the fundamentals of the project including nanopore sensing, aptamers and the chosen biomarkers; thrombin and alpha-synuclein oligomers. The problems of protein detection using the stochastic based detection of unmodified nanopores are presented alongside potential solutions.

Chapter 2 outlines the techniques and materials used throughout the PhD project, including the fabrication and modification of nanopipettes, the set-up used in the electrochemical experiments alongside data analysis.

Chapter 3 details the methodology used to fabricate the nanosensor substrate followed by the step by step methodology used for aptamer attachment. In addition, the methods for characterising the functionalised sensor via electrochemical means are described.

Chapter 4 provides characterisation of the aptamer-based nanosensor using thrombin as a model analyte. In particular, the effects of voltage and concentration dependence are explored while testing its ability to detect in a multi-protein analyte.

In **Chapter 5** the use of aptamer-modified nanosensors is described for the detection of alpha-synuclein oligomers; the biomarkers of Parkinson's Disease. Alpha-synuclein oligomers are challenging to detect due to their large variety in the presence of monomer precursors as well as lower affinity aptamer.

Chapter 6 provides a conclusion of our work so far and provides an overview of the modified sensor in application to protein biomarker detection.

Chapter 1: Introduction

1.1. Overview *27*

1.2. Protein Biomarkers *27*

1.2.1. Protein aggregates as biomarkers **27**

1.3. Single molecule detection *29*

1.4. Nanopore *31*

1.4.1. Nanopore types **32**

1.4.1.1. Biological 32

1.4.1.2. Solid state 33

1.4.1.3 Hybrid nanopores 34

1.4.1.4 Nanopipettes 35

1.4.2 Nanopore properties **36**

1.4.2.1 Ion blockade sensing 36

1.4.2.2 Electrical double layer 37

1.4.2.3. The driving forces of translocation 38

1.4.2.4. Ion current rectification 39

1.3.2.5 Ion blockade conductance 40

1.4.4 Limitations of protein detection using nanosensors **41**

1.4.4.1. Low capture rate 41

1.4.4.2. Low signal to noise ratio (SNR) 42

1.4.4.3. Effects of electroosmosis and electrophoresis 42

1.4.4.4. Limited selectivity **44**

1.5. Aptamers *46*

1.5.1. Binding mechanism **47**

1.5.2 G-quadruplex based aptamers **48**

1.5.2.1 Structure 48

1.6. Solutions to detect protein translocation in nanopores *48*

1.6.1. Receptor modified carrier **49**

1.6.2. Receptor modified nanopores **51**

1.7. Thesis aim and objectives *55*

1.8. References *56*

1.1. Overview

The introductory chapter provides insight into the importance of single molecule detection[1], especially in regards to protein biomarker detection[2]. The PhD project has been focused on the detection of thrombin[3] (Chapter 4) which has links to pulmonary metastasis[4] and cancer[5], together with protein aggregates of alpha synuclein monomers[6] (Chapter 5), which are linked to Parkinson's Disease[7] (PD). The developed sensor combines the single molecule detection capability of nanosensors,[8-14] with the selectivity of proteins recognition through the use of aptamers (short single stranded DNA)[15].

1.2. Protein Biomarkers

Biological markers commonly termed biomarkers[2], can be broadly described as being a characteristic molecule, or response, that can be measured and evaluated as being diagnostic of a biological, or pathogenic process, or a pharmacological response to a therapeutic agent. In the proposed project, the aim has been to sensitively and selectively detect two protein biomarkers; thrombin[3] and alpha synuclein oligomers[6] which are found in the bloodstream and cerebral spinal fluid (CSF) respectively. Thrombin was chosen as a well-studied model protein whose detection in a complex analyte, could allow it to be used as a biomarker of multiple sclerosis and cancer. Alpha synuclein oligomers were selected as the likely biomarkers and toxic components of Parkinson's Disease.

In both cases, protein biomarker detection is currently problematic due to their low concentration (< nM) in highly complex solutions. However, the early detection of such biomarkers could afford diseases to be treated before the onset of clinical symptoms, improving the prognosis of patients. As a result, there is a need to develop new technology to detect protein biomarkers which allows detection with high selectivity and high sensitivity. Single molecule detection[1], provides additional benefits of allowing distinct populations of biomolecules (based on size and morphology) to be probed.

1.2.1. Protein aggregates as biomarkers

Multiple neurodegenerative disorders are associated with the aggregation of proteins[16]; for example amyloid ß[17] and alpha synuclein[6] in Alzheimer's Disease and Parkinson's Disease respectively. *In vitro,* protein aggregation[18] typically occurs at 37°C (pH 7.4) with agitation significantly speeding up the process from months to days. Classical nucleated polymerisation[19] described in Figure 1.1 has been previously used to describe aggregation.

Initially, a slow lag phase (nucleation) resulting from the conversion of soluble protein to insoluble aggregates, is followed by an exponential growth (elongation) phase whereby monomer species add sequentially on to the growing aggregate. Eventually, a steady-state plateau is reached; whereby the aggregate and monomer populations are at equilibrium. The aggregation of a given protein can be studied *in-situ* using the fluorescent dye thioflavin (THF)[20]. THF fluorescence increases with ß-sheet content associated with the protein aggregation process.

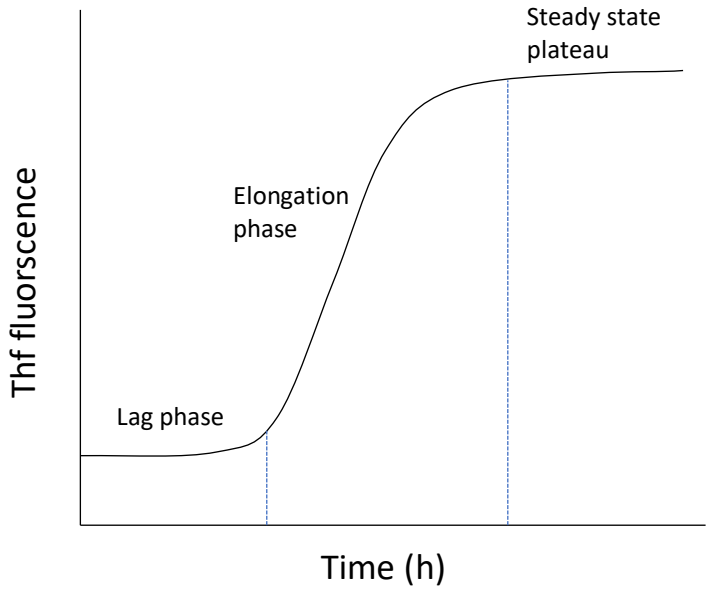


Figure 1. 1. *Aggregation of protein occurs via a nucleated polymerisation process, an initial lag phase is followed by an exponential elongation before culminating in a steady state plateau. THF fluorescence, a ß-sheet binding dye is used to characterise the aggregation process.*

In reality, the aggregation of alpha synuclein is far more complex as shown in Figure 1.2. In primary nucleation (stepwise monomer addition) there is evidence suggesting that intrinsically disordered monomers fold to a more 'active' partially folded intermediate[21]. By doing so hydrophobic regions become exposed allowing the step-wise addition of monomers to occur. Alongside the formation of off-target oligomers, the aggregation process involves the initial formation of smaller less ordered oligomers before their conversion to larger oligomers which typically have a higher proportion of ß-sheet structures. Further ordering occurs through the formation of proto-filaments which associate to form highly ordered fibrils, the major component of Lewy bodies.

Moreover, secondary nucleation (Figure 1.2, bottom) involve processes whereby aggregation is linked through the formation of new nuclei through existing aggregates. As opposed to classical nucleated polymerisation, such secondary nucleation processes are

able to occur during the lag phase, resulting in rapid growth and the alteration of kinetics. For example, the fragmentation of large aggregates, leads to the formation of smaller aggregates accompanied by an increase in 'free ends', and additional monomer growth. Furthermore, surface catalysed based seeding[22], a process by which formed fibrils act as templates for monomer growth can also lead to the acceleration of aggregation. Finally, prion-like spreading describes how amyloid aggregates are able to spatially propagate from cell to cell through mechanisms such as diffusion or seeding.

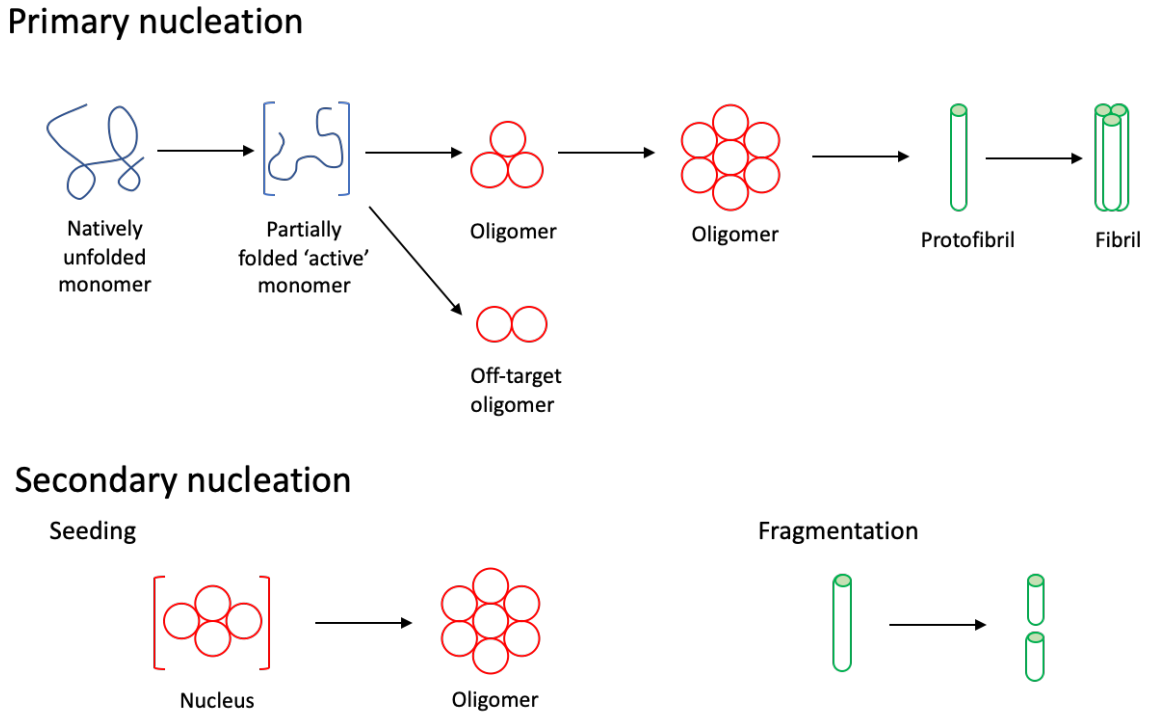


Figure 1. 2. *A schematic showing the aggregation process*

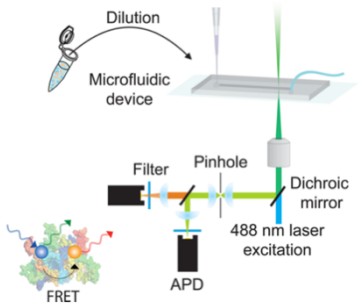
1.3. Single molecule detection

Single molecule detection is most widely characterised using microscopy (electron[23-24], scanning probe[25] and super-resolution[26]) or electrochemical (i.e. nanopore) methods. Not only does single molecule detection allow analyte detection at very low concentrations (< nM), but also allows greater information on molecular conformation which is lost in conventional bulk analysis techniques. Single molecule based electron microscopy (e.g scanning electron microscopy[23], or transmission electron microscopy[24]) require very clean non-solution based samples, while scanning-probe microscopy[25] (e.g atomic force microscopy) generally has very low throughput. Typically, such techniques while invaluable for structural characterisation, are less suitable for biomarker detection due to their low-

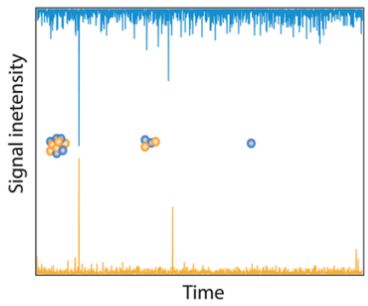
throughput and lack of specificity. On the other hand, super-resolution microscopy[26] when coupled with FRET (fluorescent resonance energy transfer) allowing determination of structural information and microfluidics (allowing increased throughput), have been previously used to study alpha synuclein aggregation and oligomer detection[27].

In the FRET study[27], alpha synuclein monomers were labelled with two compatible fluorophores (donor alexa fluorophore 488 and acceptor alexa 594) and then aggregated over several hours. The set-up (Figure 1.3(a)) involves the microfluidic delivery of the samples alongside excitation with a 488 nm laser, and fluorescence detected using Avalance Photodiode Detectors. Figure 1.3(b) shows signal intensity of donor fluorophores (blue) and acceptor fluorophores. Monomeric species are indicated by bursts in the donor channel, while simultaneous bursts in the donor and acceptor channel indicate only FRET resulting from oligomeric species. As shown in Figure 1.3(c), the frequency of donor bursts decreased with aggregation time. This could be explained by monomers being incorporated into oligomers and fibrils, resulting in a decrease in the concentration of donor fluorophores. Conversely, FRET efficiency and size increased with aggregation time ((Figure 1.3(d)). Overall, single molecule fluorescence detection showed that the aggregation process could be followed through FRET combined with the inverse relation of donor bursts over time.

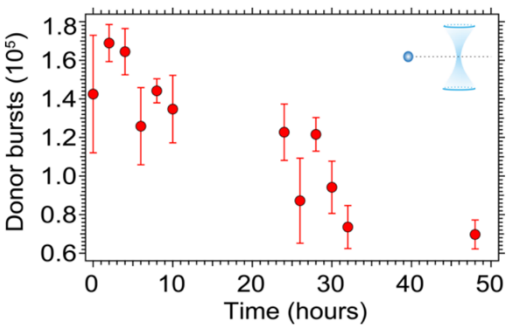
(a)



(b)



(c)



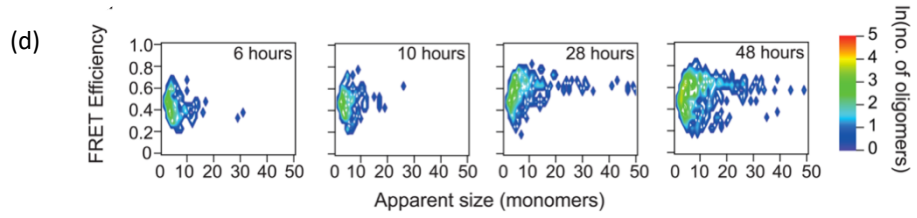


Figure 1. 3. *Single molecule fluorescent-based detection of alpha synuclein oligomers. (a) Instrumental set-up. A microfluidic device (used for sample delivery) is mounted onto a confocal microscope. Fluorescence from Alexa Fluor 488 and Alexa 594 (indirectly via FRET) are collected via separate Avalanche photodiode detectors (APD). (b) Examples of intensity traces involving donor fluorophore alexa 488 (blue) and acceptor fluorophore alexa 594 (red). Monomeric bursts are donor bursts only while oligomeric species have bursts in the donor and acceptor channel. (c) Number of donor burst as a function of time during the aggregation of alpha synuclein. The donor burst decreases as monomers incorporate into oligomers and fibrils due to the lower concentration (d) A 2D contour plot of size and FRET efficiency of alpha synuclein at various aggregation timepoints. Both the size and FRET efficiency increases with aggregation time. Figure adapted from reference 27.*

While fluorescent single molecule techniques are powerful, there are a few inherent disadvantages to the technique. Most importantly, fluorescent based detection techniques methods aside from requiring fluorescent tags, also require further labelling with recognition elements (e.g antibodies), if detection is to be carried out in complex biological samples. Labelling with antibodies, even with sufficient selectivity can result in altered protein aggregation, which is particularly critical in the case of neurodegenerative diseases (e.g Parkinson's Disease), where aggregation is a key hallmark. Alternatively using recombinant proteins expressed to contain an in-built tag (e.g His tag) are likely to have biophysical properties that deviate significantly from their wild-type counterparts. Furthermore, labelling (either with fluorophores or antibodies) often results in low yields and is expensive. As a result, an alternative label-free single molecule detection technique involving nanopores was explored.

1.4. Nanopore

A nanopore[8-14] is a small aperture (<1-100 nm) contained within an electrically insulated membrane, which in turn separates two electrolyte (typically KCl or NaCl) solutions. Nanopore sensors have attracted great promise due to their ability to detect single biomolecules without requiring analyte labelling including dsDNA[28] (typically between 5-10kbp), RNA[29], ssDNA[30] and proteins[31]. Single molecule detection allows measurement of the subtle differences between analyte molecules (i.e. folded vs linear DNA), providing a distinct advantage over the ensemble averaging seen in bulk measurement techniques[32]. Although the detection of biomolecules has been continuously improving, with the mechanism well understood in the case of DNA translocation[33], the main drive behind nanopores has always been in DNA sequencing. While nanosensors have previously shown

single base resolution[34], not only did DNA samples have to be prepared before sequencing, but had to be translocated through biological pores that had undergone site-directed mutagenesis. MinIon[35], a commercial and portable nanopore developed by Oxford nanopores, still has a relatively high error rate but has achieved significant progress in achieving high throughput DNA sequencing. Meanwhile, the modification of nanopores to include receptors (aptamers/antibodies) to form biosensors is now possible, being characterised by ion current rectification[36], a phenomenon seen in nanoscale dimensions.

1.4.1. Nanopore types

Nanopores are typically categorised as biological[10], or as solid state[8-9], although recently hybrid nanopores[37] showcasing characteristics of both have been developed. Furthermore, nanopipettes[38-39], the basis for the sensors used in the project and a sub-type of solid state nanopores prepared using a unique fabrication method have also been described. An overview of the different types of nanopores can be found in Table 1.1 below.

***Table 1. 1**. A comparison of the different types of nanopores*

	Biological	**Solid state**	**Nanopipette**
Channel Size	Fixed pore size	Can be finely tuned (and visualised if using SEM)	Can be finely tuned
Pore stability	Susceptible to extreme changes in environmental (pH, temperature)	High chemical, thermal and mechanical stability over a range of conditions	High chemical, thermal and mechanical stability over a range of conditions.
Support Stability	Lipid matrix is fragile, although can be circumvented with the use of polymers	Durable	Durable
Reproducibility	Highly reproducible	The size and shape can be engineered precisely with some variability	The size and shape can be engineered precisely but variation is still a problem
Modification	Genetic engineering provides a wealth of options but is time consuming	Modifications are based on well-defined silane chemistry	Modifications are based on well-defined silane chemistry
Integration into devices	Supporting lipid substrate is a major limitation for use	Readily integrated	Fabricated as a sensor
Cost	Large quantities at small cost can be harvested in cells.	Fabrication costs are decreasing yet remain significant	Glass capillaries are relatively cheap

1.4.1.1. Biological

Biological nanopores are formed from the self-assembly of protein channels and pores when embedded in a lipid membrane. The most widely used pore; α-hemolysin[40] (Figure 1.4) is derived from *Staphylococus aureus* which in nature functions as a toxin. The pore formed through the self-assembly of seven identical polypeptides contains a 14-stranded transmembrane β-barrel and an external cap region. Unfortunately, the α-hemolysin pore

size lumen (14 Å) is too small for dsDNA (and therefore sequencing) but remains compatible with ssDNA translocation.

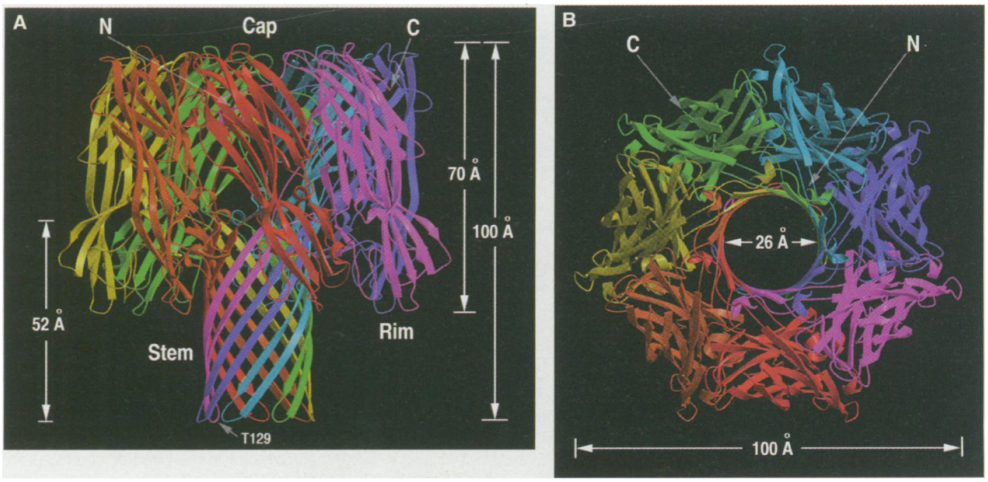


Figure 1. 4. *Ribbon representations of the αlpha-hemolysin pore. A) View perpendicular to the sevenfold axis and parallel to the membrane plane. The height is approximately 100 Å, while the stem domain measures 52 Å. Also shown are the locations of the cap, stem and rim regions. B) View from the top of the structure and parallel to the sevenfold axis highlighting the diameter of alpha-hemolysin (100 Å at parts) as well as the inner diameter of the stem region (26 Å). Figure adapted from reference 40.*

Biological nanopores are highly reproducible, cheap and easily produced with genetic engineering allowing for their precise modification. Despite these advantages, biological nanopores are unstable to extreme environmental conditions (pH, temperature), and have a fragile lipid support matrix[10, 12], and a fixed pore size that limits flexibility in design. In addition, the precise insertion of a biological nanopore in a lipid membrane is difficult due to the constant internal lateral diffusion[10, 12]. As a result, biological nanopores were concluded to be unsuitable for the project due to their limitation at detecting larger proteins (e.g. oligomers) and their instability, which would limit future construction as nanofluidic devices *in vivo*.

1.4.1.2. Solid state

Solid state nanopores are formed via a variety of techniques, but most commonly via high energy beam (electron or ion) milling of a given material, typically Silicon-based. Figure 1.5(a) shows TEM (Transmitting Electron Microscope) images of a solid state nanopore[41] (diameter 19 nm) formed by electron beam lithography in SiO_2. Pore shrinking (Figure 1.5b-d) can be accomplished through application of a low energy electron beam, resulting in pore shrinking and precise control of the nanopore diameter.

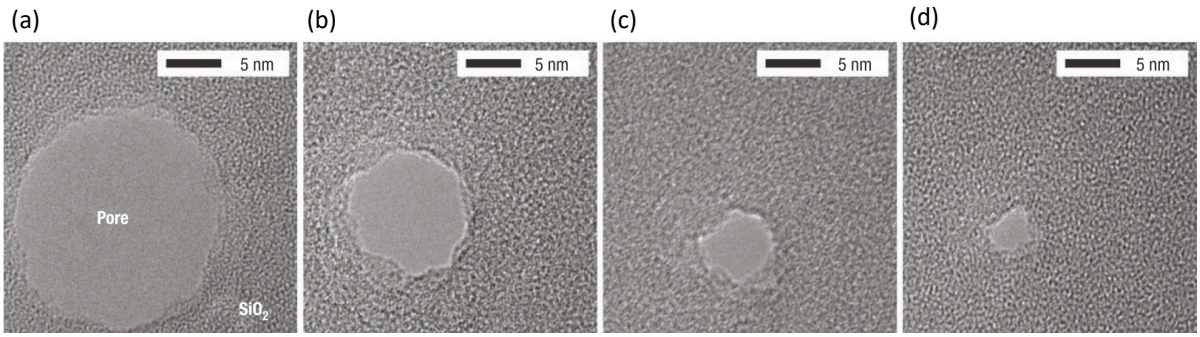


Figure 1. 5. *TEM images of solid state nanopores. Figure 1.5a shows a nanopore formed via electron beam lithography. Figures (b-d) shows pore shrinkage accomplished by subsequent application of a high energy electron beam. Figure adapted from reference 41.*

While the production of solid state nanopores in this fashion is less reproducible, and is relatively expensive and time-consuming, modifications can be carried out through well understood silane chemistry[42] and structures that are importantly stable *in vitro.* Furthermore, an inherent advantage is that pore shrinking with the ion or electron beam allows precise control and can be stopped upon reaching the desired diameter. Overall, while offering a balance between great stability and reproducibility; ultimately the high cost and time-consuming nature of such fabrication was considered to be the limiting factor. This can be attributed to the low modification efficiencies encountered with nanopores, necessitating the production of large batches (e.g above 20) of sensors.

1.4.1.3 Hybrid nanopores

Hybrid nanopores aim to combine the advantages of biological nanopores (atomically precise structures with the potential for genetic engineering) with solid state nanopores (durable and offering great control of dimensions). For example, Hall formed hybrid nanopores through the insertion of alpha-hemolysin within a solid-state silicon nitride (SiN) nanopore[37]. Alpha-hemolysin was mutated to include a cysteine allowing coupling to a thiol-derivatised single-stranded nucleotide. Hybridisation of a 3 kbp 'guide strand' (Figure 1.6(a)) then allowed the construct to be electrophoretically driven through the solid state nanopore (Figure 1.6(b)). The diameter of the solid state nanopore was chosen to be around 2.4-3.6 nm accommodating the tail and stem of alpha hemolysin but not the cap region. The hybrid nanopore could be used to detect ssDNA which was resolved as discrete blockade events.

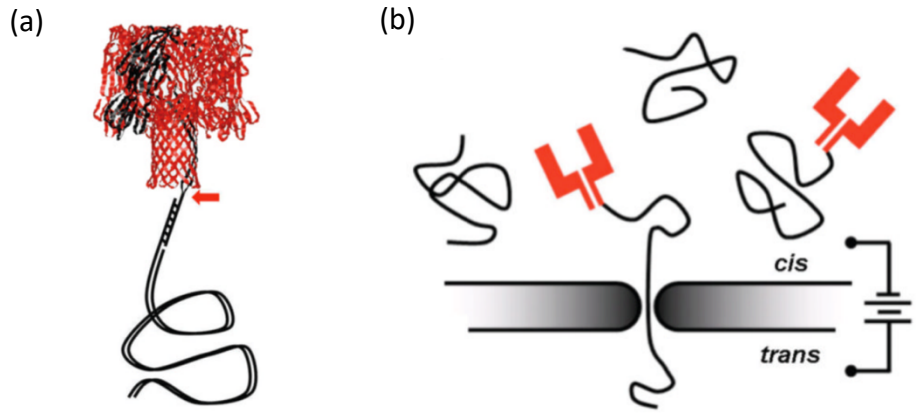


Figure 1. 6. *(a) An alpha hemolysin is mutated to contain a cysteine allowing the covalent attachment of a thiol modified 12 nucleotide. Hybridisation of the sticky end allows incorporation of a 3 kbp dsDNA 'guide' strand. (b) Insertion of the hybrid nanopore into the narrow solid state nanopore is carried out electrophoretically. Figure adapted from reference 37.*

1.4.1.4 Nanopipettes

Glass nanopipettes[43] are hollow structures with openings in the region of 1 to 100 nm (Figure 1.7). Nanopipettes can be fabricated from glass capillaries at low expense using commercially available pullers. The pulling parameters (laser power, pulling time) alongside the capillary diameter can be varied to create nanopipettes of different dimensions and taper lengths.

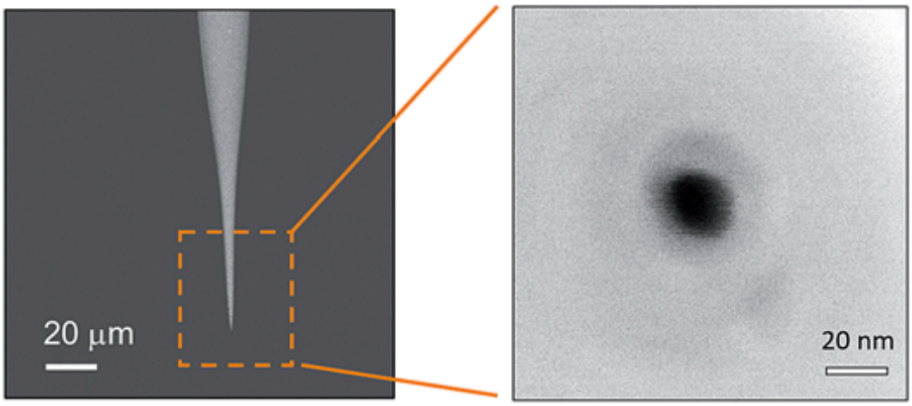


Figure 1. 7. *A glass nanopipette tip (left) alongside the zoomed in tip of the nanopore (right). Figure adapted from reference 43.*

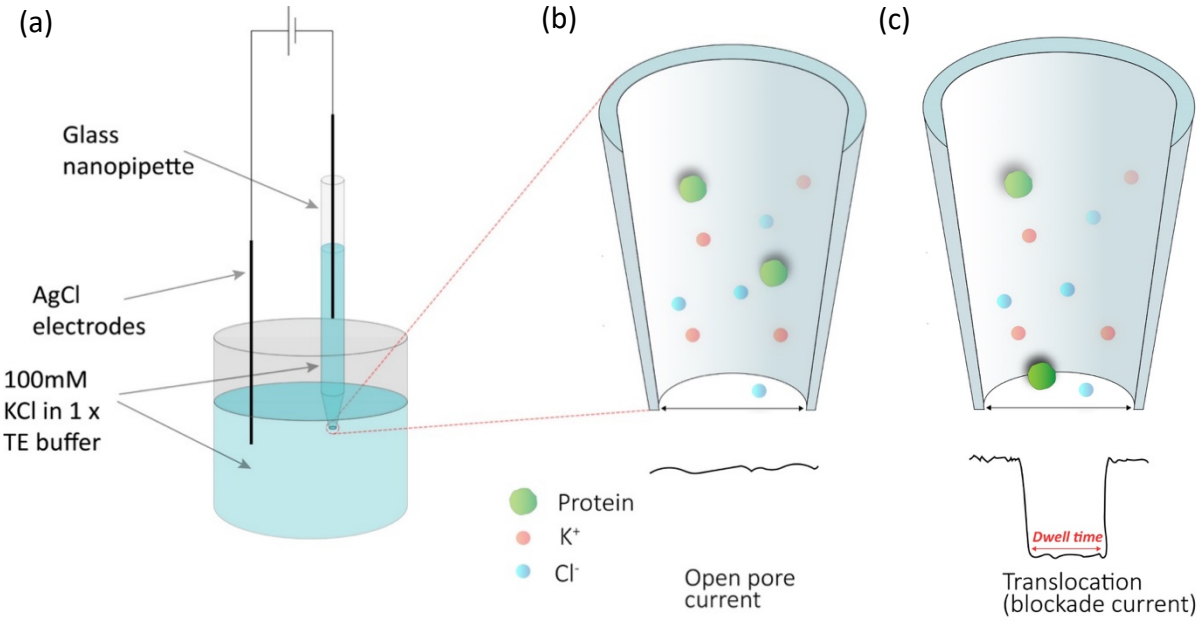
Overall, despite disadvantages in variation, nanopipettes were the preferred choice as a substrate for constructing an aptamer-based nanosensor device. The size of the nanopipettes can be tuned to detect large protein aggregates as well as monomeric precursors, while still being stable over long experimental time periods. Furthermore, the production of multiple nanopipette sensors is not only low-cost, but fast, making them a practical effective sensor for the medical industry. A more extensive overview of nanopipette fabrication can be found in chapter 2.

1.4.2 Nanopore properties

Here, an outline is provided of the workings and properties of nanopores, that are unique due to their nanoscale dimensions. Also detailed are the effects of experimental conditions used, as well as the methodologies used in their modification.

1.4.2.1 Ion blockade sensing

Nanopores function via a process known as ion-blockade sensing[44] as illustrated in Figure 1.8(a). In this system, a nanopipette filled with an analyte dissolved in electrolyte (typically KCl), is immersed into a bath containing the same electrolyte (same concentration, without the analyte). Upon application of a voltage bias (mV), ion exchange occurs leading to a small (pA) but measurable ionic current (Figure 1.8(b)). The ionic current generated commonly known as the open pore current (i_o) remains stable unless the passage of ions is blocked by an analyte in a process known as translocation. Translocation (Figure 1.8(c)) leads to an ionic-current blockade (also known as resistive pulse sensing), whereby the current either momentarily increases (enhancement), or decreases (blockade). Resultant peaks (Figure 1.8(d)) can be analysed to abstract the amplitude (ΔI) and dwell time (t_{off}) which is related to the charge and size respectively of the analyte (Figure 1.8(d)). Meanwhile, the concentration of the analyte can be inferred from the inter-event time (t_{on}).



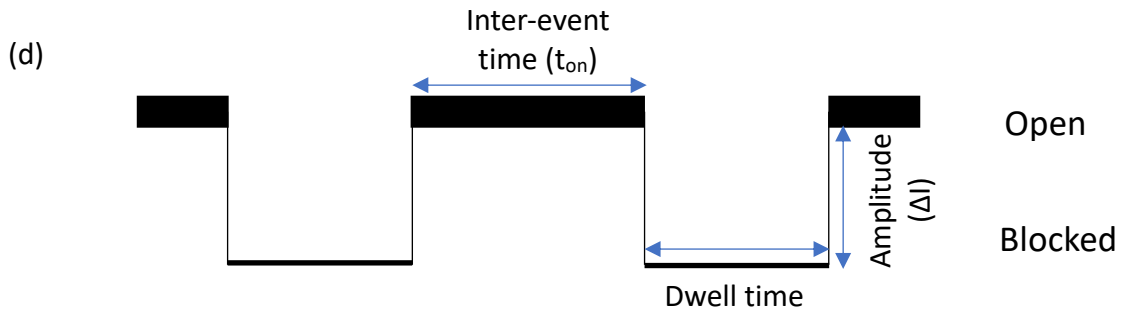


Figure 1. 8. *The basic principles of ion-blockade sensing. (a) A schematic showing a typical nanopore set-up. (b) Application of a voltage bias lead to production of an ionic current (b), which is momentarily disrupted upon passage of an analyte (c) otherwise known as translocation. (d) A schematic showing the characteristics of a typical translocation event. The dwell time (t_{off}) is the width of the peak and is related to the size of the molecule, the peak amplitude (ΔI) is related to the analyte charge and inter-event time (t_{on}) is related to the analyte concentration.*

1.4.2.2 Electrical double layer

The electrical double layer[45] has extensive implications to the function of nanoscale devices and is a vital component of rectification and electroosmosis as explained later in the chapter. As seen in Figure 1.9, intrinsic fixed negative surface charges (when conducted at pH 8.0) of the nanopipette wall attract oppositely charged ions in solution, leading to the formation of an electrical double layer (EDL), thereby maintaining electrical neutrality. The EDL typically in the region of 1-30 nm consists of an inner closely bound layer (stern layer) with an outer diffuse layer. The EDL is greater with surfaces with higher charge density as additional counterions are required to maintain charge neutrality. Likewise, in less concentrated electrolyte solutions, ions are less shielded, thereby experiencing an increased influence due to the surface charge.

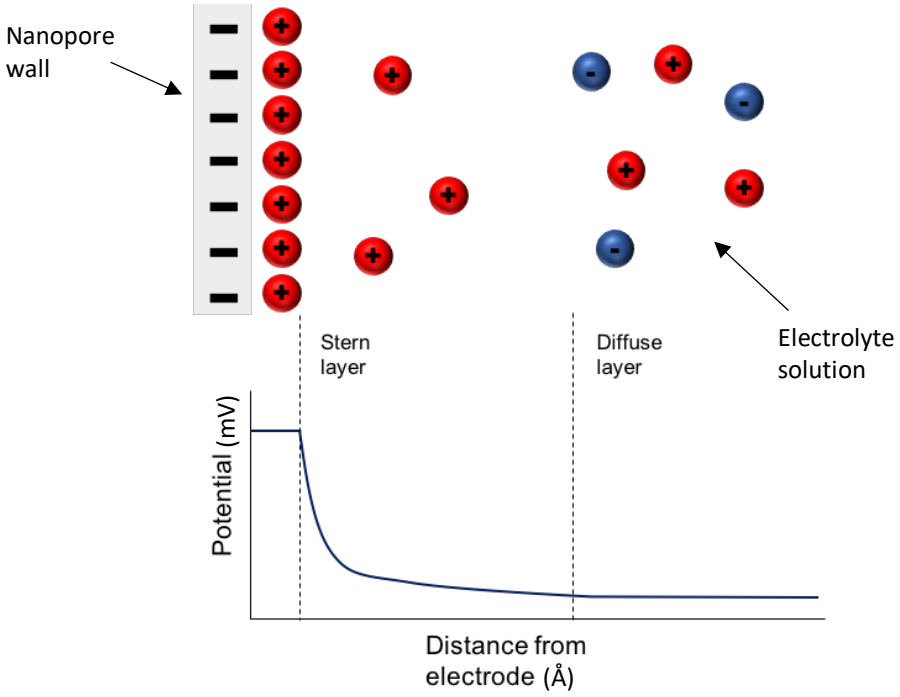


Figure 1. 9*. The EDL formed in nanochannels consist of an inner stern layer and a diffuse layer. The size of the EDL layer depends on the surface charge, as well as the electrolyte concentration.*

1.4.2.3. The driving forces of translocation

The dynamics of a given molecule through a nanopore can be described via two processes; an initial capture step, followed by a translocation step[46]. The capture step involves the stochastic process of a biomolecule in the bulk solution passing close enough to the nanopore as dictated by diffusion, although it is assisted by the application of an electric field through the pore. The rate (J) of free diffusion is governed by the Smoluchowski rate equation[47] (Equation 1.1).

$$J = 2\pi cDr_p$$

Equation 1. 1. *The Smoluchowski equation, where J is the rate of free diffusion ($mols^{-1}$), c is the bulk analyte concentration ($moldm^{-3}$), D is the diffusion constant (m^2s^{-1}) and r_p is the pore radius (nm).*

The actual translocation of a given biomolecule is influenced by passive diffusion, but dominated through the driving forces otherwise known as electrophoresis and electroosmosis (Figure 1.10(a)). Electrophoresis is attributed to the voltage bias driving a charged biomolecule; i.e the negatively charged DNA is driven towards the positive anode. Electrophoresis is particularly dominant in the case of highly charged biomolecules which show greater attraction to the oppositely charged electrode. Electroosmosis is due to the application of a parallel electrical force resulting in the movement of the EDL. Electroosmosis is particularly important in moderately charged analytes such as proteins which are less affected by electrophoretic forces. This is discussed with greater detail later in section 1.3.4.2. Another important consideration, especially for DNA translocation is the hydrodynamic drag force[48] (Figure 1.10(b)). This can be attributed to the viscous solvent associated with the un-translocated portion of the DNA molecule opposing the driving force (typically electrophoretic).

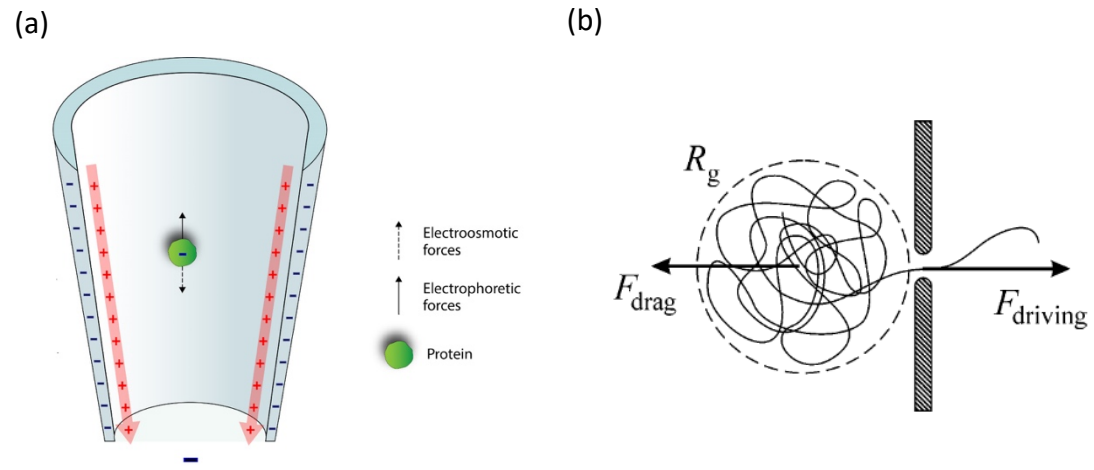


***Figure 1. 10**. A model showing the mechanism of biomolecule translocation through nanopores (a) The effects of electroosmosis and electrophoresis on the movement of an analyte (e.g protein) in a nanopore. The negatively charged protein is attracted by electrophoretic effects (black solid arrow) and also by electroosmotic effects (dashed arrow). (b) A balance between a driving Force ($F_{driving}$) that pulls the DNA through the pore and a drag Force (F_{drag}) related to the viscosity of the solvent which is in opposition. Figure adapted from reference 48.*

1.4.2.4. Ion current rectification

Ion current rectification[36] (ICR), occurs when a linear voltage input results in an asymmetric current output. ICR is observed in nanofluidic devices with either an asymmetric geometry, or with surfaces with considerable surface charge. ICR has been attributed to the formation of a diffuse electrical double layer within the nanopipette tip orifice. The comparable dimensions of the nanopipette with the diffuse electrical double layer, results in electrostatic interaction between the electrolyte and the surface charge.

As shown in Figure 1.11, in the case of glass pipettes under typical experimental conditions (pH 8.0), the surface charge is negatively charged and as a result showcase selectivity for cations over anions. As a result, when a positive voltage is applied outside of the nanopore (Figure 1.11, left), the flow of negative ions experiences repulsion from the negatively charged nanopore wall, resulting in a reduced current. Conversely, when negative charge is applied outside of the nanopore, the flow of positive charge experiences no such repulsion and therefore a higher ionic current is observed (Figure 1.11, right). The rectification ratio (r) determined from the ratio of ion current measured at two applied potentials of equal magnitude but opposite polarity allows a quantitative method of determining how the nanofluidic device rectifies current.

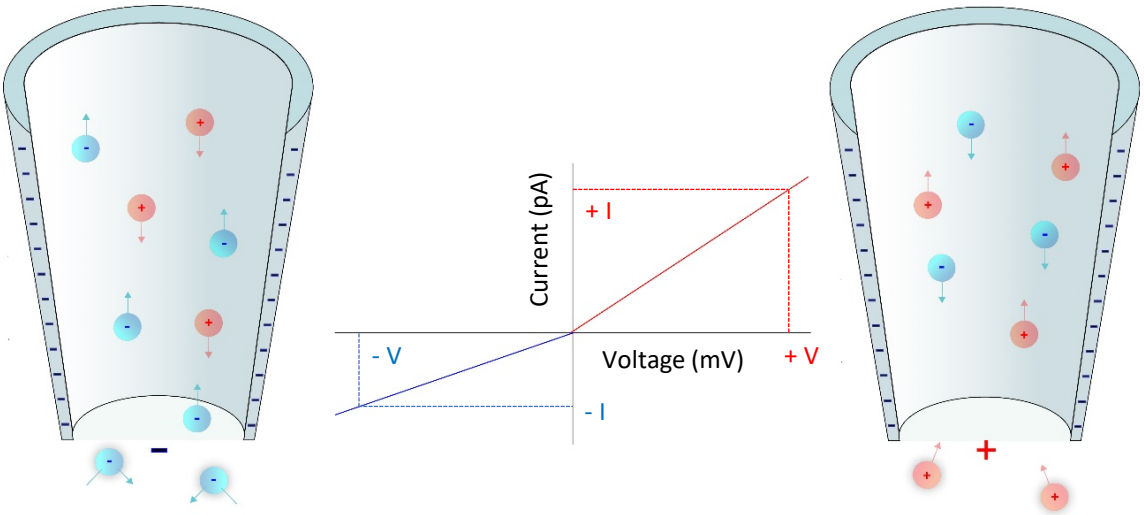


Figure 1. 11. *A schematic showing that the rectification of glass nanopipettes results in a non-linear I/V profile.*

$$r = \frac{I\,(+V)}{I\,(-V)}$$

Equation 1. 2. *The rectification ratio (r) provides a numerical value of the phenomenon. I refers to the current (pA) at voltage (mV).*

It follows that the rectification ratio is fundamental in quantitatively following changes in surface charge linked to modification. For example, silanisation can lead to the incorporation of a hydrophobic terminal functional group (r = 1), while modification to incorporate negatively charged DNA, leads to an extensive rectification (r = 1.8). Conversely, the vapour deposition of positively charged poly-L-lysine[49], a polypeptide bearing positively charged amino groups, results in anion selectivity and reversal of rectification, (r < 1).

1.3.2.5 Ion blockade conductance

The passage, or translocation of a biomolecule leads to modulation of the ionic current. The polarity of the ionic modulation is a result of two competing effects: the loss of ionic current ($-G_{resist}$) upon replacement of carrier ions by the analyte, as well as a gain in ionic current ($G_{conduct}$) due to the passage of extra carrier charges associated with the analyte as described in Equation 1.3 below.

$$\Delta G = -G_{resist} + G_{conduct}$$

Equation 1. 3. *The polarity of translocation peaks. ΔG (S) refers to the polarity of peaks while $-G_{resist}$ refers to the loss of ionic conductance (S) and $G_{conduct}$ refers to the gain in ionic conductance (S).*

A simplified model relating to the polarity of DNA translocations (as measured by change in conductance, ΔG) in KCl solution can be estimated from the following equation.

$$\Delta G = \frac{1}{L}\left(-\frac{\pi}{4} d^2 \left(\mu_K + \mu_{Cl}\right) n_{KCl}\, e + \mu_K^* q_{DNA}^*\right)$$

Equation 1. 4. *A* simplified model used to estimate the polarity of peaks as a measure of change in conductance (ΔG, S) of DNA translocations in KCl solution, where d is the diameter of the molecule (nm), L is the length of the pore (nm), μ_K and μ_{Cl} are electrophoretic mobilities of K^+ and Cl^- ions ($m^2V^{-1}s^{-1}$) respectively, n_{KCl} is the number density of potassium or chloride ions (Mm^{-3}), e is the elementary charge (C), μ_K^* is the effective electrophoretic mobility of K^+ moving along the DNA ($m^2V^{-1}s^{-1}$) and q_{DNA}^* is the effective charge on the DNA per unit length (Cm^{-1}).

A switch from blockade-based peaks, to enhancement-based peaks, can be observed with a decrease in electrolyte concentration as deduced from the equation. Keyser and others[50] have shown that DNA translocations resulted in blockades at 500mM KCl, but switch to enhancements when the KCl concentration is decreased to 150 mM.

1.4.4 Limitations of protein detection using nanosensors

DNA strands (5-10kb) are typically used for translocation studies due to their relatively long size and high localised negative charge, allowing detection at low concentrations (< nM). Conversely, proteins are very difficult to detect due to their small size and low charge which results in peaks with low dwell times (< 0.1ms), low peak amplitudes and ultimately a low capture rate alongside a poor signal to noise ratio (SNR). In addition, detection is complicated by the increased effects of electroosmosis which is able to oppose, or work in tandem, with electrophoretic effects.

1.4.4.1. Low capture rate

One study has concluded that the low rate of protein detection observed far below that expected of the Smoluchowski equation is due to the ultrafast rate of protein translocation[51]. In other words, protein translocation events are simply lost in the inherent noise of the ionic current measurements rather than their being a small number of individual translocation events. While the detection of large proteins (>100kDa) is possible, the detection of smaller proteins is still very difficult. For example, for ß-galactosidase (540kDa) there is a dependence of pore size (Figure 1.12(a)) and protein concentration (Figure 1.12(b)) on the event rate, while for the smaller human chorionic gonadotropin (hCG), a 37kDa protein no such dependence was observed.

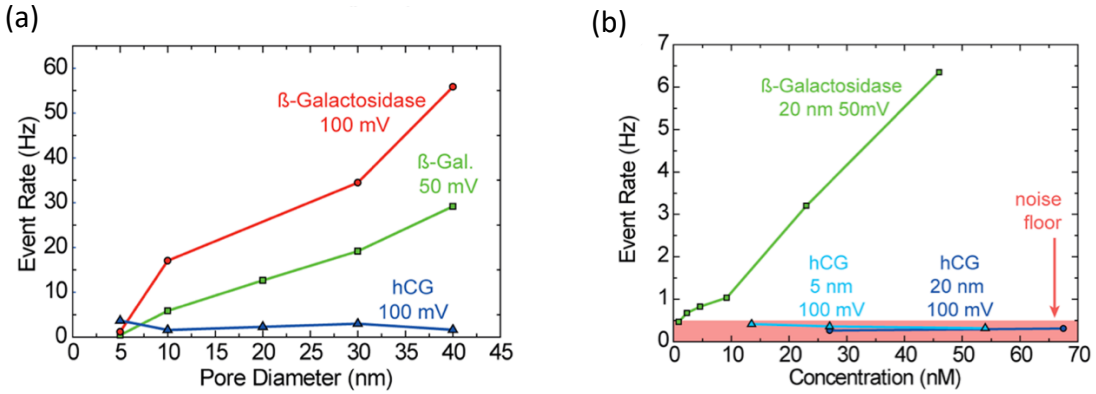


Figure 1. 12. *Detection of proteins using unmodified solid state nanopores. (a) Event rate as a function of pore diameter. ß -galactosidase is measured at two different applied voltages (b) Event rate as a function of protein concentration. hCG is measured in pores with different diameters. Figures adapted from reference 51.*

1.4.4.2. Low signal to noise ratio (SNR)

The low SNR seen in protein translocation studies is largely due to the small overall charge of proteins resulting in low peak amplitudes, not observable amongst noise. Low-pass filters are commonly employed to remove ultra-fast peaks associated with noise, allowing an increase in the SNR. Unfortunately, efforts to increase the SNR for protein translocation by employing low pass filters are often counterproductive as they simply attenuate[51] (i.e dwell time increases at the expense of peak amplitude) the ultrafast events of protein translocation when below a given threshold (66µs for 10kHz low-pass filter), as seen in Figure 1.13.

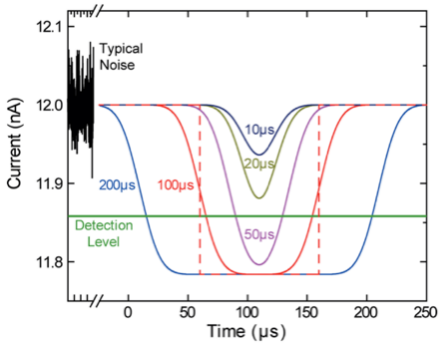


Figure 1. 13. *The distortion of rectangular pulses of 10–200 µs duration by a 10 kHz Gaussian filter. For a 100 µs pulse duration the dashed red line shows an ideal pulse (delayed 40 µs for visual clarity), before filtering, while the solid red line shows the same 100 µs pulse after filtering. All pulses have the same amplitude before filtering. Due to the limited rise time of the filter, any pulse with a duration less than twice the filter rise time (2Tr =66 µs) is distorted. Figure adapted from reference 51.*

1.4.4.3. Effects of electroosmosis and electrophoresis

The mechanism of protein translocation is especially difficult to characterise due to the combined influence of electroosmosis and electrophoresis. While the translocation of highly charged DNA is predominantly governed by electrophoretic forces, the translocation of proteins through a nanopore is complicated due to the increased effects of electroosmosis

alongside electrophoretic effects. As seen in Figure 1.14, depending on the relative charges of the nanopore surface and the protein, these effects are able to either oppose, or complement, each other.

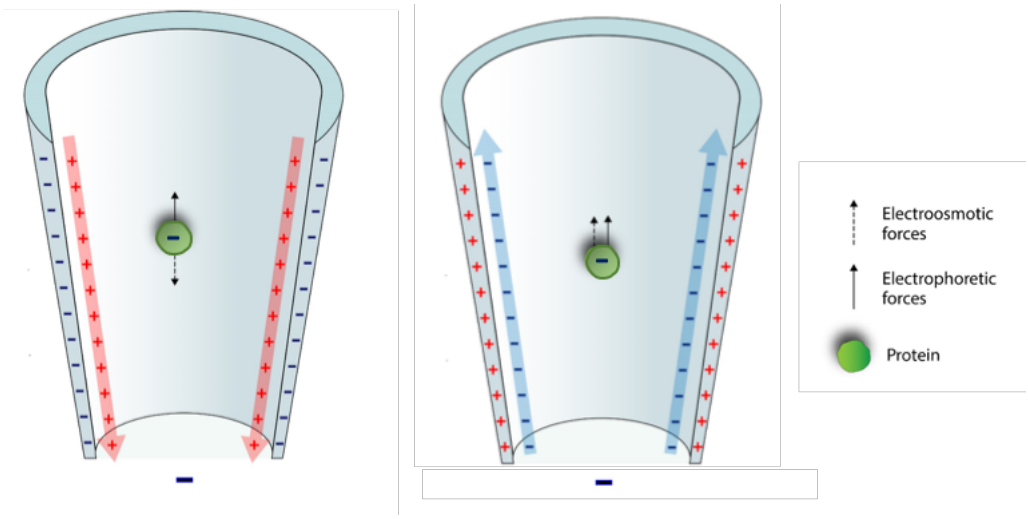


Figure 1. 14. *The effects of electroosmosis and electrophoresis on protein translocation through a nanopore. Depending on the relative charges of the nanopore wall and protein, electrophoresis and electroosmosis can oppose each other (left) or work alongside each other (right).*

Authors Firnkes, Rant and others conducted an excellent study of the effects of electroosmosis at a wide range of pH values on the translocation of the protein actin through solid state nanopores[52]. The pH affects the overall charge of the nanopore surface and the analyte, thereby determining its translocation direction. In addition, the pH affects the zeta potential and depending on its polarity can result in electroosmosis that either opposes or supports the electrophoretic forces with their respective magnitudes determining which is the dominant force. The effects of zeta potential (ζ) on the effective velocity (*v*) can be expressed in Equation 1.5, whereby η is the viscosity, *E* is the external electric field and ε is the dielectric coefficient of the electrolyte.

$$v = \frac{\varepsilon E}{\eta}(\zeta_{protein} - \zeta_{pore})$$

Equation 1. 5. *An expression showing the effective velocity (v, ms^{-1}) of protein movement through a nanopore where ζ is the zeta potential (mV), η is the viscosity (Nsm^{-2}), E is the external electric field (Vm^{-1}) and ε is the permittivity (Fm^{-1}).*

Figure 1.15 provides an overview of the effects of pH on protein translocation through a solid state nanopore. At pH 2, the protein and nanopore surface are both positively charged, resulting in electroosmotic forces and electrophoretic forces opposing each other. Electrophoretic forces however are particularly strong, dominating over the effects of electroosmosis, resulting in protein translocation only when a negative voltage is applied. At pH 4, the zeta potentials of the nanopore walls and the actin analyte are similar, resulting in

the effective cancelling of electroosmotic/electrophoretic forces and diffusion having a far greater role in translocation. In this scenario, translocation peaks can occur upon application of either positive or negative voltages. At pH 6-8, the surface charge of the nanopore is now negatively charged, resulting in the reversal of electroosmosis which now works in tandem with electrophoresis. At pH 10, actin is now weakly negatively charged, leading to electrososmosis dominating biomolecule transport and resulting in the counterintuitive movement of a negatively charged protein towards the negative anode.

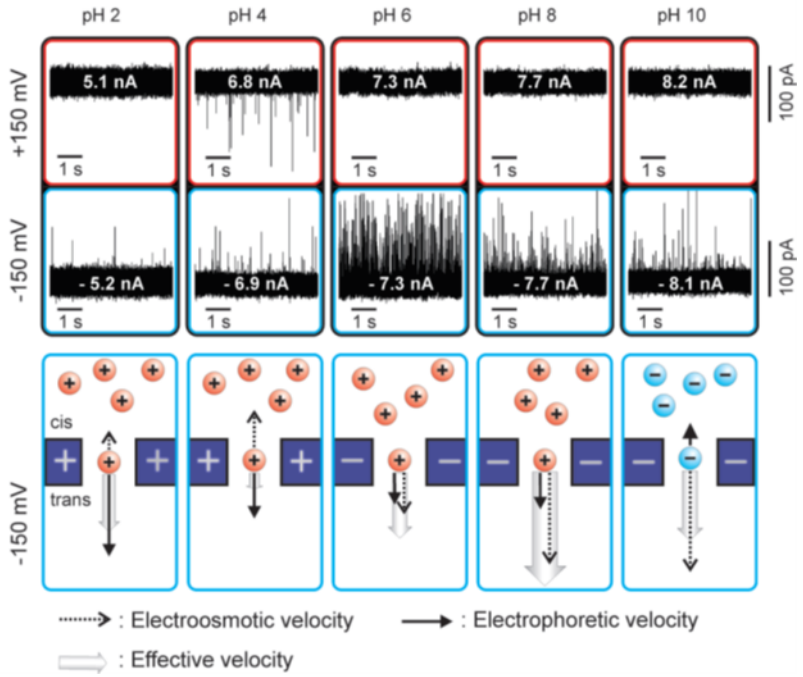


Figure 1. 15. *The effects of electroosmosis and electrophoresis on actin translocation through a nanopore as a function of solution pH. Current traces are shown at both positive and negative applied potentials while the schematic underneath show the relative velocities of electroosmosis and electrophoresis allowing determination of the direction of overall movement. Figure adapted from reference 52.*

1.4.4.4. Limited selectivity

Unmodified nanopores are highly sensitive, but have no inherent selectivity which limits their use as sensors in samples containing multiple proteins. However, modification allowing the incorporation of protein specific receptors onto the surface would allow nanopores to function as selective biosensors.

(i) Modification strategies

Incorporation of receptors (e.g antibodies and receptors) typically requires an initial modification of the surface to incorporate functionality. Modification strategies include silanising agents[42] (described in Chapter 3) as well as self-assembled monolayers (SAM)[53].

Both strategies work on a similar principle, whereby the 'headgroup' binds to the surface allowing functional group separated by the tail to incorporate receptors (Figure 1.16(a)).

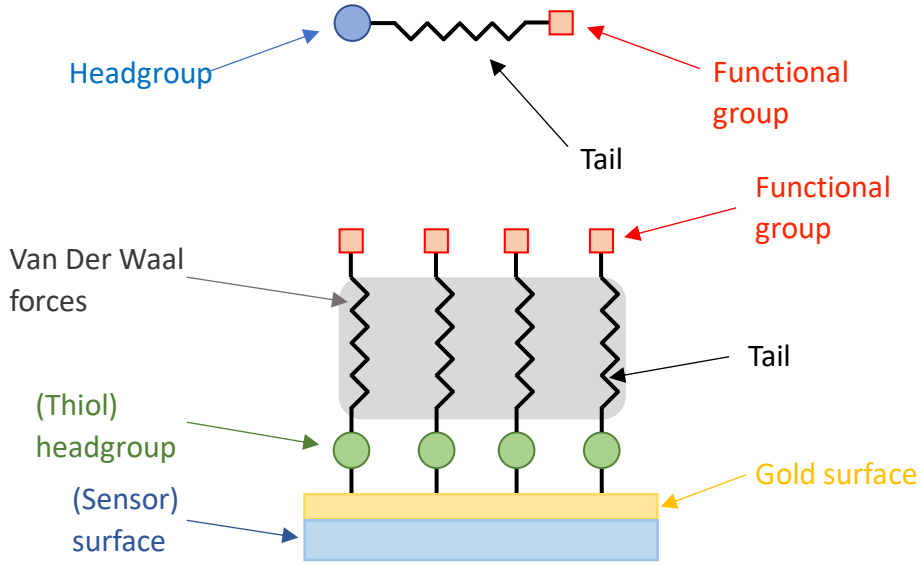


Figure 1. 16. *(a) Modification agents are composed of a headgroup which binds to the surface and a tail which leads to incorporation of a functional group. (b) A schematic of a self-assembled monolayer, formed through a thiol head binding to the gold surface and stabilised by Van Der Waal forces present between hydrocarbon chains.*

While silanisation and covalent based bioconjugation strategies are discussed in more detail in chapter 3, an alternative modification strategy involves physical based deposition, which in turn allows SAM formation to occur (Figure 1.16(b)). An initial gold deposition on the sensor surface is achieved through sputtering[54] (atomisation on the surface in the plasma phase), or via electroplating[55] (attraction to a charged surface in solution). After gold deposition, the introduction of a thiol modified receptor allows binding via the well characterised gold-thiol interaction[56], with SAM formation stabilised through Van Der Waal interactions between hydrocarbon chains.

(ii) Kinetics of receptor-modified nanopores

The modification of nanopores to include recognition elements changes the kinetics[10, 14] of the passage of the analyte. For instance, in unmodified nanopores, dwell time is largely associated with the size of the protein. Conversely, in receptor modified nanopores, dwell time is affected by the capture of the associated analyte.

In the case of receptor modified nanopores, the kinetic rate constant for analyte dissociation (K_{off}) and the rate constant for analyte association (K_{on}) can be determined from the dwell time (t_{off}) and inter-event time (t_{on}) respectively, as shown below (Equation 1.6).

$$K_{off} = \frac{1}{t_{off}}$$

$$K_{on} = \frac{1}{c}\ t_{on}$$

Equation 1. 6. *The kinetic rate constants for analyte dissociation (K_{off}, s^{-1}) and analyte association (K_{on}, $mol^{-1}dm^3s$), where t_{off} is dwell time (s), t_{on} is the inter-event time (s) and c is the concentration ($moldm^{-3}$).*

1.5. Aptamers

Aptamers[14] are short single stranded oligonucleotides (RNA and DNA) with the ability to fold into complex three-dimensional shapes that allows them to act as recognition elements (Figure 1.17). While aptamers have been found in nature (termed riboswitches[57]), they can be produced artificially in a process known as SELEX[58] or Systematic Evolution of Ligands by EXponential enrichment. Examples of aptamer structures include hairpin loops[59] formed through partial complementary binding in the stem region (Figure 1.17(a)) and G-quadruplex structures[60] formed via Hoogsteen hydrogen bonding in nucleotide chains with high guanine content (Figure 1.17(b)). By forming binding pockets and clefts, aptamers can specifically recognise and tightly bind a given molecular target including small molecules[61], whole cells[62] and protein biomarkers[63-64]. Aptamers are alternatives to the traditionally used monoclonal antibodies and have applications as research tools, recognition elements in sensors and as therapeutic agents.

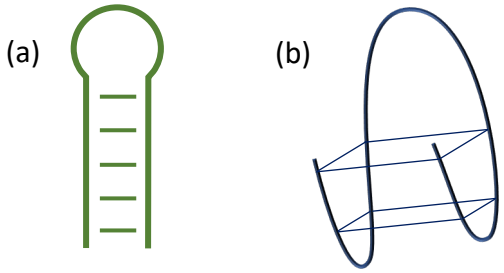


Figure 1. 17. *Examples of 3D structures formed by aptamers. (a) hairpin loop structure occurs through complementary binding in the stem region. (b) G-quadruplex is formed vis Hoogsteen hydrogen bonding between guanine bases*

Aptamers are isolated *in vitro* from large combinatorial libraries in a process known as SELEX Systematic Evolution of Ligands by Exponential Enrichment (SELEX)[58] as shown in Figure 1.18). SELEX involves the successive enzymatic selection and amplification of oligonucleotides to generate highly specific (with K_d approaching nM levels) recognition elements in the form of short RNA or DNA sequences.

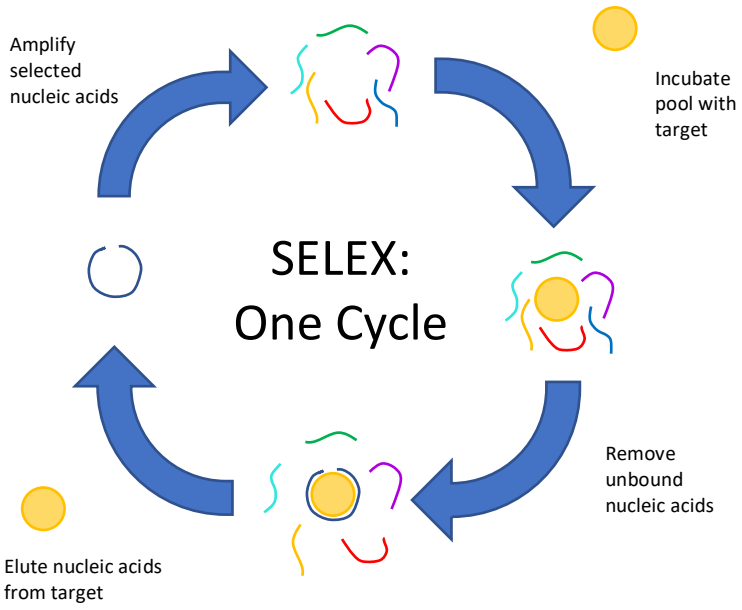


Figure 1. 18. *The SELEX process is used to generate oligonucleotide sequences known as aptamers that bind a specific analyte. A library of oligonucleotides is incubated with a specific target prior to a series of washing steps used to remove any unbound sequences. The bound sequences can now be eluted and subsequently amplified with further variations for additional SELEX cycles until necessary.*

1.5.1. Binding mechanism

Aptamers selectively bind their target through two mechanisms which can be categorised either as an induced fit model[65], or a pre-formed binding model[66] (Figure 1.19). In the former case the aptamer changes its structure in response to association with the analyte, while in the latter case the aptamer is already in its binding form to target the analyte.

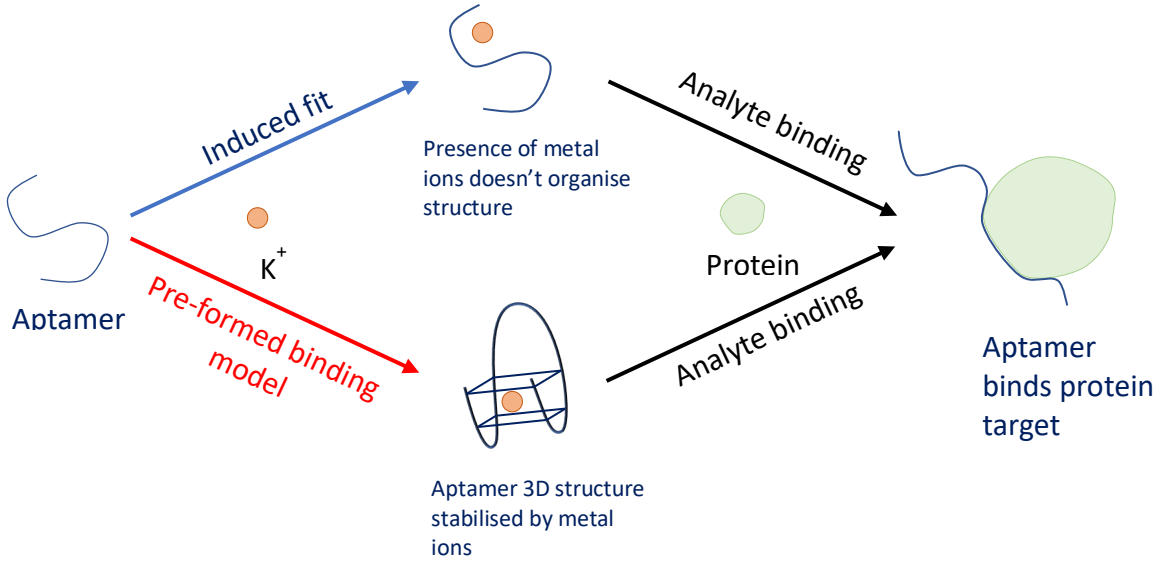


Figure 1. 19. *Binding modes of aptamer. (1) In an induced fit mechanism, the aptamer changes its shape in response to the target analyte only. (2) In a pre-formed binding model the aptamer requires prior organisation before it can bind the target analyte.*

1.5.2 G-quadruplex based aptamers

The aptamers used in this research project, thrombin binding aptamer TBA[63] (exosite ll) as well as the alpha synuclein binding aptamer[64] (TS-0530) form structures known as G-quadruplexes. G-quadruplexes are observed in oligonucleotides with high guanine content and have been considerably researched due to their localisation at the end of telomeres[67].

1.5.2.1 Structure

The core G4 quadruplex[60] component is a guanine tetrad; a cyclic planar arrangement of four guanine residues linked through Hoogsteen-type hydrogen bonds (Figure 1.20(a)). The stacking of two or more tetrads generates the G4 tetrad which is stabilised by cations (typically K^+/Na^+) in the central cavity. G4 quadruplexes can have different conformations (e.g parallel and anti-parallel) based on the orientation of the DNA strand as shown in Figure 1.20(b).

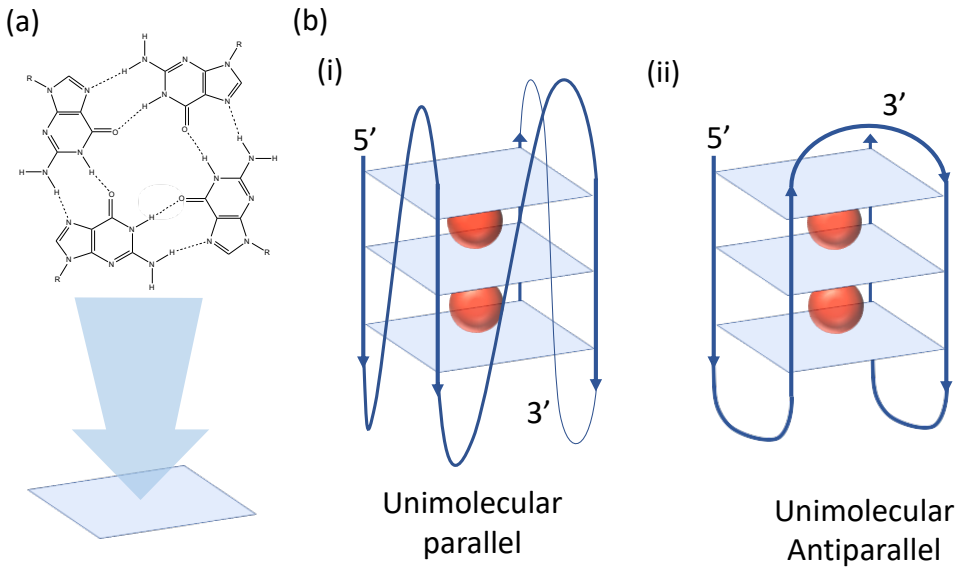


Figure 1. 20. *(a) A schematic showing a G-tetrad. (b(i) A unimolecular parallel formation (ii) A Unimolecular anti-parallel formation. G4 quadruplexes are typically made up of three tetrads stabilised with metal ions (red spheres).*

1.6. Solutions to detect protein translocation in nanopores

While DNA detection is commonplace using unmodified nanopores, protein detection for the reasons (low capture rate and electroosmosis influence) discussed previously is more demanding. While typical nanopore experiments use amplifiers with a bandwidth of 100kHz (resolution of 0.01 ms), the use of higher (1 MHz) bandwidth amplifiers[68] (1 MHz) allow for the detection of protein translocation events of 0.001 ms. Unfortunately, not only are such amplifiers expensive, but they result in increased noise while still remaining unselective for

a given analyte. However, researchers in the nanopore field have developed creative new methods of overcoming these limitations as discussed below.

1.6.1. Receptor modified carrier

A recently employed strategy has been to use a carrier system formed by attaching a receptor to a long dsDNA. After incubation with the given analyte, detection (Figure 1.21) involves sensing the sub-peak (corresponding to the analyte) of the blockade peak (corresponding to the DNA carrier).

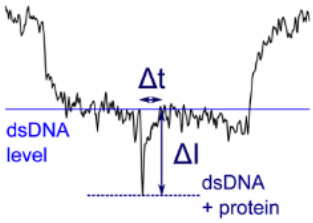


Figure 1. 21. *An example of a typical peak seen utilising a carrier system. A large blockade peak corresponds to the translocation of a dsDNA while the sub-peak can be attributed to the bound analyte. Figure adapted form reference 69.*

Initially, Bell and Keyser used a DNA carrier modified with biotin[69], allowing for the binding of streptavidin. DNA carriers (Figure 1.22(a)) were formed by cleaving the circularised ssDNA construct m13mp18 (7.2 kb) before subsequently hybridising with 38 mer nucleotide sequences. The number of binding sites could be controlled by adding the relevant number of 38 mers with biotin functional groups. Results showed that 3 biotin groups in close contact (Figure 1.22bi) led to one single peak being resolved. Conversely, upon spatial separation (600 nm) of biotin groups, three distinct sub peaks could be seen (Figure 1.22bii). Finally, the authors showed that the carrier could selectively detect streptavidin (Figure 1.22c) in a multi-protein mix (3B + mix 1) with limited positive translocations, as compared with a protein mix containing no streptavidin (3B + mix 2). Additional controls showed an insignificant number of positive peaks when tested with unmodified carriers containing streptavidin (0B + mix 1) and without streptavidin (0B + mix 2).

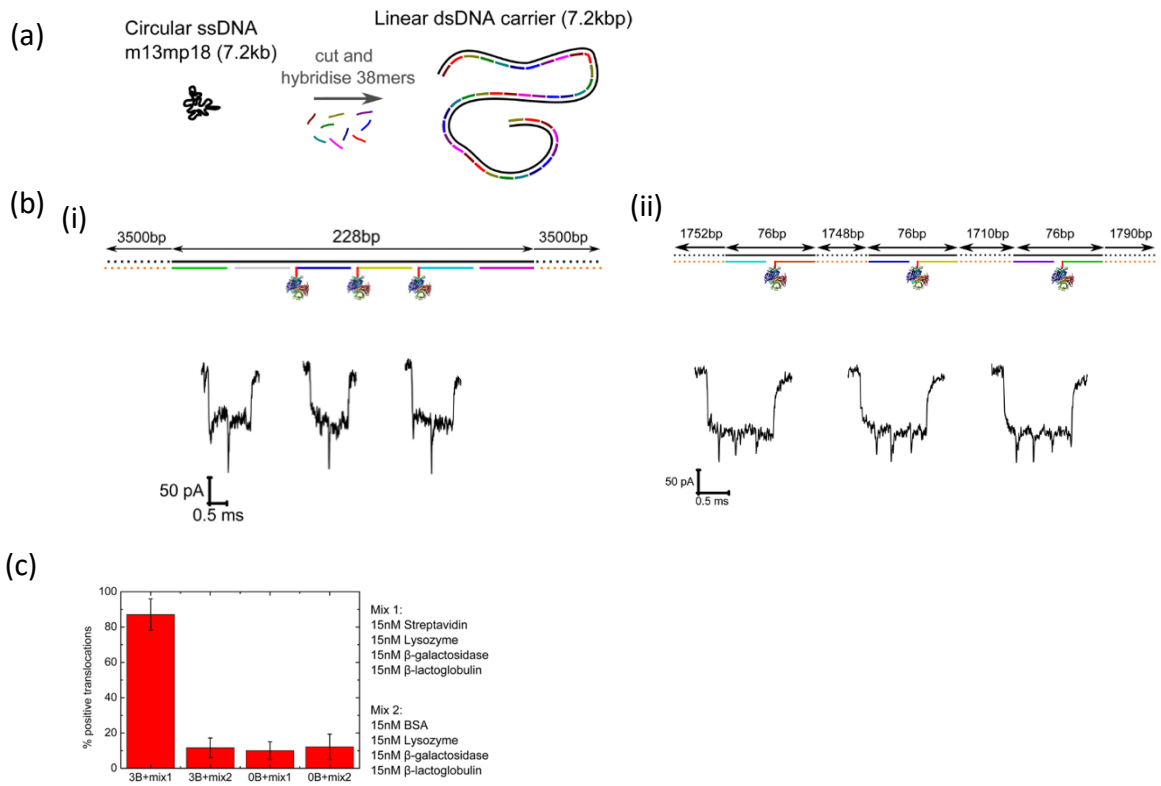


Figure 1. 22. *The formation of DNA carriers through cutting and hybridising with complementary sequences. (b) The detection of streptavidin using DNA carriers with 3 biotin receptors (i) Biotin groups in close proximity lead to one sub-peak while (ii) spatial separation of biotin groups lead to three distinct sub-peaks. (c) Selective detection of streptavidin using the carrier based system. Mix 1 contains streptavidin among 3 other proteins while in mix 2 streptavidin is replace by BSA. 3B refers to a carrier system with 3 biotin groups while 0B refers to a carrier system with no biotin groups. Figures adapted from reference 69.*

More recently, a 48kbp lambda DNA carrier was coupled with a 15mer TBA to detect thrombin[70] (Figure 1.23). Lambda DNA is a double stranded 48 kbp sequence with a 12 bp single stranded region at both ends of the construct (1.23(a)). Carriers can be formed by the hybridisation of the single stranded end with complementary nucleotide sequences (1.23(b)). A 2-carrier system was formed by the hybridisation of complementary sequences containing the aptamer sequence at both ends of the lambda DNA construct (1.23(c)). Furthermore, a 3-carrier system was formed by extension of the complementary sequence of the 2nd binding region, allowing hybridisation to a third carrier (1.23(d)). Results showed that a 2 carrier system typically had 2 subpeaks while a 3 carrier system had 3 sub-peaks.

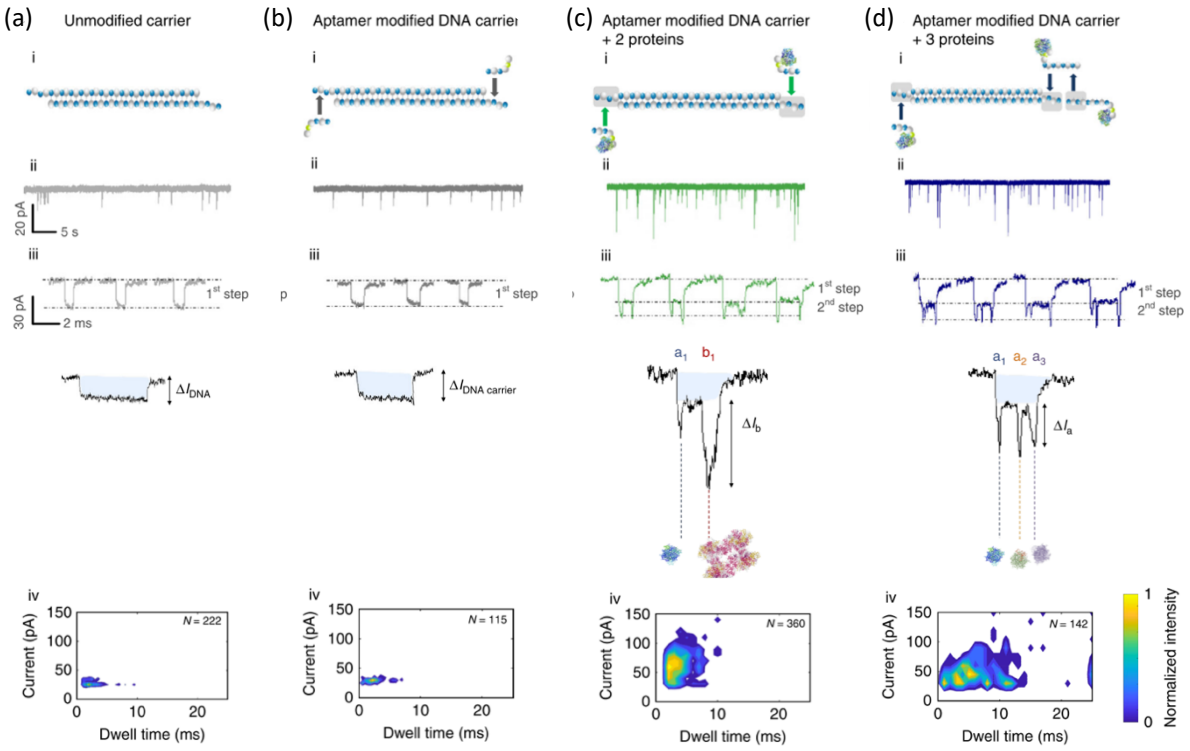


Figure 1. 23. *The detection of thrombin using a DNA carrier system. (a) An unmodified carrier (b) hybridisation with nucleotide sequences containing the complementary sequence and TBA at both ends results in a 2 carrier system (c) The 2 carrier system is incubated with proteins (d) A three carrier system formed by extension of the 2nd binding site is incubated with three protein analytes. A schematic of the carrier system (i) is shown alongside representative traces (ii) and representative peaks (iii). Data analysis can be shown via dwell time vs current scatter plots (iv). Figures adapted from reference 70.*

Overall, the carrier system has advantages of low cost and simple implementation within a typical nanopore set-up, while allowing protein detection at much lower concentrations than seen for 'free' translocation. Despite this, not only is a prior incubation step required, but the detection of sub-peaks is difficult to characterise with current software and is further complicated by the presence of false positive peaks (due to DNA folding events). Furthermore, the low binding efficiency of the aptamer can result in many translocation events not being associated with sub-peaks. As a result, in this study attention was turned to directly modifying nanopores with receptors.

1.6.2. Receptor modified nanopores

An alternative strategy involves protein detection using receptor-modified nanopores. Detection is carried out through the addition of the protein analyte to the system, with binding resulting in the peaks having significantly longer dwell times.

For example, Yusko et al[71] coated solid state nanopores with lipid bilayers allowing for the incorporation of lipid-anchored biotin. The high affinity of biotin for streptavidin allowed its subsequent capture. Figure 1.24 (a) shows a schematic of the bilayer coated nanopore

alongside lipid anchored biotin (blue circles) and streptavidin (large red). Figure 1.24 (b) shows examples of current versus time traces for the translocation of 6 pM streptavidin through bilayer coated nanopore without (top) and with (bottom) lipid biotin anchors. Importantly, the inclusion of the biotin receptor allowed resolution of streptavidin which was otherwise not seen.

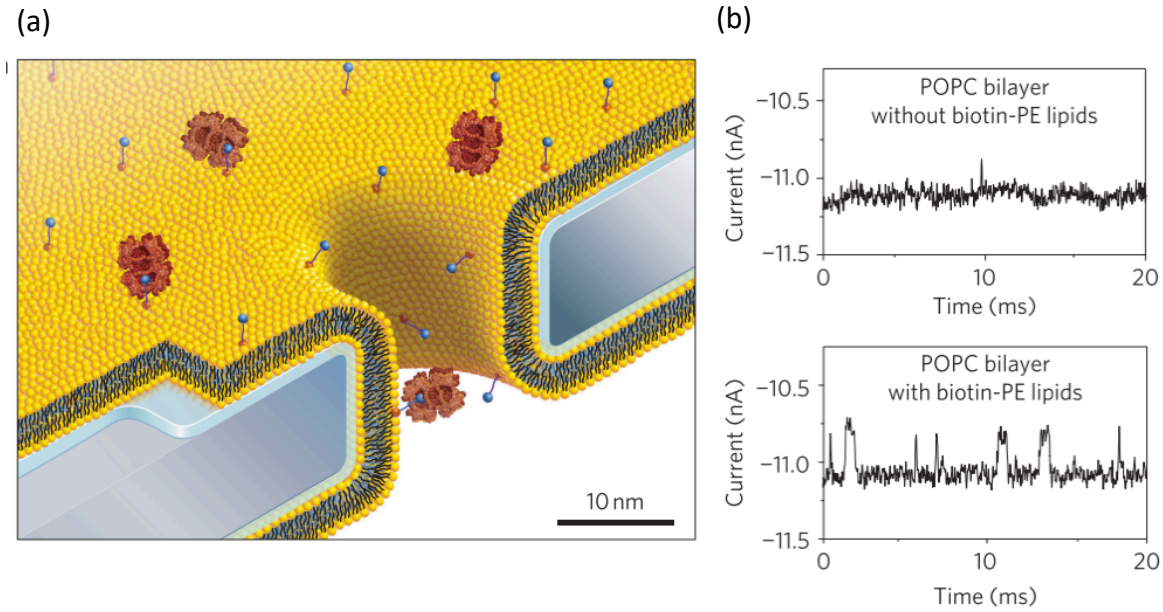


Figure 1. 24. *(a) An illustration showing the binding and subsequent translocation of streptavidin (large red) to specific lipid anchored biotin (blue circles). (b) Current versus time traces for streptavidin (6 pM) translocation through lipid bilayer coated nanopores without (top) and with (bottom) biotin lipids. Figures adapted from reference 71.*

Furthermore, Rant[72] showed that nanopores after modification with self-assembled monolayers (SAM) allowed incorporation of NTA (Nitrilotriacetic acid) receptors (Figure 1.25(a)). Immunoglobin (Ig) modified with His tags can selectively bind to NTA receptors, allowing for their detection at low concentrations (1.25 (b)). The results (1.25(c)), showed that pulse width (dwell time) increased upon introduction of His tagged immunoglobin into pores with 1 (Mono NTA) or 2 (Bis NTA) receptors in comparison to unmodified nanopores (No NTA).

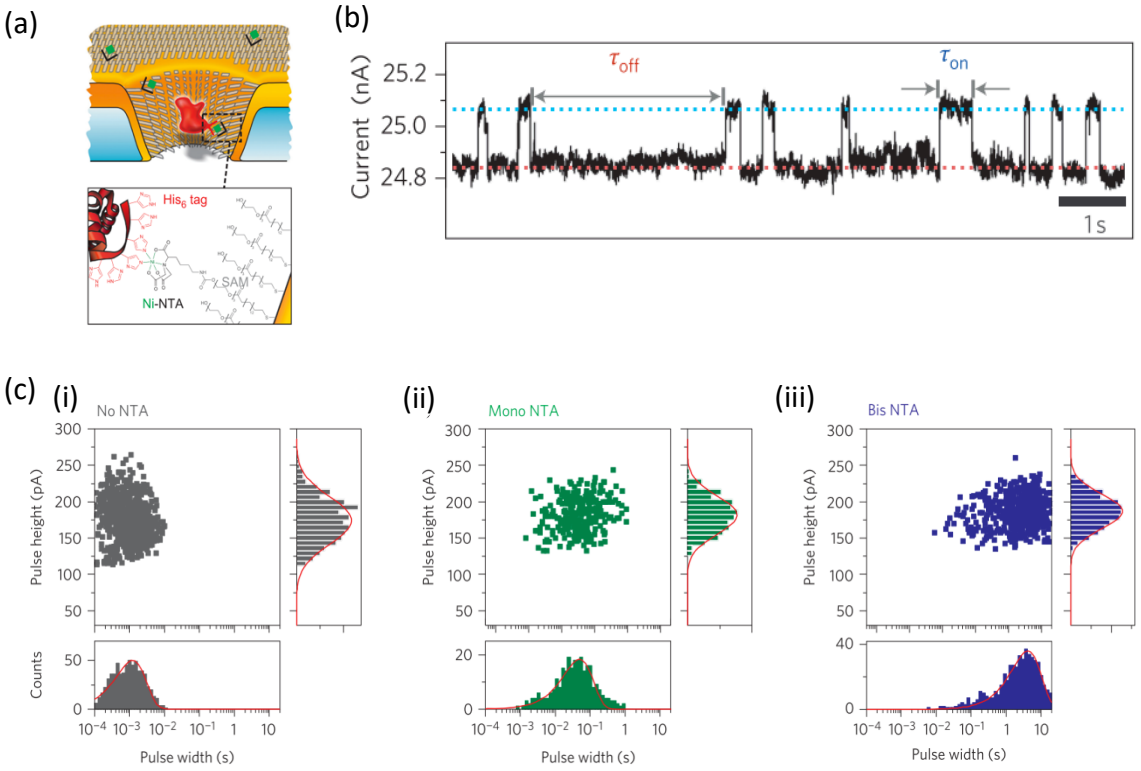


Figure 1. 25. The detection of His-tagged protein using solid state nanopores modified with Nickel-NTA receptors. (a) A schematic showing the modified nanosensor. (b) A typical trace showing binding events. (c) Dwell time (pulse width) vs peak amplitude (pulse height) scatter plots for His tagged protein translocated through nanopores with no NTA i) as well as nanopores with 1 (ii) and 2 NTA (ii) modifications. Figures adapted from reference 72.

Biological nanopores (alpha-hemolysin) externally modified with aptamers have also been employed to detect thrombin[73]. Protein engineering introduced a cysteine (and therefore a free thiol), allowing disulphide attachment via a thiol modified single stranded nucleotide outside the nanopore. The sensor is formed via hybridisation of a sequence containing a complementary portion and the 15mer thrombin binding aptamer (TBA) as well as a thymine linker which provides spatial separation. Since, the small pore size of the lumen prevented the direct translocation of thrombin, the external binding of thrombin was transmitted to the pore via ionic current modulations. Figure 1.26 shows representative traces before (a) and after (b) thrombin addition. B_1 represents insertion of the oligonucleotide whereas B_2 represents insertion of the complementary TBA into the pore. Upon addition of thrombin, a new event (UB + T) results in events with an increased amplitude. Figure 1.26 (c) provides a mechanistic overview of the origin of binding events.

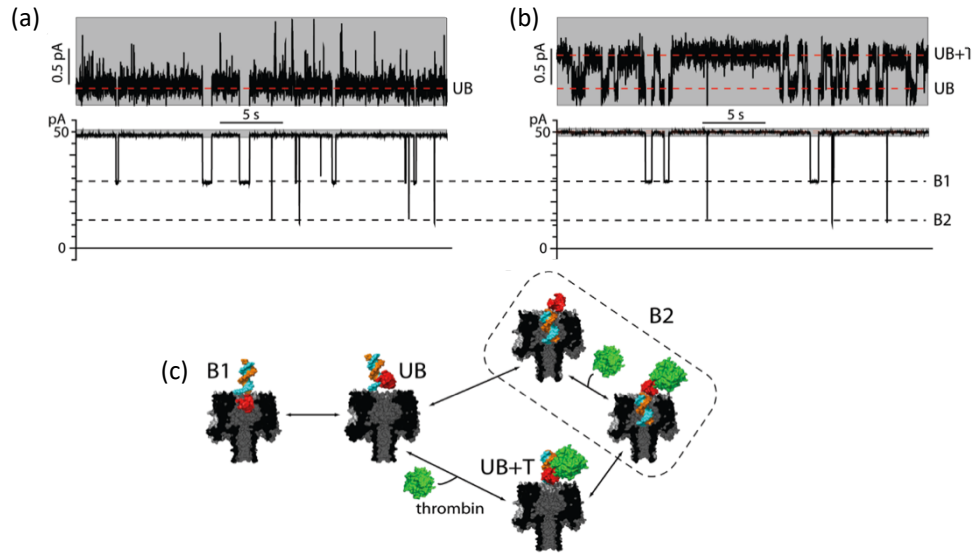


Figure 1. 26. *The detection of thrombin using alpha hemolysin externally modified with TBA. Traces before (a) and after (b) the addition of 350 nM thrombin. (c) A mechanistic overview of the different type of events encountered. Figures adapted from reference 73.*

Nanopipettes modified with aptamers have also been used for protein detection. Actis[74] modified nanopipettes with 15 mer TBA (Figure 1.27(a)) utilising a 4-step method which could be followed *in-situ* by I/V characterisation (ai). Detection was based on changes in ionic current upon addition of the thrombin analyte (150 µg/ml) as shown in a(ii). In a similar approach, Shu[75] modified nanopipettes with immunoglobulin selective aptamers (Figure 1.27(b)). Detection of immunoglobin (5nM) was based on a series of stepwise current blocks attributed to individual immunoglobin molecules (b(ii)), which were not observed in unmodified nanopipettes (b(i)).

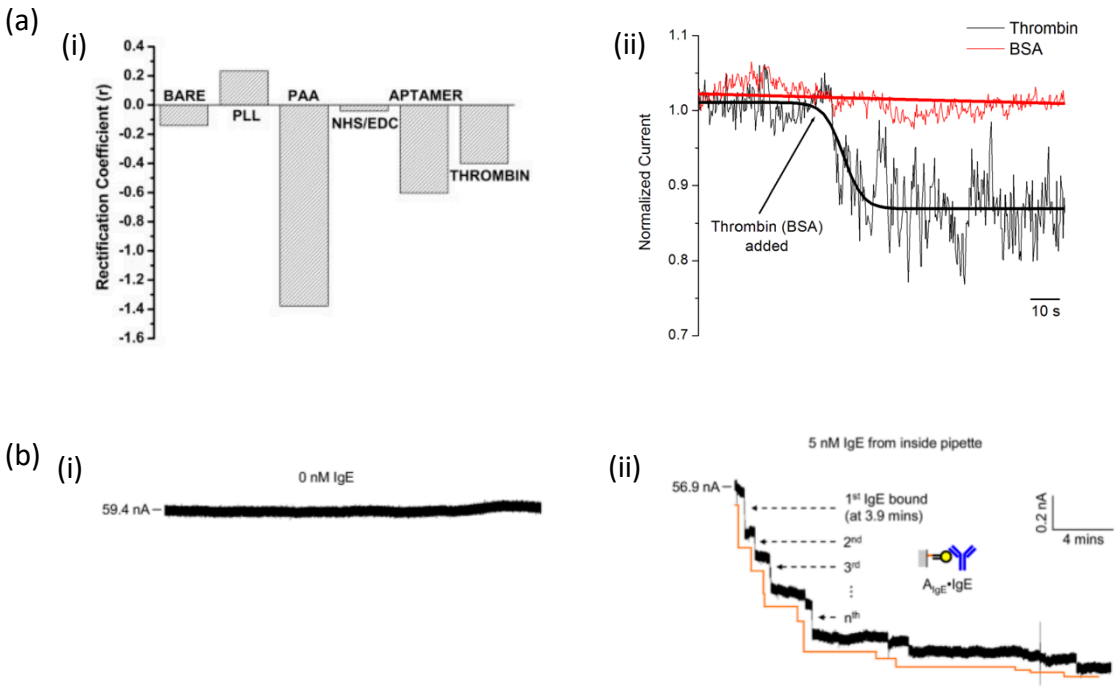


Figure 1.27. *The detection of thrombin using aptamer (15 mer TBA) modified nanopipettes. (i) The rectification ratio at each stage of the modification process. (ii) Thrombin detection is based on the reduction in current upon addition of thrombin to the modified nanopipette. Figures adapted from reference 74. (b) Traces show the detection of immunoglobin using a nanopipette modified with the corresponding aptamer. Traces before (i) and after (ii) the addition of 5nM immunoglobin. Figures adapted from reference 75.*

The direct incorporation of receptors onto nanopipettes can be highly challenging, both in terms of functionalisation and the workings of the model at the nanoscale model. Despite this, if successful, the strategy would afford sensitive, selective and direct detection at sub-nanomolar concentration levels. This approach was therefore chosen for the PhD project. To our knowledge, a solid state nanopore modified with receptors that allowed single molecule label-free blockade based events has not previously been reported. Previous attempts at the aptamer modification of nanopipettes allowed the implementation of several design criteria used throughout the project. The design of the aptamer-modified nanopipette should allow the aptamer in its 'binding form' to have good coverage across the nanopipette optimising protein capture without blocking the pore. In addition, the functionalisation method need to be carried out with the minimal number of steps possible to maximise efficiency while limiting reactions that could degrade nucleotides (e.g Copper catalysis seen in azide alkyne chemistry).

1.7. Thesis aim and objectives

The aim of the PhD project was to develop a highly sensitive, selective and label-free aptamer-based nanopore sensor for the detection of protein biomarkers. Throughout the project, a fabrication methodology has been designed to have a low number of functionalisation steps with a good aptamer ligation efficiency, while preventing the need for expensive cross-linking reagents or degrading (Cu) catalysts[76]. Throughout the sensor design, it has been ensured that an in-built linker provides spatial separation while ensuring that its length would not block the nanopore. After optimising functionalisation, characterisation of the sensor could be conducted via (1) I/V curves and (2) blockade analysis through translocation of complementary sequences. Thrombin was chosen as the protein analyte, due to its well characterised structure and high binding affinity (kD = 0.5 nM) to TBA. The detection of thrombin allowed us to ascertain the effects of analyte concentration as well as the applied voltage. Furthermore, the ability to detect thrombin in a multi-protein serum analyte demonstrated the selectivity of our system for a biomarker that could be useful in the diagnostics of neurodegenerative diseases (multiple sclerosis) and cancer. Successful demonstration of an aptamer modified nanosensor would then allow the detection of alpha synuclein oligomers; cytotoxic proteins which are heavily implicated in Parkinson's Disease. Alpha synuclein oligomers are currently particularly hard to detect

due to the large variety in the size and shape of subtypes as well as the presence of monomer precursors and fibril aggregates. Throughout the experimentation, various controls have been carried out measuring protein translocation through nanopipette precursors (glass, silane) and pipettes modified with a control sequence.

1.8. References

1 T. R. Gibb, A. P. Ivanov, J. B. Edel and T. Albrecht, *Anal. Chem.*, 2014, **86**, 1864–1871.

2 N. Rifai, M. A. Gillette and S. A. Carr, *Nat. Biotechnol.*, 2006, **24**, 971–983.

3 J. T. B. Crawley, S. Zanardelli, C. K. N. K. Chion and D. A. Lane, *J. Thromb. Haemost.*, 2007, **5**, 95–101.

4 E. W. Davie and J. D. Kulman, *Semin. Thromb. Hemost.*, 2006, **32**, 3–15.

5 M. A. Petersen, J. K. Ryu and K. Akassoglou, *Nat. Rev. Neurosci.*, 2018, **19**, 283–301.

6 H. A. Lashuel, C. R. Overk, A. Oueslati and E. Masliah, *Nat. Rev. Neurosci.*, 2013, **14**, 38–48.

7 P. Werner, S. Klaus, M. T. Caroline, G. M. Halliday, P. Brundin, J. Volkmann, A.-E. Schrag and A. E. Lang, *Clin. Proc. Child. Hosp. Dist. Columbia*, 2017, **3**, 328–332.

8 C. Dekker, *Nat. Nanotechnol.*, 2007, **2**, 209–215.

9 B. N. Miles, A. P. Ivanov, K. A. Wilson, F. Doğan, D. Japrung and J. B. Edel, *Chem. Soc. Rev.*, 2013, **42**, 15–28.

10 S. Howorka and Z. Siwy, *Chem. Soc. Rev.*, 2009, **38**, 2360.

11 M. Wanunu, *Phys. Life Rev.*, 2012, **9**, 125–158.

12 F. Haque, J. Li, H. C. Wu, X. J. Liang and P. Guo, *Nano Today*, 2013, **8**, 56–74.

13 S. Song, L. Wang, J. Li, C. Fan and J. Zhao, *TrAC - Trends Anal. Chem.*, 2008, **27**, 108–117.

14 A. Oukhaled, L. Bacri, M. Pastoriza-Gallego, J. M. Betton and J. Pelta, *ACS Chem. Biol.*, 2012, **7**, 1935–1949.

15 J. D. Munzar, A. Ng and D. Juncker, *Chem. Soc. Rev.*, 2019, **48**, 1390–1419.

16 T. P. J. Knowles, M. Vendruscolo and C. M. Dobson, *Nat. Rev. Mol. Cell Biol.*, 2014, **15**, 384–396.

17 D. M. Walsh, D. M. Hartley, Y. Kusumoto, Y. Fezoui, M. M. Condron, A. Lomakin, G. B. Benedek, D. J. Selkoe, D. B. Teplow and D. B. J. Biol, 1999, **274**, 25945–25952.

18 J. Narkiewicz, G. Giachin and G. Legname, *Prion*, 2014, **8**, 19–32.

19 T. R. Serio, A. G. Cashikar, A. S. Kowal, G. J. Sawicki, J. J. Moslehi, L. Serpell, M. F. Arnsdorf and S. L. Lindquist, *Science (80-.).*, 2000, **289**, 1317–1321.

20 C. Xue, T. Y. Lin, D. Chang and Z. Guo, *R. Soc. Open Sci.* DOI:10.1098/rsos.160696.

21 V. N. Uversky, J. Li and A. L. Fink, *J. Biol. Chem.*, 2001, **276**, 10737–10744.

22 K. C. Luk, C. Song, P. O'Brien, A. Stieber, J. R. Branch, K. R. Brunden, J. Q. Trojanowski and V. M.-Y. Lee, *Proc. Natl. Acad. Sci.*, 2009, **106**, 20051–20056.

23 K. D. Vernon-Parry, *III-Vs Rev.*, 2000, **13**, 40–44.

24 M. Winey, J. B. Meehl, E. T. O'Toole and T. H. Giddings, *Mol. Biol. Cell*, 2014, **25**, 319–323.

25 A. Cricenti, S. Colonna, M. Girasole, P. Gori, F. Ronci, G. Longo, S. Dinarelli, M. Luce, M. Rinaldi and M. Ortenzi, *J. Phys. D. Appl. Phys.*, , DOI:10.1088/0022-3727/44/46/464008.

26 L. Schermelleh, A. Ferrand, T. Huser, C. Eggeling, M. Sauer, O. Biehlmaier and G. P. C. Drummen, *Nat. Cell Biol.*, 2019, **21**, 72–84.

27 M. H. Horrocks, L. Tosatto, A. J. Dear, G. A. Garcia, M. Iljina, N. Cremades, M. Dalla Serra, T. P. J. Knowles, C. M. Dobson and D. Klenerman, *Anal. Chem.*, 2015, **87**, 8818–8826.

28 D. Wendell, P. Jing, J. Geng, V. Subramaniam, T. J. Lee, C. Montemagno and P. Guo, *Nat. Nanotechnol.*, 2009, **4**, 765–772.

29 M. Wanunu, T. Dadosh, V. Ray, J. Jin, L. McReynolds and M. Drndić, *Nat. Nanotechnol.*, 2010, **5**, 807–814.

30 R. Kawano, A. E. P. Schibel, C. Cauley and H. S. White, *Langmuir*, 2009, **25**, 1233–1237.

31 W. Li, N. A. W. Bell, S. Hernández-Ainsa, V. V. Thacker, A. M. Thackray, R. Bujdoso and U. F. Keyser, *ACS Nano*, 2013, **7**, 4129–4134.

32 J. Li, M. Gershow, D. Stein, E. Brandin and J. A. Golovchenko, *Nat. Mater.*, 2003, **2**, 611–615.

33 J. J. Kasianowicz, E. Brandin, D. Branton and D. W. Deamer, *Proc. Natl. Acad. Sci.*, 1996, **93**, 13770–13773.

34 I. M. Derrington, T. Z. Butler, M. D. Collins, E. Manrao, M. Pavlenok, M. Niederweis and J. H. Gundlach, *Proc. Natl. Acad. Sci. U. S. A.*, 2010, **107**, 16060–16065.

35 https://nanoporetech.com Accessed on 01/06/20

36 H. S. White and A. Bund, *Langmuir*, 2008, **24**, 2212–2218.

37 A. R. Hall, A. Scott, R. Dvir, K. K. Mehta, H. Bayley and C. Dekker, *Nat. Nanotechnol.*, 2010, **5**, 874–877.

38 W. Shi, N. Sa, R. Thakar and L. A. Baker, *Analyst*, 2015, **140**, 4835–4842.

39 D. Perry, D. Momotenko, R. A. Lazenby, M. Kang and P. R. Unwin, *Anal. Chem.*, 2016, **88**, 5523–5530.

40 L. Song, M. R. Hobaugh, C. Shustak, S. Cheley, H. Bayley and J. E. Gouaux, *Science (80-.).*, 1996, **274**, 1859–1866.

41 A. J. Storm, J. H. Chen, X. S. Ling, H. W. Zandbergen and C. Dekker, *Nat. Mater.*, 2003, **2**, 537–540.

42 F. Zhang, K. Sautter, A. M. Larsen, D. A. Findley, R. C. Davis, H. Samha and M. R. Linford, *Langmuir*, 2010, **26**, 14648–14654.

43 X. Lin, A. P. Ivanov and J. B. Edel, *Chem. Sci.*, 2017, **8**, 3905–3912.

44 H. Bayley and C. R. Martin, *Chem. Rev.*, 2000, **100**, 2575–2594.

45 D. C. Grahame, *Chem. Rev.*, 1947, **41**, 441–501.

46 M. Wanunu, W. Morrison, Y. Rabin, A. Y. Grosberg and A. Meller, *Nat. Nanotechnol.*, 2010, **5**, 160–165.

47 Smoluchowski, M. v. Z. *Phys. Chem.* 1917, 92, 129

48 A. J. Storm, C. Storm, J. Chen, H. Zandbergen, J. F. Joanny and C. Dekker, *Nano Lett.*, 2005, **5**, 1193–1197.

49 S. Umehara, N. Pourmand, C. D. Webb, R. W. Davis, K. Yasuda and M. Karhanek, *Nano Lett.*, 2006, **6**, 2486–2492.

50 R. M. M. Smeets, U. F. Keyser, D. Krapf, M. Y. Wu, N. H. Dekker and C. Dekker, *Nano Lett.*, 2006, **6**, 89–95.

51 C. Plesa, S. W. Kowalczyk, R. Zinsmeester, A. Y. Grosberg, Y. Rabin and C. Dekker, *Nano Lett.*, 2013, **13**, 658–663.

52 M. Firnkes, D. Pedone, J. Knezevic, M. Döblinger and U. Rant, *Nano Lett.*, 2010, **10**, 2162–2167.

53 A. Ulman, *Chem. Rev.*, 1996, **96**, 1533–1554.

54 A. Baptista, F. Silva, J. Porteiro, J. Míguez and G. Pinto, *Coatings*, 2018, **8**, 0.

55 A. P. Abbott, G. Frisch and K. S. Ryder, *Annu. Rev. Mater. Res.*, 2013, **43**, 335–358.

56 E. Pensa, E. Cortés, G. Corthey, P. Carro, C. Vericat, M. H. Fonticelli, G. Benítez, A. A. Rubert and R. C. Salvarezza, *Acc. Chem. Res.*, 2012, **45**, 1183–1192.

56 D. Pedone, M. Firnkes and U. Rant, *Anal. Chem.*, 2009, **81**, 9689–9694.

57 R. R. Breaker, W. Winkler and A. Nahvi, *Nature*, 2002, **419**, 952–956.

58 C. Tuerk and L. Gold, *Science*, 1990, **249**, 505–510.

59 https://www.atdbio.com/content/61/Nucleic-acid-aptamers Accessed on 01/06/20

60 S. Burge, G. N. Parkinson, P. Hazel, A. K. Todd and S. Neidle, *Nucleic Acids Res.*, 2006, **34**, 5402–5415.

61 M. McKeague and M. C. Derosa, *J. Nucleic Acids*, , DOI:10.1155/2012/748913.

62 Z. Xiao, D. Shangguan, Z. Cao, X. Fang and W. Tan, *Chem. - A Eur. J.*, 2008, **14**, 1769–1775.

63 D. M. Tasset, M. F. Kubik and W. Steiner, *J. Mol. Biol.*, 1997, **272**, 688–698.

64 K. Tsukakoshi, K. Abe, K. Sode and K. Ikebukuro, *Anal. Chem.*, 2012, **84**, 5542–5547.

65 D. E. Koshland, J. G. Nemethy and D. Filmer, *Biochemistry*, 1966, **5**, 365–385.

66 J. Monod, J. Wyman and J. P. Changeux, *J. Mol. Biol.*, 1965, **12**, 88–118.

67 Q. Wang, J. Q. Liu, Z. Chen, K. W. Zheng, C. Y. Chen, Y. H. Hao and Z. Tan, *Nucleic Acids Res.*, 2011, **39**, 6229–6237.

68 J. Larkin, R. Y. Henley, M. Muthukumar, J. K. Rosenstein and M. Wanunu, *Biophys. J.*, 2014, **106**, 696–704.

69 N. A. W. Bell and U. F. Keyser, *J. Am. Chem. Soc.*, 2015, **137**, 2035–2041. https://pubs.acs.org/doi/full/10.1021/ja512521w. Further use of figures should be directed to the ACS.

70 J. Y. Y. Sze, A. P. Ivanov, A. E. G. Cass and J. B. Edel, *Nat. Commun.*, 2017, **8**, 1–10.

71 E. C. Yusko, J. M. Johnson, S. Majd, P. Prangkio, R. C. Rollings, J. Li, J. Yang and M. Mayer, *Nat. Nanotechnol.*, 2011, **6**, 253–260.

72 R. Wei, V. Gatterdam, R. Wieneke, R. Tampé and U. Rant, *Nat. Nanotechnol.*, 2012, **7**, 257–263.

73 D. Rotem, L. Jayasinghe, M. Salichou and H. Bayley, *J. Am. Chem. Soc.*, 2012, **134**, 2781–2787. https://pubs.acs.org/doi/full/10.1021/ja2105653. Further use of figures should be directed to the ACS.

74 P. Actis, A. Rogers, J. Nivala, B. Vilozny, R. A. Seger, O. Jejelowo and N. Pourmand, *Biosens. Bioelectron.*, 2011, **26**, 4503–4507.

75 D. Shu, G. Changlu and G. Li-Qun, *Anal.Chem.*, 2009, **81**, 6649–6655.

76 G. R. Abel, Z. A. Calabrese, J. Ayco, J. E. Hein and T. Ye, *Bioconjug. Chem.*, 2016, **27**, 698–704.

Chapter 2: Materials and methods

2.1. Overview *62*
2.2. Nanopipette fabrication *62*
2.3. Nanopipette functionalisation *63*
2.3.1. Nanopipette aptamer modification **64**
2.4. Experimental *65*
2.4.1. Ag/AgCl electrode preparation **65**
2.4.2. Electrolyte solutions **65**
2.4.3. Electrochemical set-up **66**
2.4.4. Translocation studies **67**
2.4.5. Data acquisition **68**
2.5. Data analysis *68*
2.5.1. I/V curves **68**
2.5.2. Gap-free studies **69**
2.5.3. Noise analysis **73**
2.5.3.1. Root mean square (RMS) 73
2.5.3.2. Power spectrum density (PSD) 73
2.6. Materials utilised: proteins and DNA aptamers *73*
2.7. References *75*

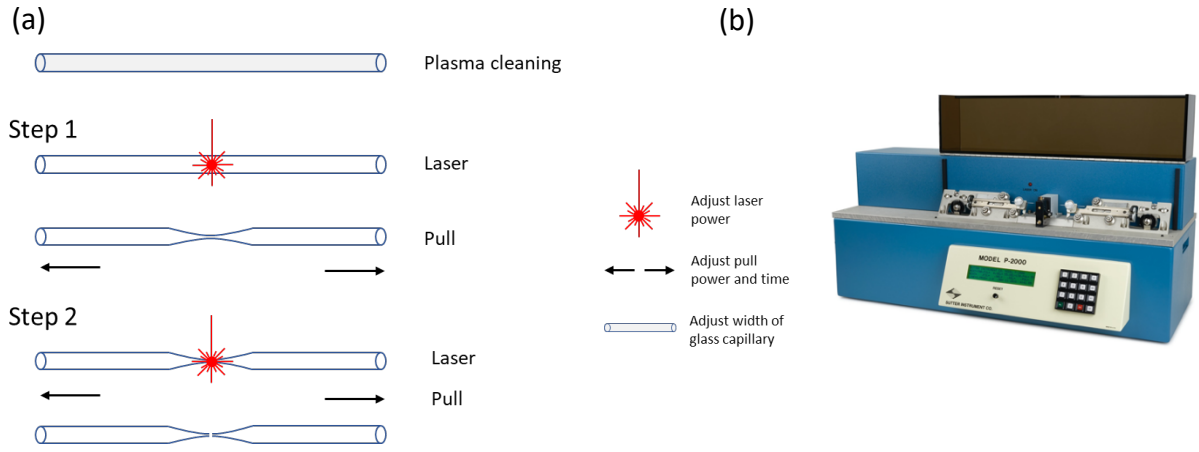
2.1 Overview

In this chapter, an overview of the materials and methods used throughout the PhD thesis are provided. Initially, the fabrication process alongside characterisation studies of the aptamer bound glass nanopipettes are described. Next, the set-up and materials used in electrochemical experiments as well as the methods used in data analysis are described. Finally, the protein analytes and DNA oligonucleotide sequences used throughout the experiments are detailed including storage details and suppliers.

2.2. Nanopipette fabrication

The process of nanopipette fabrication is described in Figure 2.1(a). Quartz capillaries (7.5cm length, 0.5mm diameter) were initially plasma cleaned for twenty minutes to remove any surface contaminants while hydrolysing the surface. The capillaries were then carefully placed and aligned into a pipette puller (Sutter P-2000) before tightening via adjustable clamps (Figure 2.1(b)) The puller functions via a two-step programme, with the first step forming a taper in the capillary and the second step forming two nanopipettes. An SEM image of a single-barrelled nanopipette produced through this technique can be seen in Figure 2.1(c)[1].

Pulling programmes are not only highly specific to a given instrument but are also highly dependent on environmental conditions (humidity and temperature), leading to nanopipettes with variable geometries and diameters. Furthermore, the pulling programme may need to be modified to maintain the correct taper length and nanopore diameter.



(c)

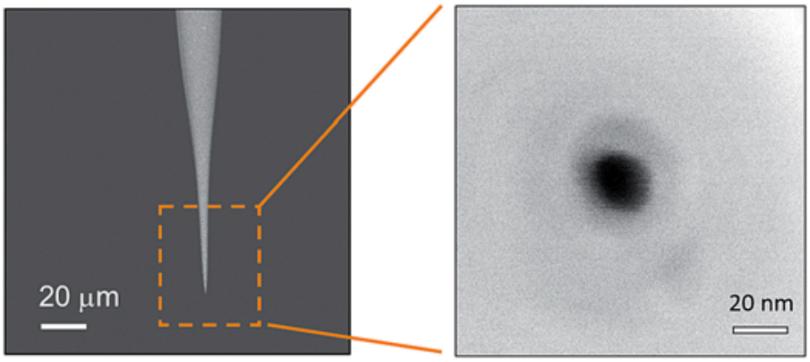


Figure 2. 1. *(a) The process of nanopipette fabrication. An initial plasma cleaning step removes contaminants and hydrolyses the surface. The nanopipette is then placed in a pipette puller where it is heated by a laser and subsequently pulled. The nanopipette dimensions (taper length, pore diameter) can be adjusted by varying the laser power, glass capillary width and pull time/strength. (b) The Sutter P-2000 pipette puller. (c) SEM images of a single barrelled nanopipette. (c) An SEM image of a nanopipette (left) alongside the nanopore (right). Figure adapted from reference 1.*

The pulling programme used throughout the studies is presented in Table 2.1. Adjustable parameters included heat, filament, velocity, delay and pull. 'Heat' refers to the magnitude of laser power used, while 'Filament' refers to the longitudinal length of the capillary heated. 'Velocity' is related to the speed of the pull while 'Delay' refers to the time between the laser being switched off and the subsequent pull. Finally, 'Pull' is related to the force of the pulling motion.

Table 2. 1. *The pulling programme parameters used in the construction of nanopipettes utilising the Sutter P-2000 instrument. Heat' refers to the magnitude of laser power used while 'Filament' refers to the longitudinal length of the capillary heated. 'Velocity' is related to the speed of the pull while 'Delay' refers to the time between the laser being switched off and the subsequent pull and finally 'Pull' is related to the force of the pulling motion.*

Step 1					**Step 2**				
Heat	Filament	Velocity	Delay	Pull	Heat	Filament	Velocity	Delay	Pull
575	3	3	145	75	600	0	15	128	200

2.3. Nanopipette functionalisation

The set-up used in the vapour silanisation[2] of nanopipettes is shown in Figure 2.2. Twin nanopipettes fabricated from the same glass capillary were suspended over a pre-heated (20 minutes, 90°C) glass vial, containing 400uL of the silanising agent 3-(trimethoxysilyl)propyl methacrylate (TMSPM). The glass vials were transferred to a desiccator and silanised under vacuum for two hours.

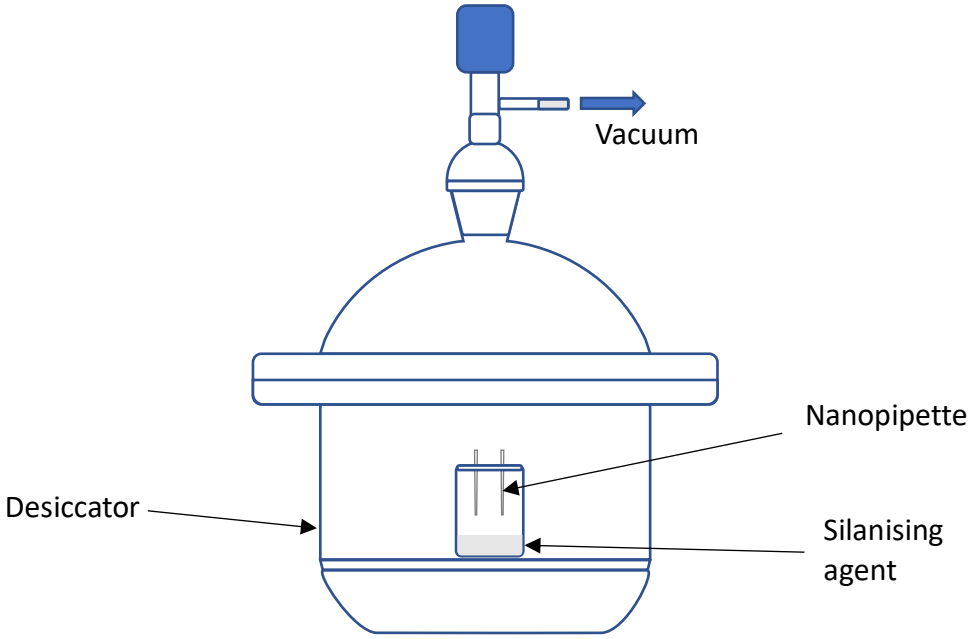


Figure 2. 2. *The set-up used to vapour silanise nanopipettes. Pre-heated glass beakers were filled with the silanising agent with nanopipettes suspended above. The beakers were then placed in a desiccator and a vacuum applied for 2 hours.*

2.3.1. Nanopipette aptamer modification

(i) Thiol aptamer reduction

The thiol aptamer shipped in its protected disulphide form required reduction for experimentation. The disulphide protecting group of the thiol aptamer (500pM) was removed through the addition of the reducing agent TCEP (2.5nM, 5eq) as carried out in 1 x TE (TRIS-EDTA) buffer (pH 8.0)[3]. The solution was incubated for 2 hours at room temperature to ensure complete reduction of the thiol prior to the subsequent bioconjugation reaction.

(ii) Nanopipette bioconjugation

The silanised nanopipette tip was suspended in the DNA aptamer/TCEP solution mix for at least 24 hours to maximise bioconjugation efficiency. In addition to acting as a reductant, TCEP has also been reported to act as a nucleophilic catalyst[4-7] in the bioconjugation reaction.

(iii) Optimisation

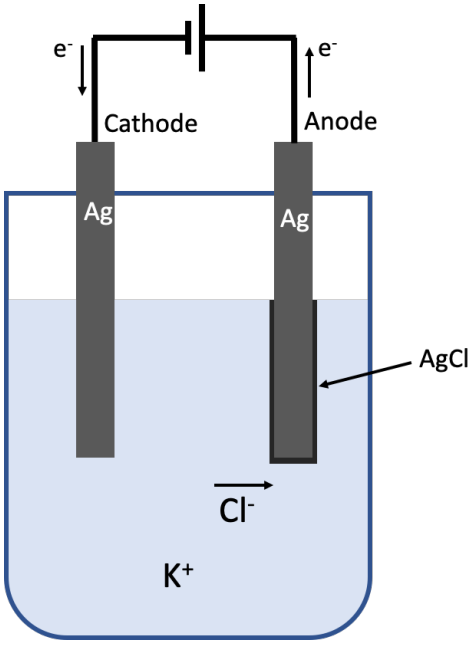
Silanisation was initially carried out at over a shorter reaction time (1h), but the low silanisation efficiency subsequently resulted in increased incubation times being used. In addition, the TCEP to thiol aptamer ratio was increased from the original protocol (1.7:1) to 5:1 as a way of increasing bioconjugation efficiency.

Even after optimisation, subsequent modification of the nanopipette with aptamers was low (~10 %), necessitating the use of large batches (20-30 nanopipettes) for experiments. Fortunately, it was found that as long as the tip was kept in solution, modified pipettes could be used for several weeks.

2.4. Experimental

2.4.1. Ag/AgCl electrode preparation

Non-polarisable Ag/AgCl electrodes were used solely in all electrochemical experiments. Ag wires (roughly 5cm long) were connected to the positive and the negative electrodes of a battery (Figure 2.3). The electrodes were dipped in 1M KCl solution until the electrode at the anode was coated in AgCl. The electroplating process can be described via the half-equations below. Once prepared, AgCl electrodes were stored in 1M KCl and were used within 2 days.



Anode: $Ag_{(s)} + Cl^-_{(aq)} \rightleftharpoons AgCl(s) + e^-$

Cathode: $2H^+_{(aq)} + 2e^- \rightleftharpoons H_{2(g)}$

Figure 2. 3. *The set-up used to fabricate AgCl electrodes*

2.4.2. Electrolyte solutions

The electrolyte solution used in all nanopore experiments was 100 mM KCl 1 x TE buffer (pH 8.0), although in each case were made up as 1 M KCl 1 x TE stock solutions and diluted when required to save time. 1 x TE was initially prepared through dilution of 100 x TE using autoclaved deionised water, ensuring that the final electrolyte solutions contained only K^+ and Cl^- ions. To prepare the stock solutions, KCl crystals were carefully weighed out prior to

the addition of the 1 x TE buffer. The pH of the electrolyte was subsequently adjusted to pH 8.0 using 1M KOH, and filtered (0.2µm) to remove any particulates. The 1M KCl 1 x TE was simply diluted with 1 x TE as required for experimentation.

2.4.3. Electrochemical set-up

Nanopipettes were filled with the electrolyte solution using a microfil needle with any resultant nanobubbles removed via application of negative pressure, using a syringe and/or rasping using corrugated tweezers.

A glass bath pre-rinsed with deionised water was filled with 100 mM 1 x TE electrolyte solution. AgCl electrodes were then inserted into the filled nanopipette and bath and connected to the head-stage using electrode clips (Figure 2.4). The application of a voltage bias then leads to the generation of ionic current. Current vs time traces (typically recorded at minute intervals) could be subsequently measured using Axopatch 200B (molecular devices) and digitised using Digidata 1440A (molecular devices).

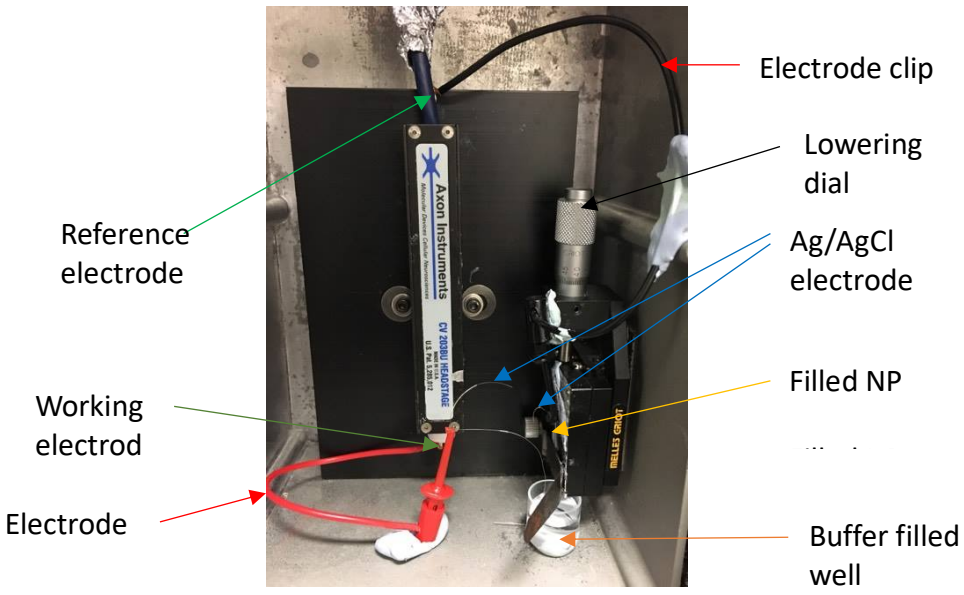


Figure 2.4. *The axopatch set-up used in electrochemical experiments is shown above. The analyte dissolved in filled nanopipette with an inserted Ag/AgCl electrode was placed into the well containing the same electrolyte concentration and electrode.*

(i) Optimisation

Nanobubbles were prevalent in modified nanosensors. Typically they required removal via the application of negative pressure (via syringe) and agitation (with tweezers) at the same time. In addition to blocking the nanopore, nanobubbles could also lead to significant noise and/or drops in the ionic current.

2.4.4. Translocation studies

In all cases, the analyte was introduced in the nanopipette, with the working electrode placed outside the nanopipette. In this set-up (Figure 2.5), the application of a positive voltage leads to the translocation of negatively charged analytes. Gap-free measurements were recorded at 250kHz and filtered at 10kHz, and re-filtered and resampled as required.

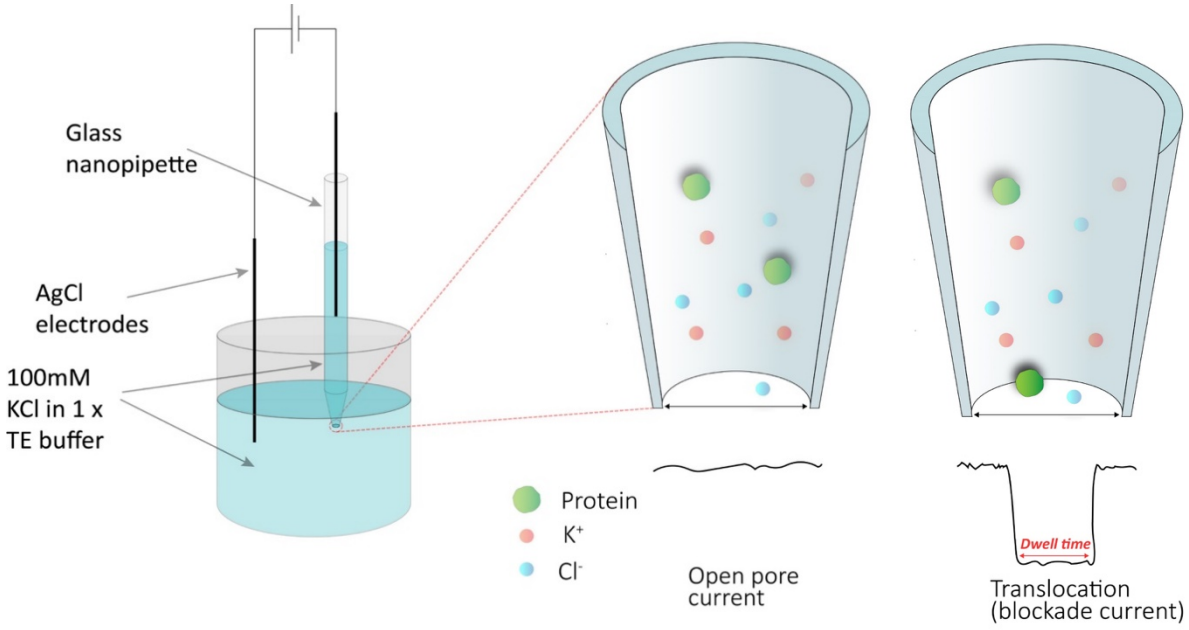


Figure 2.5. *The experimental set-up used in electrochemical based nanopipette experiments. Nanopipettes filled with electrolyte is lowered into a bath filled with the same electrolyte. The application of a voltage bias leads to the generation of ionic current.*

(i) Protein translocation studies

In protein binding studies, nanopipettes at every stage of the modification process (non-modified, silanised and aptamer modified), as well as those modified with control DNA sequences (same length), were initially tested and recorded using 100mM KCl 1 x TE as the electrolyte. The electrolyte was then removed before being flushed out and replaced with electrolyte solution containing the protein of interest. The method chosen is less accurate (any remaining KCl electrolyte would dilute the protein concentration at the tip) than filling the pipette directly with a protein solution, but was overall still preferred. Conducting experiments in this way allows a direct comparison before and after protein addition while allowing the most efficient use of the sensor when considering the low functionalisation success rate.

(ii) Characterisation studies

A series of translocation studies were used to confirm whether aptamer modification had taken place. A DNA sequence complementary to the thrombin aptamer (TBA) as well as a scrambled control sequence were translocated through TBA-modified nanopipette and any change in ionic current was measured.

(iii) Sensor regeneration studies

The aptamer-modified sensor could be regenerated as follows. Initially, the sensor was measured (I/V curves and representative traces) in KCl, before being replaced with thrombin. The thrombin solution was then removed from the aptamer-modified pipette using the microfil needle while multiple flushings with 1 x TE buffer was used to remove any traces of thrombin. 1 x TE was removed from the sensor and refilled with 100 mM KCl allowing measurements to be retaken. This process can be repeated as many time as required.

2.4.5. Data acquisition

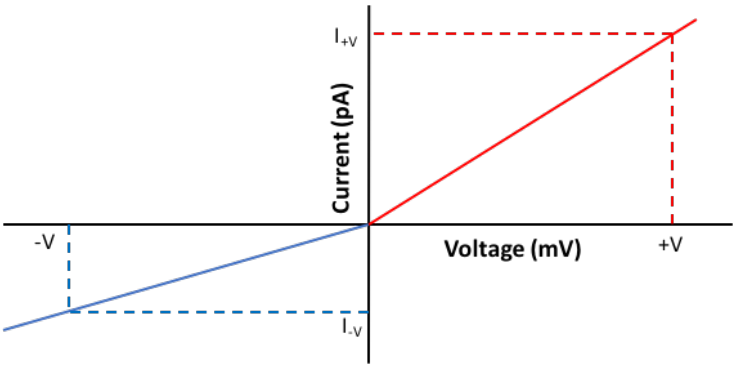
Electrochemical based data was acquired using Clampex software via two programmes: I/V curves provided information on the size of the nanopipettes as well as its surface charge and were measured by recording current under a range of voltages. Resistive pulse-based studies were carried out using gap-free measurements, whereby the current was measured at a constant voltage.

2.5. Data analysis

Nanopipettes were first calibrated by ensuring that 0 pA of current was shown at 0 mV before recording any measurements.

2.5.1. I/V curves

Clampfit was used to determine I-V curves (Figure 2.6), providing an easy way of determining rectification which in turn indicated the surface charge and modification of the nanopipette. The rectification ratio was determined by dividing the current at a given voltage over the current at a voltage with the same magnitude, but opposite polarity, as described in the following equation.



$$r = \frac{I_{V=+X}}{I_{V=-X}}$$

Figure 2. 6. *A schematic showing an I-V curve. The rectification ratio (right) is determined by the current at a given voltage (+V) over the current at its negative equivalent (-V).*

2.5.2. Gap-free studies

Custom-built Matlab analysis software developed by the Edel/Ivanov group was used to analyse translocation, with the general procedure summarised below:

(1) Data sets were resampled and re-filtered in line with the respective S:N ratio of the trace and the dwell times of peaks (Figure 2.7). Generally, data was only re-filtered if traces were exceedingly noisy, with care taken to ensure that the low-pass filter is not greater than the dwell times of the peak. The effects of low-pass filters are explored more thoroughly in chapter 4 and include data sets accompanied by events with different dwell times necessitating the use of different low-pass filters. For example, a low-pass filter of 10 kHz, equivalent to 0.1 ms, should not be used with peaks with dwell times less than 0.1 ms due to the aliasing that can occur. Furthermore, the sampling rate should be at least 2 x (although in practice normally 5 x) the filter as dictated by Nyquist theorem.

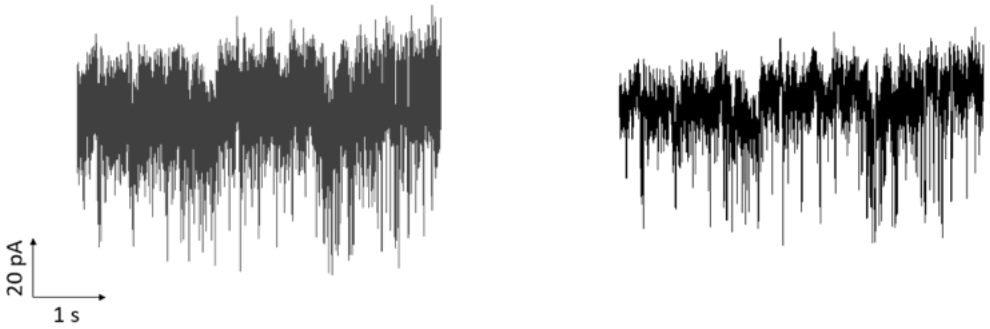


Figure 2. 7. *The effects of low-pass filters on 10 pM thrombin translocation through TBA-modified pipettes. The trace (left) is filtered with a 10 kHz low-pass filter, before filtering with a 1 kHz low-pass filter.*

(2) The baseline of the trace is fitted as a polynomial with associated parameters determining how closely the code 'fits' the trace (Figure 2.8(a)). In particular, a

balance is required between following the baseline closely enough without oversampling (Figure 2.8(b)) or undersampling (Figure 2.8(c)).

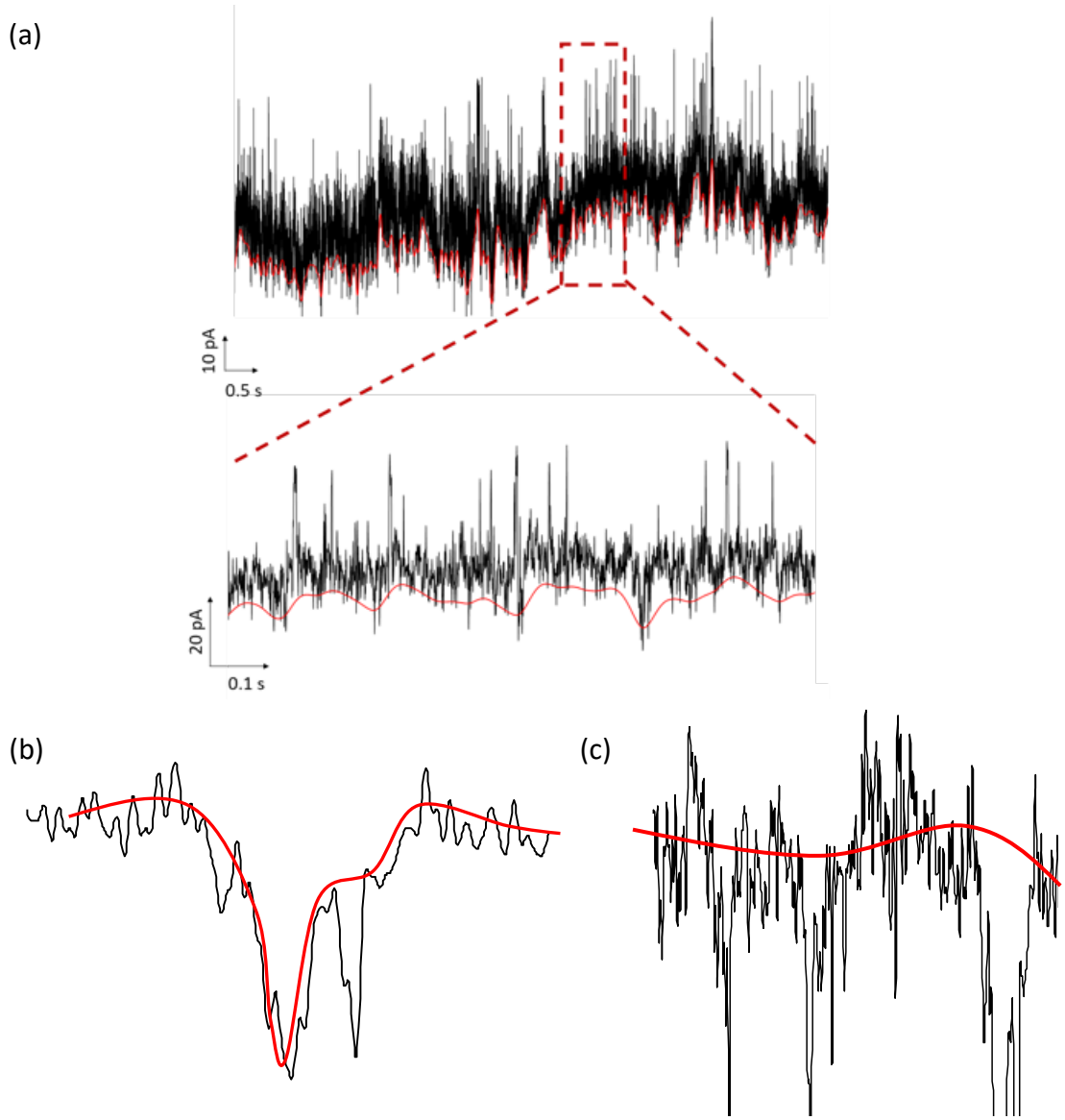


Figure 2. 8. *(a) The baseline is fitted using Poisson distribution (b) The trace is oversampled with translocation peaks counted as part of the baseline. (c) The trace is undersampled with fitting not following the baseline as closely as required.*

(3) A threshold defined by standard deviation (Figure 2.9) is used to discriminate between noise and translocation peaks. Peaks that cross the threshold were counted as events while those that do not cross were discarded. Overall, the maximum number of peaks were chosen while preventing background noise from being counted as translocation peaks.

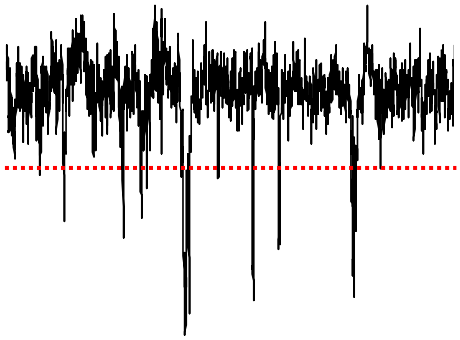


Figure 2. 9. *A threshold (red dotted lines) based on standard deviation is used to discriminate between translocation peaks and background noise.*

(4) Peaks could now be selected (Figure 2.10), although care has to be taken to ensure that the characteristics of the calculated peak reflect those shown in the trace. In particular, peaks are typically selected at full width at half maximum (fwhm), although this could be altered, or switched off, in accordance with each individual trace. Furthermore, other restrictions could be applied, including a minimum peak width or minimum peak amplitude.

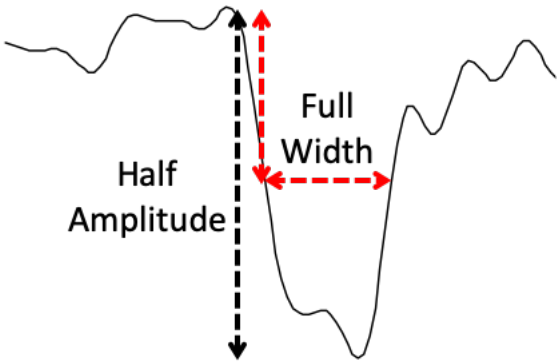


Figure 2.10. *Peaks selected by the software are typically done at full width at half maximum*

(5) Data analysis can be carried out to extract peak characteristics (peak amplitude and dwell time), while also allowing determination of the capture rate and identifying trends via scatter plots.

(i) Histogram analysis

Histogram analysis (Figure 2.11) involves fitting data to an appropriate distribution (Gaussian) in turn, allowing mean values of dwell time and peak amplitude to be determined. The correct bin width must be appropriately chosen to display the most accurate average value.

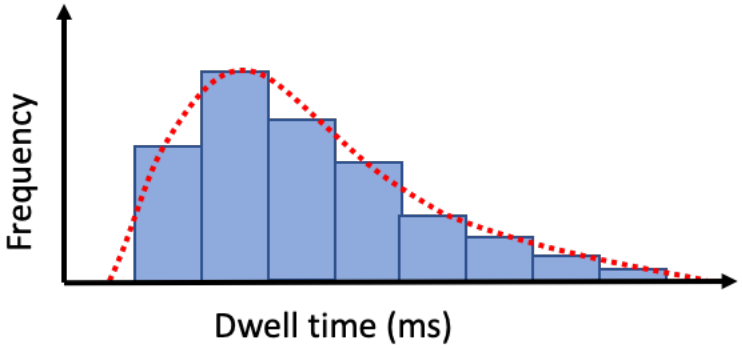


Figure 2. 11. *Histogram analysis of the translocation peak dwell time. Correct bin width provides a far more accurate value of the average dwell time.*

(ii) Scatter plots

Scatter plots (e.g. dwell time vs peak amplitude) shown below (Figure 2.12) allow the identification of trends in data, for example, whether dwell time (e.g. molecule size) is dependent on peak amplitude (molecule charge). A confidence interval (red circles) allows determination of where the true mean is to a 68% degree of accuracy.

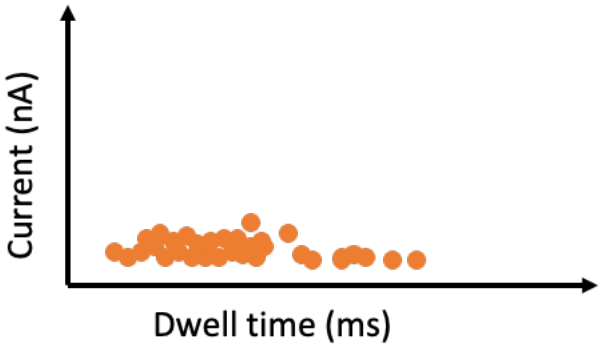


Figure 2.12. *A dwell time vs peak current scatter plot*

(iii) Capture rate

The capture rate can be determined in two ways: via fitting the exponential decay of the inter-event time (t_{on}) as shown in Figure 2.13 or through simply dividing the number of events by the amount of time. As detailed in chapter 4, the inter-event is under-estimated by peak clustering, thereby over-estimating the capture rate. As a result, the capture rate was designated simply as events per time.

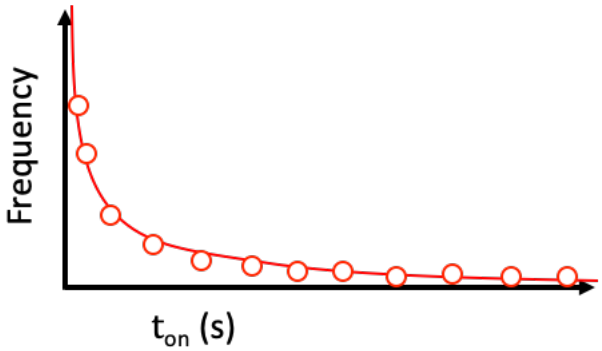


Figure 2. 13. *An exponential decay plot of inter-event time (t_{on}) allows determination of the capture rate.*

2.5.3. Noise analysis

2.5.3.1. Root mean square (RMS)

Root-mean-square (RMS) analysis indicated the noise of each trace. In simple terms, the RMS calculated from the equation below provides the width of the electronic trace and is expected to differ not only between different modifications but also upon the addition of the analyte.

$$RMS = \sqrt{\frac{1}{n}(x_1^2 + x_2^2 + x_n^2)}$$

Equation 2. 1. *Calculation of the root-mean-square (RMS) for the total number of samples (n) over a set of values (x_n).*

2.5.3.2. Power spectrum density (PSD)

The power spectrum density (PSD) measures noise as a function of wavelength. The PSD allows researchers to determine whether the noise is due to flicker noise (low frequency) or thermal (high frequency). In addition, the PSD is particularly crucial in distinguishing between different nanopipette modifications and/or the binding state of recognition elements.

2.6. Materials utilised: proteins and DNA aptamers

Protein samples

α-human thrombin was bought from Cambridge Biosciences, while human serum (from clotted human whole blood) was purchased from Sigma Aldrich. For long term storage samples were kept at -20°C in aliquots. For short term use samples were kept at 4°C and used within 2 weeks.

Acetylated α-synuclein monomer expression

Acetylated α-synuclein monomers were expressed by PhD student Mike Lloyd of the Edel group with an overview of the procedure as follows.

Transformed *E.coli* cells were initially incubated in LB buffer alongside ampicillin (100 µg/ml) at 37°C. Expression was then induced through the addition of Isopropyl β- d-1-thiogalactopyranoside (IPTG) resulting at a final concentration of 1 mM. When the optical density at 600 nm wavelength (OD_{600}) reached 0.5, the cells were then allowed to incubate for 3 hours. The cells could then be harvested by centrifugation (8000 x g) before re-suspension in 50 mM NaCl, 20 mM Tris-HCl (pH 7.4), 5 mM EDTA, containing 1 mM protease inhibitor buffer. The cells were lysed by sonication (2 minutes), boiled (90^0C, 20 minutes)

and centrifuged (16,000 x g, 20 minutes). The resulting supernatant was in turn filtered (0.2 µM syringe filter) before streptomycin sulphate was added.

Acetylated α-synuclein monomer aggregation

Acetylated α-synuclein monomers (800uL at 70 µM in 25mM Tris 100mM NaCl) were ultracentrifuged (1h, 90,000 rpm). The upper 600 µL of the supernatant was removed, allowing the bottom 200 µL containing seeds to be discarded. NaN_3 (2%, 2 µL) was added (to prevent bacterial growth) to 400 µL (70 µM) of the ultracentrifuged acetylated alpha-synuclein monomers and were shaken (37°C, 200 rpm) allowing the formation of oligomers to occur. Oligomers (20 µL) were taken at various time points (2-16h) and stored in the fridge for up to two weeks until required for experimentation.

DNA aptamers

DNA aptamer sequences both non-modified and 5'SH modified were bought from either Sigma Aldrich or IDT. DNA samples were bought as lyophilised samples and re-suspended in 1 x TE buffer as necessary. Samples were stored at 4°C and aliquoted out as required.

(a) Bioconjugation studies

As part of the modification process, thiol modified nucleotide sequences need to be deprotected (with TCEP) before functionalisation with the silanised nanopipette. Shown below are aptamer sequences; thrombin binding aptamer[8] (TBA) and oligomer binding aptamer[9] (TS-0530) alongside a corresponding control sequence containing the same number of nucleotides.

(i) TBA

```
TBA      (29mer):   5'SH AGT CCG TGG TAG GGC AGG TTG GGG TGA CT

CONTROL (29mer):   5'SH AAC ACG TCG GGG CTC GAC CGT GAT CCC GT
```

(ii) TS-0530

```
TS-0530 (24mer):   5'SH GGT GCG GCG GGA CTA GTG GGT GTG

CONTROL (24mer):   5'SH AAT AAA ATG TCC AGA ACG CAA AAG
```

(b) Translocation studies

An additional characterisation method involved translocation of unmodified nucleotide sequences; a complementary sequence to TBA and a control nucleotide sequence, through TBA-modified pipette.

(i) Characterisation

```
TBA Complementary:      TCA GGC ACC ATC CCG TCC AAC CCC ACT GA
TBA Control:            TTG GTA AAA TTT TAC TGG ATA GCG TAT GA
```

2.7. References

1 X. Lin, A. P. Ivanov and J. B. Edel, *Chem. Sci.*, 2017, **8**, 3905–3912.

2 F. Zhang, K. Sautter, A. M. Larsen, D. A. Findley, R. C. Davis, H. Samha and M. R. Linford, *Langmuir*, 2010, **26**, 14648–14654.

3 J. A. Burns, J. C. Butler, J. Moran and G. M. Whitesides, *J. Org. Chem.*, 1991, **56**, 2648–2650.

4 M. W. Jones, G. Mantovani, S. M. Ryan, X. Wang, D. J. Brayden and D. M. Haddleton, *Chem. Commun.*, 2009, 5272–5274.

5 A. B. Lowe, *Polym. Chem.*, 2010, **1**, 17–36.

6 V. S. Khire, T. Y. Lee and C. N. Bowman, *Macromolecues*, 2007, **40**, 5669–5677.

7 G. Z. Li, R. K. Randev, A. H. Soeriyadi, G. Rees, C. Boyer, Z. Tong, T. P. Davis, C. R. Becer and D. M. Haddleton, *Polym. Chem.*, 2010, **1**, 1196–1204.

8 D. M. Tasset, M. F. Kubik and W. Steiner, *J. Mol. Biol.*, 1997, **272**, 688–698.

9 K. Tsukakoshi, K. Abe, K. Sode and K. Ikebukuro, *Anal. Chem.*, 2012, **84**, 5542–5547.

Chapter 3: Construction of an aptamer-modified nanopore sensor

3.1. Overview *77*

3.2 Introduction *77*

3.2.1 Silanisation **77**

3.2.2. Bioconjugation **79**

3.3. Aim *80*

3.4. Results *80*

3.4.1. Nanopipette functionalisation with an aptamer modified pipette. **80**

3.4.1.1 Silanisation 81

3.4.1.2. Aptamer reduction 81

3.4.1.3. Bioconjugation 81

3.5. Characterisation *81*

3.5.1. Fabrication Characterisation **81**

3.5.1.1. I/V curves 81

3.5.1.2. Translocation studies 82

3.5.2. Noise characterisation 83

3.6. Sensor design *84*

3.7. Discussion *87*

3.8. Conclusion *92*

3.9. References *92*

3.1. Overview

In this chapter the functionalisation strategy of the aptamer-modified nanosensor is described. In the introduction, the reactions underpinning sensor development; silanisation and bioconjugation, are discussed. As part of the results, the characterisation methods are described including electrochemical based *in situ* I/V curves and the translocation of nucleotide sequences complementary to thrombin binding aptamer (TBA). In addition, noise analysis[1-2] including root mean square (RMS) and power spectrum density (PSD) provided further insight into the fabrication process. Finally, the pore diameter throughout the fabrication process is also estimated via conductance and bond length/angle measurements allowing the sensor design to be formulated. In the discussion, the reaction mechanisms involved in the functionalisation methods are explored, alongside the rationale for selecting this particular bioconjugation method over other commonly utilised methods. At the end of the chapter a model of the sensor is presented suitable for the detection of thrombin and alpha synuclein oligomers as described in chapters 4 and 5 respectively.

3.2 Introduction

Construction of the aptamer-modified nanosensor requires the attachment of an appropriately modified aptamer to a nanopipette modified with the compatible functional group. One strategy commonly utilised by researchers involves gold sputtering[4] of a surface, followed by the non-covalent attachment of a thiol derivatised aptamer. Unfortunately, gold-thiol bonds are relatively weaker[5] (418 $kJmol^{-1}$) and prone to dissociation upon application of high voltages[6]. Conversely, an aptamer bound to the glass nanopipette via strong covalent (C-S) bonds (699 $kJmol^{-1}$) would allow its use in detection for long periods of time when subjected to high voltages, making such a functionalised surface ideal for electrochemical sensing. As a result, our chosen functionalisation strategy utilises an initial silanisation step followed by aptamer attachment via covalent bonding, i.e. bioconjugation.

3.2.1 Silanisation

Glass nanopipettes possess silanol functional groups and therefore specific coupling with silanising agents (Figure 3.1) was an easy route to add functionality. As an example, (3-aminopropyl)trimethoxysilane and 3-azidopropyltriethoxysilane can react with NHS activated esters[7] and alkynes[8] (under Cu catalysis) respectively.

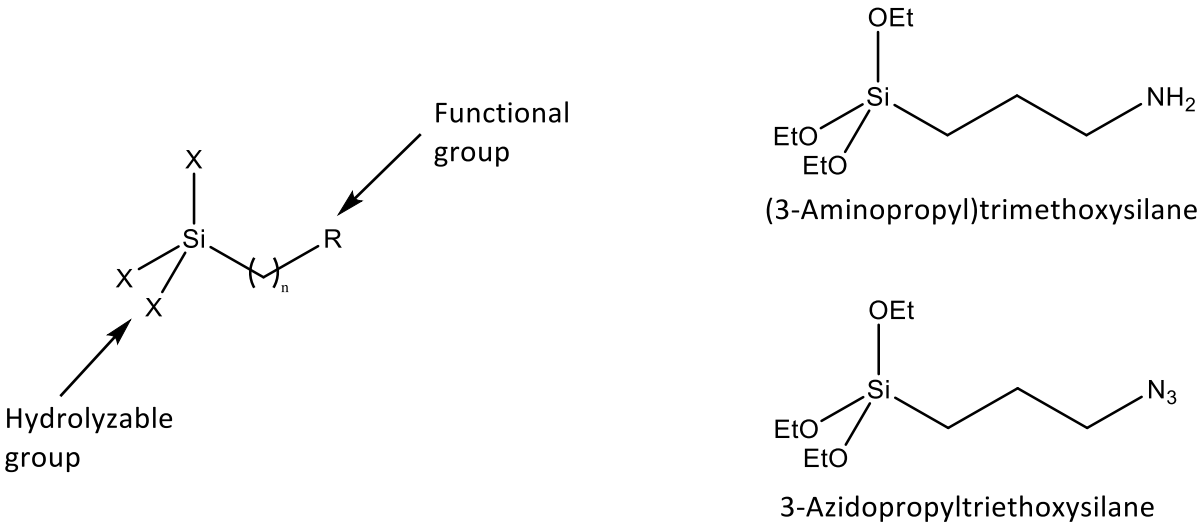


Figure 3. 1. *A silanising agent includes hydrolysable groups alongside a functional group*

The process of silanisation[9] is described in Figure 3.2. The first step involves the hydrolysis (i) of the silanising agent allowing cross-linking with other silanols via hydrogen bonding (ii) and subsequently via condensation (iii). The cross-linked silanols are now able to interact with the hydroxyl groups on the glass surface (iv), and upon a second condensation reaction, lead to the formation of siloxane covalent bonds (v).

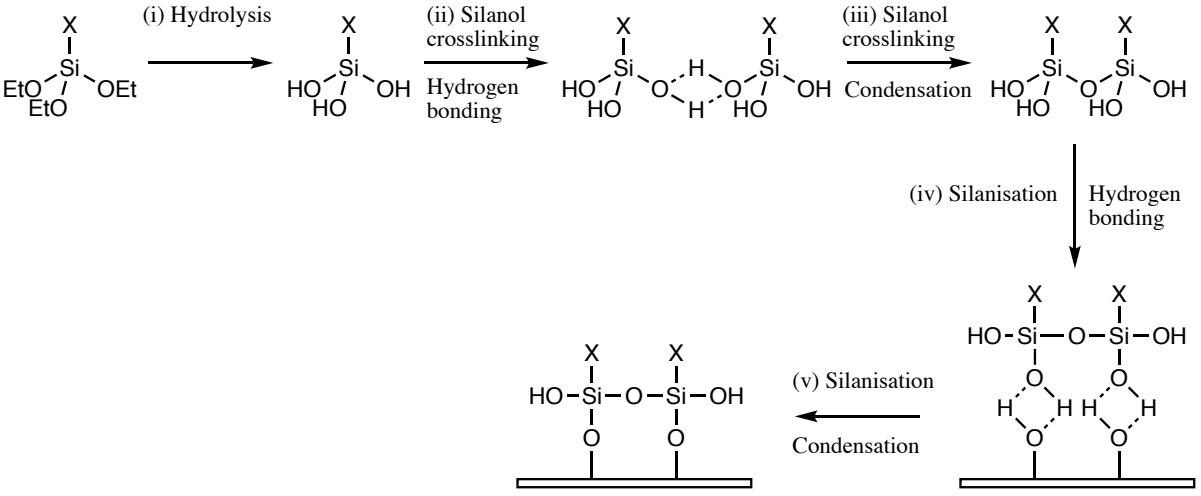


Figure 3. 2. *The process of silanisation. An initial hydrolysis reaction (i) leads to silanol cross-linking via hydrogen bonding (ii) and subsequently a condensation reaction (iii). The cross-linked silanol can now react with silanol surface groups through hydrogen bonds (iv) and a final condensation reaction (v).*

A further consideration is whether to carry out silanisation in solution, or vapour phase. In solution-based silanisation[10], the thickness of the silanol surface layer is dependent on the concentration of the silanising agent and the amount of water present.

This can potentially result in 'over-silanisation'[11] and poly-layer formation. Conversely, vapour based silanisation[12] requires more sophisticated equipment (vacuum chamber) and longer reaction times (typically hours vs minutes) but when carried out in low water vapour-based environments result in the formation of mono-silane layers.

3.2.2. Bioconjugation

After incorporating functionality to the glass nanopipette, a subsequent bioconjugation reaction is required to attach the DNA aptamer. Bioconjugation based click chemistry utilises a 'one pot' methodology to generate an irreversible, highly specific product without the need for coupling agents, or harmful solvents. Copper-catalysed azide alkyne cycloaddition[8] (CuAAC) is a commonly used bioconjugation strategy that provides a highly specific and strong covalent linkage (Figure 3.3). However, the presence of copper ions can lead to oxidative based degradation of oligonucleotides[13].

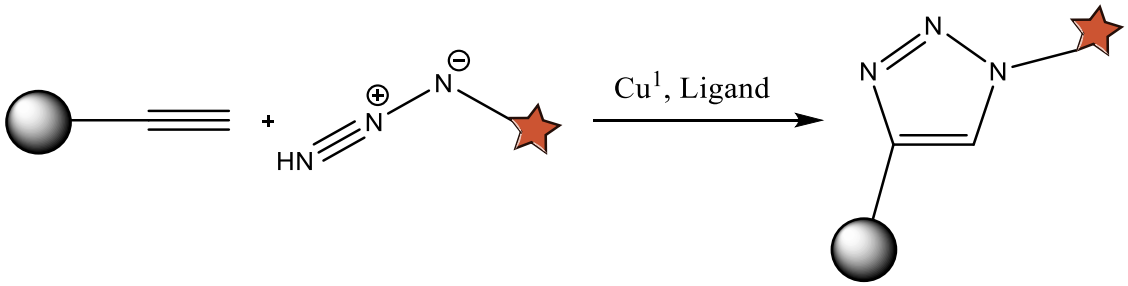


Figure 3. 3. *A scheme highlighting the commonly used bioconjugation strategy; copper catalysed azide alkyne cycloaddition (CuAAC). An azide couples with an alkyne under copper catalysis in a Diers-Alder type reaction.*

As such, alternative methods were investigated so as to determine a highly efficient bioconjugation strategy without resulting in the degradation of the DNA aptamer. In any context, aptamer attachment should ideally be carried out in the minimum number of steps (i.e avoid crosslinking agents), allowing for the greatest bioconjugation efficiency.

3.3. Aim

The proposed strategy outlined in Figure 3.4 describes the aptamer attachment strategy used utilising a terminal methyl acrylate functional group[14-19]. In a separate one-pot mix, Tris(2-carboxyethyl)phosphine (TCEP) acts as a reducing agent removing the protecting group from the thiol aptamer and then subsequently serves as a nucleophilic catalyst for aptamer attachment in the presence of the silanised nanopipettes[19]. This strategy allows aptamer attachment in a cost-effective two-step methodology, while preventing the aptamer degradation seen with copper catalysis[13], or 'over-silanisation'[11], seen in solution based silanisation. Confirmation of aptamer attachment was determined through electrochemical methods; *in situ* I/V curves and the translocation of DNA sequences complementary to the aptamer alongside noise characterisation[1-2]; PSD and RMS. The use of such characterisation provided insight into aptamer conformation and the likely protein-binding mechanism of the aptamer modified pipette.

3.4. Results

3.4.1. Nanopipette functionalisation with an aptamer modified pipette.

Figure 3.4 provides an overall scheme of the functionalisation strategy used. Silanisation of the glass nanopipette (i) occurs alongside the removal of the protecting group of the thiol aptamer via TCEP (ii). Finally, bioconjugation (iii) can occur when the deprotected thiol aptamer reacts with the methacrylate silanised nanopipette.

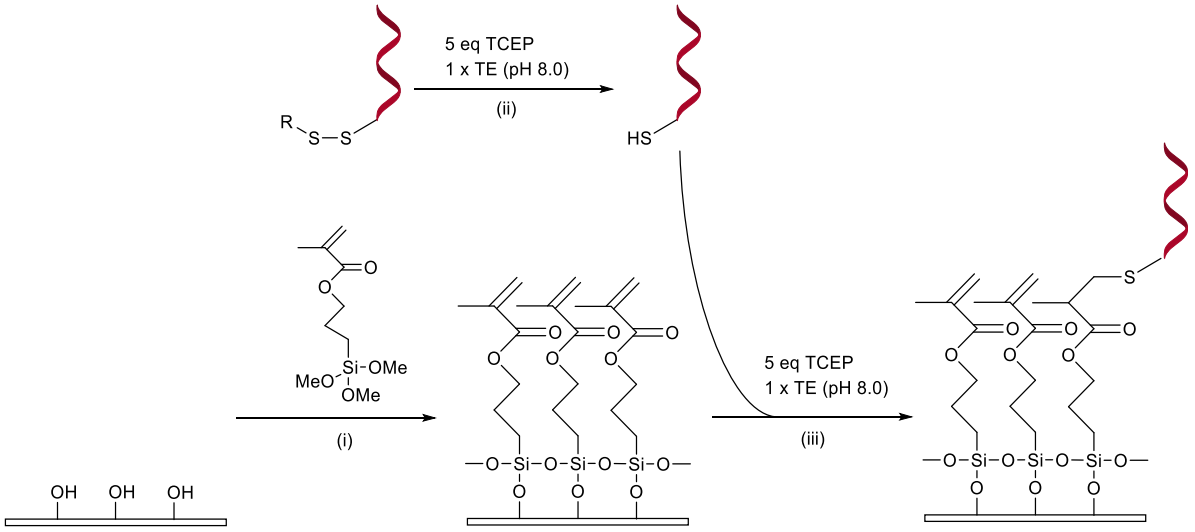


Figure 3. 4. *An overview of the bioconjugation strategy used to construct our aptamer based nanosensor.*

3.4.1.1 Silanisation

An initial plasma cleaning step prior to pipette pulling (as described in chapter 2) not only removes foreign matter (e.g dust) but importantly hydrolyses the surface. Furthermore, the silanisation step carried out in the vapour phase utilised pre-heated vials which in turn limited the presence of water vapour and thereby reduced the likelihood of formation of poly-silane layers[12].

3.4.1.2. Aptamer reduction

The thiol-modified aptamer is provided in its protected form and needs removal before the subsequent bioconjugation reaction can occur. TCEP, a well-known reducing agent, was used as part of the process. A relatively low molar equivalent of TCEP to aptamer (5:1) and high pH (8.0) was used to limit possible side reactions.

3.4.1.3. Bioconjugation

In the final step, silanised nanopipette tips were simply dipped into the aptamer/TCEP mix and left overnight. The bioconjugation reaction occurs via a thiol-methacrylate mechanism and leads to the generation of a strong covalent bond avoiding the need for Cu(I) catalysis[8] (as seen in azide/alkyne chemistry) which is known for its ability to degrade nucleotides[13]. Interestingly, TCEP has also been reported as a nucleophilic catalyst for this reaction, resulting in a highly efficient process.

3.5. Characterisation

3.5.1. Fabrication Characterisation

The fabrication process was monitored by carrying out electrochemically (I/V curves and translocation studies) and using noise characterisation[1-2] (RMS and PSD).

3.5.1.1. I/V curves

I/V curves and the corresponding rectification ratio determined from recording the current at a series of voltages provide an accurate *in-situ* way of determining the surface charge and therefore the degree of modification of the nanopipette. Table 3.1 provides the rectification ratio for different stages of modification; glass, silanised and nucleotide (TBA, 29mer control, TS-0530 and 24 control). Figure 3.5 provides a typical set of I/V curves for unmodified pipettes, silanised pipettes and TBA-modified pipettes in KCl electrolyte only. Shown in the legend are the rectification ratios (at V = 430 mV) obtained for 8 separate pipettes.

Table 3. 1. *The rectification ratio (V = ± 430) at each stage of the modification process (n =8)*

Pore modification	Rectification ratio
glass	1.48 ± 0.2
silane	1.12 ± 0.1
TBA	1.69 ± 0.2
29 control	1.52 ± 0.3
TS-0530	1.70 ± 0.2
24 control	1.42 ± 0.2

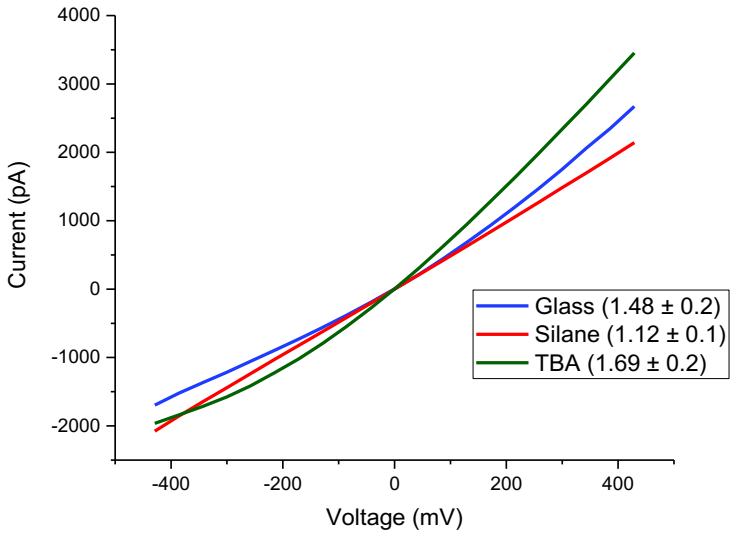


Figure 3. 5. *I/V curves at each stage of the modification process recorded in 100 mM KCl. Shown in the legend is the rectification ratio ± SD (n = 8).*

Unmodified glass nanopipettes demonstrated moderate rectification ratios (1.48), which decrease upon silanisation (1.12) and then increase again upon attachment (1.4-1.7) of DNA sequences.

3.5.1.2. Translocation studies

While I/V curves provide an excellent indication that modification has occurred, there was still significant variability between functionalised pipettes. Given that aptamers are single stranded (ss) DNA, we were able to translocate complementary DNA sequences through our TBA-nanopipette to see if Watson-Crick binding would occur. As seen in Figure 3.6, after recording our TBA-sensor in electrolyte only (i) the translocation of a random 10 pM 29-mer control sequence was carried out (ii) before its removal allowing translocation of the 10 pM

complementary sequence (iii). All traces were conducted at -400 mV with a scanning rate of 250 kHz and a low pass filter of 10 kHz.

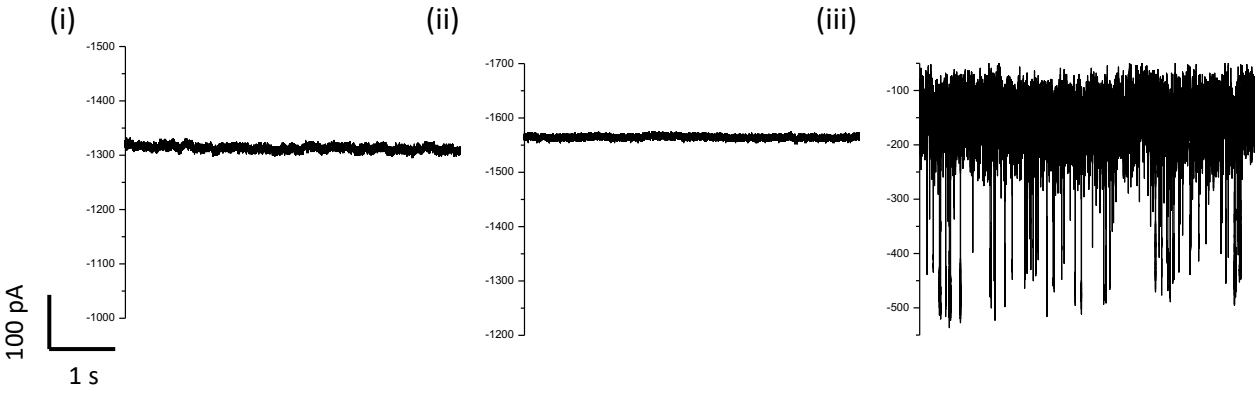


Figure 3. 6. *TBA modified nanopipettes in (i) 100mM KCl electrolyte only, (ii) 10 pM control sequence and (iii) 10 pM complementary sequence. Traces have a sampling frequency of 100 kHz and had a low-pass filter of 10 kHz.*

Table 3. 2. *The RMS value of KCl electrolyte only alongside translocation of 10 pM 29 mer control sequence and a 10 pM 29 mer complementary sequence.*

Experiment	RMS
KCl only	6.56
29 mer control	3.15
29 mer complementray	66.77

As shown in Figure 3.6 while there was no clear difference between (i) and (ii), several changes were seen upon introduction of the complementary sequence (iii). Not only did the ionic current drop significantly (from -1550 pA to -150 pA), accompanied by an increase in RMS noise (Table 3.2) but blockade peaks could also be observed. This demonstrated that Watson Crick binding had occurred and confirmed aptamer modification of the silanised nanopipette.

3.5.2. Noise characterisation

Noise analysis[1-2] including root mean square (RMS) and power spectrum density (PSD) also provided an alternative way of characterising the fabrication process. Figure 3.7 shows traces recorded at 0 mV (10 kHz low pass filter and scanning rate of 250 kHz) for unmodified (i), silanised (ii) and TBA-modified nanopipettes (iii).

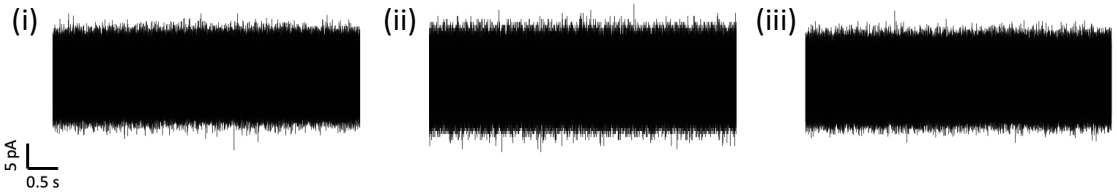


Figure 3. 7. *Traces recorded at 0 mV for each stage of the modification process; unmodified (i), silanised (ii) and TBA-modified (iii) nanopipettes. Traces were low-pass filtered at 10 kHz with a scanning rate of 250 kHz.*

The RMS (Table 3.3) and the PSD (Figure 3.8) was calculated at different stages of the modification. In both cases the applied voltage was 0 mV utilising a low-pass filter of 10 kHz and a scanning rate of 250 kHz.

Table 3. 3. *The RMS value of KCl electrolyte only alongside translocation of 10 pM 29 mer control sequence and a 10 pM 29 mer complementary sequence.*

Modification	RMS (pA)
Unmodified	4.13
Silanised	4.03
TBA	4.09

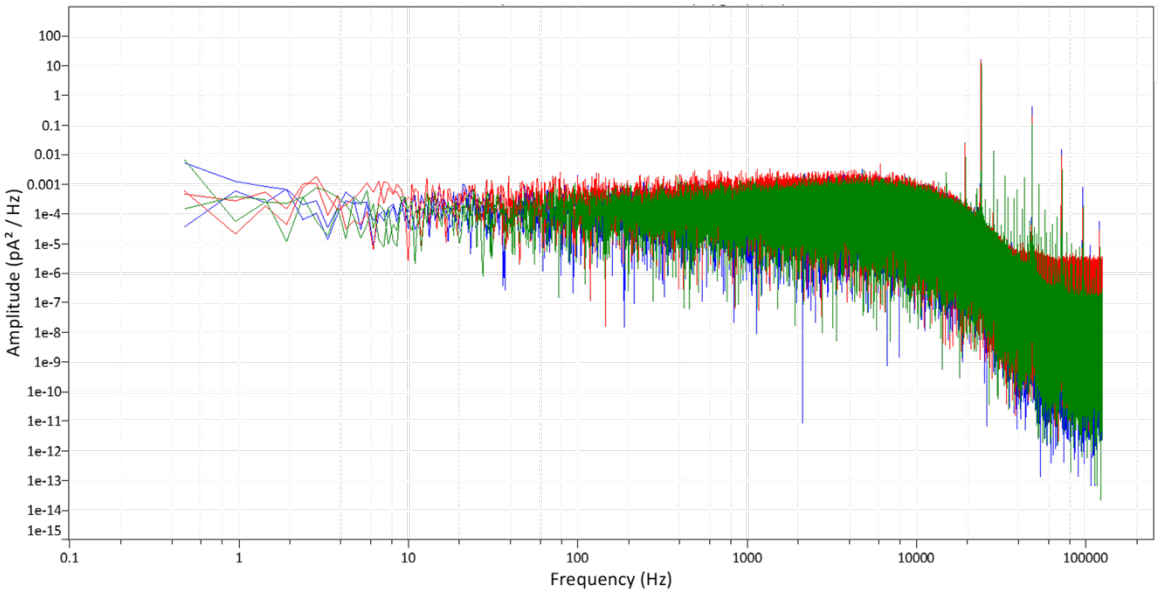


Figure 3. 8. *PSD of the fabrication process; unmodified (blue), silanised (red) and TBA modified (green). The top PSD was recorded at 0 mV while the bottom PSD was recorded at 500mV. Traces have a scanning rate of 250 kHz and were filtered at 10 kHz.*

In both cases, there were no significant changes between nanopipettes as determined at the different stages of the modification process.

3.6. Sensor design

The pore size of the nanosensor is critical and should ideally be of similar dimensions to that of the protein analyte. The pore diameter of unmodified pipettes can be calculated through conductance measurements[3], while alternative approaches were used in the characterisation of modified pipettes (silanised and nucleotide modified) due to the variance in conductance encountered.

The tip diameter of unmodified pipette was estimated to be 26 ± 7 nm through conductance measurements (n = 8) as seen in equation 3.1 below.

$$G = \frac{d_i D_i \pi \sigma}{4(l + \frac{\pi}{8}(d_i + D_i))}$$

Equation 3. 1. *Estimation of the nanopore tip diameter, where d_i = nanopore diameter (nm), D_i = internal glass capillary diameter (mm), σ = electrolyte conductivity (Sm^{-1}), G = conductance (S) and l = taper length (mm).*

The silane layer was assumed to be a monolayer due to the use of vapour silanisation in low-humidity. A computational model conducted in ChemBio3D allowed the 3D structure of the silane (Figure 3.9) to be generated with appropriate bond lengths/angles. The use of in-built cartesian coordinates in turn allowed the thickness of the silane layer to be estimated at 0.6nm.

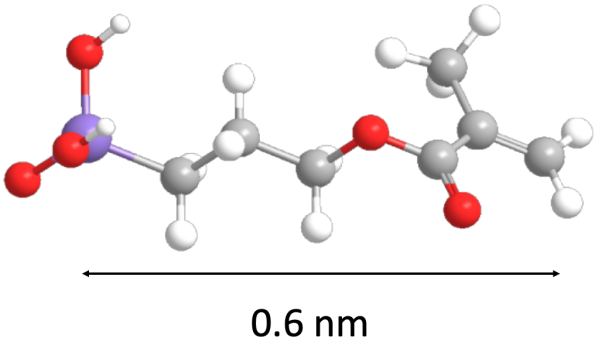


Figure 3. 9. *The length of the silanising agent is estimated via bond lengths and bond angle calculations with the use of the program ChemBio3D. The purple sphere is a silicon atom, the red sphere is an oxygen atom, the grey sphere is a carbon atom while the white sphere is a hydrogen atom.*

Linker design is particularly critical in the construction of the aptamer-modified sensor. Spatial separation between the aptamer and the nanopipette wall is vital in ensuring that protein binding can occur. Conversely, excessive spatial separation could prevent protein binding or result in pore blocking. The in-built 6 carbon spacer (Figure 3.10) as part of the thiol modification was likewise measured in ChemBio3D resulting in a length of 0.6 nm. This was deemed sufficient, preventing the necessity for additional thrombin nucleotides to be added before the 5’ end of aptamer sequence.

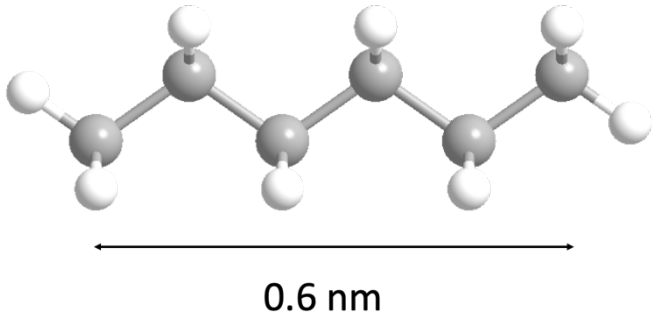


Figure 3. 10. *The length of the 6 carbon linker is estimated via bond length and angles calculations via use of the program ChemBio3D. The grey spheres are carbon atoms while the white spheres are hydrogen atoms.*

The pore diameter of the aptamer modified pipette was highly challenging to predict due to the various conformations that nucleotide sequences can assume. While radius of gyration measurements were considered, the complex interplay of high salt concentration that would decrease nucleotide length due to electrostatic interaction and the applied voltage that would stretch out nucleotide length would likely mean that such calculations would be inaccurate. As a result, the aptamer was assumed to be in a G-quadruplex formation as required for analyte binding. Figure 3.11 shows the expected conformation of TBA 29mer through the addition of two nucleotides (T_{29} and A_1) to HD22[20] its shorter equivalent. Assuming a rigid structure (i.e stem loop regions) and allowing an additional nucleotide to be added to the length of the G-quadruplex, the structure could be estimated to be around 3.4 nm long.

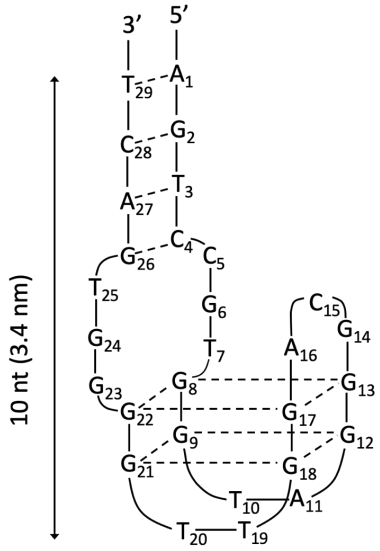


Figure 3. 11. *The predicted structure of the 29mer TBA was estimated through its related structure; HD 22 missing nucleotides A_1 and T_{29}). The G-quadruplex is assumed to be a rigid structure allowing a length calculation based on dsDNA measurements. Figure adapted from reference 20.*

Table 3.4 provides an estimation of the pore diameter following subtraction of the modification length two-fold due to modification at both sides of the nanopipette. Figure 3.12 provides a schematic of what the aptamer modified sensor could look like.

Table 3. 4. *An overview of the length of the modification as well as the resulting diameter of the functionalised pipette.*

Pore modification	Modification size (nm)	Pore diameter (nm)
Unmodified	-	26.0 ± 7
Silane	0.6	24.8
TBA (+ linker)	3.4 (0.6)	16.8

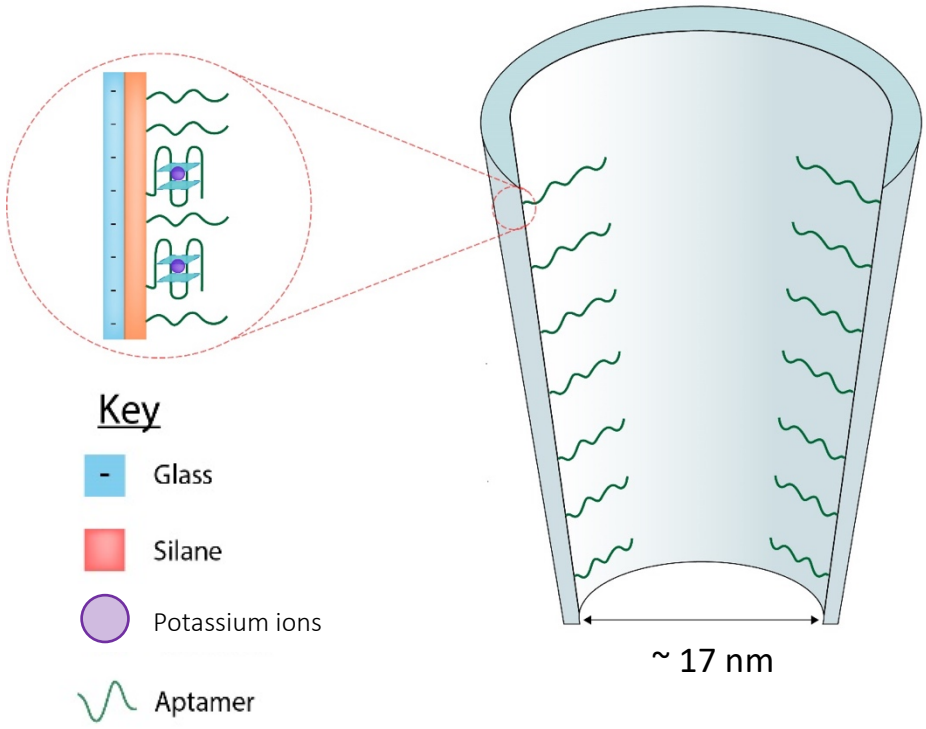


Figure 3. 12. *A schematic of the aptamer functionalised nanosensor with an estimated diameter of 17 nm. The zoomed in section (top-left) provides a layer by layer overview of the modified nanopipette while showing differing conformations of the aptamer. The unmodified glass layer is shown in blue, the silane layer is shown in red while the aptamer sequences are shown either in their linear form or as G-quadruplex when stabilised by potassium ions.*

3.7. Discussion

The bioconjugation strategy (Figure 3.4) was carefully chosen to maximise efficiency (i.e 2 steps), while preventing degradation[13] (e.g from Cu catalysis) and remaining cost effective (cheap thiol modifications and silane). An unexpected benefit of this strategy was the ability of TCEP to not only act as the reducing agent but also as a nucleophilic catalyst in the final bioconjugation step[19]. TCEP's (R_3P) role as a nucleophilic catalyst is outlined in Figure 3.13 below.

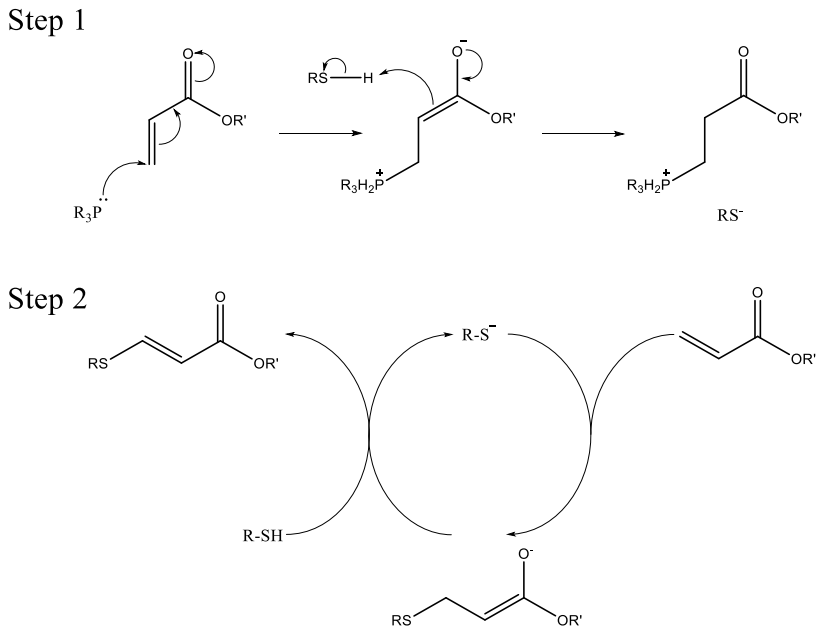


Figure 3. 13. *Mechanistic overview of thiol Michael addition. Step 1: TCEP (R_3P) acts as a nucleophilic catalyst through conjugate addition on the methacrylate functional group resulting in the formation of an adduct intermediate. Regeneration of the carbonyl through abstraction of a proton from a nearby thiol results in formation of the more reactive thiolate ion. Step 2: The thiolate ion undergoes nucleophilic attack on the methacrylate system. The α,β system is regenerated through abstraction of a proton from a nearby thiol.*

In step 1, TCEP (R_3P) undergoes nucleophilic attack at the methacrylate moiety forming an adduct intermediate in the process. Regeneration of the carbonyl group results in deprotonation of the thiol and formation of the highly nucleophilic thiolate ion. In step 2, the thiolate ion can now undergo Michael addition across the double bond resulting in the carbonyl bond being disrupted. Regeneration of the α, β system occurs through abstraction of a proton from a nearby thiol, regenerating the thiolate ion allowing the reaction to proceed for subsequent cycles.

The molar equivalent of TCEP compared to the aptamer and the pH was optimised for our reaction and was compared to that encountered in the similar thiol maleimide reaction[7] (Figure 3.14).

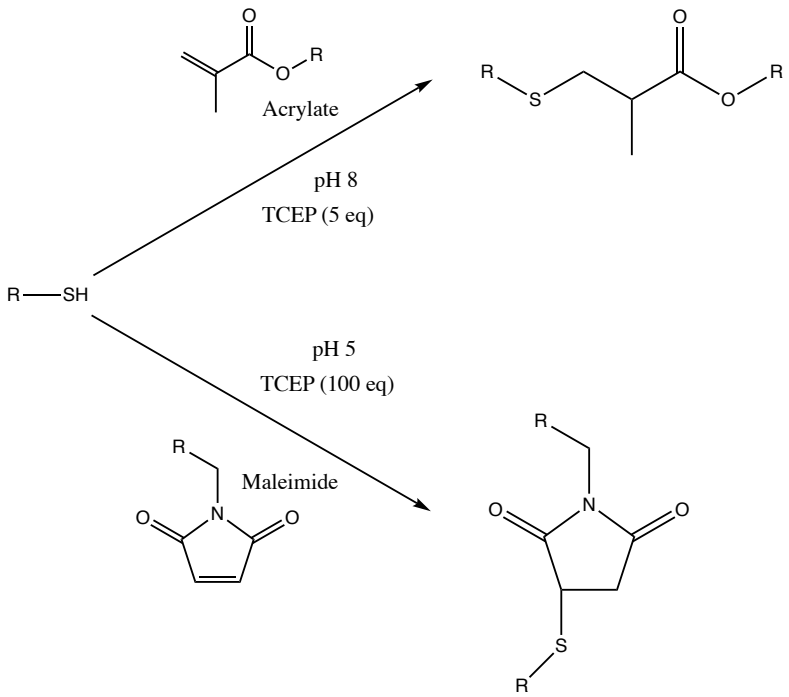


Figure 3. 14. *A comparison between the thiol methacrylate reaction (top) and the thiol maleimide reaction (bottom).*

In thiol maleimide reactions, alongside a low pH (5.0), a high (100 eq) molar equivalent of TCEP is used to ensure the protecting group is fully removed without fear of side reactions occurring. Conversely, in thiol methacrylate reaction a low TCEP equivalent (5.0) is used alongside a high pH (8.0) as a way of limiting side reactions. For example, researchers have shown that m/z peaks (Figure 3.15) relating to phosphine side products (P) were seen at low pH (3.0) but not at high pH (8.0).

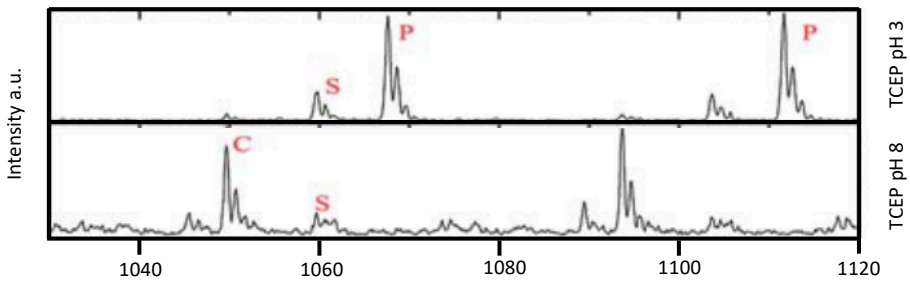


Figure 3. 15. *ESI-MS of oligo(PEGMEMA$_{475}$). S = Starting material, P = Phosphine conjugated species, C = thiol oligomer conjugate species. Adapted from reference 15*

A likely side reaction (Figure 3.16) at lower pH can be attributed to the direct nucleophilic attack of TCEP on the vinyl bond rather than conjugate addition. Instead of the formation of an adduct intermediate occurring as seen in Michael addition, the greater availability of H^+ results in proton abstraction from the buffer and formation of a P=C bond.

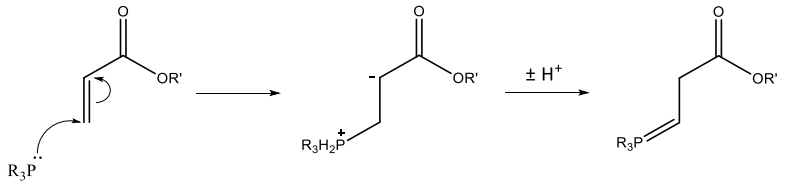


Figure 3. 16. *Possible side reaction of the phosphine catalyst attacking the vinyl group alongside proton abstraction results in the formation of a phosphine conjugate.*

While noise analysis proved unfruitful in the characterisation of the aptamer-modified pipette, electrochemical based analysis was highly insightful. Calculation of the rectification ratio is an *in-situ* and highly effective method of determining the surface charge and therefore degree of surface modification. As shown in Table 3.5, the rectification ratio value was compared with the estimated pKa value (experiments undergone in pH 8.0) at each stage of the modification process. Unmodified glass nanopipettes possessed a pKa of 5.6 – 8.5[22] (depending on silanol orientation) indicating that deprotonation had occurred. This correlated with a moderate rectification ratio (1.5) which overall suggested a moderate negative charge. The silanising agent is predicted to have a pKa of around 10 correlating to moderate protonation/neutral charge, with a rectification ratio of 1 and an overall a neutral charge. Finally, the pKa of nucleotides determined from their phosphate backbone (pKa = 2.15), indicates that deprotonation has (fully) occurred in turn correlating to the observed rectification ratio of 1.8 and overall a high negative charge.

Table 3. 5. *The experimentally calculated rectification ratio and theoretical pKa values for each stage of the modification process*

Modification	Rectification ratio	pKa
Glass	1.5	5.6-8.5
Silane	1.3	~10
Aptamer	1.8	2.15

Translocation studies of our complementary sequence through TBA modified pipettes provide further evidence of the success of the modification as shown in Figure 3.17. As the complementary sequence passes through the nanopore, it is able to bind to the bound aptamer sequence via Watson-Crick base pairing. The act of binding transforms the flexible single stranded (ss) DNA aptamer chain into an inflexible double stranded (ds) DNA complex. Since the length of the dsDNA (11 nm) is comparable to the radius of the modified

nanopore (c. 10 nm) this results in the nanopore being blocked as seen by a significant decrease in the ionic current. Subsequently, the peaks that occur can be attributed to the slow unzipping off the complementary sequence due to the applied voltage.

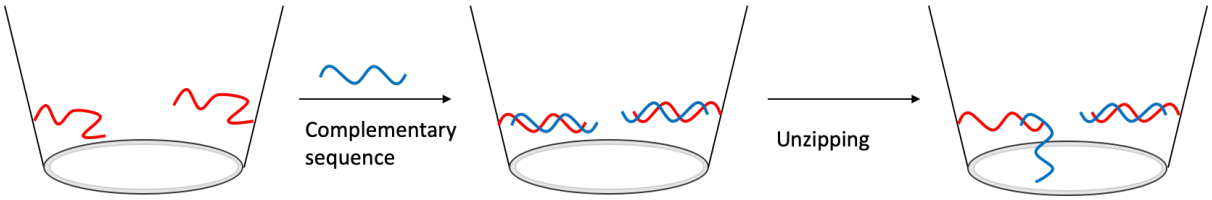


Figure 3. 17. *ssDNA aptamers are highly flexible allowing free movement in solution. Upon the addition of a complementary sequence, rigid dsDNA structures are formed resulting in a large decrease in ionic current. Peaks can be attributed to unzipping off the complementary sequence.*

The likely conformation of the bound aptamer is important due to its relevance in future chapters. Pore size calculations estimated the pore diameter of TBA modified pipettes to be around 17 nm when assuming that aptamers are present in a G-quadruplex formation. In reality, the aptamer conformation is likely to be in equilibrium between two conformations (Figure 3.18), affected by 2 opposing factors; electrolyte concentration (i.e K^+ ions) and the applied voltage. The high electrolyte concentration[23] will favour G-quadruplex formation while the applied voltage[24] 'stretches out' the nucleotide sequence favouring ssDNA. The relative position of the aptamer sequence in the pipette is also likely to be critical, with sequences close to the tip experiencing a greater electric field than sequences further from the tip.

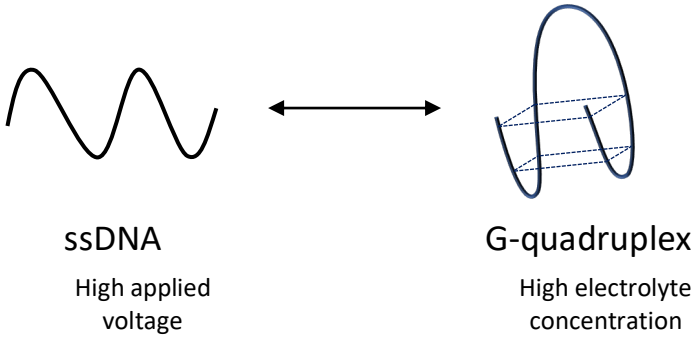


Figure 3. 18. *ssDNA are favoured at high voltages although G-quadruplexes are expected to dominate at higher electrolyte concentrations.*

Finally, a binding model of the aptamer modified nanosensor was formulated incorporating the reasonable kD values of the aptamer and the application of an applied voltage.

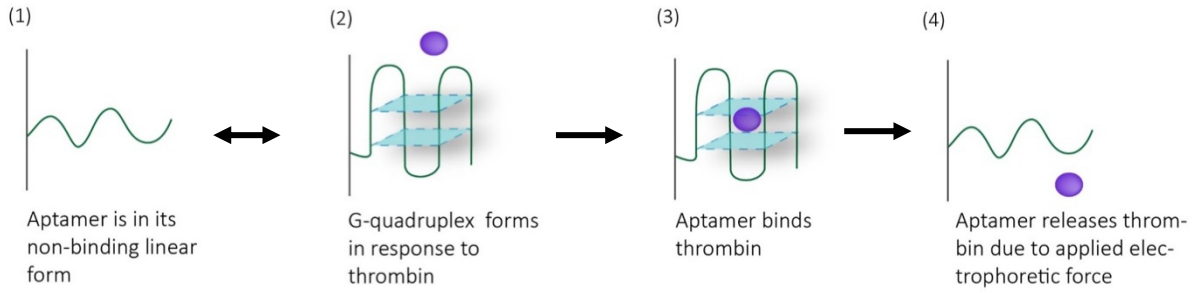


Figure 3. 19. *A likely binding mechanism of aptamer modified nanopipette*

As shown in Figure 3.19, bound aptamers are initially present as ssDNA (1), which form a G-quadruplex in the presence of the protein analyte (2) allowing binding (3) to occur. Finally, the continuous application of an electric field results in the release of the protein and the return of the aptamer to its linear form (4).

3.8. Conclusion

A cost effective and efficient 2-step functionalisation strategy has been developed for the attachment of an aptamer sequence with a strong covalent linker to a suitably modified glass nanopipette. Each step of the modification could be followed *in-situ* by determining the rectification ratio from the IV profile, while translocation studies of the complementary sequence through TBA-modified pipettes provided further confirmation. In the next chapter, the ability of the sensor to detect thrombin; a widely characterised analyte with links to neurodegenerative diseases and cancer is presented.

3.9. References

1 J. D. Uram, K. Ke and M. L. Mayer, *ACS Nano*, 2008, **2**, 857–872.

2 R. M. M. Smeets, U. F. Keyser, N. H. Dekker and C. Dekker, 2008, **105**, 417–421.

3 L. J. Steinbock, A. Lucas, O. Otto and U. F. Keyser, *Electrophoresis*, 2012, **33**, 3480–3487.

4 A. Baptista, F. Silva, J. Porteiro, J. Míguez and G. Pinto, *Coatings*, 2018, **8**.

5 https://labs.chem.ucsb.edu/zakarian/armen/11---bonddissociationenergy.pdf Accessed on 01/06/20

6 J. J. Calvente, Z. Kováčová, M. D. Sanchez, R. Andreu and W. R. Fawcett, *Langmuir*, 1996, **12**, 5696–5703.

7 N. Nakajima and Y. Ikada, *Bioconjug. Chem.*, 1995, **6**, 123–130.

8 S. I. Presolski, V. P. Hong and Vu Phong Hong and M.G. Finn, *Curr Protoc Chem Biol*, 2011, **3**, 153–162.

9 G. Hermanson, *Bioconjugate techniques*, Third edit., 2013.

10 A. R. Yadav, R. Sriram, J. A. Carter and B. L. Miller, *Mater. Sci. Eng. C*, 2014, **35**, 283–290.

11 Y. Wang, J. Velmurugan, M. V. Mirkin, P. J. Rodgers, J. Kim and S. Amemiya, *Anal. Chem.*, 2010, **82**, 77–83.

12 F. Zhang, K. Sautter, A. M. Larsen, D. A. Findley, R. C. Davis, H. Samha and M. R. Linford, *Langmuir*, 2010, **26**, 14648–14654.

13 C. S. McKay and M. G. Finn, *Chem. Biol.*, 2014, **21**, 1075–1101.

14 G. R. Abel, Z. A. Calabrese, J. Ayco, J. E. Hein and T. Ye, *Bioconjug. Chem.*, 2016, **27**, 698–704.

15 G. Z. Li, R. K. Randev, A. H. Soeriyadi, G. Rees, C. Boyer, Z. Tong, T. P. Davis, C. R. Becer and D. M. Haddleton, *Polym. Chem.*, 2010, **1**, 1196–1204.

16 V. S. Khire, T. Y. Lee and C. N. Bowman, *Macromolecues*, 2007, **40**, 5669–5677.

17 A. B. Lowe, *Polym. Chem.*, 2010, **1**, 17–36.

18 J. Nilsson, J. R. I. Lee, T. V. Ratto and S. E. Létant, *Adv. Mater.*, 2006, **18**, 427–431.

19 M. W. Jones, G. Mantovani, S. M. Ryan, X. Wang, D. J. Brayden and D. M. Haddleton, *Chem. Commun.*, 2009, 5272–5274.

20 I. R. Krauss, A. Pica, A. Merlino, L. Mazzarella and F. Sica, *Acta Crystallogr. Sect. D Biol. Crystallogr.*, 2013, **69**, 2403–2411.

21 M. Sulpizi, M. P. Gaigeot and M. Sprik, *J. Chem. Theory Comput.*, 2012, **8**, 1037–1047.

22 G. Nguyen, S. Howorka and Z. S. Siwy, *J. Membr. Biol.*, 2011, **239**, 105–113.

23 S. F. Buchsbaum, G. Nguyen, S. Howorka and Z. S. Siwy, *J. Am. Chem. Soc.*, 2014, **136**, 9902–9905.

Chapter 4: Detection of thrombin using an aptamer-modified nanopore sensor

4.1. Overview *95*

4.2. Introduction *95*

4.2.1. Thrombin structure **95**

4.2.2. Thrombin's role in the coagulation cascade **96**

4.2.3. Thrombin as a biomarker **97**

4.2.4. Current detection of thrombin **100**

4.3. Aim *102*

4.4. Challenges *103*

4.4.1. Experimental **103**

4.4.2. Data analysis **103**

4.5. Results *108*

4.5.1. Concentration dependence **108**

4.5.2. Voltage dependence **111**

4.5.3. Electrolyte concentration dependence **112**

4.5.4. Detection in a multi-protein analyte **113**

4.5.5. Noise analysis **115**

4.5.5.1. RMS 115

4.5.5.2. Power spectrum density 116

4.5.6. Low-pass filter effects **117**

4.5.7. Sensor regeneration **118**

4.6. Discussion *119*

4.7. Conclusion *124*

4.8. References *124*

4.1. Overview

In this chapter, the detection of thrombin is described using a nanosensor functionalised with a 29-mer thrombin binding aptamer (TBA)[1]; a complementary recognition element with a high binding affinity (kD = 0.5nM). A short introduction to thrombin is presented including its structure[2,3], its role in the coagulation cascade[4] as well as its role as a potential biomarker in cancer[5] and neurodegenerative diseases[6]. Current techniques are then discussed including *in-vivo* imaging agents such as fluorescent activatable cell-penetrating peptides[7] (ACPC) and *in-vitro* biosensors[8,9].

The detection of thrombin using our novel aptamer-functionalised nanosensor is then described, including defining detection limits and regeneration properties before demonstrating selectivity in a multi-analyte system. The chapter is concluded by providing a likely mechanism of action of our sensor before describing implication for the detection of oligomers, a more complicated analyte in the following chapter.

4.2. Introduction

4.2.1. Thrombin structure

The structure of thrombin[2], a small (37 kDa) serine proteinase is shown below in Figure 4.1 (a). The active site of thrombin is governed through the catalytic triad; peptides S195, H57 and D189 with its specificity retained by surface loops and charged patches known as exosites. The hydrophobic 60-loop interacts with hydrophobic residues contained within the amino-terminal of the substrate alongside the hydrophilic y loop, which interacts with residues on the substrates carboxyl terminal. Furthermore, thrombin has two anion binding exosites composed of basic residues which in turn interact with negatively charged cofactors and substrates. Importantly, in our studies, the exosites are the areas targeted by aptamers[3] as shown in Figure 4.1 (b). The 29-mer aptamer used in our biosensor targets exosite I of thrombin, while the lower affinity 15-mer (not shown) aptamer targets exosite ll.

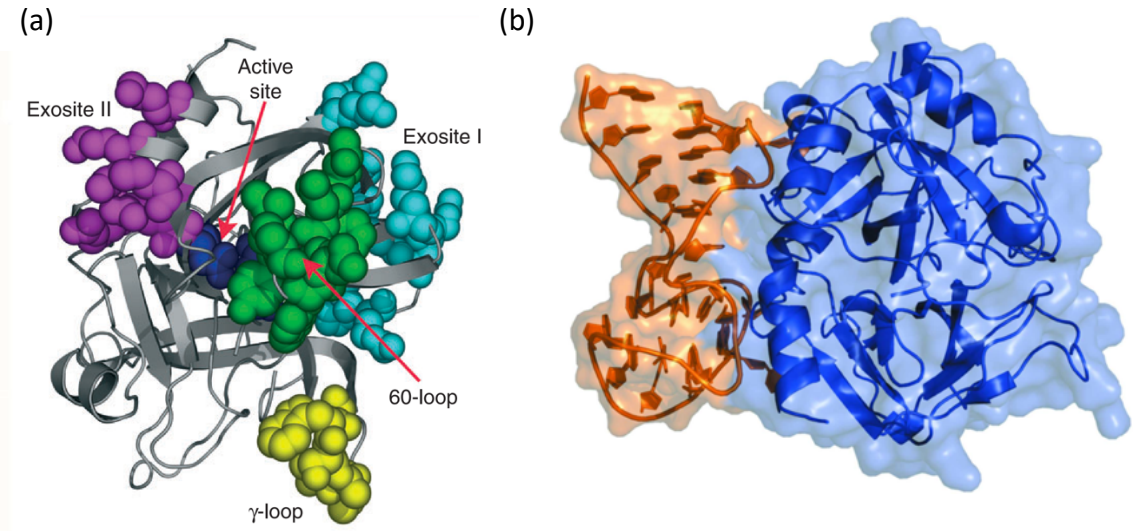


Figure 4. 1. *(a) A 3D schematic structure (left) of thrombin. Figure adapted from reference 2. (b) A schematic structure (right) showing the 29-mer aptamer (red) bound to exosite I of thrombin (blue). Figures adaoted from reference 3.*

4.2.2. Thrombin's role in the coagulation cascade.

Thrombin is widely known for its role in the coagulation cascade[4], as summarised in Figure 4.2, where its most common role is in the digestion of fibrinogen. Fibrinogen, a 340 kDa soluble homodimer glycoprotein is secreted from the liver where it circulates throughout the bloodstream. Upon activation of the coagulation cascade, thrombin cleaves fibrinopeptide A and fibrinopeptide B from fibrinogen, leading to the formation of insoluble fibrin. The act of cleaving unmasks polymerisation sites on fibrin, which in turn allows blood clot formation to occur. However, thrombin's role is not limited to fibrinogen digestion as it can act on other substrates having a variety of roles in anti-inflammation[10] and even feedback-based anti-coagulant[11] and anti-fibrinolytic[12] functions.

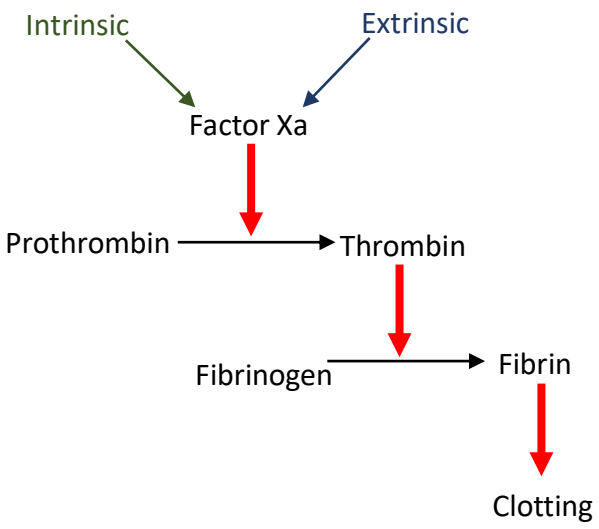


Figure 4. 2. *A simplified version of the coagulation cascade.*

4.2.3. Thrombin as a biomarker

Thrombin is a well-studied disease biomarker in humans due to its functional links in neurodegenerative diseases such as MS and AD as well as pulmonary metastasis, a form of lung cancer.

(i) Pulmonary metastasis

The thrombin generated from thrombosis (blood clots occurring inside blood vessels) has been known to augment pulmonary metastasis[5], as detailed in Figure 4.3. Tissue factors present on the surface of tumour cells activate thrombin, in turn allowing their passage through blood vessels. In addition, thrombin activates endothelial cells so that they present P-selectin on their surface, which allows tumour cells to bind via their P-selectin receptors. Platelets, in turn, can bind to tumour cells via P-selectin forming an endothelium-tumour-platelet 'matrix'. As the matrix develops further, the enhanced surface area of the platelet leads to a greater catalytic area, allowing increased thrombin generation from coagulant proteins, in a cyclical manner. The adhesion of proteins is mediated by platelet integrin IIb-IIa binding to tumour integrins via VWF and fibronectin. Angiogenesis (formation of blood vessels) which is associated with tumour growth can now occur due to thrombin stimulated synthesis and secretion of pro-angiogenic growth factors which are dominant with respect to anti-angiogenic factors. Finally, platelet-tumour aggregates protect tumour cells from NK cells.

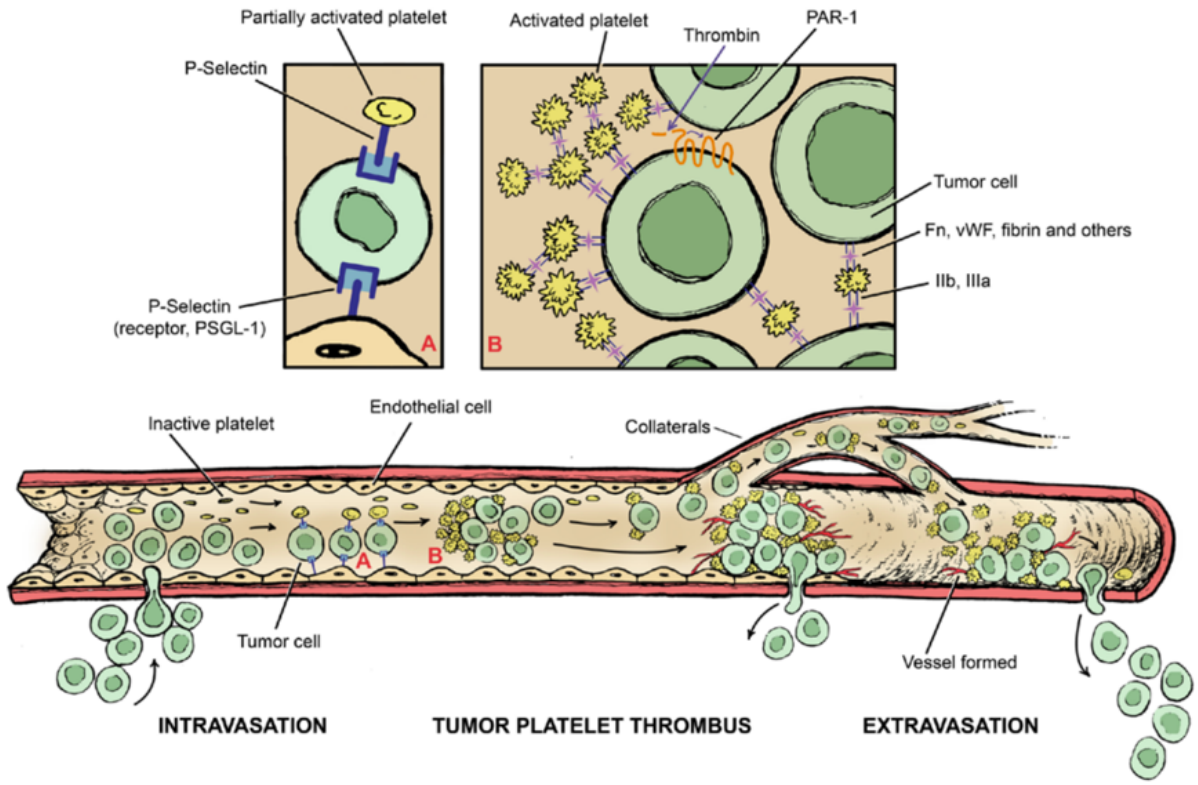


Figure 4. 3. *A schematic showing a summary of the effects of thrombin on pulmonary metastasis. Figure adapted from reference 5.*

(ii) Neurodegenerative diseases

Thrombin is also implicated in neurodegenerative disorders and brain/spinal injuries[6]. A common hallmark of such diseases and injuries is the breakdown of the blood-brain barrier (BBB), allowing fibrinogen, a key thrombin substrate to permeate into the central nervous system (CNS). Fibrinogen alongside the thrombin product, fibrin is known to interact with the receptors of cells in the CNS allowing neuroinflammation, as shown in Figure 4.4 to occur. For example, fibrinogen is able to induce growth factor pathway activation of astrocytes, oligodendrocytes and pericytes where it can regulate scar formation[13], cell differentiation[14] and inhibit neurite growth[15] respectively. Additionally, the conversion of fibrinogen to fibrin leads to the exposure of an epitope (area of an antigen to which antibodies bind) which result in binding to the CD118b/CD18 integrin receptor[16]. This binding activates microglia and macrophages that can lead to the promotion of various neuroinflammatory responses.

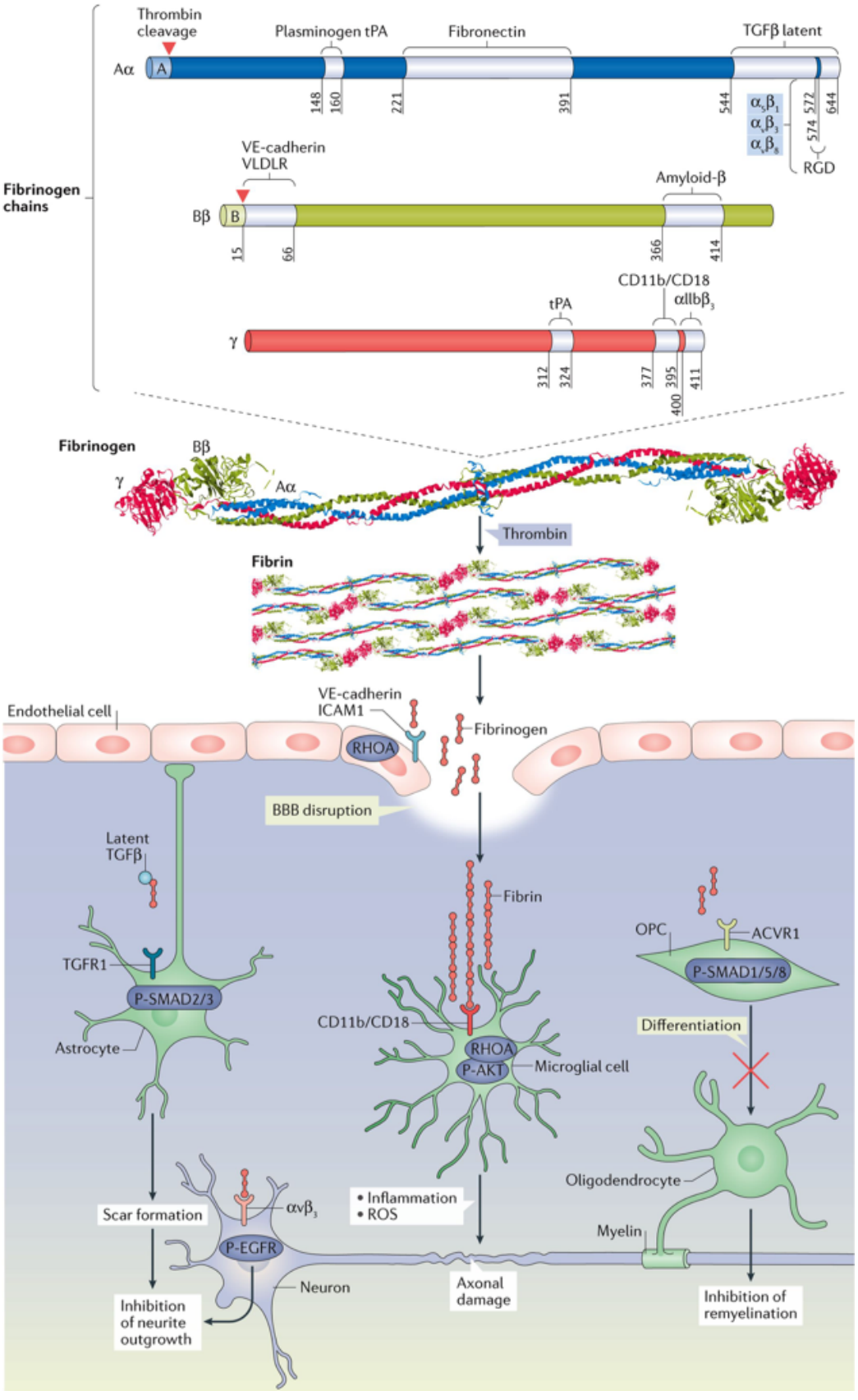


Figure 4. 4. *The passage of thrombin, its substrate fibrinogen and product fibrin through the BBB, whereby it can lead to neuroinflammation. For example, fibrinogen can induce growth factor pathway activation in astrocyte, oligodendrocytes and pericytes, whereby it can regulate scar formation, cell differentiation and inhibition of neurite growth respectively. Upon conversion of fibrinogen to fibrin, a cryptic epitope (e.g. y377-395) is revealed which is the binding site for the CD11b/CD18 integrin receptor. Furthermore, the immobilisation of fibrinogen and fibrin can lead to the activation of microglia and macrophages. Figure adapted from reference 6.*

4.2.4. Current detection of thrombin

Given thrombin's role in various debilitating and fatal diseases, researchers have developed various biosensors (using aptamers as the recognition element) and imaging agents for its detection. While biosensors utilise a range of analytical techniques, a common theme in detection is the conformation change of the aptamer upon binding. In one case, a biosensor was formed through the bioconjugation of TBA to a gold electrode[8], as shown in Figure 4.5(a). In the absence of thrombin, electron transfer occurs uninterrupted giving rise to a large signal. Upon introduction of thrombin, a conformational change in the aptamer blocks electron transfer resulting in a reduced signal. As shown in Figure 4.5(b), a detection limit of 6.8 nM was recorded when conducted in electrolyte only while achieving a detection limit of ~ 64nM when conducted in serum (Figure 4.5(c)) for their biosensor. An alternative thrombin detection technique; a SERS (surface-enhanced Raman scattering) based biosensor[9] involved conjugating methylene blue modified TBA to a gold nanoparticle. As before, the introduction of thrombin leads to the dissociation of the aptamer sequence resulting in a diminished signal.

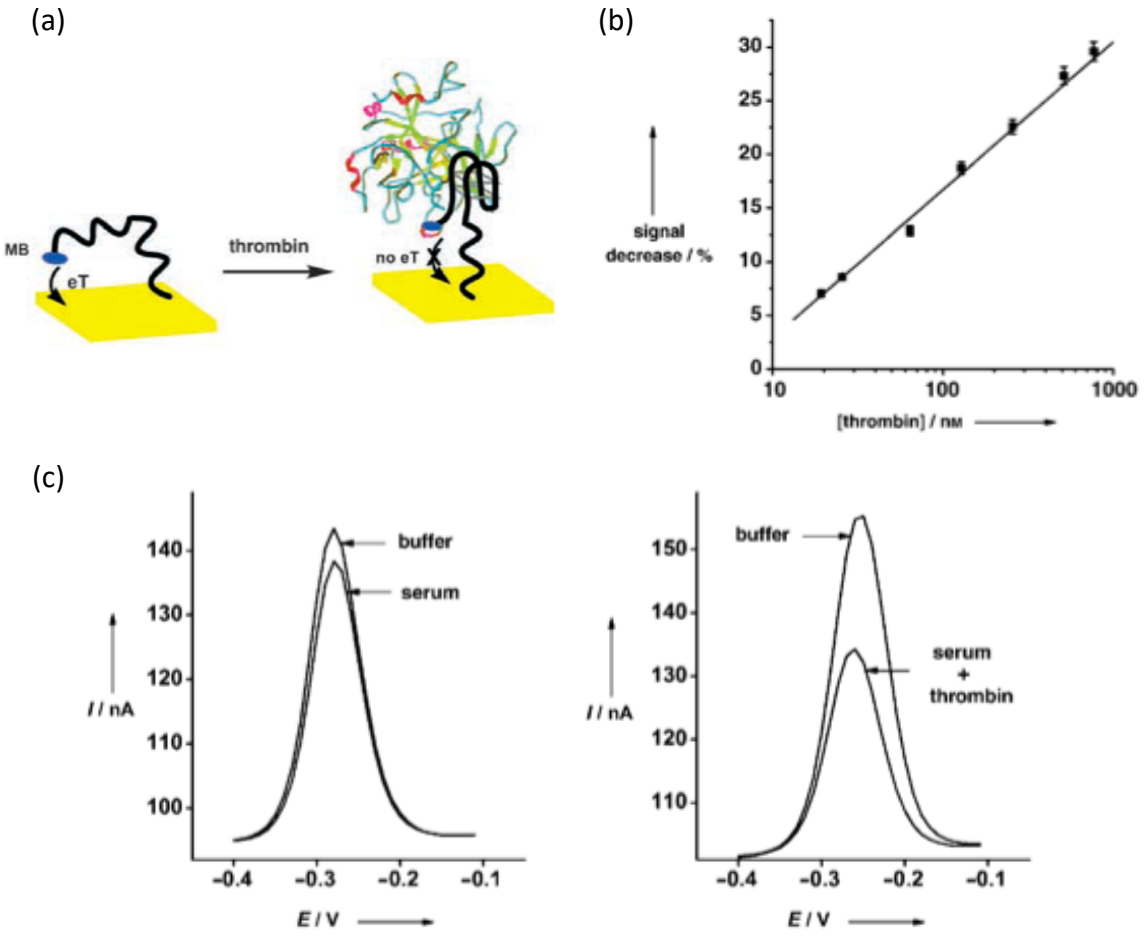


Figure 4. 5. *(a) A schematic of the biosensor. In the unbound state (left), the aptamer is free to interact with the electrode surface with its molecular beacon (MB) redox tag in turn allowing electron transfer (eT) to occur. Upon the addition of thrombin (right), aptamer binding prevents close contact of the MB to the electrode preventing eT from occurring. (b) A concentration profile of thrombin alongside the signal decrease. (c) The biosensor (compared with buffered saline) is carried out in 50% fetal calf serum (left) and 50% fetal calf serum when spiked with 64 nM thrombin (right). Figures adapted from reference 8.*

Alternatively, thrombin has been detected *in-vivo,* in experimental autoimmune encephalomyelitis (EAE), an MS animal model. The molecular probe (Figure 4.6(a)) consists of an activatable cell-penetrating peptide (ACPP)/Cy5 dye complex[7] attached to a non-penetratable polyanion via a thrombin-specific cleavable (PPRSFL) sequence. In the presence of thrombin, the linker is cleaved resulting in the uptake of the Cy5-labelled peptide capable of penetrating into cells where it can be imaged with confocal microscopy. In Figure 4.6(b), the fluorescent signal showed that the ACPP probe showed a greater fluorescent signal in mice with peak EAE in comparison to healthy controls. Furthermore, it was shown that the fluorescent signal was higher in comparison to samples including a control probe (mPEG-ACPP) and when down without a probe. In Figure 4.6(c), it was shown that the fluorescent signal increased as EAE progressed.

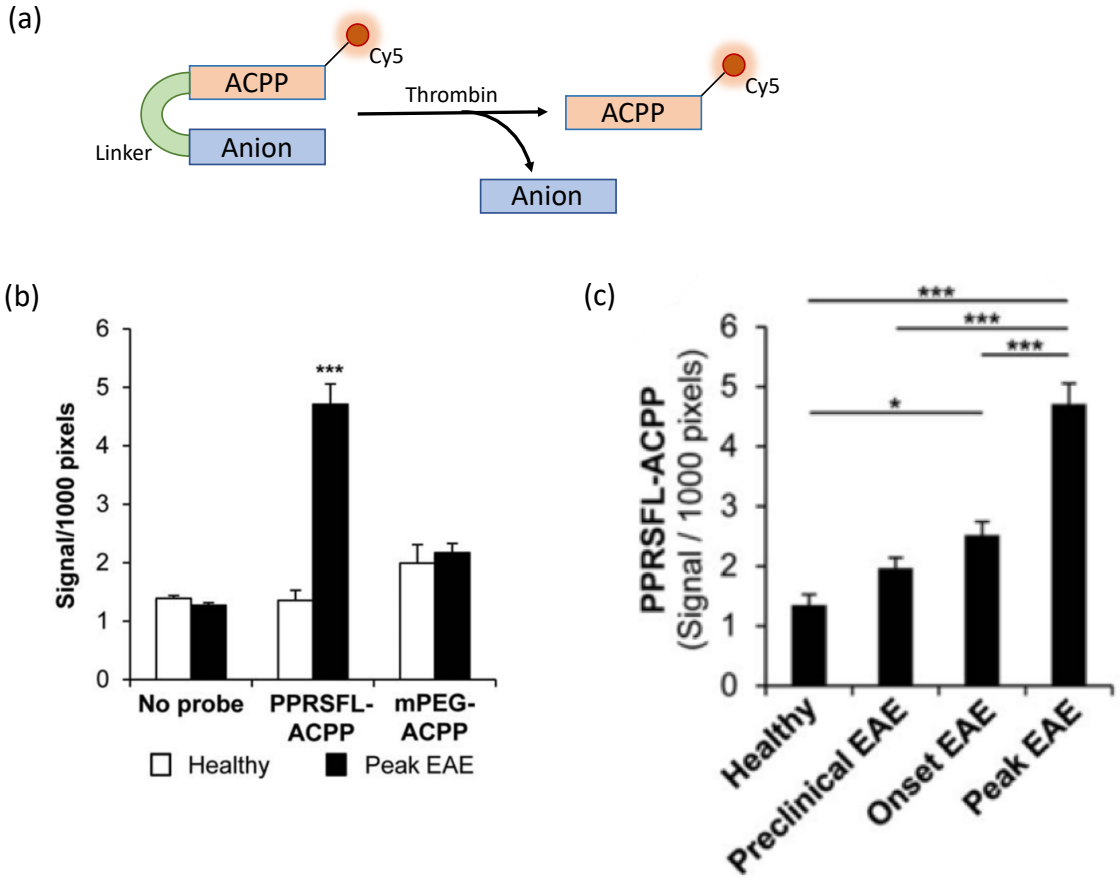


Figure 4. 6. (a) A schematic showing the mechanism of the probe. The probe consisting of ACPP conjugated with Cy5 is linked to a non-penetratable anion. Upon introduction of thrombin, the linker is cleaved allowing ACPP to penetrate through cells. (c) Fluorescent signal in whole spinal cord scans from mice injected with PPRSFL-ACPP at different timepoints of EAE. Figures adapted from reference 7.

While thrombin detection has been shown in the above examples with good sensitivity and selectivity, challenges remain for such detection to be implemented in the medical industry. The aptamer modified electronic transfer-based biosensor[8] previously described has reasonable sensitivity and selectivity while remaining label-free. However, only a small signal change was seen at low concentrations (e.g 5% decrease at 6.8 nM), while non-specific interactions preventing electron transfer could lead to false positive readings. Furthermore, selectivity measurements carried out in serum required the use of relatively high thrombin concentrations (68 nM), limiting its use as a detection technology for patient samples. In addition, long incubation times (3 hours) were required significantly reducing throughput. On the other hand, imaging agents[7] (e.g. ACPP) have a distinct advantage of tracking the state of the diseae (Pre/Peak EAE) as well as its location in the brain. Despite this, imaging agents require an invasive injection while providing no quantitative measurement of thrombin detection. In addition, ACPP have only been used in mice and would therefore require extensive testing before use in humans, whereas *in-vitro* sensors require no such procedures.

The sensor developed in the project will offer label-free, highly sensitive and selective detection while requiring no prior sample clean-up steps. Label-free sensing forgoes the use of expensive tags (e.g fluorophores or histidine) while direct detection increases throughput and provides even greater cost reduction. Finally, the ability to detect with high sensitivity and selectivity has the potential for early detection, significantly improving the prognosis of patients suffering from MS or cancer.

4.3. Aim

Throughout this chapter, the primary objective has been to stochastically detect thrombin, a model protein, using a nanopipette covalently modified to incorporate a specific artificial receptor. Detection using the aptamer based nanosensor is label-free, highly sensitive and selective with the added benefit of insight into binding dynamics via single molecule detection. Thrombin is a widely utilised analyte, due to its well-established structure and availability of a high-affinity binding aptamer, while remaining less prone to aggregation. In particular, we aimed to determine a concentration range and voltage profile, alongside defining binding affinities as well as describing the sensors regeneration properties. Our successful development of an aptamer-bound nanosensor then allowed for

the detection of more complicated biomarkers (i.e. alpha-synuclein oligomers) as discussed in the following chapter.

Additionally, we have aimed to show that thrombin detection can be carried out in complicated matrices such as multi-protein human serum solution, paving its way as a detection method for its biomarker in neurodegenerative disorders such as MS and AD.

4.4. Challenges

Alongside the low functionalisation efficiency (as discussed in chapter 2) seen in the modification of nanopipettes with aptamers, several challenges needed to be overcome in the detection of thrombin.

4.4.1. Experimental

Working with fragile nanopipettes is challenging to begin with, but the presence of nanobubbles in modified nanopipette alongside multiple fillings of the nanopipettes (i.e. removing KCl to replace with thrombin solution) means that extreme care had to be taken. TBA-modified nanopipettes were prone to both current fluctuations and periods of significant noise which limited the ability to detect events. Furthermore, stretches of events that could be successfully analysed were typically short-lived preventing effective voltage based studies from being carried out.

4.4.2. Data analysis

The data analysis of recorded traces was particularly challenging due to variable noise, current fluctuations and peak clustering. Ideally, traces should have a good SNR (SNR up to 3 have been reported for 10 pM thrombin translocation in TBA-modified pipettes), with help from low-pass filters if required, allowing clear distinction between events and noise. In addition, traces should avoid peak clustering, whereby the inter-event time is smaller than expected which can result in over-estimation of the capture rate. Finally, current fluctuations should be minimal allowing the baseline to be fitted effectively.

A less than ideal trace encountered with thrombin translocation in a TBA-modified pipette is shown below. Measures taken to analyse the trace as effectively as possible are discussed below.

(i) Baseline simplification

Shown below are traces showing the translocation of 10 pM thrombin through TBA-modified nanopipettes. In Figure 4.7(a), the trace (filtered at 10 kHz) is difficult to analyse

due to the low S:N ratio as well as subsections that were just noise. Upon application of a 1 kHz low-pass filter (b), the trace becomes far easier to analyse due to an increase in the S:N ratio. Finally, parts of the trace containing only noise (i.e. no analysable peaks) are removed (c), thereby simplifying the trace for subsequent analysis.

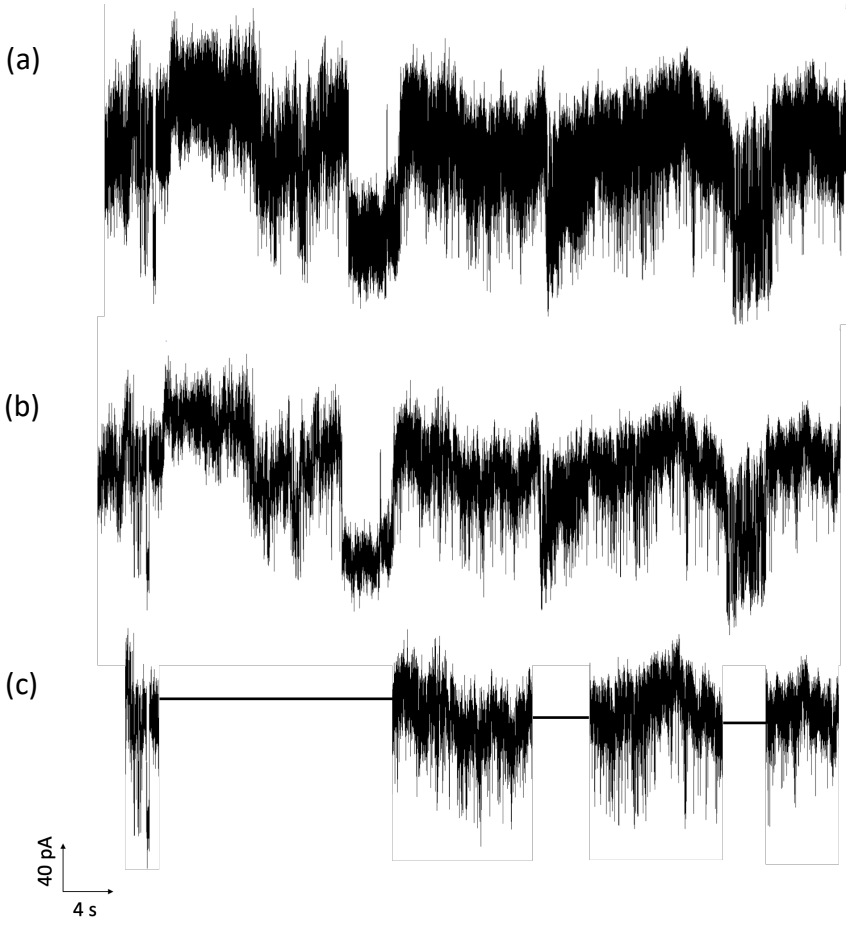


Figure 4. 7. *Figure showing methods used to simplify traces for subsequent analysis. (a) A trace showing 10 pM thrombin translocation through TBA-modified pipettes with a low-pass filter of 10 kHz. (b) The same trace with a 1 kHz low-pass filter. (c) The trace in (b) has noisy sections with non-analysable translocation peaks removed to simply the trace.*

(ii) Baseline fitting and threshold

Even with the application of low-pass filters as well as removal of subsections of traces containing only noise, the baselines remains difficult to fit. In Figure 4.8(a), the baseline is fitted with different parameters resulting in a tight fit (i) and a less tight fit (ii). In (b), the threshold (cut-off) was applied for the fitted baselines seen in (a).

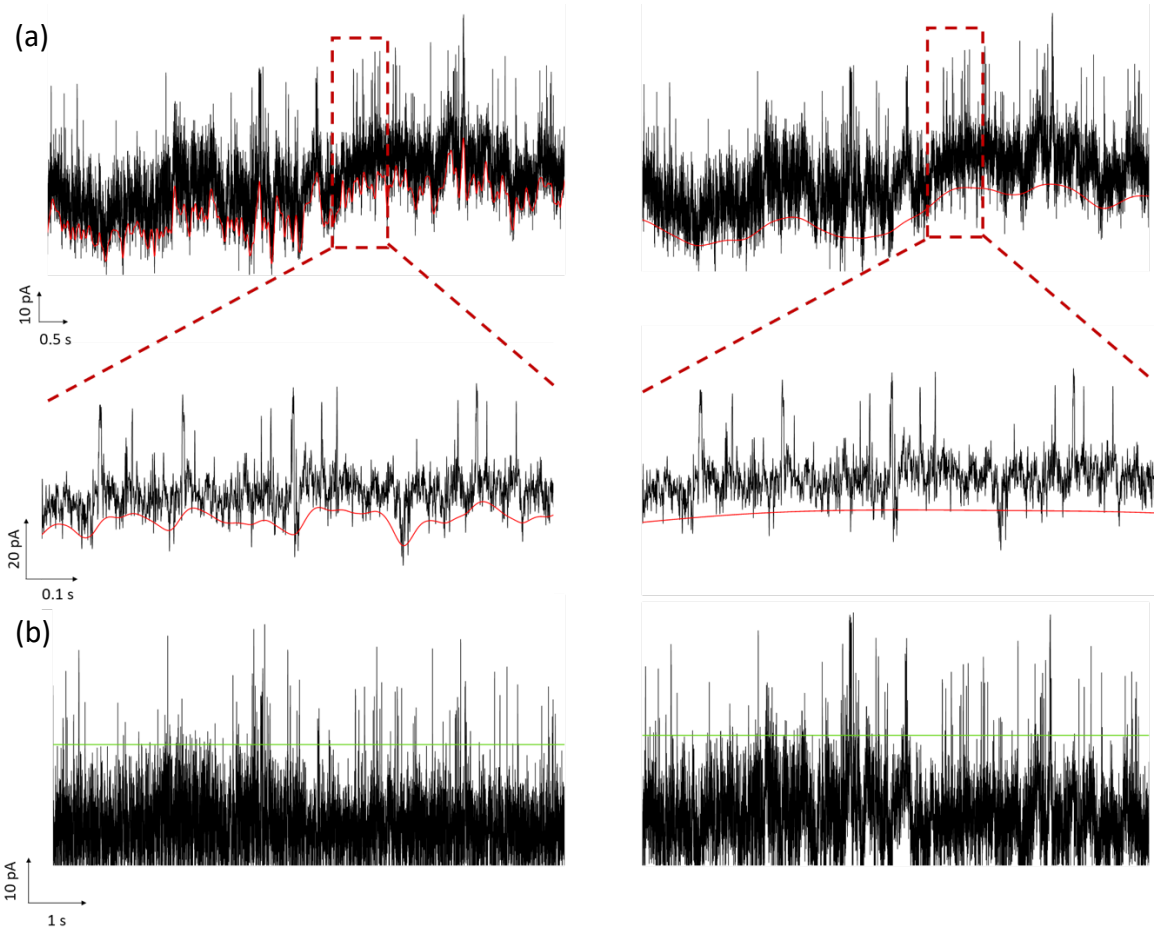


Figure 4. 8. *Baseline and threshold fitting for the same trace when conducted in pipettes modified with TBA-29mer. (a) Baseline fitting alongside zoomed in subsections utilising a tight fit (left) and loose fit (right). (b) Threshold analysis corresponding to the fitted baseline of (a).*

Selecting the correct threshold (cut-off) between basleline noise and translocation peaks was critical. As such a balance was employed to ensure the maximum number of translocation peaks while limiting as much noise as possible.

(iii) Peak selection

The irregular shape of a small number of peaks led to challenges in determining the correct peak characteristics (e.g dwell time) as shown in Figure 4.9. Overall, a FWHM of 2 was chosen which ensured that most peaks were selected correctly while allowing those that deviated from being chosen.

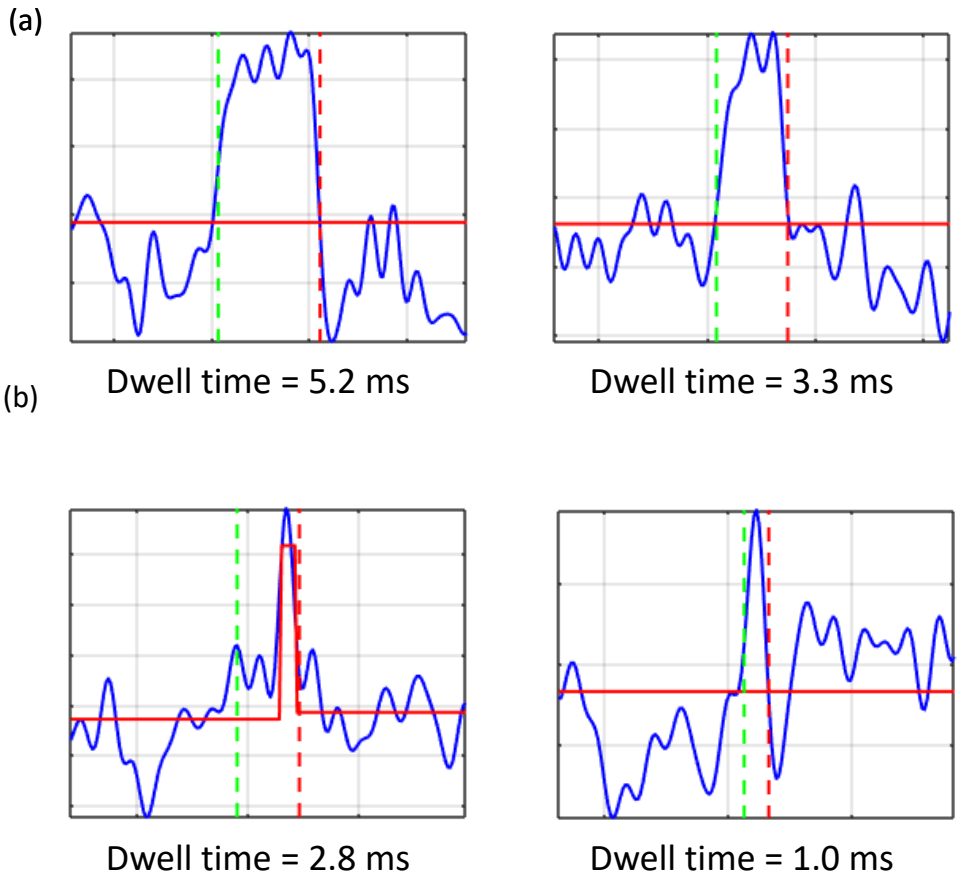


Figure 4. 9. *Peak selection alongside deterimination of dwell times. (a) Peak selection is fitted correctly allowing dwell tme to be selected carefully, while in (b) dwell times are incorrectly picked resulting in overestimation (left) and underestimation (right).*

Figure 4.9(a) shows examples of peak fitting result in the correct determination of the dwell time. Conversely in (b), dwell times are not selected correctly, resulting in overestimation (left) and underestimation (right). The small number of peaks that were selected incorrectly could be simply discarded.

(iv) Data analysis

(a) Histogram analysis

Histogram analysis (Figure 4.10) allowing ascertainment of the mean values of peak characteristics (e.g dwell time) was difficult due to the skewed non-Gaussian behaviour observed. The correct bin-width was carefully tailored to each data set ensuring that the mean value was as accurate as possible. In Figure 4.10(a), the correct bin width is shown resulting in accurate dwell time determination, whereas in Figure 4.10(b), incorrect bin width prevents accurate determination.

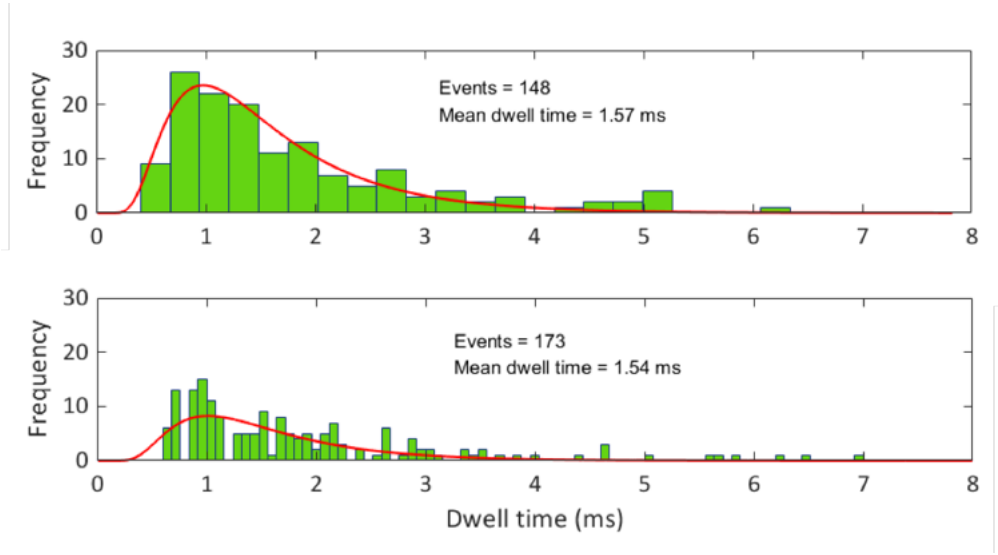


Figure 4. 10. *Histogram analysis of dwell time with correct bin width (top) and incorrect bin width (bottom).*

(b) Peak clustering

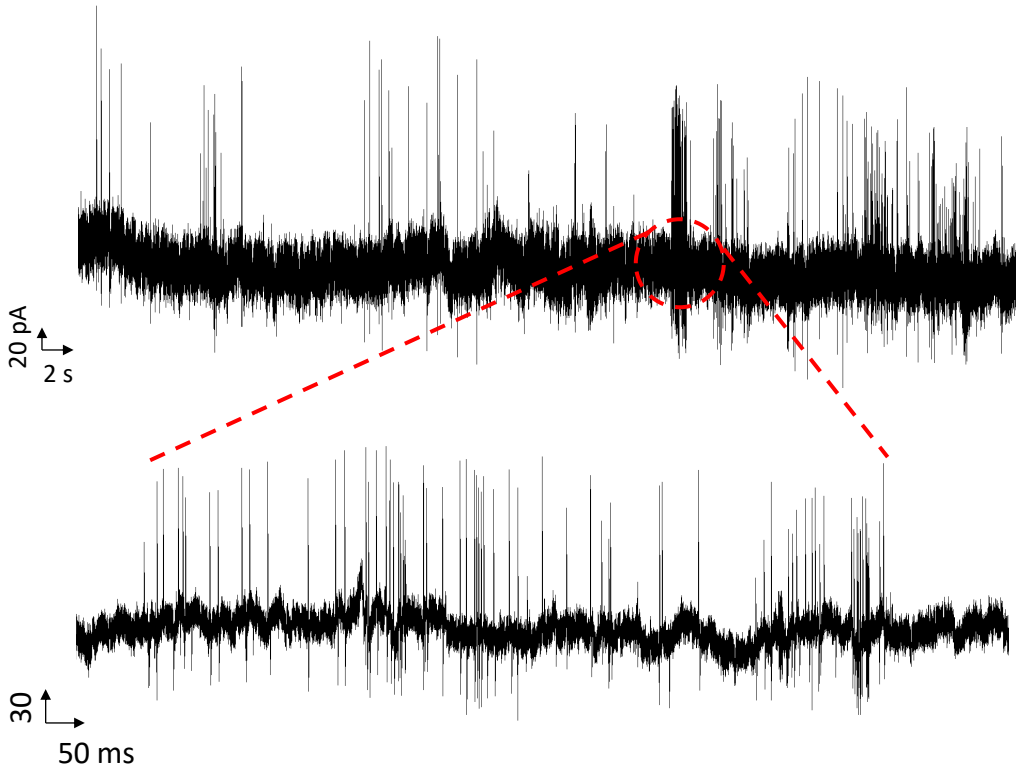


Figure 4. 11. *A trace alongside a zoomed in subsection showng the effects of peak clustering.*

In addition, determination of the capture rate from the inter-event time provided additional challenges due to peak clustering as shown in Figure 4.11. Peak clustering underestimated the inter-event time and thereby overestimated the capture rate. Peak clustering can be likely be attributed to aggregation and/or blocking at the nanopore tip, resulting in events occurring in close succession rather than a constant rate.

4.5. Results

4.5.1. Concentration dependence

Initially, the sensor was characterised electrochemically (as detailed in Chapter 2) by undertaking a concentration-based assay allowing our detection limit to be determined while providing insight into the binding mechanism. A thrombin concentration range (1 pM – 5 nM) was chosen with traces (shown as ionic current (pA) vs time (s) graphs) obtained representing peaks of thrombin translocation at different stages of the functionalisation process as shown in Figure 4.12. The different stages of functionalisation selected were unmodified, silanised and TBA-modified, alongside controls which included a random 29-mer DNA sequence as well as the TBA modified sensor before the addition of thrombin. Traces at 1 – 10 pM are recorded at 10 kHz and low-pass filtered at 1 kHz, while traces with concentrations including 500 pM and above are recorded at 50 kHz and low-pass filtered at 5 kHz. Translocation experiments with unmodified and silanised nanopipettes would allow the determination of whether thrombin could be detected without recognition elements. Meanwhile, thrombin translocation with the 29 mer control sequence, would show whether events were due to binding or due to the nucleotide sequence simply slowing down translocation. Finally, the measurement of TBA-modified pipettes without addition of the protein analyte would show whether events could be attributed to aptamer movement in and out of the pore.

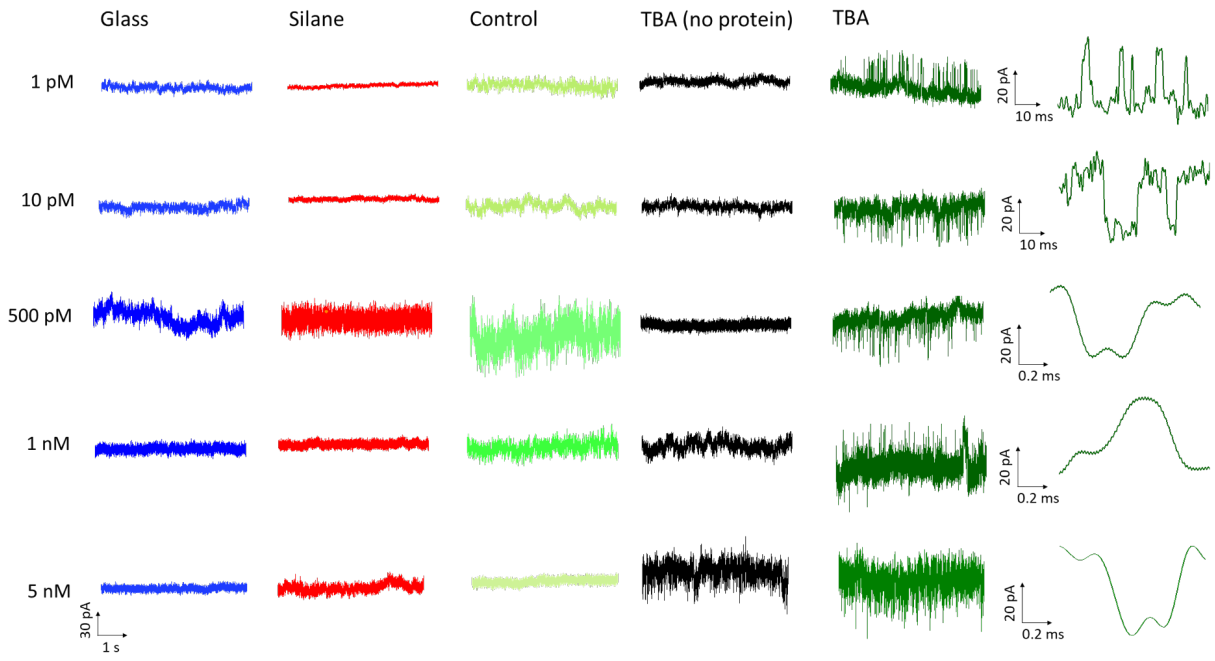


Figure 4. 12. *Representative traces of current (pA) vs time (s) at each stage of modification (glass, silanised and TBA) alongside controls (random DNA sequence and TBA without protein over a concentration range (1 pM – 5nM) of thrombin. Additionally, representative peaks are shown for TBA-modified peaks. Thrombin concentrations (1-10 pM) are recorded at 10 kHz and low-pass filtered at 1 kHz, while concentrations (500 pM and above) are recorded at 50 kHz and low-pass filtered at 5 kHz.*

Across the concentration range, peaks were only seen in TBA-modified sensors following the introduction of thrombin. However, representative peaks at each concentration showed that dwell times varied significantly, with lower concentrations showing long dwell times (> 1ms) and higher concentrations showing short (< 1 ms) dwell times.

Further analysis, including histograms of dwell times and peak amplitudes alongside, scatter plots of peak amplitude vs dwell amplitude of the TBA-modified sensor at different concentrations are shown in Figure 4.13. The analysis consists of the determination of averages for peak amplitude (Table 4.1). Furthermore, Figure 4.14 shows (left) dwell time and the related (right) dissociation constant (K_{off}). The capture rate (Table 4.2) can be defined through fitting the exponential of the inter-event time (see chapter 2) or through calculation of the number of events per second. Peak clustering resulted in very low inter-event times thereby overestimating the capture rate (see values in red). As a result, the capture rate was instead defined as events/second. Finally, the polarity of our repeats across the concentration assay was determined in Table 4.3.

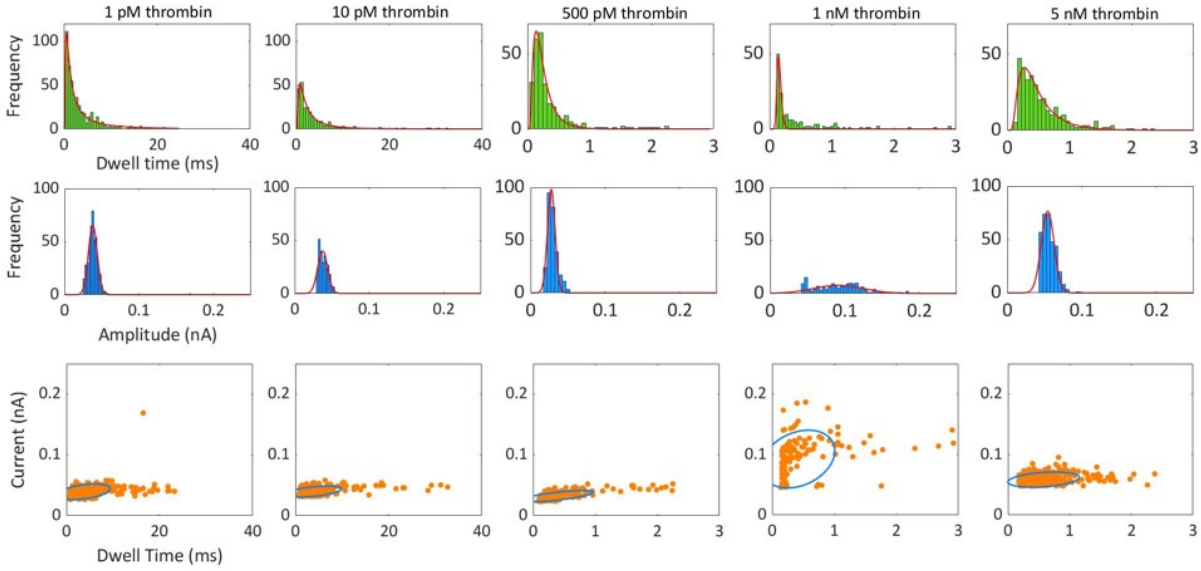


Figure 4. 13. *Histogram analysis of dwell time and peak amplitudes alongside dwell time vs peak amplitude scatter plots for a concentration range (1 pM – 5 nM) of thrombin in aptamer-modified pipettes. Number of events (N) at each concentration are as follows. N = 491 for 1 pM thrombin, N = 527 for 10 pM thrombin, N = 270 for 500 pM thrombin, N = 158 for 1 nM thrombin and N = 756 for 5nM thrombin.*

Table 4. 1. Normalised peak amplitudes of events for a thrombin concentration range. Values represent mean ± standard deviation (n = 3)

Concentration (nM)	Normalised Peak Amplitude (pA)		
	Repeat 1	Repeat 2	Repeat 3
0.0001	77.76 ± 7.0	158.62 ± 37	28.72 ± 4.5
0.001	83.59 ± 15	53.55 ± 6.9	43.72 ± 3.7
0.5	38.39 ± 6.2	41.73 ± 7.8	103.94 ± 23
1	39.39 ± 6.2	43.05 ± 4.8	131.69 ± 49
5	52.39 ± 6.4	67.59 ± 11	75.69 ± 5.7

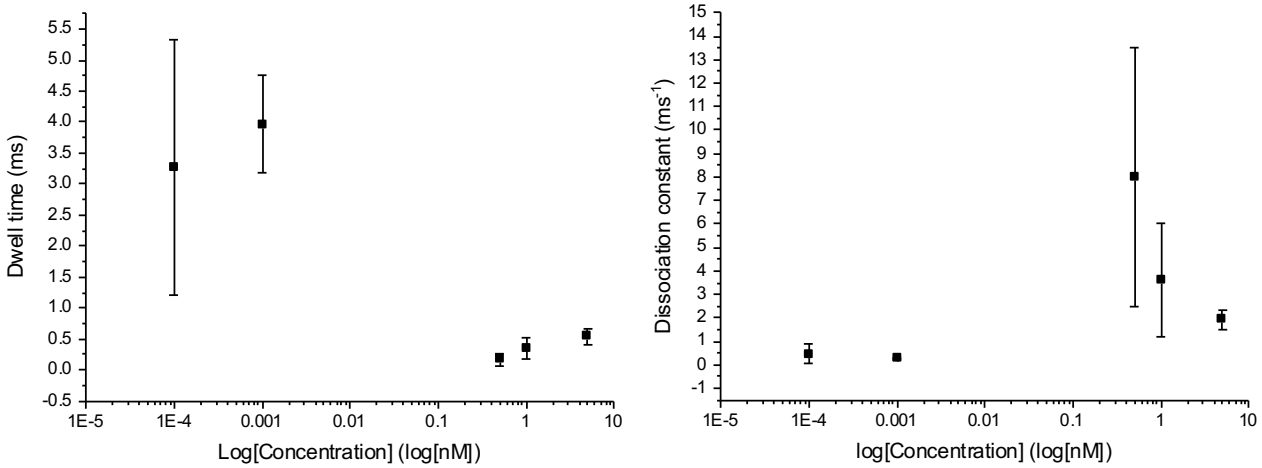


Figure 4. 14. *The dependence of concentration shown on a logarithmic scale as a function of dwell time (left) and dissociation constant (right).*

Table 4. 2. *Capture rates of events for thrombin (1 pM – 5 nM).* Values represent *mean ± standard deviation (n = 3). Values in red showcases examples of the capture rate being over-estimated when calculated via inter-event (t_{on}) measurements.*

Concentration (nM)	**Capture rate (s^{-1})**							
	Repeat 1		**Repeat 2**		**Repeat 3**		**Average**	
	t_{on}	**events/s**	**t_{on}**	**events/s**	**t_{on}**	**events/s**	**t_{on}**	**events/s**
0.0001	3.34	2.52	5.18	3.01	7.77	4.49	5.43	3.34
0.001	18.05	8.10	18.99	17.38	12.83	8.01	16.62	11.16
0.5	261.08	3.53	55.33	12.12	7.60	7.47	108.00	7.71
1	16.41	9.88	66.13	15.17	18.57	2.71	33.71	9.25
5	30.86	18.81	43.43	15.57	36.40	27.21	36.90	20.53

Table 4. 3. *Polarity of binding events for thrombin (1 pM – 5 nM) used in the concentration assay for each repeat (n = 3).*

Concentration (nM)	Polarity	
	Positive	Negative
0.001	3	0
0.01	0	3
0.5	2	1
1	2	1
5	0	3

Histogram analysis of dwell times provided further evidence of the concentration dependence of dwell time. Interestingly, dwell times did not fit a typical Gaussian curve, instead resulting in a skewed distribution, with a tail moving to longer dwell times. This can be attributed to the presence of the recognition elements within the pore which is discussed later on in the chapter. Despite this, dwell times showed consistency between repeats. Conversely, while peak amplitudes showcased typical gaussian curve behaviour, not only did they vary significantly within repeats, they also showed no clear trend with increasing thrombin concentration. Peak amplitude vs dwell time scatter plots showed that dwell time is independent of peak amplitude across all concentrations. Capture rates (events/s) as shown in Table 4.2 overall show a positive correlation with concentration, despite significant discrepancy between individually modified pipettes. Finally, as shown in Table 4.3, peaks generally showed positive polarity at low thrombin concentration and negative polarity at high thrombin concentrations.

4.5.2. Voltage dependence

After performing a concentration assay, attention was turned to determining a voltage profile for the aptamer modified sensor. Table 4.4 provides an overview of the voltage assay, including dwell time, peak amplitude and capture rates at low (10 pM) and high (500pM) thrombin concentrations.

Table 4. 4. *A voltage-based (300-500 mV) assay at 10 pM and 500 pM including peak amplitude, dwell time and capture rate analysis for aptamer-based nanopipettes.*

	Amplitude (pA)		Dwell time (ms)		Capture rate (s^{-1})	
Voltage (mV)	10 pM	500 pM	10 pM	500 pM	10 pM	500 pM
300	17.07	44.25	2.47	0.080	14.40	1.25
400	29.37	71.96	2.47	0.080	16.90	4.42
500	43.16	57.84	4.87	0.070	17.38	7.47

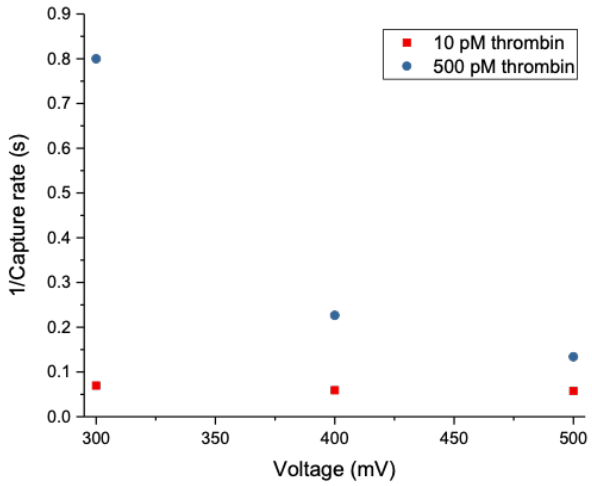


Figure 4. 15. *A graph showing voltage plotted against 1/capture rate for 10 pM and 500 pM thrombin in aptamer-based nanopipettes.*

The peak amplitude increased from 300-500 mV at both 10 pM and 500 pM, despite a slight reduction at 400 mV with 500 pM thrombin. The dwell time remained consistent at 10 pM between 300-400 mV, until doubling at 500 mV; at 500 pM thrombin, the dwell time remains effectively constant. Meanwhile, the capture rate remained effectively steady at 10 pM, while increasing steadily at 500 pM when an increase in the voltage is applied. This is further exemplified in the voltage vs the capture rate reciprocal plot seen in Figure 4.15.

4.5.3. Electrolyte concentration dependence

Next, the behaviour of TBA-modified pipettes in 100 mM KCl and 1 M KCl electrolyte was compared. I/V curves (Figure 4.16(a)) showed that alongside higher ionic currents, a smaller rectification ratio was observed when pipettes were measured in 1 M KCl electrolyte (1.16) in comparison to 100 mM KCl (1.47). Traces of thrombin translocation at different electrolyte concentrations were also measured in TBA-modified nanopipettes. 1 pM thrombin in 1 M KCl was initially tested showcasing no observable translocation peaks (Figure 4.16(b)). Despite this, peaks were seen in the same TBA-modified pipette, when 500 pM thrombin was translocated in 100 mM KCl electrolyte (Figure 4.16(c)).

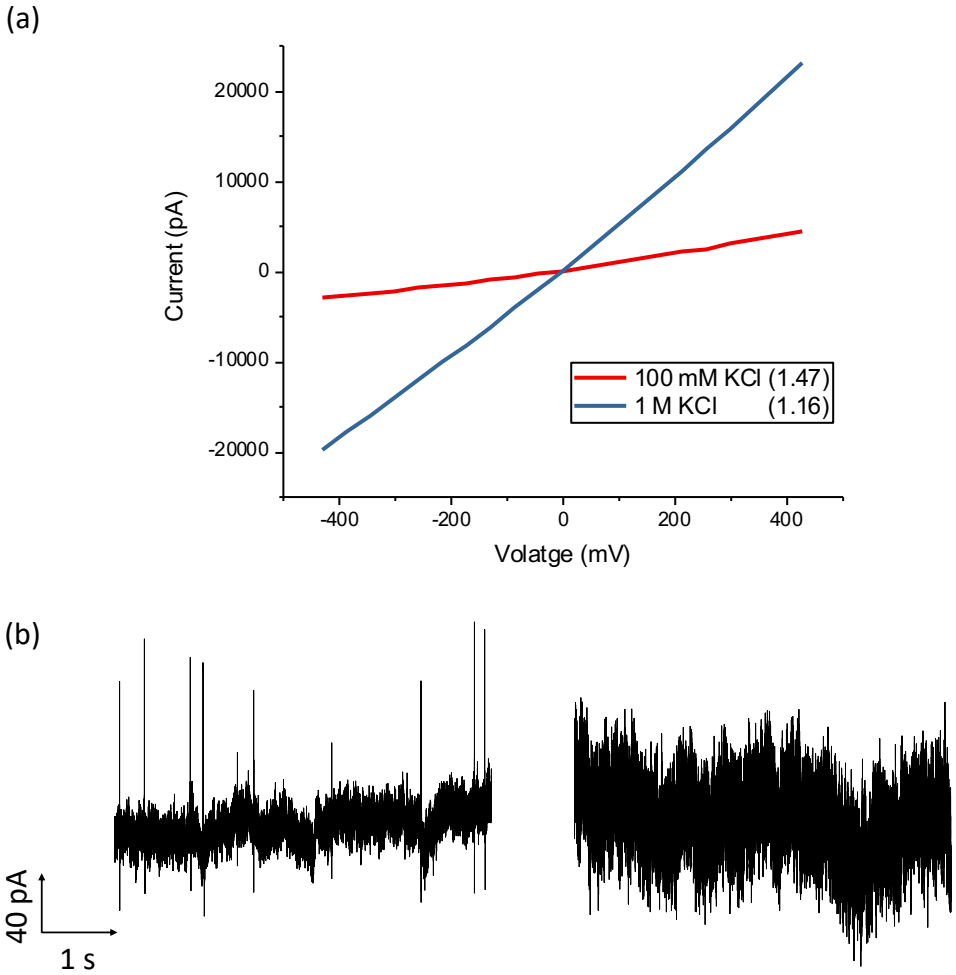


Figure 4. 16. *The dependence of molar electrolyte concentration on TBA-modified pipettes. (a) I/V traces of TBA - modified pipettes measured in 100 mM KCl (red) and 1 M KCl (blue), with the rectification ratio shown in brackets. (b) The dependence of molar concentration on thrombin translocation through TBA-modified pipettes. Traces show the translocation of 500 pM thrombin in 100mM KCl (left) alongside the translocation of 1pM thrombin in 1M KCl (right).*

4.5.4. Detection in a multi-protein analyte

Next, it was determined whether thrombin could be detected in a multiple-protein human serum solution. As detailed in Figure 4.17, traces are shown using TBA-modified pipettes filled with a 1:50 ratio of human serum diluted in in 100mM KCl in 1 x TE electrolyte (i) before spiking with 10 pM thrombin (ii). Results can be compared with thrombin translocation in KCl electrolyte only (iii). All traces were low-pass filtered at 1 kHz and recorded at 10 kHz.

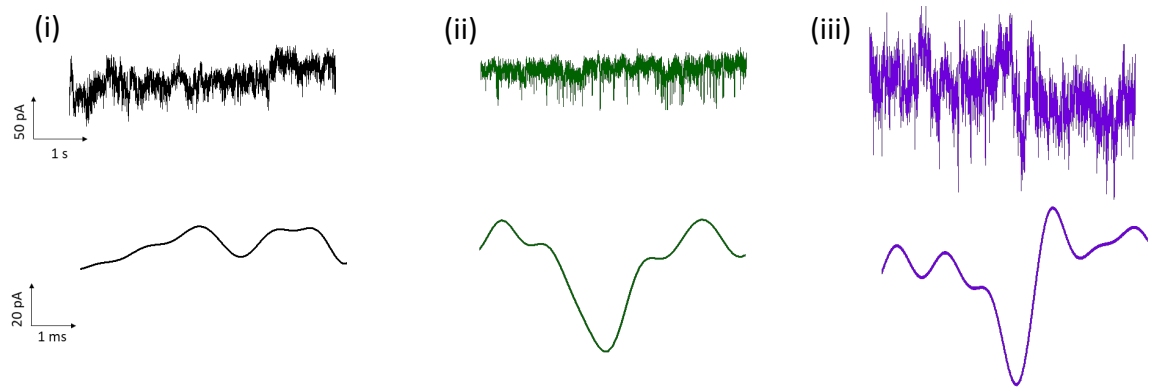


***Figure 4. 17**. Traces of current (pA) vs time (s) alongside representative peaks for (i) 1:50 human serum/100 mM KCl 1 x TE electrolyte mix, (ii) 10 pM thrombin in 100 mM KCl 1 x TE electrolyte (ii) and 10 pM thrombin in 1:50 human serum:100 mM KCl in 1 x TE electrolyte mix. All traces were filtered at 1 kHz and recorded at 10 kHz.*

Figure 4.18, showcases dwell time (top row), peak amplitude (middle row) and scatter analysis (bottom row) while Table 4.5 shows average values of peak amplitude, dwell time and capture rates for 3 repeats (different nanopipettes) of 10 pM in human serum in TBA modified nanopipettes.

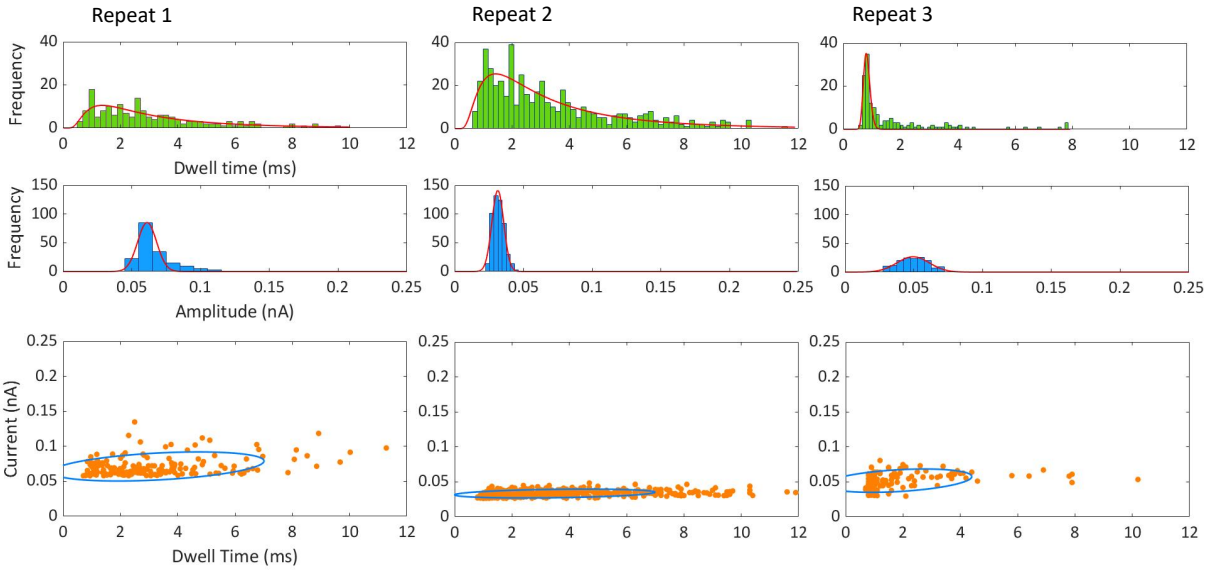


***Figure 4. 18.** Histogram analysis of dwell time (top row), peak amplitude (middle row) alongside dwell time vs peak amplitude scatter plots (bottom row) for three repeats of 10 pM thrombin in 1:50 human serum:100mM KCl in 1 x TE. Number of events for each repeat are as follows. N = 175 for repeat 1, N = 503 for repeat 2 and N = 154 for repeat 3.*

Table 4. 5. *Average values of normalised peak amplitudes, dwell times and capture rates for three repeats of 10 pM thrombin translocation conducted using 1:50 human serum:100mM KCl in 1 x TE in TBA-modified pipettes.*

	Normalised peak amplitude (pA)	Dwell time (ms)	Capture rate (s^{-1})
Repeat 1	70.21 ± 7.9	3.51	25.22
Repeat 2	25.25 ± 3.5	3.66	12.88
Repeat 3	55.82 ± 13.2	0.83	15.66

The traces in Figure 4.17 show that peaks are not present in (i) yet are present when spiked with thrombin (ii), despite the loss of SNR when compared to (iii). Dwell time histogram analysis not only shows similarities between different repeats with the distorted Gaussian curves as seen previously (despite repeat 3 showing a lower dwell time than expected due to poor fitting) but is also in line with analysis seen in electrolyte alone. Peak amplitudes histograms and dwell time vs peak amplitudes scatter plots compare with thrombin binding in the absence of serum, though significant variation was observed between repeats as recorded before.

4.5.5. Noise analysis

4.5.5.1. RMS

Next, the root mean square (RMS) noise profile in our translocation/binding experiments was determined. RMS noise was initially calculated at different stages of the modification process (Table 4.6(a)) when pipettes were filled with electrolyte prior to 10 pM thrombin. A comparison with TBA-modified pipettes in serum before and after spiking with thrombin was also undertaken (Table 4.6(b)). Experiments were run at 500mV and recorded at 250 kHz with a 10 kHz low-pass filter applied.

Table 4. 6. *RMS values at different stages of the modification process when recorded in 100 mM KCl 1 x TE only and 10 pM thrombin in 100 mM KCl in 1 x TE. (b) RMS values of different solutions in TBA-modified pipettes include 100mM KCl, 1 x TE, with and without 10 pM thrombin as well as 1:50 human serum to 100 mM KCl with and without 10 pM thrombin.*

(a)

Nanopipette modification	**RMS (pA)**	
	100 mM KCl	**10pM Thrombin**
Glass	4.70	12.03
Silane	4.38	4.61
TBA	7.25	26.67

(b)

Solution	**RMS (pA)**
100 mM KCl	7.25
10 pM thrombin (100mM KCl)	26.67
1:50 HS:KCl	30.7
10 pM thrombin (1: 50 HS:KCl)	45.68

Upon introduction of 10 pM thrombin, the RMS remained effectively constant in silanised pipettes, yet increased moderately in unmodified pipettes and significantly in TBA-modified pipettes. Additionally, the RMS was enhanced in serum but increased even further when the serum was spiked with thrombin.

4.5.5.2. Power spectrum density

The power spectrum density (Figure 4.19) was determined for TBA-modified pipettes with (red) and without (blue) 10 pM thrombin in both KCl (top) and a 1:50 HS:KCl solution (bottom). In both cases PSD were performed at 250 kHz with a 10 kHz low-pass filter.

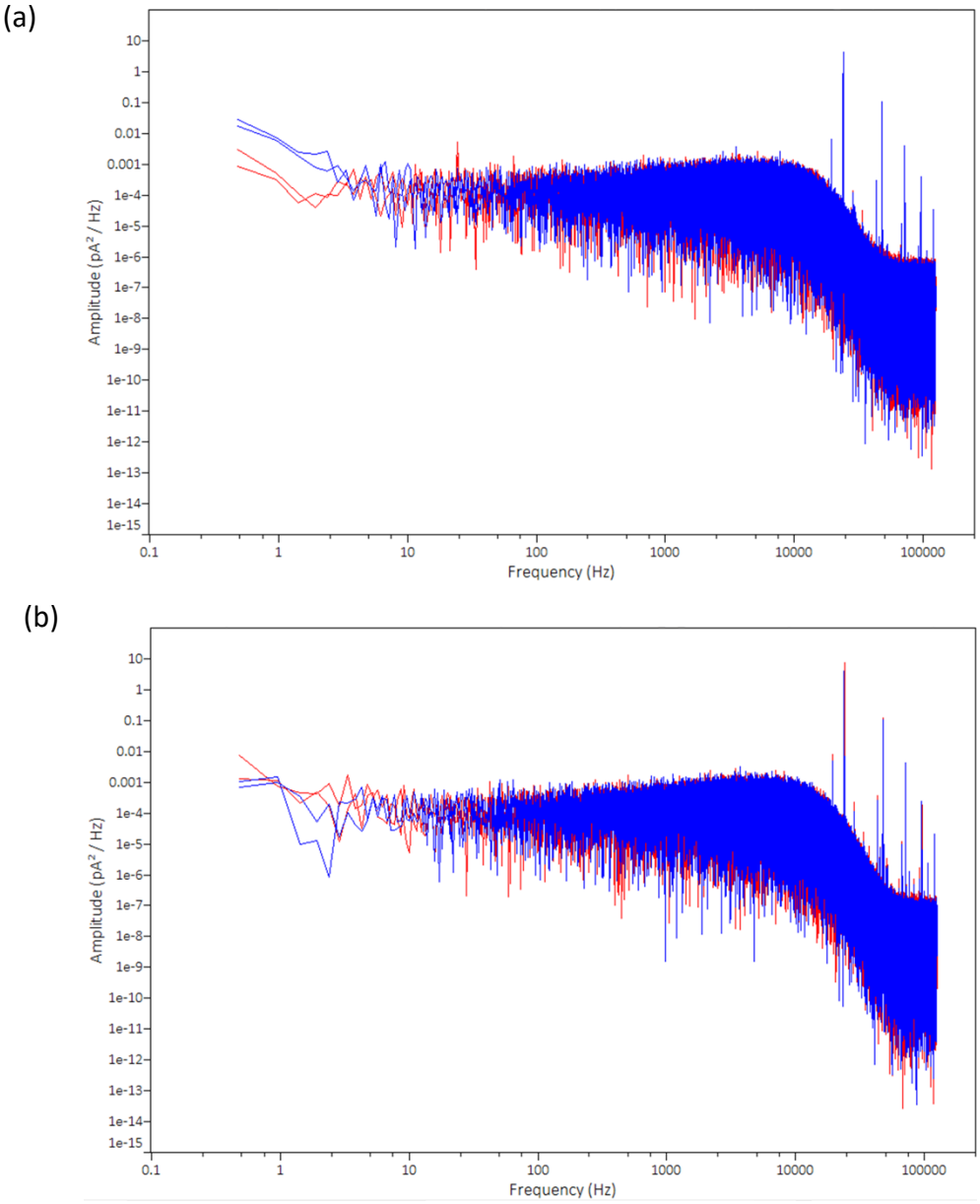


Figure 4. 19. *PSD of TBA-modified nanopipettes. (a) TBA-modified pipettes conducted in 100mM KCl without (blue) and with (red) 10 pM thrombin. (b) TBA-modified pipettes conducted in a 1:50 HS:100mM KCl without (blue) and with (red) 10 pM thrombn.*

4.5.6. Low-pass filter effects

By employing low-pass filters, traces could be simplified whereby any frequencies above the low-pass filter were removed. For high thrombin (500 pM) concentrations (Figure 4.19a), dwell times were fairly small (~ 0.2 ms). As a result, original data with a 10 kHz low-pass filter (Figure 4.20a(i)) could only be facilitated with the use of a 5 kHz low-pass filter (Figure 4.20a(ii)) corresponding to a cut-off of 0.2 ms. Conversely, at low thrombin (10 pM) concentration (Figure 4.20b), dwell times were large (> 1ms). As a result, original data with a 10 kHz low-pass filter (Figure 4.20b(i)) could be refiltered with a low-pass filter of 1 kHz (b(ii), corresponding to a cut-off of 1 ms. In addition, low-pass filters were particularly critical for thrombin detection (10 pM) in multi-analyte serum (Figure 4.20(c)). The long dwell times (> 1 ms) again facilitated the use of 1 kHz low-pass filters allowing data to be successfully analysed.

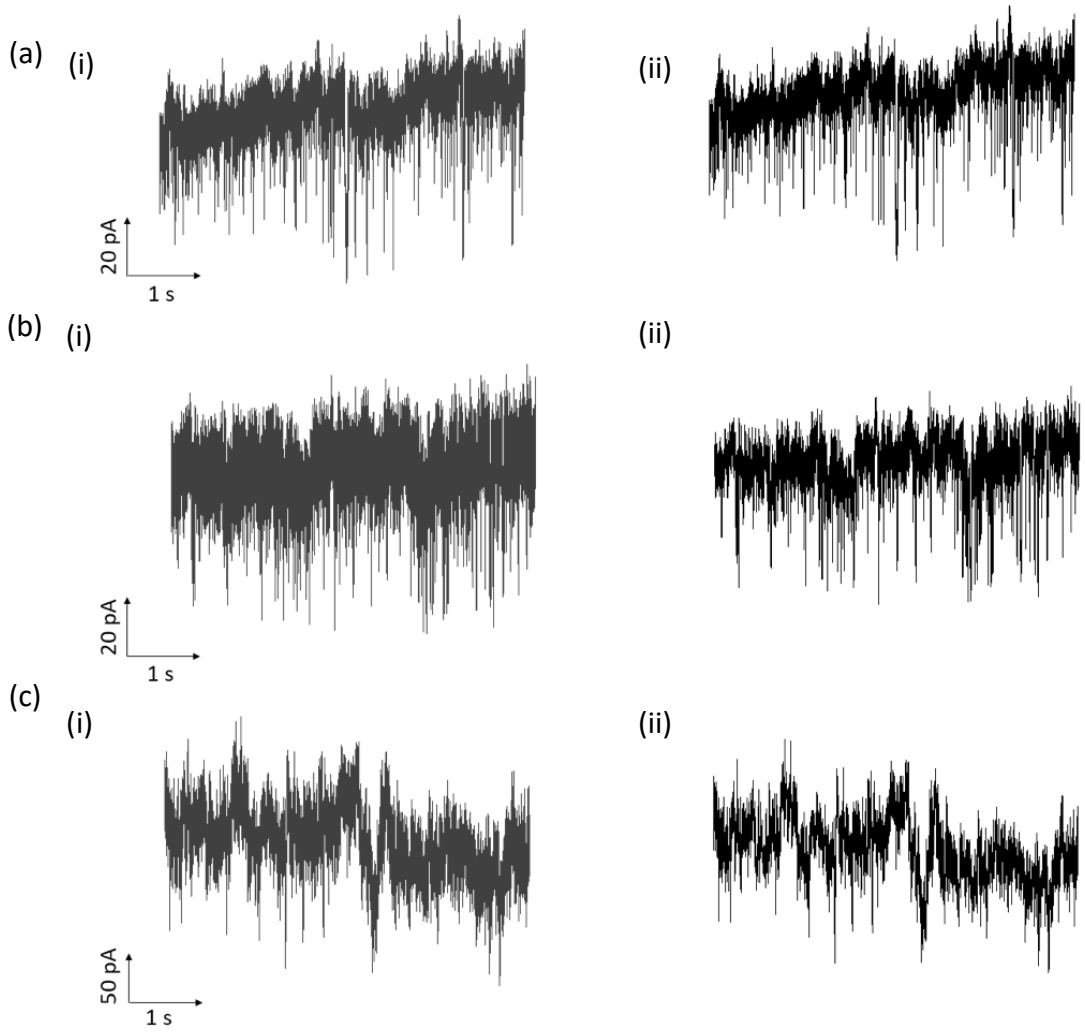


Figure 4.20. *The effects of low-pass filters on thrombin translocation through TBA-modified pipettes. (a) 500 pM thrombin translocation using a low-pass 10 kHz filter (i) as well as a low-pass 5 kHz filter (ii). (b) 10 pM thrombin using a low-pass 10 kHz filter as well as a low-pass 1 kHz filter (ii). (c) 10 pM thrombin translocation conducted in 1:50 HS:100mM KCl using a low-pass 10 kHz filter (i) and a low-pass filter 1 kHz filter (ii).*

4.5.7. Sensor regeneration

Finally, we looked to determine whether the developed TBA-functionalised sensor could be used multiple times. As shown in Figure 4.21(a) aptamer-modified sensors were measured in KCl and thrombin with TE washings used between repeat measurements. A higher rectification ratio was seen in nanopipettes when filled with KCl in comparison to thrombin, and could switch between the two states multiple times before the difference in rectification ratio became insignificant. Figure 4.21(b) shows traces corresponding to the experiment seen in the rectification ratio plot.

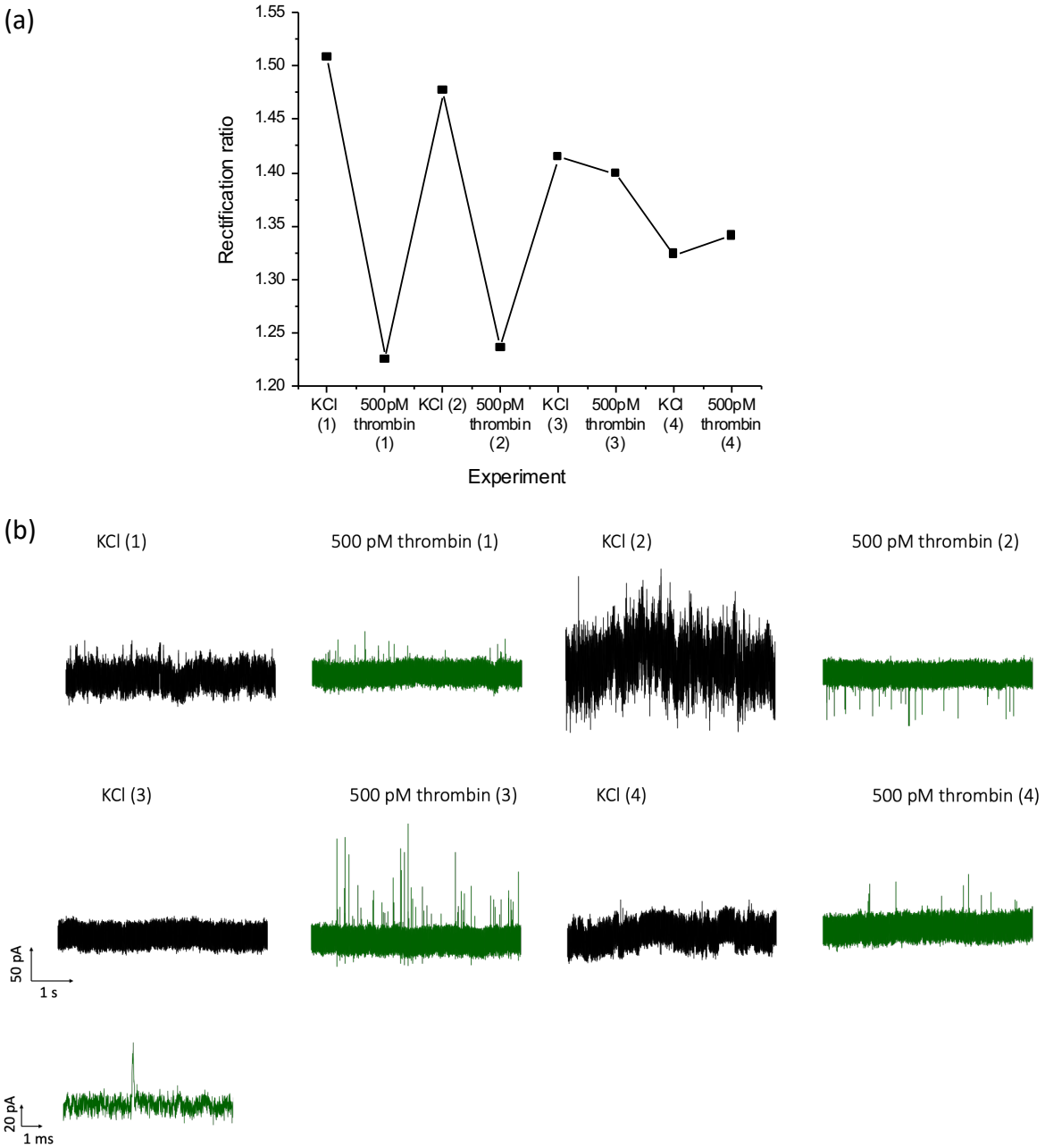


Figure 4. 21. *Regeneration experiments conducted using TBA-modified nanopipettes. TBA-modified pipettes could be measured in solutions containing KCl only and 10pM thrombin with washing in TE buffer used to remove any thrombin. (a) The graph shows the rectification ratio plotted with each experiment corresponding to whether the TBA-modified pipettes is filled with thrombin or KCl. Traces corresponding to the above experiment were recorded with a sampling frequency of 50 kHz with a low-pass filter of 5 kHz.*

The same TBA-modified pipette was also measured with 1 pM thrombin (Figure 4.22) to see if not only the concentration based assay applied but also if the sensor could be regenerated.

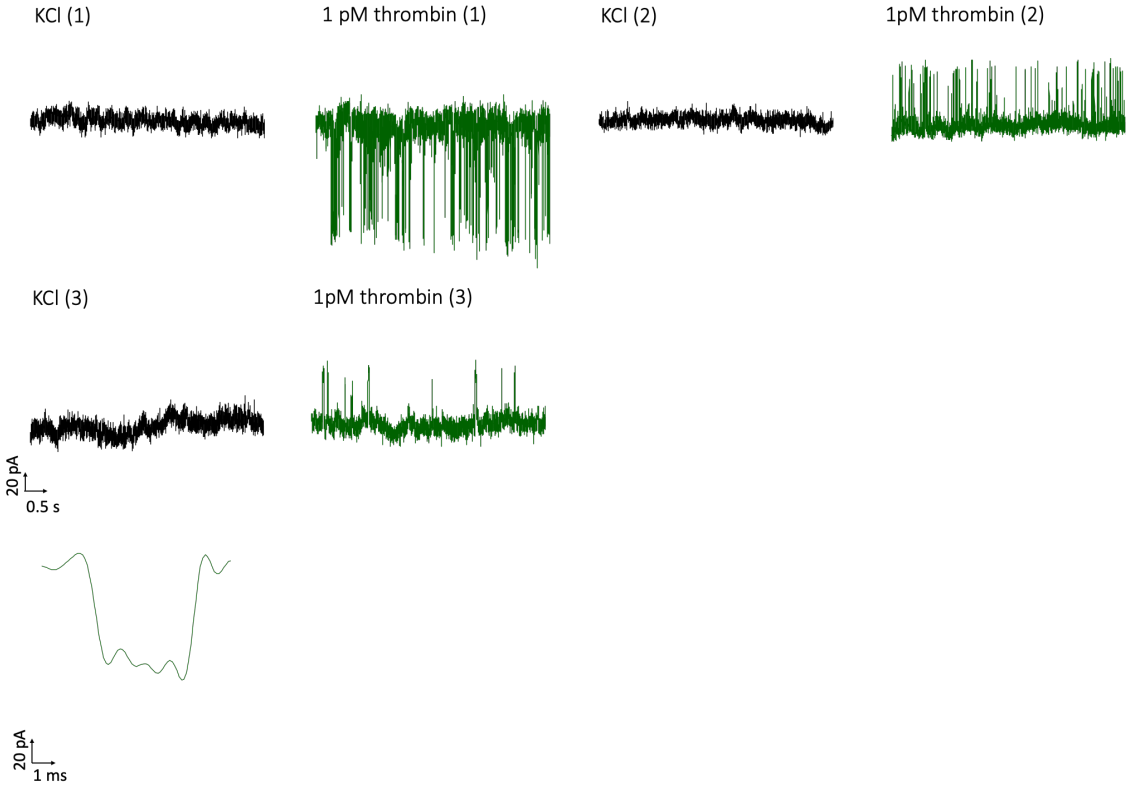


Figure 4. 22. *Traces showing the regeneration of the TBA-modified pipette using 1 pM thrombin as the substrate with TE washings were used to remove any residual thrombin. Trcaces were recorded at 10 kHz with a low-pass filter of 1 kHz.*

4.6. Discussion

In this chapter, the behaviour of the developed aptamer-modified sensor has been determined for the detection of thrombin through the use of concentration and voltage profiles while outlining its use in disease diagnosis through detection in a multi-protein (serum) analyte and its compatibility as a medical device through I/V regeneration experiments.

The thrombin concentration-dependence studies are atypical in comparison to DNA translocation studies through nanopipettes. In such cases, while the inter-event time typically decreases with increasing analyte (thrombin) concentration, the dwell time remains constant. In the case of the TBA-modified sensor, through the observation that far longer dwell times are seen at low thrombin concentrations and that the capture rate is independent of voltage a likely translocation/binding mechanism has been determined as shown in Figure 4.23. It was theorised that at low thrombin (1-10 pM) concentrations,

aptamer binding predominantly occurs. This results in significantly slower dwell times as the aptamer binds and subsequently releases the analyte. Meanwhile, the capture rate is not affected by voltage as aptamer binding holds thrombin resulting in a steady rate of thrombin passage events. Conversely, at higher thrombin concentrations, aptamer sites are effectively constantly fully occupied despite the cycles of reversible binding that continuously occur. As a result, rather than protein binding, the mechanism of movement is due to translocation across occupied aptamer sites within the nanopore tip; resulting in events with significantly shorter dwell times. However, unlike control experiments (e.g thrombin translocation in unmodified/silanised pipettes), events are still slow enough to be detected. This can be attributed to interactions between thrombin and the thrombin/TBA complex as it passes through the nanopore tip. The change of mechanism from predominantly binding events to translocation events is evidenced through the voltage dependence on capture rate at high thrombin concentrations.

Furthermore, evidence of aptamer binding can be seen in the type of distribution seen in the histogram analysis of dwell times. In comparison to the Gaussian based distribution of dwell times that occur with DNA translocation through unmodified nanopores, protein translocation through nanopores equipped with recognition elements result in skewed or decay exponential distribution fits. For example, Rant[17] showed that the translocation of His-tagged proteins through nanopores equipped with specific Nitriloacetic acid (NTA) receptors resulted in a decay exponential fit. In the case of thrombin translocation, at low concentrations (1-10 pM), fits showed exponential decay, before fitting as a non-Gaussian skewed histograms for higher concentrations (500 pM – 5 nM). This suggests that binding predominates at low thrombin concentrations, while mixture of non-resolvable binding and translocation occurs at higher thrombin concentration. Overall, this results in translocation events dominating over binding events, giving rise to events with very short dwell times. In addition, the applied voltage has a far greater effect on 'free' translocation, whereby the capture rate increases.

Ultimately, the ability to detect thrombin at concentrations significantly lower than the kD (500 pM) of TBA emphasises another key advantage of the coupling of single molecule detection with receptor binding. In other words, analyte detection can be readily observed even when only a fraction of aptamer sites are filled (and as described previously is preferred due to events with long binding times) rather than necessitating half of the

receptor sites to be filled (the definition of kD). Additionally, the single molecule detection exhibited by aptamer-based nanopores also allows detection at very low concentrations without signal loss (i.e loss in amplitude). This is in contrast to other detection techniques (e.g the electrochemical based aptasensor[8] described in 4.1.2) whereby signal intensity is inversely dependent on the analyte concentration. Overall, dwell time is an effective indicator of protein concentration, while the capture rate provides further insight for voltage assays.

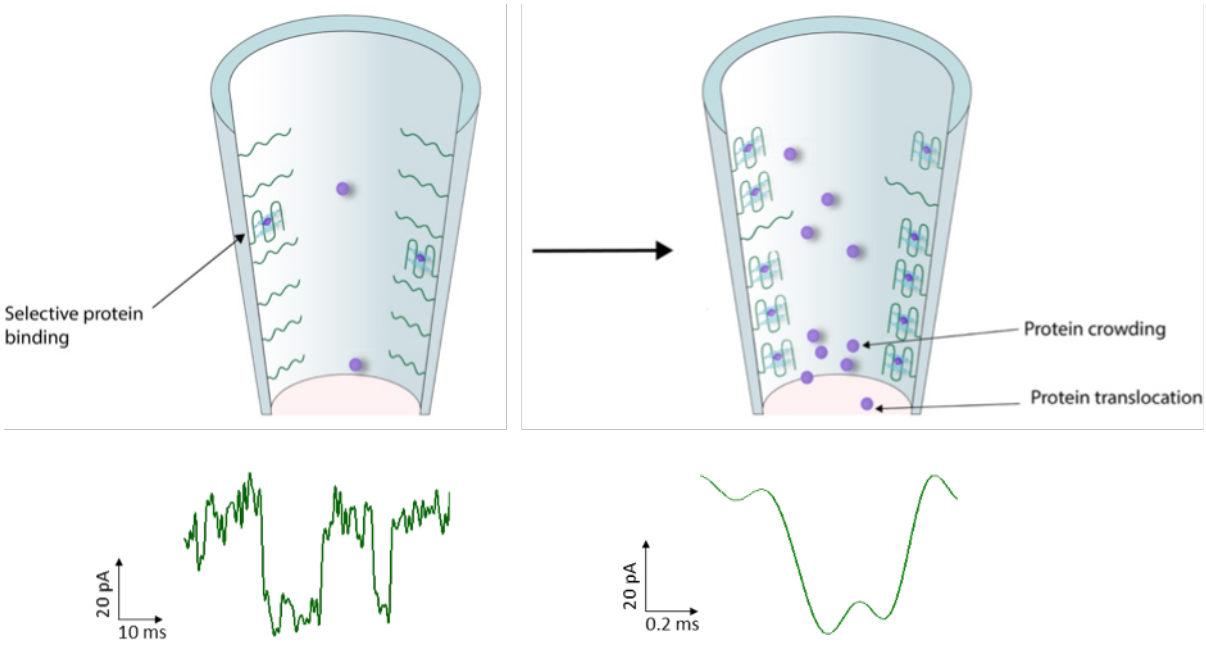


Figure 4.23. *A likely mechanism of protein transport in aptamer modified pipettes alongside representative peaks. At low thrombin concentrations aptamer binding occurs (long dwell times) while at higher thrombin concentrations protein translocation dominates (short dwell times).*

Conversely, the amplitude and polarity of peaks were inconsistent in the concentration assay and even amongst cycles in the regeneration assay. Despite this, enhancement peaks were typically observed at lower thrombin concentrations, while blockade peaks were generally observed at higher thrombin concentrations (Table 4.3). While the effects of electrolyte concentration on the polarity of peaks, have not been characterised for protein translocation they have been for DNA translocation. In particular, Keyser and Chen[18] showed that blockade based events were observed at high electrolyte concentrations, while enhancement based events were seen at low electrolye concentrations. It was therefore reasoned that an increase in the electrolyte concentration form 100 mM to 1 M KCl, would result in only blockade peaks occurring. Unfortunately, the passage of thrombin (1 pM)

could not be observed at 1 M KCl, although thrombin translocation (500 pM) could occur at 100 mM KCl in the same TBA-modified pipette. It was was likely that the 1M KCl electrolyte concentration was too high thereby preventing aptamer binding, and this can be inferred from the binding conditions (100 mM NaCl, 1 mM $MgCl_2$, 50 mM Tris-HCl at pH 7.5) used when TBA 29mer was first characterised via SELEX[1]. In addition, the changes in polarity of peaks was therefore concluded to be from local changes in the ion concentration.

Thrombin binding studies in human serum not only yielded results that were close to those seen in KCl electrolyte alone but were also consistent between repeats despite the loss of S:N ratio and current fluctuations. The greater noise in the serum assay can be attributed to non-specific interactions between the bound aptamer and other biomolecules present in serum. Detection of thrombin in a complicated multi-analyte solution demonstrates not only the selectivity of our system for a protein biomarker but could pave the way to detection of thrombin linked diseases such as cancer, MS and AD. Thrombin and thrombosis have causal links with cancer, while this biomarker is indirectly implicated, alongside its substrate fibrinogen and product fibrin in the case of MS and AD. To our knowledge thrombin detection in serum has not been reported at pM concentrations in serum and as a result, the nanosensor technology presents a new approach in the detection of neurodegenerative disorders (AD, MS) and cancer.

The regeneration experiments carried out suggests that the aptamer functionalised nanopipettes can be used multiple times as identified by I/V curves. Aptamer functionalised pipettes in the absence of the protein analyte promoted a greater rectification ratio than when protein binding occurs. This can be attributed to the electrostatic interaction[19] involved in protein binding, reducing the effective surface charge. Washing of the bound thrombin with TE buffer removes potassium ions, preventing the aptamer from forming a G-quadruplex formation and thereby preventing protein binding from occurring. This observation not only confirms that the aptamer functions via a pre-conformed structure, but opens up the possibility for a sensor to be used multiple times upon development of a suitable washing and regeneration protocol. In addition, the difference in dwell times between the translocation of 1 pM and 500 pM thrombin leads to greater proof for the mechanism of the TBA-modified sensor.

While thrombin (37 kDa) has not been detected in unmodified pipettes, the detection of similarly sized proteins (Figure 4.24), namely the 18 kDa ß-lactoglobin (left) and the 42 kDa

ovalbumin have been detected[20]. In comparison to the developed sensor, far greater protein concentrations; ß-lactoglobin (0.6 µM) and ovalbumin (1.0 µM) were required for detection in comparison to unmodified pipettes. Furthermore, dwell times were short with the majority of translocation events below 250 µs for ß-lactoglobin and below 150 µs for ovalbumin preventing the use of low-pass filters below 10 kHz. While the low peak amplitude (10-20 pA, ß-lactoglobin) and (20-40 pA, ovalbumin), could limit discrimination between tranlocation peaks and baseline noise.

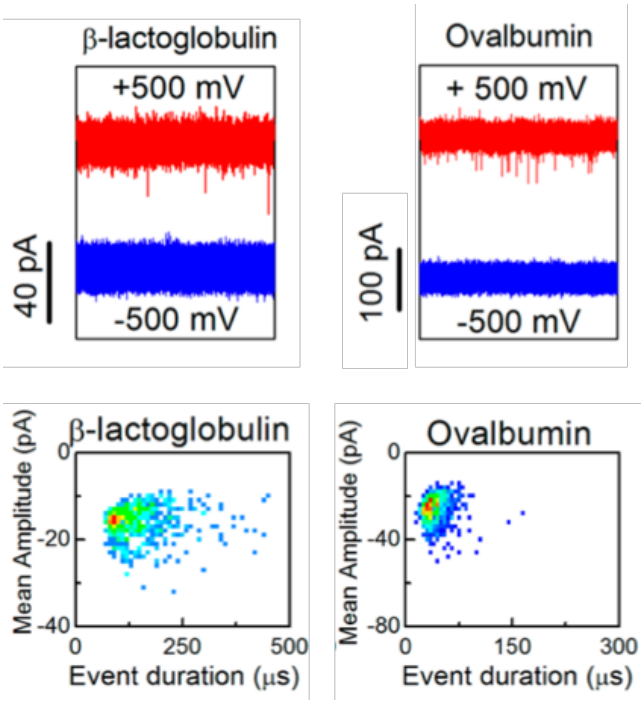


Figure 4.24. *The detection of ß-lactoglobin and ovalbumin using glass nanopipettes. 1 second traces (top) are shown at + 500 mV (red) and – 500 mV (blue) alongside dwell time vs amplitude scatter plots (bottom), with N = 1059 (ß-lactoglobin) and N = 1820 (ovalbumin). ß-lactoglobin was filtered with a low-pass filter 10 kHz and sampled at 100 kHz sampling rate, while ovalbumin was filtered with a 50 kHz low-pass filter and sampled at 500 kHz sampling rate. Figures adapted from reference 20.*

Imaging agents allow an excellent time based assay of thrombin detection despite requiring intravenous injection and only providing qualitative images. Aptamer-based electronic transfer electrochemical sensor meanwhile maintain reasonable sensitivity (up to 6.8 nM), while being label-free. However, long incubation times significantly reduce the throughput, while sensitivity in serum is lower than required for use in patient samples. In addition, aptamer based carriers have been used to detect thrombin (as described in chapter 1). Overall, this strategy affords good sensitivity and selectivity, while remaining easy to implement. Despite this, detection is based on the presence of binding sub-peaks which means that not only is detection indirect but the presence of false positive sub-peaks

are due to DNA folding. Overall, the developed sensor described throughout this chapter despite difficulty in data analysis and low functionalisation efficiency affords several advantages over other techniques.

4.7. Conclusion

Overall, the aptamer-based nanosensor is shown to not only be highly sensitive in detecting thrombin (~ 1 pM) but is also highly selective in detecting the protein biomarker in multi-protein solutions. Furthermore, our voltage and concentration profiles suggest a likely mechanism, whereby selective binding and long dwell times gives way to non-selective translocation and short dwell times as the concentration increases (Figure 4.23). Furthermore, regeneration studies that our sensor can be used multiple times allowing it to be potentially used as a medical sensor. These findings with thrombin detection have then allowed us to characterise the more complex alpha-synuclein oligomer analytes but also show the potential for a highly valuable biomarker sensing technology for MS/AD/cancer when used in multi-protein solutions as shown.

4.8. References

1 D. M. Tasset, M. F. Kubik and W. Steiner, *J. Mol. Biol.*, 1997, **272**, 688–698.

2 J. T. B. Crawley, S. Zanardelli, C. K. N. K. Chion and D. A. Lane, *J. Thromb. Haemost.*, 2007, **5**, 95–101.

3 I. R. Krauss, A. Pica, A. Merlino, L. Mazzarella and F. Sica, *Acta Crystallogr. Sect. D Biol. Crystallogr.*, 2013, **69**, 2403–2411.

4 S. Palta, R. Saroa and A. Palta, *Indian J. Anaesth.*, 2014, **58**, 515–523.

5 M. L. Nierodzik and S. Karpatkin, *Cancer Cell*, 2006, **10**, 355–362.

6 M. A. Petersen, J. K. Ryu and K. Akassoglou, *Nat. Rev. Neurosci.*, 2018, **19**, 283–301.

7 D. Davalos, K. M. Baeten, M. A. Whitney, E. S. Mullins, B. Friedman, E. S. Olson, J. K. Ryu, D. S. Smirnoff, M. A. Petersen, C. Bedard, J. L. Degen, R. Y. Tsien and K. Akassoglou, *Ann. Neurol.*, 2014, **75**, 303–308.

8 Y. Xiao, A. A. Lubin, A. J. Heeger and K. W. Plaxco, *Angew. Chemie - Int. Ed.*, 2005, **44**, 5456–5459.

9 H. Cho, B. R. Baker, S. Wachsmann-Hogiu, C. V. Pagba, T. A. Laurence, S. M. Lane, L. P. Lee and J. B. H. Tok, *Nano Lett.*, 2008, **8**, 4386–4390.

10 T. Nishimura, T. Myles, A. M. Piliposky, P. N. Kao, G. J. Berry and L. L. K. Leung, *Blood*, 2007, **109**, 1992–1997.

11 B. Dahlbäck and B. O. Villoutreix, *FEBS Lett.*, 2005, **579**, 3310–3316.

12 M. Nagashima, Z. Yin, L. Zhao, K. White, Y. Zhu, N. Lasky, M. Halks-miller, G. J. Broze, W. P. Fay and J. Morser, *Methods*, 2002, **109**, 101–110.

13 C. Schachtrup, J. K. Ryu, M. J. Helmrick, E. Vagena, D. K. Galanakis, J. L. Degen, R. U. Margolis and K. Akassoglou, *J. Neurosci.*, 2010, **30**, 5843–5854.

14 M. A. Petersen, J. K. Ryu, K. Chang, A. Etxeberria, A. S. Mendiola, W. Kamau-devers, S. P. J. Fancy, A. Thor, E. A. Bushong, B. Baeza-raja, C. A. Syme, M. D. Wu, P. E. R. Coronado, A. Meyer-franke, S. Yahn, L. Pous, K. Jae, C. Schachtrup, H. Lassmann, E. J. Huang and M. H. Han, *Neuron*, 2018, **96**, 1003–1012.

15 C. Schachtrup, P. Lu, L. L. Jones, J. K. Lee, J. Lu, B. D. Sachs, B. Zheng and K. Akassoglou, *Proc. Natl. Acad. Sci. U. S. A.*, 2007, **104**, 11814–11819.

16 T. P. Ugarova, V. K. Lishko, N. P. Podolnikova, N. Okumura, S. M. Merkulov, V. P. Yakubenko, V. C. Yee, S. T. Lord and T. A. Haas, *Biochemistry*, 2003, **42**, 9365–9373.

17 R. Wei, V. Gatterdam, R. Wieneke, R. Tampé and U. Rant, *Nat. Nanotechnol.*, 2012, **7**, 257–263.

18 K. Chen, N. A. W. Bell, J. Kong, Y. Tian and U. F. Keyser, *Biophys. J.*, 2017, **112**, 674–682.

19 S. Cai, J. Yan, H. Xiong, Y. Liu, D. Peng and Z. Liu, *Analyst*, 2018, **143**, 5317–5338.

20 W. Li, N. A. W. Bell, S. Hernández-Ainsa, V. V. Thacker, A. M. Thackray, R. Bujdoso and U. F. Keyser, *ACS Nano*, 2013, **7**, 4129–4134.

Chapter 5: Detection of alpha synuclein oligomers using an aptamer-modified nanopore sensor

5.1. Overview **127**

5.2. Introduction ***127***

5.2.1. Parkinson's Disease **127**

5.2.2.Oligomer structure **129**

5.2.3. Physiological function of alpha synuclein monomers and pathological mechanisms of alpha synuclein oligomers **129**

5.2.4. Oligomer detection **131**

5.3. Aim and challenges ***135***

5.4. Results ***135***

5.4.1. Concentration dependence **135**

5.4.2. Oligomer AFM images **140**

5.5. Discussion ***141***

5.6. Conclusion ***143***

5.7. References ***144***

5.1. Overview

In this chapter, the detection of alpha synuclein oligomers; a biomarker of Parkinson's Disease is described. To achieve this, nanopipettes were modified with a G-quadruplex forming 24mer anti-oligomer aptamer (kD = 68 nM), termed TS-0530[1]. After introducing the causes and prognosis of Parkinson's Disease[2-5], the structure[6-8] and toxicity[9-10] mechanism of the alpha synuclein oligomers are described. Current methods including ELISA[11-12] and unmodified nanopores[13-14] used to detect alpha synuclein oligomers and their inherent limitations are also detailed.

Alongside mechanistic insight from the previous chapter, the detection of alpha synuclein oligomers using the aptamer-based nanopipette are described. As described for thrombin, a concentration dependence assay is employed to determine detection limits. Finally, after optimising the optimal oligomer concentration range, detection of oligomers at different aggregation timepoints (hours) allowed determination of the aptamers preferred oligomer binding species.

5.2. Introduction

5.2.1. Parkinson's Disease

Parkinson's Disease (PD), a synucleinopathy based disease, is a progressive neurological degenerative disorder, that has become increasingly prevalent in an ever-increasing ageing population. The disease is associated with the loss of dopaminergic neurons in the *substantia nigra pars compacta (SNpc)* of the midbrain[15] and the development of α-synuclein based Lewy bodies through intermediates, such as oligomers and protofibrils[1]. Identified risk factors for the aggregation of alpha synuclein summarised in Figure 5.1(a) involve the increased production of alpha synuclein, the reduced capacity of protein clearance mechanisms and conditions that support protein aggregation. The increased synthesis of alpha synuclein monomers involve single point mutations (Figure 5.1(b): A30P, E46K, A53T)[16-18] and multiplications of the SCNA gene[19-20] encoding alpha synuclein. Meanwhile, aging leading to the reduction of protein clearance mechanisms[21] (e.g autophagy dysfunction and proteasome failure), which also result in the accumulation of alpha synuclein. Finally, the aggregation process can be accelerated through oxidative stress[22] and post-translational modifications[23].

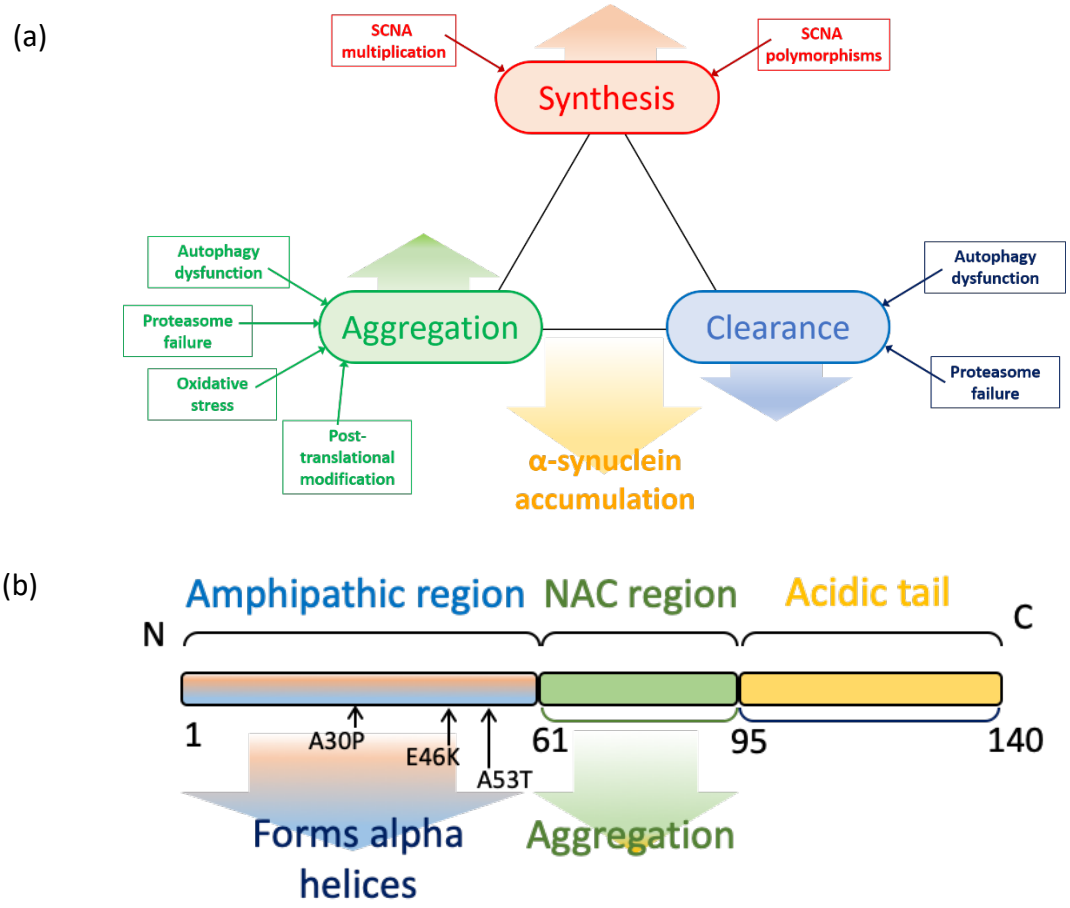


Figure 5. 1. *(a) An overview of the causes of alpha synuclein monomer aggregation. (b) A schematic showing the primary structure of alpha synuclein monomers. The amphipathic region contains three mutants (A30P, E46K and A53T), while the non-amyloid component (NAC) region is responsible for aggregation.*

There are numerous problems associated with current treatments for Parkinson's Disease, such as a lack of their effectiveness and the severity of side effects associated with pharmacological drugs/stem cell based treatments[24]. Even if improved, pharmacological treatments are still likely to be administered too late to deliver their full effect, as by the time symptoms are observed, 60-80% of dopaminergic neurons have already been destroyed. Detection technologies are currently based on the presence of late stage parkinsonian motor features (bradykinesia, rigidity and resting tremor) that are significantly developed during disease progression.

Currently there is no laboratory based diagnostic test to identify individuals with the disease or its progression. The detection of α-synuclein in cereberospinal fluid (CSF) is a promising candidate biomarker for the diagnosis of PD. While, the α-synuclein concentration is typically low (1-10pM in CSF), distinct aggregate oligomeric forms have

been identified as specific biomarkers for Parkinson's disease both in diagnosis and treatment efficiacy[3].

5.2.2.Oligomer structure

Oligomers, are intermediates in the protein aggregation pathway (see chapter 1) and display a broad range of structures and sizes, ranging from tetramers, to multimers. Many techniques including atomic force microscopy (AFM)[7], circular dichroism (CD)[18], analytical ultracentrifugation (AU)[8] and gel electrophoresis[25] have been employed to characterize oligomeric structures. Determining structures is particularly challenging due to their transient nature; which can result in degradation, conversion into more stable oligomers or aggregation into protofibrils and fibrils[26]. Experimental aggregation protocols are not standardised but require preparation of stabilised oligomers that are likely to differ from oligomers formed *in-vivo.* Some of the commonly encountered oligomeric structures are shown in Figure 5.2 below. Annular structures are ring shaped[27], while protofibrils are rod-shaped pre-fibrillar structures[10] and globular structures[28] are spherical-based structures.

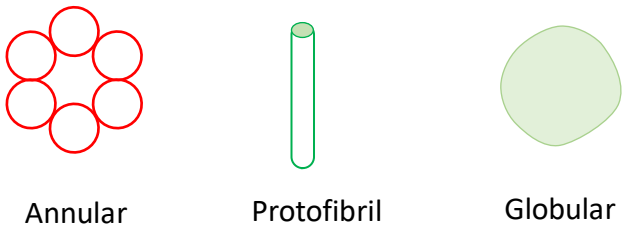


Figure 5. 2. *Commonly encountered alpha synuclein oligomer structures.*

5.2.3. Physiological function of alpha synuclein monomers and pathological mechanisms of alpha synuclein oligomers

α-synuclein is believed to have a major role in neurotransmitter release due to its close proximity to the synaptic vesicles in the presynaptic terminal. Therefore, it has been theorised that alpha synuclein has a role in controlling the refilling and trafficking of synaptic vesicles from the reserve pool to the site of synaptic vesicle release[29,30] (Figure 5.3). Experiments have shown that when SNCA-knocked down mice underwent an impaired hippocampal synaptic response under pro-longed high frequency stimulation, it led to the depletion of docked and reserve pool synaptic vesicles as well as their impaired replenishment.

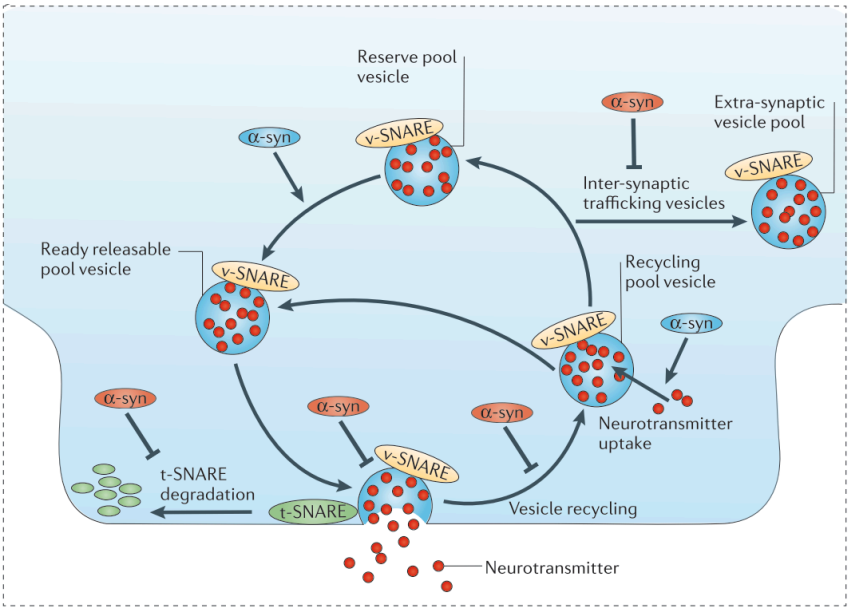


Figure 5. 3. *Native function of alpha synuclein monomers. Alpha synuclein monomers are believed to have roles in the refilling and trafficking of synaptic vesicles from the reserve pool to the site of synaptic release. Figure adapted from reference 6.*

Large oligomers have also been shown to prevent alpha synuclein monomers from regulating SNARE complex assembly by binding vesicle associated membrane protein (VAMP2)[31] which is used to promote synaptic-vesicle fusion at the pre-synaptic terminal. The result is a reduction in dopamine release, synaptic-vesicle recycling and mobility and neurotransmitter release.

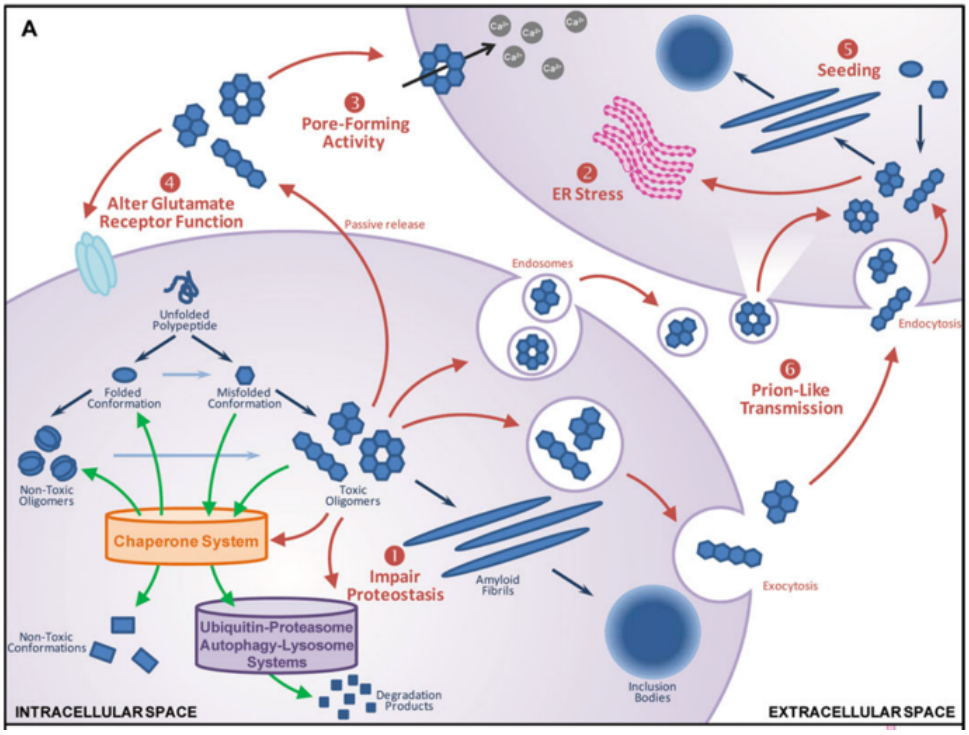


Figure 5. 4. *The various pathological disruptive mechanisms of toxic oligomers in neurons. Figure adapted from reference 5.*

Figure 5.4 provides an overview of additional pathological effects of alpha synuclein oligomers with the mechanism, being highly dependent on its morphology. Disruption is not just localised at the synapse, where alpha synuclein monomers typically operate, but occurs throughout the cell, resulting in mitochondrial damage and nuclear dysfunction.
For example, annular or 'ring-shaped' oligomers are known to increase membrane permeability, allowing calcium ion influx and eventual cell death. In addition, the extracellular application of globular oligomers has been known to alter glutamatergic receptors. The effects of the subsequent increase in the amplitude of α-amino-3-hydroxy-5-methylis-oxazole-4-propionic acid[32] (AMPA) receptor-mediated excitatory postsynaptic currents still requires further elucidation, but are thought to lead to dysfunctional synaptic signalling, and/or activation of intracellular pathways leading to excitotoxicity and neuronal death. In addition, globular and protofibril oligomers are known to cause seeding, a process whereby oligomers act as nuclei, allow further aggregation and ultimately catalyse the propagation of the disease throughout the cell.

5.2.4. Oligomer detection

There is currently no widespread diagnostic for the clinal detection of oligomers, but at the experimental level ELISA (**E**nzyme-**L**inked **I**mmuno**S**orbent **A**ssay) and unmodified solid state nanopores have been used for their detection and probing aggregation kinetics respectively.

(i) ELISA

Oligomer detection has been carried out selectively and sensitively (< nM) by sandwich based ELISA[11-12], a plate-based assay technique (Figure 5.5). In this set-up, the target antigen (i.e. oligomers) are sandwiched between a capture antibody (human anti-alpha synuclein monoclonal antibody (mab211)) and a detection antibody (biotinylated mab 211). This set-up allows simple washing steps to remove any unbound antibodies, while preventing monomer detection as since they only possess one binding site can only bind to the capture antibody. Detection involves assessing the activity of an enzyme (horseradish peroxidase; HRP) conjugated to the detection antibody upon the introduction of a suitable substrate resulting in a product measurable by spectroscopy. Sandwich ELISA is preferred over

classical ELISA whereby the antigen is simply attached to the solid substrate due to its high sensitivity, robust nature and ability to selectively target oligomers.

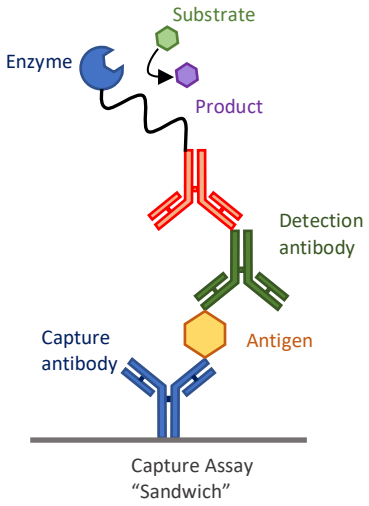


Figure 5. 5. *The principles of sandwich based ELISA, an indirect yet highly sensitive based detection method. A 'capture' antibody localised on a well plate and 'detection' antibody linked to an enzyme (e.g Horseradish Peroxidase) are both selective to a specific antigen. Upon antigen binding and subsequent washing steps the introduction of enzyme based activity on a specific product leads to detection of a measurable product.*

Sandwich ELISA data[11] (not shown due to copyright) of patient samples has a readout using the function of relative luminescent units (RLU)/second. Results showed a significant level of alpha synuclein oligomers in the PD group (mean ± SEM = 19,791 ± 2,458, N =32) in comparison to the disease group (mean ± SEM = 8,096 ± 596, N = 12) and the normal control group (mean ± SEM = 10,796 ± 1,715, N = 16). From the chemiluminescence assay, the alpha synuclein oligomer concentration was estimated to be about 2.5 ng/ml (180 pM) when conducted in CSF.

(ii) Nanopore detection

Solid state nanopore (pore size 5 nm) formed via high energy beam milling onto SiN wafers have been used to probe the aggregation kinetics of wild type (WT) as well as mutant alpha synuclein (A30P and E46K) oligomers at different aggregation timepoints (6/12/15 days)[13]. Figure 5.6 shows traces of oligomer aggregation (WT, A30P and E46K) at different timepoints (6 -12 days) of an alpha synuclein concentration of 450 nM. Figure 5.7 shows (log) dwell time vs fractional current blockage ($\Delta I/I_o$) as well as fractional current blockage plots for E46K oligomer aggregates at 6 days (a), 12 days (b) and 15 days.

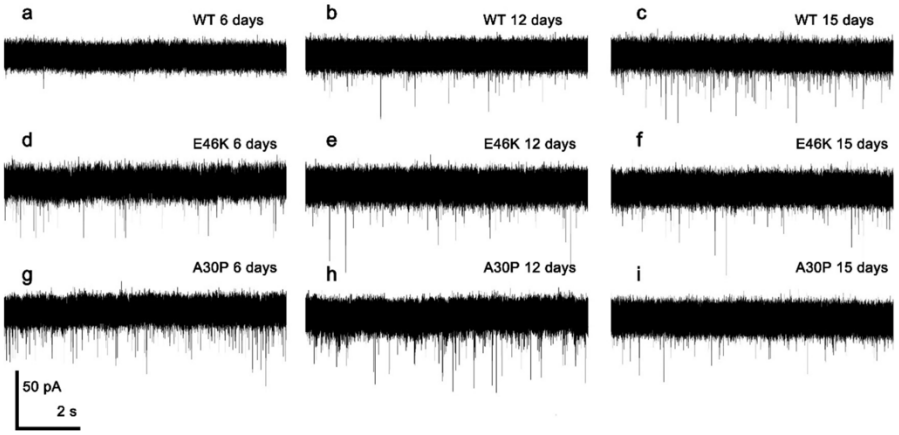


Figure 5. 6. *Representative traces arising from alpha synuclein oligomer translocation through solid state nanopores at 100 mV in a 0.5M NaCl solution at pH 8.0. (a-c) WT oligomer detection after 6, 12 and 15 days. (d-f) E46K oligomer detection after 6, 12 and 15 days. (g-i) A30P oligomer detection after 6, 12 and 15 days. Figure adapted from reference 13.*

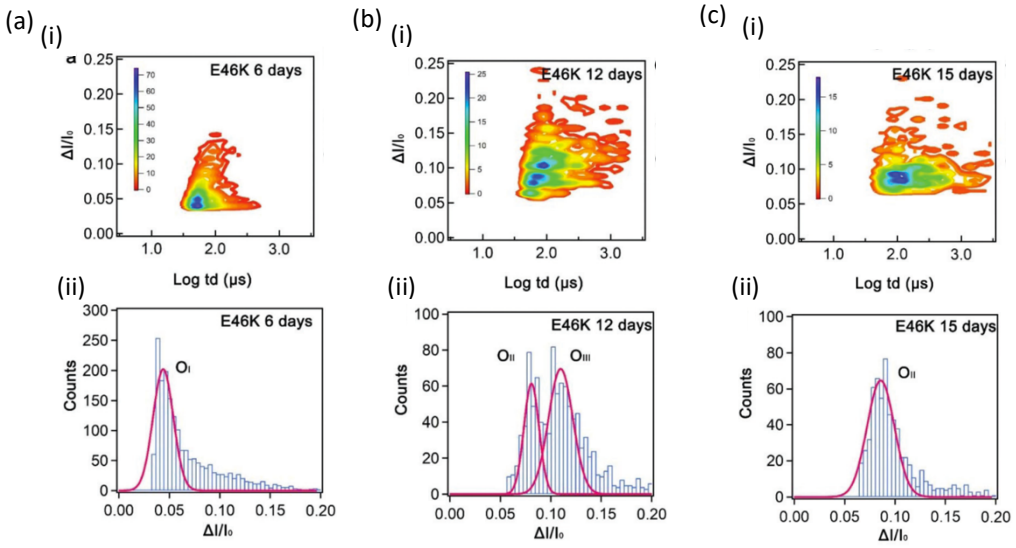


Figure 5. 7. *Colour contour plots of* $\Delta I/I_o$ *vs log td (μs)(i) and* $\Delta I/I_o$ histogram plots for E46K mutant oligomer aggregates at (a) 6 days, (b) 12 days and (c) 15 days. Figure adapted from reference 13.

Traces showed that mutant oligomer aggregates were detected at the earlier timepoints as compared with their WT counterparts in the order A30P > E46K > WT. In addition, analysis showed that aggregates included different oligomer subtypes which altered over time. The authors suggested that a likely aggregation mechanism involved the initial (day 6) generation of smaller (O_I) oligomers which in turn culminated in larger oligomer (O_{II} and O_{III}) aggregates by day 12. It was theorised that at day 15 the largest oligomer aggregates (O_{III}) had been converted into protofibrils (too large to fit through the pore) resulting in the O_{II} subtypes dominating.

In addition, the folding of the disorded alpha synuclein monomer has also been studied *in-situ* by alpha-hemolysin[14]. The pore size of alpha-hemolysin does not allow the passage of oligomeric aggregates, only allowing the passage of the disorded alpha synuclein monomer, whereby either translocation or capture occurs (Figure 5.8(a)). Figure 5.8(b) shows a characteristic event of alpha synuclein monomer translocation due to the application of voltage (100 mV). The open pore current (L_o) to capture current (L_c) transition can occur upon partial folding of the alpha synuclein monomer, while the Lc to blockade current (Lb) corresponds to further ordering of the alpha synuclein monomer. The capture of the alpha synuclein monomer could be reversed upon reduction of the applied voltage. For example, a reduction from 100 mV to 70 mV results in the L_b to L_c transition with a further reduction to 40 mV resulting in the L_c to L_o transition. Finally, figure 5.8c, showcases a dwell time vs peak current scatter plot for translocation events (TE) corresponding to the L_o to L_c transition and capture events (CE) corresponding to the L_c to L_b transition. TE events were more spread out and generally had shorter dwell times (ms to s) as well as longer amplitudes (20 pA to 80 pA), while CE events had longer dwell times (up to minutes) and smaller peak amplitudes (18 pA).

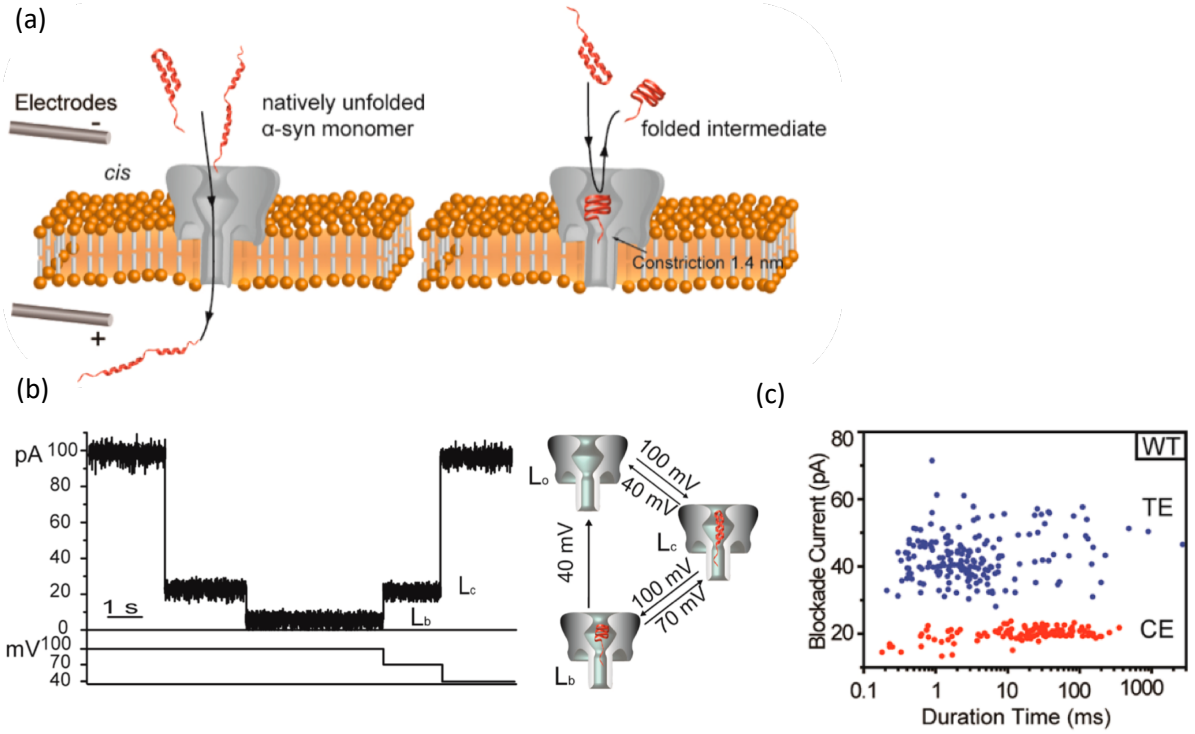


Figure 5. 8. *(a) A schematic showing the movement of alpha synuclein through the alpha-hemolysin pore. Unfolded alpha synuclein monomer (left) is allowed to freely translocate through the pore while a partially folded intermediate (right) is captured. (b) A characteristic event (left) alongside mechanism of capture for an alpha synuclein monomer within the vestibule of alpha-hemolysin. (1) Upon application of voltage (100 mV), a drop in the open pore current (L_o) is observed due to translocation of the unfolded alpha synuclein monomer. (2) The applied field can induce folding allowing capture (L_c). (3) Elongation/ordering of the alpha synuclein can result in a further current decrease (L_b). Capture can be reversed by reducing the applied voltage to 40 mV. (c) A dwell time vs peak current scatter plot shows two different event types. The translocation events (TE) corresponding to the L_o to L_c (blue scatter) are generally short-lived (ms to s) and have greater amplitudes (20-80 pA). Capture events (CE) corresponding to the Lc to Lb transition generally have small amplitude (18pA) and longer dwell times (up to minutes). Figure adapted from reference 14.*

5.3. Aim and challenges

In this chapter, alpha synuclein oligomers; the biomarkers of Parkinson's Disease were targeted for detection. While the challenges of protein (thrombin) detection have been elaborated on in the previous chapter, alpha synuclein oligomer detection utilising aptamer-based nanopipettes presented additional challenges. Alpha synuclein oligomers are highly challenging to detect due to their fragility (requiring use within two weeks) and high number of sub-types (various shapes and sizes) present at different ratios, depending on the extent of aggregation. In addition, the presence of pre-oligomer monomers and post oligomer fibrils requires aptamer binding to be selective. Finally, the TS-0530 aptamer used is not well characterised and it is unclear if it targeted a particular oligomer or binds a variety of oligomers with differing affinities. Findings from the previous chapter, showed that the analyte concentration was critical on the dwell time and was therefore initially optimised for the oligomer system. Finally, oligomers aggregated at different timepoints were detected, allowing for a binding profile to be formulated.

Aptamer-modified nanopipettes (using the 24mer anti-oligomer termed TS-0530) were constructed and characterised as previously described in chapter 2. Alpha synuclein monomer and the associated aggregation protocol can be additionally found in chapter 2.

5.4. Results

5.4.1. Concentration dependence

A concentration assay was initially used to characterise the aptamer modified sensor. This was necessary due to the lower binding affinity (kD = 68 nM) of the TS-0530 aptamer compared to that of TBA (kD = 0.5 nM). In addition, the larger size of the oligomer analyte in comparison to thrombin may be prone to aggregation at high concentrations . As shown in Figure 5.9, traces showed a concentration dependence (500 pM – 5nM) for oligomers aggregates formed after 8 hours as determined across the modification process (unmodified, silanised and TS-0530 modified) as well as controls (24mer control sequence and TS-0530 before the addition of oligomers). Traces were recorded with a scanning rate of 50 kHz with a low-pass filter of 5 kHz.

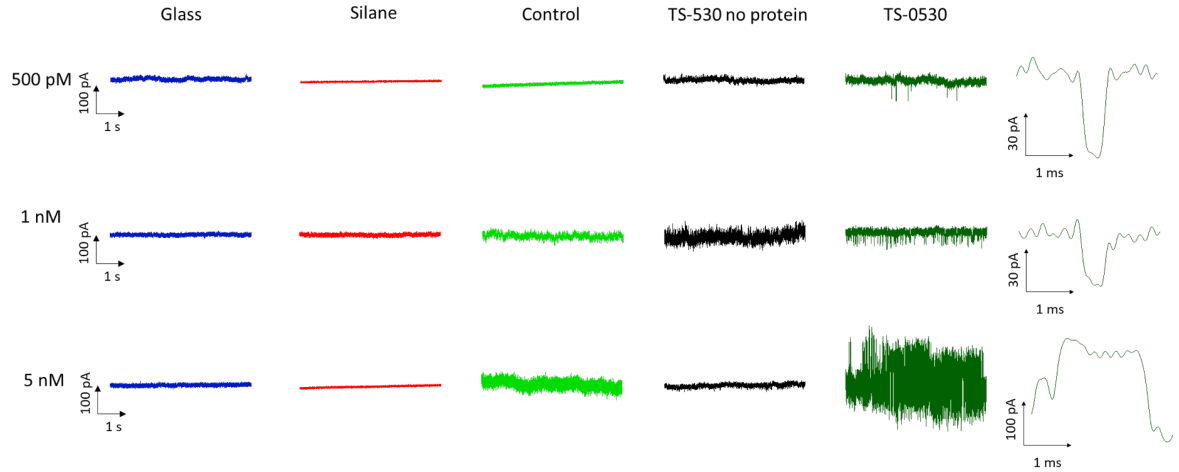


Figure 5. 9. *Traces (current (pA) over time (s)) alongside representative peaks at each stage of the modification process (unmodified, silanised and TS-0530 modified) alongside controls (random 24mer control sequence and TS-0530 before protein addition) over a concentration range (500 pM – 5 nM) for 8 h oligomers aggregates. A low pass filter of 5 kHz was used alongside a scanning rate of 50 kHz.*

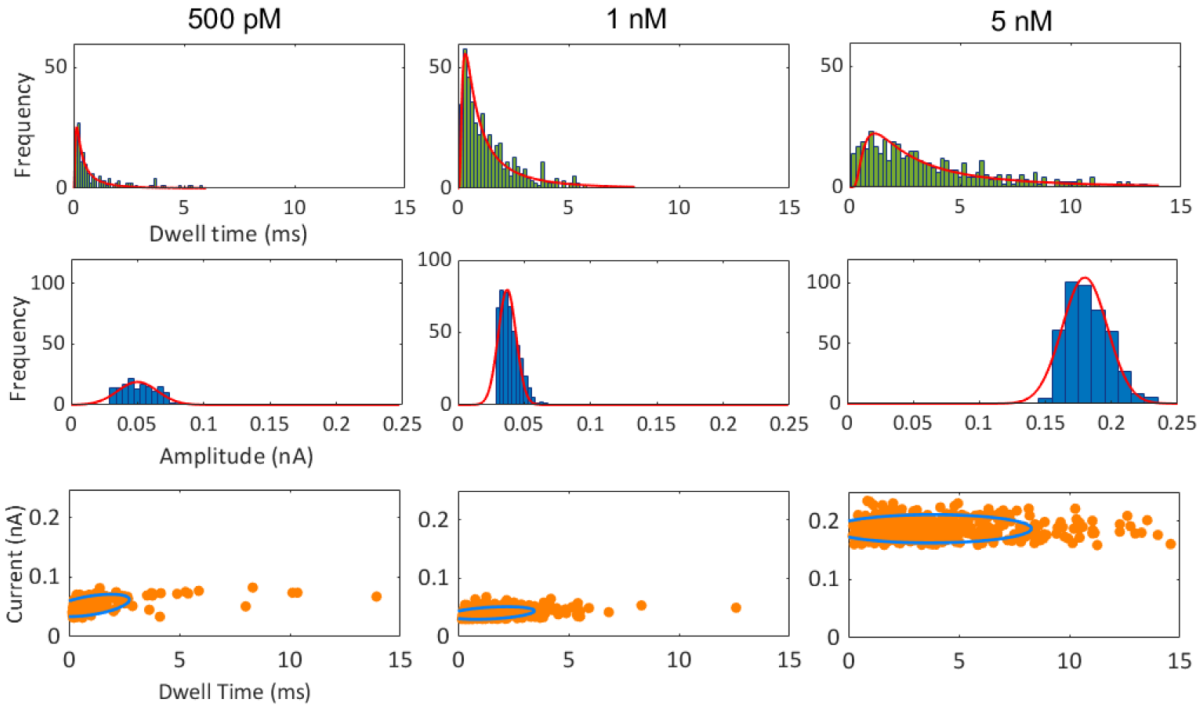


Figure 5. 10. *Histogram analysis of dwell time (top row), peak amplitude (middle row) alongside dwell time vs peak amplitude scatter plots (bottom row) for a concentration range (500 pM – 5 nM) of 8h oligomer aggregates. Number of events (N): N = 151 for 500 pM, N = 457 for 1 nM and N = 442 for 5 nM.*

Figure 5.10 shows the histogram analysis of dwell time (top row) and peak amplitude (medium row) alongside dwell time vs peak amplitude scatter plots (bottom row) for a concentration range (500 pM – 5nM) of 8h oligomer aggregates in TS-0530 modified nanopipettes. Further analyses including mean dwell time and normalised peak amplitude as well as capture rate are presented in table 5.1.

Table 5. 1. *Average values of normalised peak amplitude, dwell time and capture rate (n = 1)*

Concentration (nM)	Normalised peak amplitude (pA)	Dwell time (ms)	Capture rate (s^{-1})
0.5	55.76 ± 17	0.87	0.39
1	36.09 ± 6.6	1.74	11.79
5	162.42 ± 15	4.39	78.93

Overall, results show that dwell time, capture rate and the normalised peak amplitude (except the normalised peak amplitude at 1 nM) increased with oligomer aggregate concentration. In particular, 5 nM 8h oligomer aggregates were associated with very high values for all peak characteristics.

(i) Aggregation timepoint dependence

The concentration dependence showed that 1 nM was the optimal concentration for oligomer detection, allowing an aggregation timepoint assay to be carried out alongside the binding profile of the TS-0530 aptamer. In Figure 5.11, traces show a timepoint overview (0 – 16 h) recorded at 1 nM at different stages of nanopipette modification (unmodified, silanised and TS-0530 modified) alongside controls (24 mer control sequence and TS-0530 without analyte). Traces were recorded with a scanning rate of 50 kHz with a low-pass filter of 5 kHz.

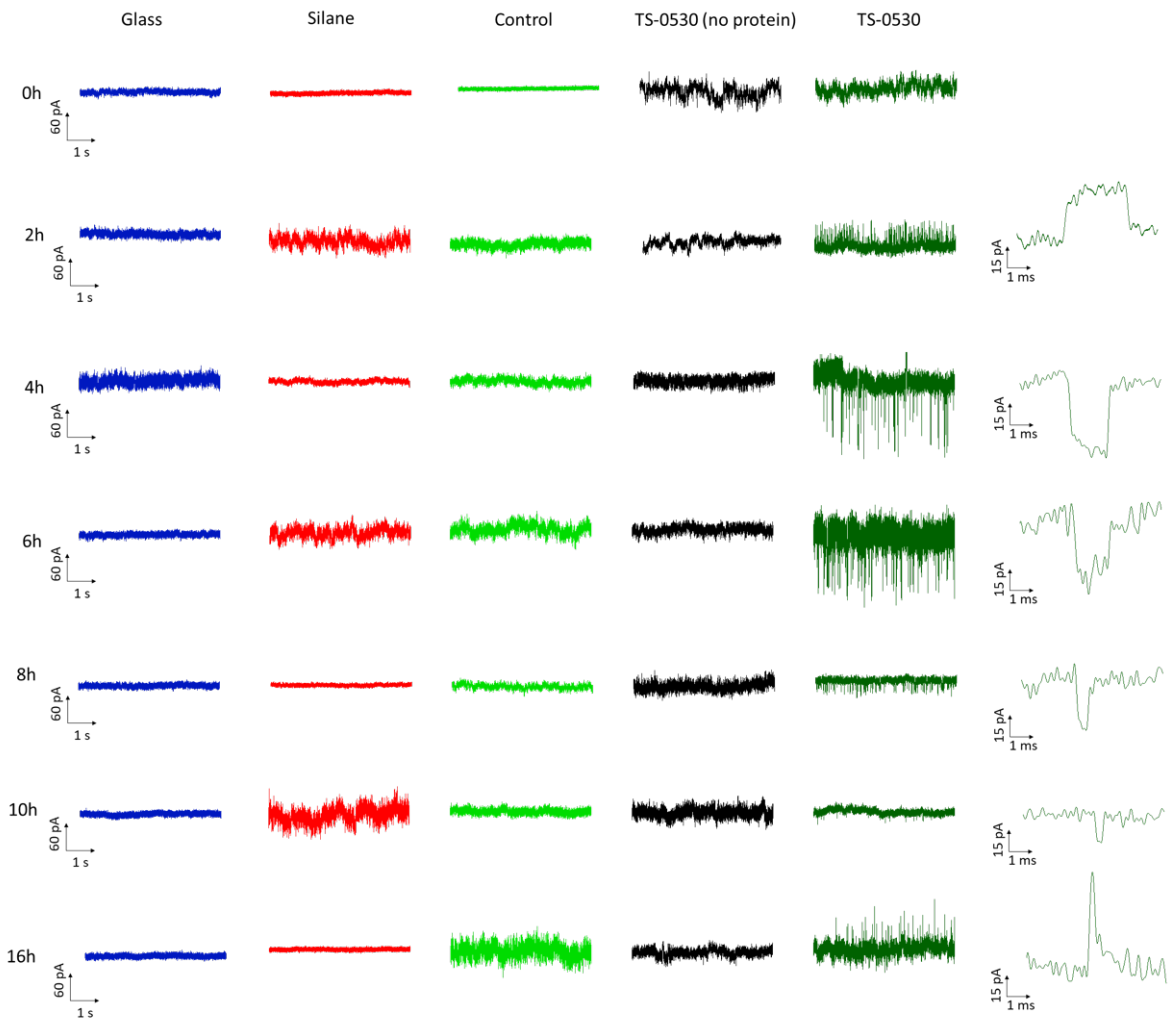


Figure 5. 11. *Traces (current (pA) over time (s)) alongside representative peaks at each stage of the modification process (unmodified, silanised and TS-0530 modified) alongside controls (random 24mer control sequence and TS-0530 before protein addition) over an aggregation timepoint range (0h – 16h). The oligomer concentration was 1 nM while a low-pass filter of 5 kHz was used alongside a scanning rate of 50 kHz.*

Figure 5.12(a) shows histogram analysis for dwell time (top row) and peak amplitude (middle row) as well as dwell time vs peak amplitude scatter plots (bottom row) for different oligomer aggregates (0 – 16 h) when translocated through nanopipettes modified with TS-0530. Further analysis is present in a plot of dwell time vs aggregation timepoint (Figure 12(b)) as well as Table 5.2 providing an overview of normalised peak amplitude and capture rate.

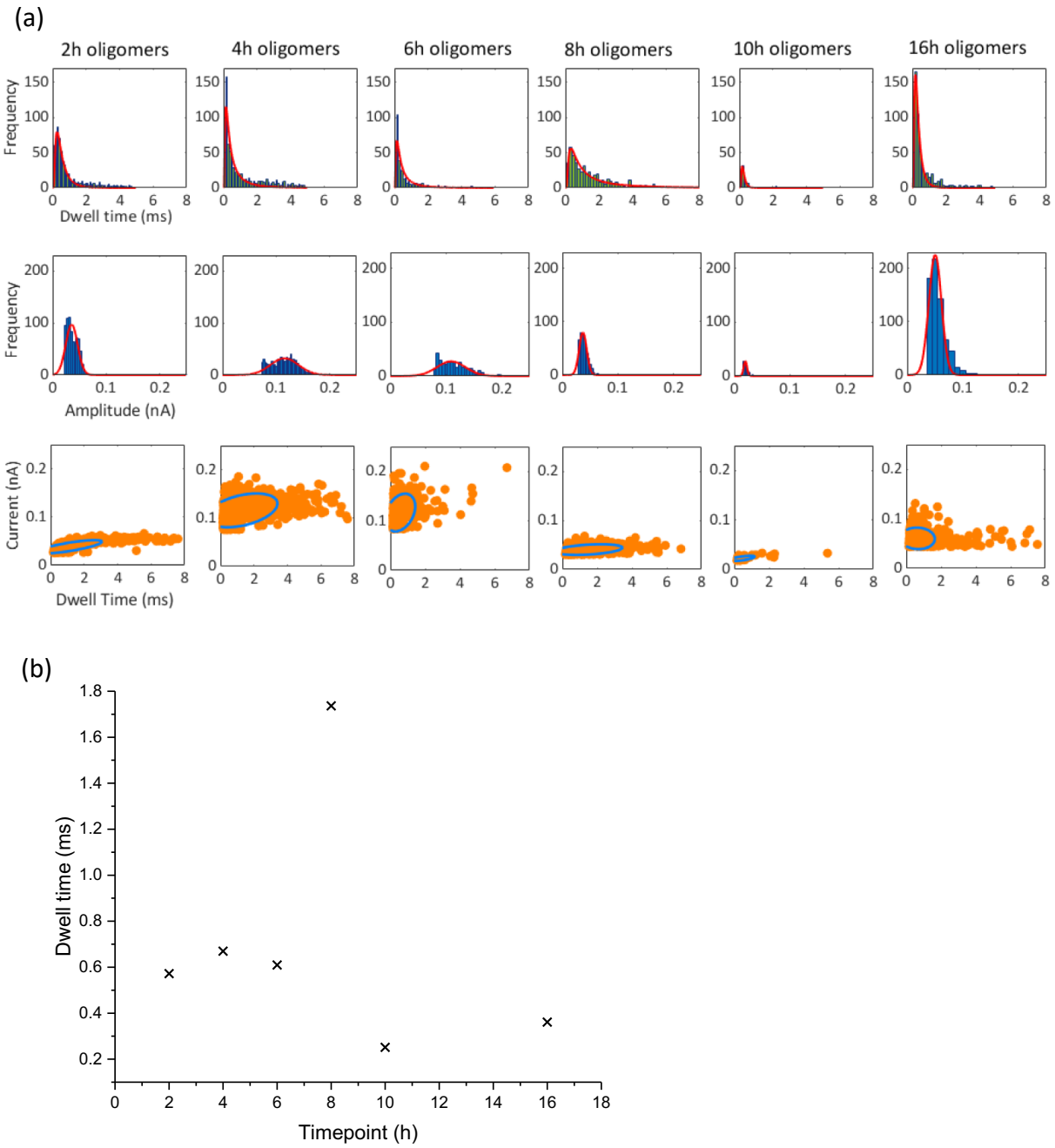


Figure 5. 12. *(a) Histogram analysis of dwell time (top row), peak amplitude (middle row) alongside dwell time vs peak amplitude scatter plots (bottom row) across an oligomer (1 nM) aggregate timepoint range (2 – 16 h). Number of events (N) are as follows. N = 739 for 2 hours, N = 814 for 4 hours, N = 348 for 6 hours, N = 457 for 8 hours, N = 88 for 10 hours and N = 681 for 16 hours. (b) A plot showing the dwell time of binding events as a function of the oligomer aggregation timepoint.*

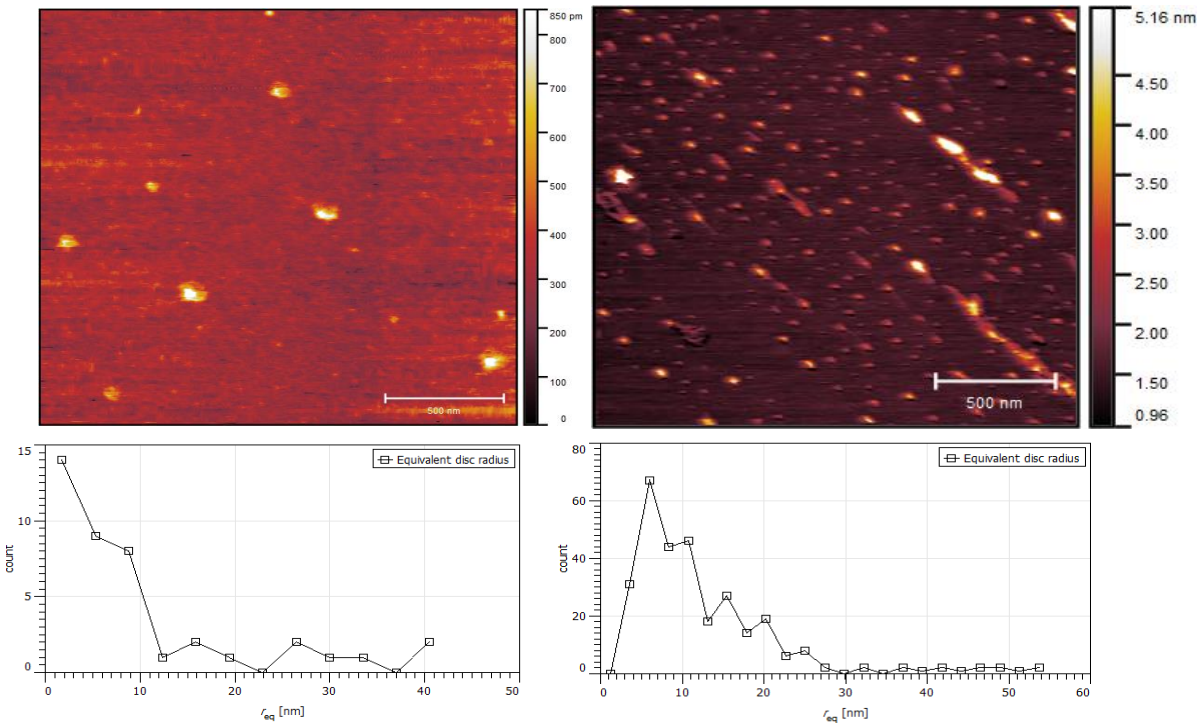
Table 5. 2. *The normalised peak amplitude and capture rate across the oligomer aggregation timepoint.*

Timepoint (h)	Normalised peak amplitude (pA)	Capture rate (s^{-1})
2	38.98 ± 12	36.51
4	85.90 ± 20	3.71
6	231.21 ± 54	15.99
8	50.63 ± 9.2	11.79
10	20.24 ± 3.1	1.47
16	54.13 ± 12	11.35

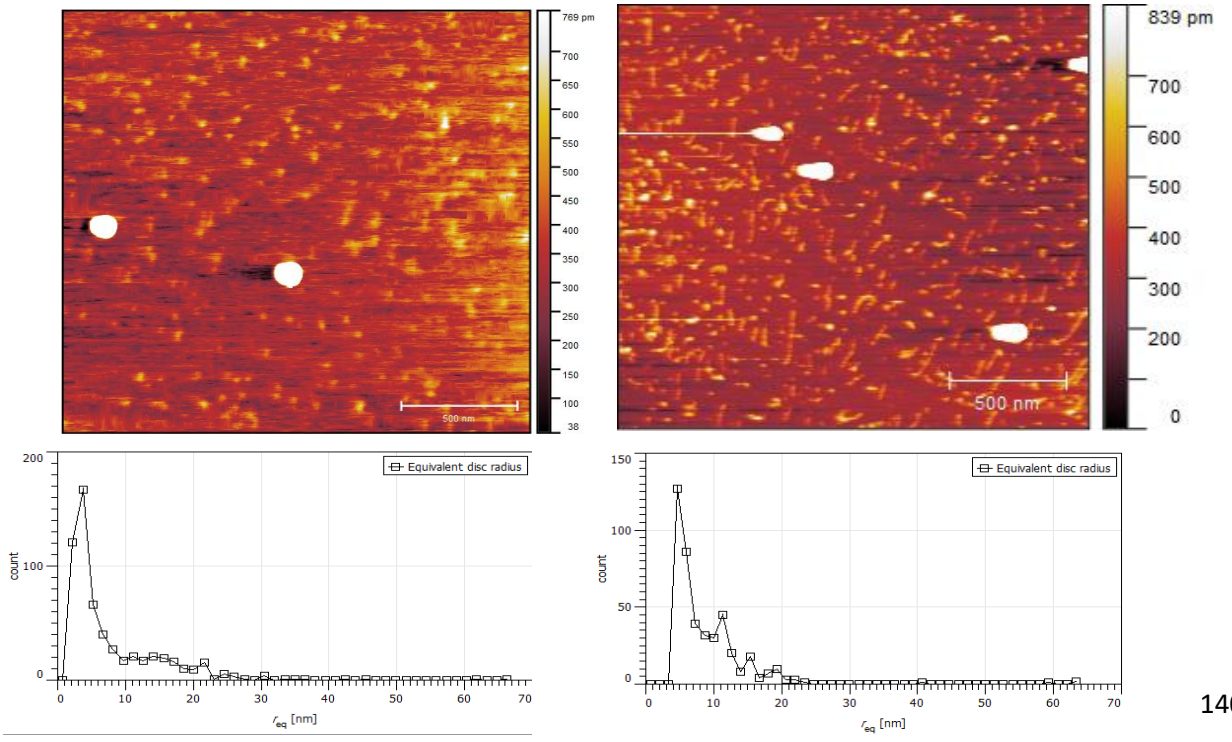
5.4.2. Oligomer AFM images

Atomic Force Microscopy (AFM) carried out by PhD student Giulia Campolo (Edel/Ivanov group) was used to characterise the radius of oligomers at different timepoints of the aggregation process as shown below in Figure 5.13. Higher concentrations were used at longer aggregation timepoints to compensate for the lower proportion of larger aggregates. As expected the radius of the oligomer increased as the aggregation timepoint increases.

2 h, 50 nM **4 h, 50 nM**



6 h, 500 nM **8 h, 500 nM**



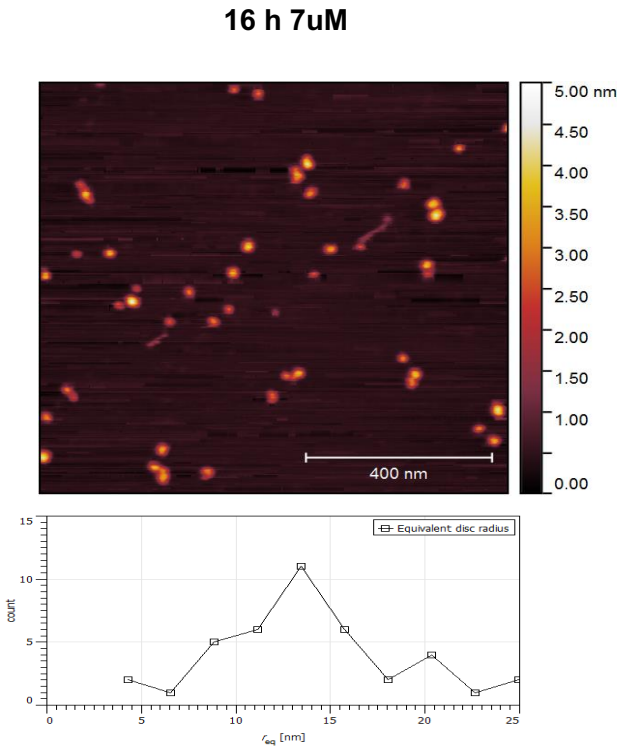


Figure 5. 13. *AFM images allowing determination of the oligomer radius at different stages of the aggregation process. Images courtesy of Imperial PhD student Giulia Campolo.*

5.5. Discussion

In this chapter, the detection of alpha synuclein oligomers; a functional biomarker of PD has been described. After determining the detection limits and optimal concentration, focus shifted to determining binding profiles at different oligomer aggregation timepoints.

The concentration profile based on 8h oligomer aggregates was vital in determining the optimal concentration for our modified sensor. 8h oligomers were chosen since their size (radius = 5-11 nm) gathered from AFM experiments were close to the dimensions of the nanopipette tip. While it was shown that oligomers at concentration of 500 pM and 1 nM showed translocations with similar dwell times, the capture rate was deemed too low in the former. Conversely, at 5 nM the large dwell times (> 4ms), high peak amplitudes and very high capture rate highly suggested that pore clogging and/or protein aggregation at the tip had occurred. Ultimately, 1 nM was chosen for subsequent studies due to its reliable capture rate without resulting in pore clogging.

Next, we looked at characterising alpha synuclein oligomers at different aggregation timepoints (hours). As before, specificity of our aptamer modified sensor was confirmed through comparison with various controls. The lack of translocation events using precursor modified nanopipettes (unmodified/silane) showed that recognition elements (aptamer)

was required for detection. Furthermore, in contrast to binding events seen with TS-0530 modified nanopipettes, the lack of translocation events with pipettes modified with a random 24mer showed that aptamer binding was the reason for events rather than by nucleotides simply slowing translocation. Meanwhile, the lack of binding events in TS-0530 modified pipettes without oligomers showed that events could not be attributed to movement of the bound aptamer within the pore. Finally the lack of binding events upon monomer translocation showed that specificity was retained for alpha synuclein oligomers

While dwell times remained largely consistent (0.7 ms) for aggregates formed between 2-6 hours, a large (1.7 ms) increase was seen with 8 hour aggregates which significantly decreased (< 0.4 ms) with the formation of larger aggregates formed at 10 and 16 hours. As seen in Figure 5.14, it is theorised that the TS-0530 aptamer preferentially binds to the large oligomeric species predominantly seen in the 8h sample, although is still able to bind to the smaller proportion of larger oligomers present in the 2-6 h samples. Conversely, oligomeric species seen in 10 h and 16 h samples are too big to translocate through the aptamer modified pipette, with only smaller oligomeric species passing through the sensor.

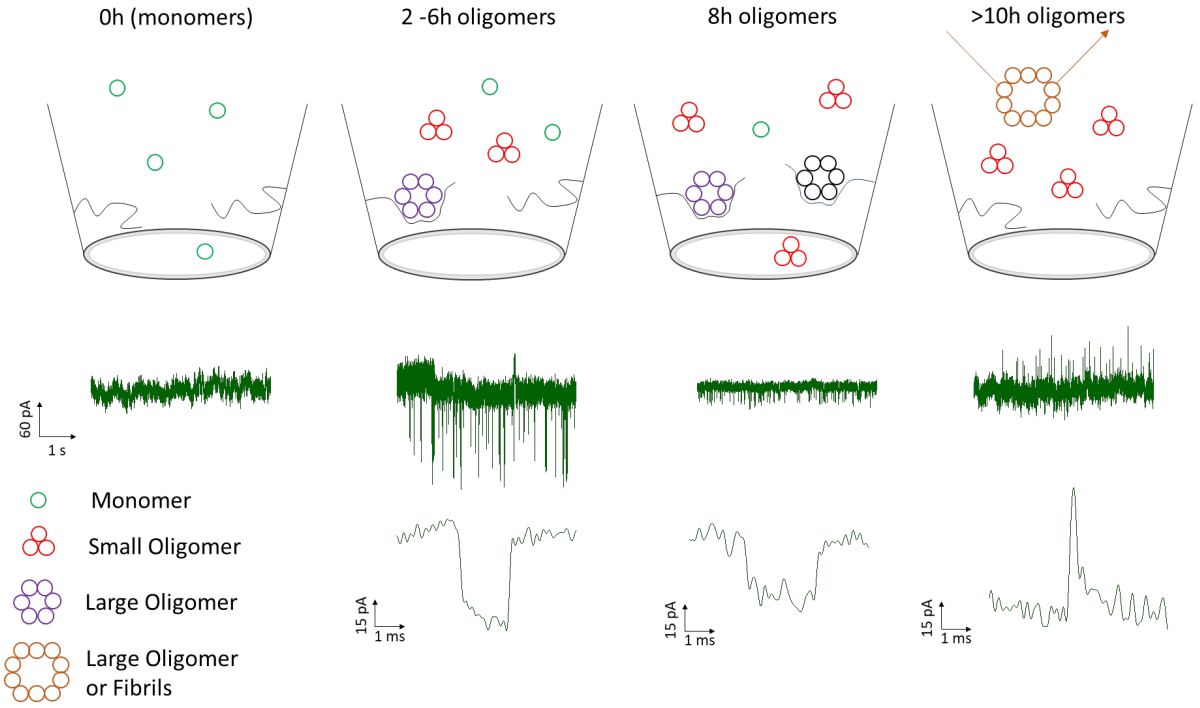


Figure 5. 14. *A schematic showing the dwell time magnitude as a response to the aggregation timepoint.*

The detection of alpha synuclein oligomers provides a fundamental step into the early detection of Parkinson's Disease. While ELISA-based detection shows high sensitivity (~200 pM) and selectivity, the set-up not only requires expensive antibodies but most importantly

due to the bulk measurement detection reveals limited information about the aggregation kinetics of alpha synuclein monomers. For example, ELISA cannot discriminate between different oligomer aggregates. Such discrimination could be critical in diagnosis allowing differentiation between patients with and without the disease. Conversely, while previous unmodified nanopore studies have been able to characterise oligomer subtypes and show aggregation kinetics dependant on the alpha synuclein mutant, the detection limit was not sensitive enough (450 nM) and required the production of large oligomer aggregates.

The sensor developed in the current project shows good detection limits (of 500 pM) while allowing detection of oligomers at a range of aggregation timepoints, showcasing that larger oligomers predominantly in the 8h sample were the likely preferred analyte. An additional benefit of the sensor is the ability to exclude unwanted aggregates (e.g fibrils) through size exclusion. In other words, by ensuring that the pore diameter is below that of the fibril size, one can prevent translocation and therefore false positive peaks while limiting associated noise. Downsides of the developed sensor alongside the relatively low functionalisation efficiency and dependence of dwell time for concentration characterisation (as described in the previous chapter) can be attributed to the limited characterisation of the TS-0530 aptamer. While findings support the original results that the aptamer predominantly binds to large oligomers formed after 8h due to longer average dwell times (1.7 ms) as compared with oligomers formed over 2- 6h (0.7 ms), further characterisation of binding specificity is critical. Future experiments will be more thoroughly detailed in the subsequent chapter but in brief follow-up experiments could include the following. More extensive binding assays of different oligomer aggregation timepoints could include ELONA analysis coupled with structural characterisation of oligomers including ß-sheet determination. Furthermore, *in-vivo* toxicity experiments could identify if the high-binding oligomeric species are indeed toxic. Furthermore, experiments using samples gathered from Parkinson Disease patients would allow the selectivity to be ascertained alongside whether *in-vitro* prepared oligomers are comparable to those found *in-vivo*.

5.6. Conclusion

After determining the optimum concentration for oligomer detection, the timepoint assay showed that the aptamer preferentially binds to larger oligomers predominantly found in the 8h oligomers. While our sensor proved to be too small for 10 h and 16 h oligomeric

samples and would likely need to be re-designed, this design principle could allow oligomer binding while preventing fibril translocation. In addition to increased selectivity, the introduction of the aptamer recognition element clearly provides benefits of increased sensitivity in comparison to detection using unmodified solid state nanopores. Furthermore, the developed sensor retains the sensitivity and selectivity of ELISA, with the added advantages of probing oligomer sub-types. Overall, the detection of alpha synuclein oligomers could pave way into their detection as part of multi-analyte samples and finally patient samples.

5.7. References

1 K. Tsukakoshi, K. Abe, K. Sode and K. Ikebukuro, *Anal. Chem.*, 2012, **84**, 5542–5547.

2 P. Werner, S. Klaus, M. T. Caroline, G. M. Halliday, P. Brundin, J. Volkmann, A.-E. Schrag and A. E. Lang, *Clin. Proc. Child. Hosp. Dist. Columbia*, 2017, **3**, 328–332.

3 W. Dauer and S. Przedborski, *Neuron*, 2003, **39**, 889–909.

4 P. Werner, S. Klaus, M. T. Caroline, G. M. Halliday, P. Brundin, J. Volkmann, A.-E. Schrag and A. E. Lang, *Clin. Proc. Child. Hosp. Dist. Columbia*, 2017, **3**, 328–332.

5 L. V. Kalia, S. K. Kalia, P. J. McLean, A. M. Lozano and A. E. Lang, *Ann. Neurol.*, 2013, **73**, 155–169.

6 H. A. Lashuel, C. R. Overk, A. Oueslati and E. Masliah, *Nat. Rev. Neurosci.*, 2012, **14**, 38–48.

7 M. M. Apetri, N. C. Maiti, M. G. Zagorski, P. R. Carey and V. E. Anderson, *J. Mol. Biol.*, 2006, **355**, 63–71.

8 L. Bousset, L. Pieri, G. Ruiz-Arlandis, J. Gath, P. H. Jensen, B. Habenstein, K. Madiona, V. Olieric, A. Böckmann, B. H. Meier and R. Melki, *Nat. Commun.*, , DOI:10.1038/ncomms3575.

9 K. A. Conway, S.-J. Lee, J.-C. Rochet, T. T. Ding, J. D. Harper, R. E. Williamson and P. T. Lansbury, *Ann. N. Y. Acad. Sci.*, 2006, **920**, 42–45.

10 K. A. Conway, S. J. Lee, J. C. Rochet, T. T. Ding, R. E. Williamson and P. T. Lansbury, *Proc. Natl. Acad. Sci. U. S. A.*, 2000, **97**, 571–576.

11 T. Tokuda, M. M. Qureshi, M. T. Ardah, S. Varghese, S. a Shehab, T. Kasai, N. Ishigami, a Tamaoka, M. Nakagawa and O. M. El-Agnaf, *Neurology*, 2010, **75**, 1766–1772.

12 O. M. A. El-Agnaf, S. A. Salem, K. E. Paleologou, M. D. Curran, M. J. Gibson, J. A. Court, M. G. Schlossmacher and D. Allsop, *FASEB J.*, 2006, **20**, 419–425.

13 X. Li, X. Tong, W. Lu, D. Yu, J. Diao and Q. Zhao, *Nanoscale*, 2019, **11**, 6480–6488.

14 H. Y. Wang, Z. Gu, C. Cao, J. Wang and Y. T. Long, *Anal. Chem.*, 2013, **85**, 8254–8261.

15 R. S. Burns, C. C. Chiueh, S. P. Markey, M. H. Ebert, D. M. Jacobowitz and I. J. Kopin, *Proc. Natl. Acad. Sci. U. S. A.*, 1983, **80**, 4546–4550.

16 N. G. Larsson, J. Wang, H. Wilhelmsson, A. Oldfors, P. Rustin, M. Lewandoski, G. S. Barsh and D. a Clayton, *Nat. Genet.*, 1998, **18**, 231–236.

17 J. J. Zarranz, J. Alegre, J. C. Gómez-Esteban, E. Lezcano, R. Ros, I. Ampuero, L. Vidal, J. Hoenicka, O. Rodriguez, B. Atarés, V. Llorens, E. Gomez Tortosa, T. Del Ser, D. G. Muñoz and J. G. De Yebenes, *Ann. Neurol.*, 2004, **55**, 164–173.

18 O. M. El-Agnaf, R. Jakes, M. D. Curran and A. Wallace, *FEBS Lett.*, 1998, **440**, 67–70.

19 A. B. Singleton, M. Farrer, J. Johnson, A. Singleton, S. Hague, J. Kachergus, M. Hulihan, T. Peuralinna, A. Dutra, R. Nussbaum, S. Lincoln, A. Crawley, M. Hanson, D. Maraganore, C. Adler, M. R. Cookson, M. Muenter, M. Baptista, D. Miller, J. Blancato, J. Hardy and K. Gwinn-Hardy, *Science.*, 2003, **302**, 841.

20 P. Ibáñez, A.-M. Bonnet, B. Débarges, E. Lohmann, F. Tison, Y. Agid, A. Dürr, A. Brice and P. Pollak, *Lancet*, 2004, **364**, 1169–1171.

21 A. Iwata, M. Maruyama, T. Akagi, T. Hashikawa, I. Kanazawa, S. Tsuji and N. Nukina, *Hum. Mol. Genet.*, 2003, **12**, 2625–2635.

22 M. Hashimoto, L. J. Hsu, Y. Xia, A. Takeda, A. Sisk, M. Sundsmo and E. Masliah, *Neuroreport*, 1999, **10**, 717–721.

23 K. E. Paleologou, A. Oueslati, G. Shakked, C. C. Rospigliosi, H. Y. Kim, G. R. Lamberto, C. O. Fernandez, A. Schmid, F. Chegini, W. P. Gai, D. Chiappe, M. Moniatte, B. L. Schneider, P. Aebischer, D. Eliezer, M. Zweckstetter, E. Masliah and H. A. Lashuel, *J. Neurosci.*, 2010, **30**, 3184–3198.

24 R. A. Barker, J. Drouin-Ouellet and M. Parmar, *Nat. Rev. Neurol.*, 2015, **11**, 492–503.

25 B. Fauvet, M. K. Mbefo, M. B. Fares, C. Desobry, S. Michael, M. T. Ardah, E. Tsika, P. Coune, M. Prudent, N. Lion, D. Eliezer, D. J. Moore, B. Schneider, P. Aebischer, O. M. El-Agnaf, E. Masliah and H. A. Lashuel, *J. Biol. Chem.*, 2012, **287**, 15345–15364.

26 N. Cremades, S. I. A. Cohen, E. Deas, A. Y. Abramov, A. Y. Chen, A. Orte, M. Sandal, R. W. Clarke, P. Dunne, F. A. Aprile, C. W. Bertoncini, N. W. Wood, T. P. J. Knowles, C. M. Dobson and D. Klenerman, *Cell*, 2012, **149**, 1048–1059.

27 K. M. Danzer, D. Haasen, A. R. Karow, S. Moussaud, M. Habeck, A. Giese, H. Kretzschmar, B. Hengerer and M. Kostka, *J. Neurosci.*, 2007, **27**, 9220–9232.

28 D. P. Hong, A. L. Fink and V. N. Uversky, *J. Mol. Biol.*, 2008, **383**, 214–223.

29 V. M. Nemani, W. Lu, V. Berge, K. Nakamura, B. Onoa, M. K. Lee, F. A. Chaudhry, R. A. Nicoll and R. H. Edwards, *Neuron*, 2010, **65**, 66–79.

30 D. E. Cabin, K. Shimazu, D. Murphy, N. B. Cole, W. Gottschalk, K. L. McIlwain, B. Orrison, A. Chen, C. E. Ellis, R. Paylor, B. Lu and R. L. Nussbaum, *J. Neurosci.*, 2002, **22**, 8797–807.

31 B. K. Choi, M. G. Choi, J. Y. Kim, Y. Yang, Y. Lai, D. H. Kweon, N. K. Lee and Y. K. Shin, *Proc. Natl. Acad. Sci. U. S. A.*, 2013, **110**, 4087–4092.

32 S. Hüls, T. Högen, N. Vassallo, K. M. Danzer, B. Hengerer, A. Giese and J. Herms, *J. Neurochem.*, 2011, **117**, 868–878.

Chapter 6: Conclusion

The final chapter of the thesis aims to present a summary of the PhD project, the results obtained and potential future experiments including further characterisation and optimisation studies. In particular, the results obtained are given context through comparison with other nanopore based detection techniques and other commonly used sensing technologies.

Nanopore sensors[1] have emerged as powerful diagnostic techniques for DNA detection and more recently sequencing; due to their high sensitivity, high throughput, and their ability to directly detect samples without labelling or preparation steps. Despite this, protein detection in unmodified nanopores is far more challenging due to the low detection limits encountered[2] (typically > μM), as well as the influence of electroosmosis[3] resulting in a more complicated translocation mechanism. In the case of unmodified nanosensors, such detection is not selective, limiting the ability to detect a specific protein biomarker in multi-complex protein samples. The ability to covalently attach recognition elements[4] (e.g aptamers) can improve both sensitivity and selectivity through the specific and high affinity detection of a given biomarker.

In chapter 3, it was shown that nanopipettes could be covalently modified with aptamers using a two-step protocol; encompassing a vapour silanisation step[5] followed by covalent attachment via thiol Michael addition[6]. The main benefits to the chosen functionalisation technique was the low cost and availability of reagents, the ability to limit the likelihood of polysilane formation via vapour deposition and the dual role of TCEP[7]; allowing it to act first as a reducing agent and then as a nucleophilic catalyst. Characterisation of the aptamer-based nanosensor was carried out *in-situ* using I/V curves and could be further confirmed through observation of the nanopore blocking (ionic current is effectively zero) upon translocation of nucleotide sequences complementary to TBA. A likely model of the aptamer modified pipette; could then be developed to aid in the design and binding mechanism of the detection.

In chapter 4, the model protein thrombin was detected using nanopipettes modified with TBA[8]. Thrombin was initially chosen due to its well characterised structure and the availability of a high affinity (kD = 0.5 nM) aptamer. It was shown that through implemented

controls that not only were recognition elements required for detection, but also that translocation events were due to specific protein binding and not due to the aptamer sequence non-specifically slowing down protein translocation or aptamer movement within the nanopore tip. A concentration-based assay showed a dependence on dwell time, whereby increased dwell time were observed at lower concentrations and conversely short dwell times were apparent at high concentrations. This observation could be explained by the high availability of aptamer sites present at low thrombin concentrations allowing binding and therefore events with long dwell times to occur. Conversely, at higher thrombin concentrations, aptamer sites are fully filled, thereby preventing further binding and only allowing translocation events with shorter dwell times to occur. Additionally, it was shown that specific detection could be carried out in a multi-analyte serum with similar binding dynamics to those conducted in electrolyte only, despite a loss in S:N. Such measurements are critical, paving way for the nanosensing technology to be used as a biosensor for protein biomarkers. Finally, it could be shown that the aptamer based nanosensor could be regenerated after thrombin detection, through washings with 1 x TE buffer. The ability to use a sensor multiple time not only increases throughput, but significantly reduces costs, allowing usage as a point of care device.

In chapter 5, it was shown that alpha synuclein oligomers could be detected using nanopipettes functionalised with an anti-oligomer aptamer (TS-0530)[9]. As for thrombin, a concentration assay was first employed to determine detection limits, whereby a concentration of 1 nM was found to give optimal detection without blocking the pore, as seen at higher concentrations (5nM). Importantly, an aggregation timepoint assay showed that the developed sensor relays single molecule information; allowing distinction between different oligomer sub-types. This could be seen through the observation that longer dwell times occurred with oligomers aggregated for 8 hours in comparison to oligomer aggregated at earlier timepoints. This highly suggests that more efficient binding was encountered for larger oligomers predominantly present in 8h samples, in comparison to the smaller aggregates present at earlier timepoints (2-6 hours). Conversely, samples aggregated for longer periods of time (10 and 16 hours), were of such a size (diameter = 26 nm for 16 hours) that they were unable to translocate through the nanopore (estimated to be 17 nm). While the lack of data corresponding to larger alpha synuclein oligomer aggregates was disappointing, the ability to discriminate aggregates based on size has the

potential to ease future analysis. In other words, the non-specific translocation events due to fibrils can be filtered out, preventing both nanopore clogging and simplifying data analysis.

The developed aptamer-functionalised sensor has clear benefits over unmodified sensors. Aptamer-based nanosensors have shown detection limits as low as 1 pM for thrombin, which is far greater than the detection limits observed in unmodified sensors (typically in the uM range). Additionally, after employment of low-pass filters, possible due to the long dwell times encountered, data was found to have a good SNR improvement (up to 3 fold).

An alternative set-up to aptamer functionalised nanopipettes is to detect proteins bound to DNA carriers via attached aptamers[10]. While this method can boast the use of a simple set-up achieving both sensitive (nM) and selective binding, the inherent indirect detection technique has associated drawbacks. Detection involves discriminating between carriers without bound proteins while ensuring that sub-peaks are due to protein binding and not false-positive peaks associated with DNA folding.

Sandwich-based ELISA[11] still remains the gold standard in the detection of biomarkers allowing direct label-free detection that has high sensitivity and high selectivity. While powerful, the technique requires analytes that possess two distinct epitopes and importantly does not relay single molecule information which is critical for biomarkers with distinct sub-types (e.g. alpha synuclein oligomers).

If time permitted, further characterisation of both the nanopipette modification and binding mechanism would have been employed. Fluorescent-based experiments are highly challenging to integrate with nanopore sensing, but could involve the translocation of fluorescently labelled thrombin through TBA-modified sensors, allowing binding to be followed in real time. Alternatively, the translocation of fluorescently labelled complementary sequences to TBA could allow detection based on electrical means (i.e blockade in ionic current) and optical (high intensity signal). While nanopore experiments are typically carried out in KCl, experiments could also have been carried out with alternative metals salts. For example, characterisation studies could be carried out in different salts which support G-quadruplex formation[12] (for example Na^+) to see whether binding dynamics could be optimised. Conversely, G-quadruplexes are unable to form in the presence of Li^+ ions, meaning the presence or lack thereof binding events would provide insight into the binding mechanism. Changes in the pH of the electrolyte could also prove

insightful; for example a decrease to pH 7.0 would give thrombin (pI = 7.4) a slight positive charge compared to the slight negative charge seen at pH 8.0. Since the charge on aptamer sequences would be (largely) unaffected (pKa close to zero), this change would allow us to better understand the effects of electroosmosis on protein binding.

Finally, after further characterisation of thrombin and oligomer detection, focus would shift to the highly specific and sensitive detection of other protein biomarkers. Switching between protein targets has been proven to be largely straightforward, allowing use of the same modification process, requiring only a change in the nucleotide sequence encoding the aptamer. A concentration based assay would then be employed to determine the optimal concentration range with likely factors including the binding affinity of the aptamer alongside the size of the protein analyte. Aptamers[13-16] with a high binding affinity (kD < 70 nM) and small size (<30 mers), similar to those used throughout the project have already been developed as shown in Table 6.1. While, commercially available ELISA kits are commonly available for detection of such biomarkers with high sensitivity and specificity, their high cost and time-consuming sample preparation limits their widespread use. Immunosensors can likewise achieve high sensitivity in protein biomarker detection. For example, an electrochemical-based immunosensor for tumour necrosis factor alpha (TNF-α)[17] was based on the $Ru(bpy)_3$ catalysed oxidation peak of guanine (G_{20}) strands. While such a method achieves excellent sensitivity, the method was not shown to have selective detection and is limited by its low throughput due to the need for washing steps. Alternatively, an anti-$VEGF_{121}$ aptamer attached to CdSe/ZnS quantum dots[18] had its chemiluminescence blocked by the partially complementary binding of a black-hole quencher. Upon introduction of the $VEGF_{121}$ analyte, aptamer binding occurs, preventing the attachment of the quencher to the aptamer in turn allowing chemiluminescence to occur. Such a sensing strategy allows use of a simple detection system and good detection limits. However, the reported signal change was low at 1 nM VEGF and such detection was only carried out in buffer.

Table 6. 1. *An overview of protein biomarkers and their associated aptamers.*

Protein Biomarker	Aptamer length (number of nucleotides)	Dissociation constant kD (nM)	Relevant disease	Current detection method and detection range
Vascular endothelial growth factor ($VEGF_{121}$)[13]	25	1.1	Cancer	ELISA (15.6-1000 pg/ml) Optical Aptasensor[18] (nM range)
Aflatoxin M1[14]	21	0.0182	Hepatocellular carcinoma, aflatoxicosis	ELISA (5 – 135 ppt) Electrochemical immunosensor 0.01 ppb
Tumour necrosis factor alpha (TNF-α)[15]	26	7	Inflammatory diseases	ELISA (3.16-1000 pg/ml) Immunoassay (2 pM)[17]
C-kit/CD 117[16]	29	12.21	Cancer	ELISA (45-10000 pg/ml)

While selectivity based measurements were shown to be successful for thrombin detection, paving their way as a biosensor of MS; similar experiments were not conducted for alpha synuclein oligomers due to time constraints. While alpha synuclein oligomer detection proved highly promising with results showing excellent S:N alongside the high affinity of specific oligomer sub-types, additional experiments would be required before testing samples of patient with PD. In particular, more extensive binding assays of different oligomer aggregation timepoints could include ELONA analysis coupled with structural characterisation of oligomers including ß-sheet determination. This would help to indicate the specific oligomer sub-type targeted by the anti-oligomer aptamer. Furthermore, coupling with *in-vivo* toxicity experiments would identify if the high-binding oligomeric species were indeed toxic as currently proposed. Finally, experiments using samples gathered from Parkinson Disease patients would allow the selectivity to be ascertained alongside whether *in-vitro* prepared oligomers are comparable to those found *in-vivo*.

There are several optimisation steps that could be implemented to improve aptamer functionalisation. While current variability (different tip diameters/shapes) in nanopipette production is an underlying problem, a bigger problem of functionalised nanopores is likely

due to the variability in aptamer binding in term of density and position. It is highly likely that the aptamer density and location differs between pipettes giving rise to binding events with different amplitudes as well as different capture rates. For example, through computer modelling, Rant[4] showed that the receptors positioned closer to the nanopore tip (Figure 6.1) experience a higher applied voltage and thereby have an increased dissociation constant (K_{off}).

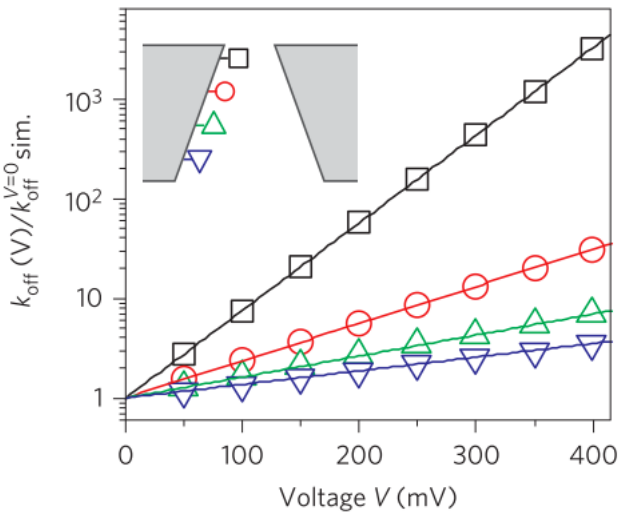


Figure 6. 1. *The dissociation constant as a function of voltage at different distances away from the nanopore tip. Inset z_1 = 5.5 nm (black circles), z_2 = 25.5 nm (red circles), z_3 = 45.5 nm (green triangles) and z_4 = 65.5 nm (inverted blue triangles).*

In addition, the functionalisation efficiency for the bioconjugation step is low. While the reasons for such low efficiencies are unclear, possible explanations include steric limitations due to the formations of poly-silane layers occurring thereby preventing aptamer attachment as the tip of the nanopore. Different ratios of reagents alongside different reaction conditions could be employed to increase the effectiveness of aptamer attachment or entire new methodologies could be implemented. In addition, methods to precisely and reliably localise aptamers at the nanopore tip would be explored, allowing greater repeatability between modified nanosensors. Optimisation of the pore diameter allowing the translocation of smaller oligomer aggregates and not larger fibrils would also be considered. As such, a timepoint assay using AFM measurements would be carried out to discriminate between oligomer and fibrils, in turn allowing the pore size to be tailored as required.

Overall, despite difficulties in fabrication and testing the developed nanosensor not only confirms the proof of concept but holds numerous advantages allowing for its potential to be used as a point of care medical device. The developed sensor maintains regenerative, label-free and direct sensing that is also highly sensitive and selective, while providing critical single molecule based information for biomarkers with diverse structures. After additional optimisation, characterisation and validation studies detection based on the combination of aptamers and nanosensors could result in a powerful sensing tool for clinicians and the medical industry.

6.1. References

1 M. Wanunu, *Phys. Life Rev.*, 2012, **9**, 125–158.

2 C. Plesa, S. W. Kowalczyk, R. Zinsmeester, A. Y. Grosberg, Y. Rabin and C. Dekker, *Nano Lett.*, 2013, **13**, 658–663.

3 M. Firnkes, D. Pedone, J. Knezevic, M. Döblinger and U. Rant, *Nano Lett.*, 2010, **10**, 2162–2167.

4 R. Wei, V. Gatterdam, R. Wieneke, R. Tampé and U. Rant, *Nat. Nanotechnol.*, 2012, **7**, 257–263.

5 A. R. Yadav, R. Sriram, J. A. Carter and B. L. Miller, *Mater. Sci. Eng. C*, 2014, **35**, 283–290.

6 G. Z. Li, R. K. Randev, A. H. Soeriyadi, G. Rees, C. Boyer, Z. Tong, T. P. Davis, C. R. Becer and D. M. Haddleton, *Polym. Chem.*, 2010, **1**, 1196–1204.

7 M. W. Jones, G. Mantovani, S. M. Ryan, X. Wang, D. J. Brayden and D. M. Haddleton, *Chem. Commun.*, 2009, 5272–5274.

8 D. M. Tasset, M. F. Kubik and W. Steiner, *J. Mol. Biol.*, 1997, **272**, 688–698.

9 K. Tsukakoshi, K. Abe, K. Sode and K. Ikebukuro, *Anal. Chem.*, 2012, **84**, 5542–5547.

10 J. Y. Y. Sze, A. P. Ivanov, A. E. G. Cass and J. B. Edel, *Nat. Commun.*, 2017, **8**, 1–10.

11 T. Tokuda, M. M. Qureshi, M. T. Ardah, S. Varghese, S. a Shehab, T. Kasai, N. Ishigami, a Tamaoka, M. Nakagawa and O. M. El-Agnaf, *Neurology*, 2010, **75**, 1766–1772.

12 S. Burge, G. N. Parkinson, P. Hazel, A. K. Todd and S. Neidle, *Nucleic Acids Res.*, 2006, **34**, 5402–5415.

13 Y. Nonaka, K. Sode and K. Ikebukuro, *Molecules*, 2010, **15**, 215–225.

14 B. H. Nguyen, L. D. Tran, Q. P. Do, H. Le Nguyen, N. H. Tran and P. X. Nguyen, *Mater. Sci. Eng. C*, 2013, **33**, 2229–2234.

15 E. W. Orava, N. Jarvik, Y. L. Shek, S. S. Sidhu and J. Gariépy, *ACS Chem. Biol.*, 2013, **8**, 170–178.

16 S. Meyer, J. P. Maufort, J. Nie, R. Stewart, B. E. McIntosh, L. R. Conti, K. M. Ahmad, H. T. Soh and J. A. Thomson, *PLoS One*, 2013, **8**, 9–14.

17 J. Wang, G. Liu, M. H. Engelhard and Y. Lin, *Anal. Chem.*, 2006, **78**, 6974–6979.

18 R. Freeman, J. Girsh, A. Fang-Ju Jou, J. A. A. Ho, T. Hug, J. Dernedde and I. Willner, *Anal. Chem.*, 2012, **84**, 6192–6198.

Appendices

Summary of permissions for third party copyright works.

Figure 1.3



ACS Publications
Most Trusted. Most Cited. Most Read.

Fast Flow Microfluidics and Single-Molecule Fluorescence for the Rapid Characterization of α-Synuclein Oligomers

Author: Mathew H. Horrocks, Laura Tosatto, Alexander J. Dear, et al
Publication: Analytical Chemistry
Publisher: American Chemical Society
Date: Sep 1, 2015

Copyright © 2015, American Chemical Society

PERMISSION/LICENSE IS GRANTED FOR YOUR ORDER AT NO CHARGE

This type of permission/license, instead of the standard Terms & Conditions, is sent to you because no fee is being charged for your order. Please note the following:

- Permission is granted for your request in both print and electronic formats, and translations.
- If figures and/or tables were requested, they may be adapted or used in part.
- Please print this page for your records and send a copy of it to your publisher/graduate school.
- Appropriate credit for the requested material should be given as follows: "Reprinted (adapted) with permission from (COMPLETE REFERENCE CITATION). Copyright (YEAR) American Chemical Society." Insert appropriate information in place of the capitalized words.
- One-time permission is granted only for the use specified in your request. No additional uses are granted (such as derivative works or other editions). For any other uses, please submit a new request.

If credit is given to another source for the material you requested, permission must be obtained from that source.

BACK CLOSE WINDOW

Figure 1.4

License Number	4837270369580
License date	May 27, 2020
Licensed Content Publisher	The American Association for the Advancement of Science
Licensed Content Publication	Science
Licensed Content Title	Structure of Staphylococcal α-Hemolysin, a Heptameric Transmembrane Pore
Licensed Content Author	Langzhou Song,Michael R. Hobaugh,Christopher Shustak,Stephen Cheley,Hagan Bayley,J. Eric Gouaux
Licensed Content Date	Dec 13, 1996
Licensed Content Volume	274
Licensed Content Issue	5294
Type of Use	Thesis / Dissertation
Requestor type	Scientist/individual at a research institution
Format	Print and electronic
Portion	Figure
Number of figures/tables	1
Title	The highly sensitive and selective detection of protein biomarkers using aptamer-based nanopores
Institution name	Imperial College
Expected presentation date	Jul 2020
Portions	Figure 2

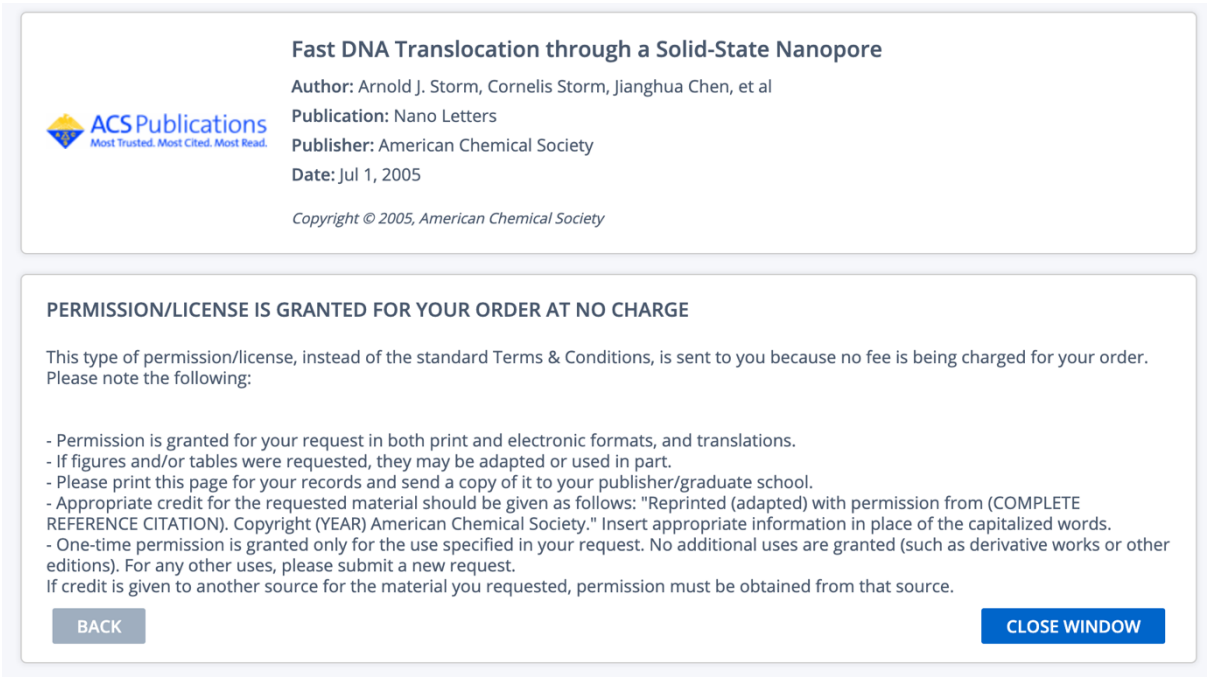
Figure 1.5

License Number	4837140156940
License date	May 27, 2020
Licensed Content Publisher	Springer Nature
Licensed Content Publication	Nature Materials
Licensed Content Title	Fabrication of solid-state nanopores with single-nanometre precision
Licensed Content Author	A. J. Storm et al
Licensed Content Date	Jul 13, 2003
Type of Use	Thesis/Dissertation
Requestor type	academic/university or research institute
Format	print and electronic
Portion	figures/tables/illustrations
Number of figures/tables/illustrations	4
High-res required	no
Will you be translating?	no
Circulation/distribution	1 - 29
Author of this Springer Nature content	no
Title	The detection of protein biomarkers using aptamer-based nanopores
Institution name	Imperial College
Expected presentation date	Jul 2020
Portions	Figure 1

Figure 1.6

License Number	4837151406006
License date	May 27, 2020
Licensed Content Publisher	Springer Nature
Licensed Content Publication	Nature Nanotechnology
Licensed Content Title	Hybrid pore formation by directed insertion of α-haemolysin into solid-state nanopores
Licensed Content Author	Adam R. Hall et al
Licensed Content Date	Nov 28, 2010
Type of Use	Thesis/Dissertation
Requestor type	academic/university or research institute
Format	print and electronic
Portion	figures/tables/illustrations
Number of figures/tables/illustrations	1
High-res required	no
Will you be translating?	no
Circulation/distribution	1 - 29
Author of this Springer Nature content	no
Title	The detection of protein biomarkers using aptamer-based nanopores
Institution name	Imperial College
Expected presentation date	Jul 2020
Portions	Figure 1

Figure 1.10



Fast DNA Translocation through a Solid-State Nanopore

Author: Arnold J. Storm, Cornelis Storm, Jianghua Chen, et al
Publication: Nano Letters
Publisher: American Chemical Society
Date: Jul 1, 2005

Copyright © 2005, American Chemical Society

PERMISSION/LICENSE IS GRANTED FOR YOUR ORDER AT NO CHARGE

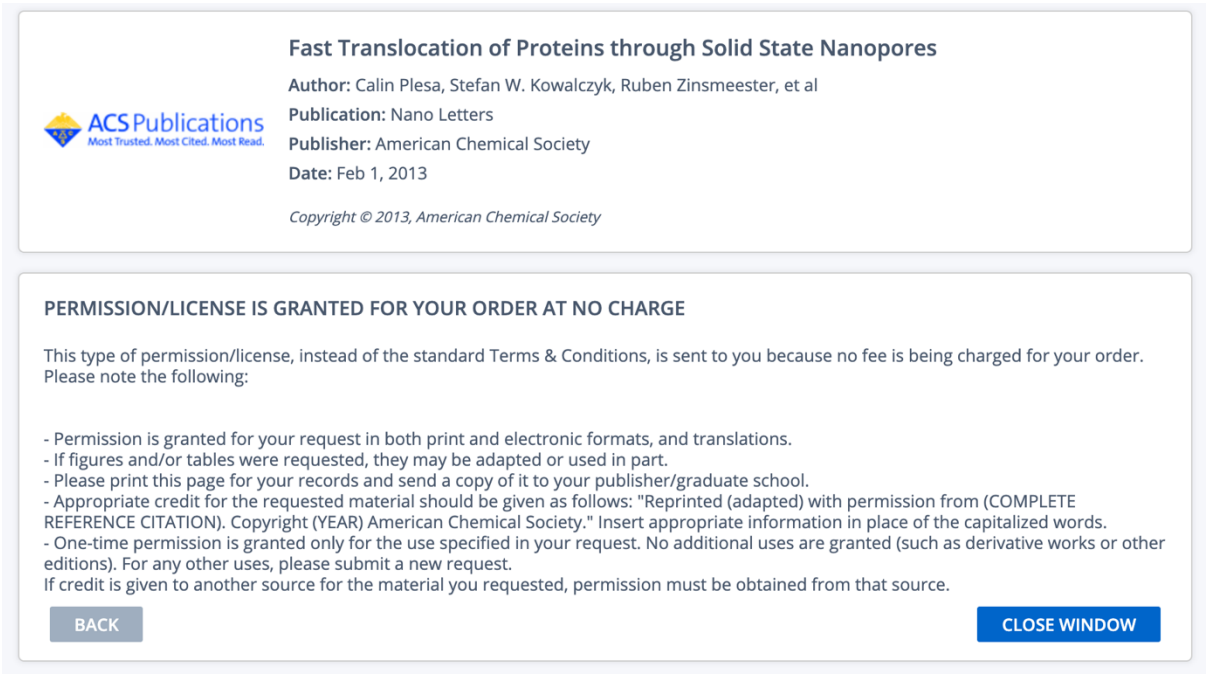
This type of permission/license, instead of the standard Terms & Conditions, is sent to you because no fee is being charged for your order. Please note the following:

- Permission is granted for your request in both print and electronic formats, and translations.
- If figures and/or tables were requested, they may be adapted or used in part.
- Please print this page for your records and send a copy of it to your publisher/graduate school.
- Appropriate credit for the requested material should be given as follows: "Reprinted (adapted) with permission from (COMPLETE REFERENCE CITATION). Copyright (YEAR) American Chemical Society." Insert appropriate information in place of the capitalized words.
- One-time permission is granted only for the use specified in your request. No additional uses are granted (such as derivative works or other editions). For any other uses, please submit a new request.

If credit is given to another source for the material you requested, permission must be obtained from that source.

BACK CLOSE WINDOW

Figure 1.14



Fast Translocation of Proteins through Solid State Nanopores

Author: Calin Plesa, Stefan W. Kowalczyk, Ruben Zinsmeester, et al
Publication: Nano Letters
Publisher: American Chemical Society
Date: Feb 1, 2013

Copyright © 2013, American Chemical Society

PERMISSION/LICENSE IS GRANTED FOR YOUR ORDER AT NO CHARGE

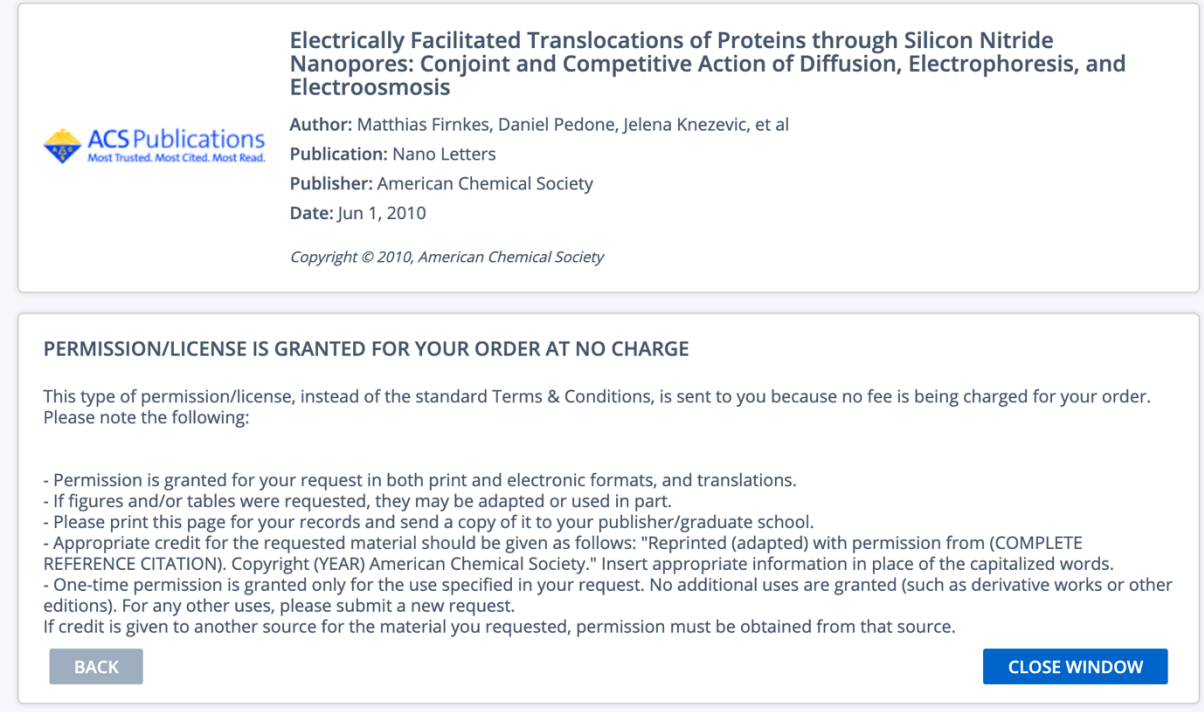
This type of permission/license, instead of the standard Terms & Conditions, is sent to you because no fee is being charged for your order. Please note the following:

- Permission is granted for your request in both print and electronic formats, and translations.
- If figures and/or tables were requested, they may be adapted or used in part.
- Please print this page for your records and send a copy of it to your publisher/graduate school.
- Appropriate credit for the requested material should be given as follows: "Reprinted (adapted) with permission from (COMPLETE REFERENCE CITATION). Copyright (YEAR) American Chemical Society." Insert appropriate information in place of the capitalized words.
- One-time permission is granted only for the use specified in your request. No additional uses are granted (such as derivative works or other editions). For any other uses, please submit a new request.

If credit is given to another source for the material you requested, permission must be obtained from that source.

BACK CLOSE WINDOW

Figure 1.16



ACS Publications
Most Trusted. Most Cited. Most Read.

Electrically Facilitated Translocations of Proteins through Silicon Nitride Nanopores: Conjoint and Competitive Action of Diffusion, Electrophoresis, and Electroosmosis

Author: Matthias Firnkes, Daniel Pedone, Jelena Knezevic, et al
Publication: Nano Letters
Publisher: American Chemical Society
Date: Jun 1, 2010

Copyright © 2010, American Chemical Society

PERMISSION/LICENSE IS GRANTED FOR YOUR ORDER AT NO CHARGE

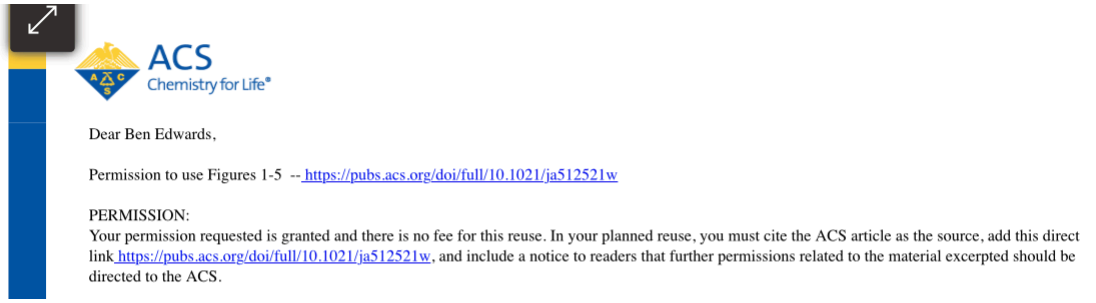
This type of permission/license, instead of the standard Terms & Conditions, is sent to you because no fee is being charged for your order. Please note the following:

- Permission is granted for your request in both print and electronic formats, and translations.
- If figures and/or tables were requested, they may be adapted or used in part.
- Please print this page for your records and send a copy of it to your publisher/graduate school.
- Appropriate credit for the requested material should be given as follows: "Reprinted (adapted) with permission from (COMPLETE REFERENCE CITATION). Copyright (YEAR) American Chemical Society." Insert appropriate information in place of the capitalized words.
- One-time permission is granted only for the use specified in your request. No additional uses are granted (such as derivative works or other editions). For any other uses, please submit a new request.

If credit is given to another source for the material you requested, permission must be obtained from that source.

BACK CLOSE WINDOW

Figure 1.21



ACS Chemistry for Life®

Dear Ben Edwards,

Permission to use Figures 1-5 -- https://pubs.acs.org/doi/full/10.1021/ja512521w

PERMISSION:
Your permission requested is granted and there is no fee for this reuse. In your planned reuse, you must cite the ACS article as the source, add this direct link https://pubs.acs.org/doi/full/10.1021/ja512521w, and include a notice to readers that further permissions related to the material excerpted should be directed to the ACS.

Figure 1.24

License Number	4837170340524
License date	May 27, 2020
Licensed Content Publisher	Springer Nature
Licensed Content Publication	Nature Nanotechnology
Licensed Content Title	Controlling protein translocation through nanopores with bio-inspired fluid walls
Licensed Content Author	Erik C. Yusko et al
Licensed Content Date	Feb 20, 2011
Type of Use	Thesis/Dissertation
Requestor type	academic/university or research institute
Format	print and electronic
Portion	figures/tables/illustrations
Number of figures/tables/illustrations	1
High-res required	no
Will you be translating?	no
Circulation/distribution	1 - 29
Author of this Springer Nature content	no
Title	The detection of protein biomarkers using aptamer-based nanopores
Institution name	Imperial College
Expected presentation date	Jul 2020
Portions	Figure 2

Figure 1.25

License Number	4837691412440
License date	May 28, 2020
Licensed Content Publisher	Springer Nature
Licensed Content Publication	Nature Nanotechnology
Licensed Content Title	Stochastic sensing of proteins with receptor-modified solid-state nanopores
Licensed Content Author	Ruoshan Wei et al
Licensed Content Date	Mar 11, 2012
Type of Use	Thesis/Dissertation
Requestor type	non-commercial (non-profit)
Format	print and electronic
Portion	figures/tables/illustrations
Number of figures/tables/illustrations	3
High-res required	no
Will you be translating?	no
Circulation/distribution	1 - 29
Author of this Springer Nature content	no
Title	The highly sensitive and selective detection of protein biomarkers using aptamer-based nanopores
Institution name	Imperial College
Expected presentation date	Jul 2020
Portions	Figure 1 Figure 3 Figure 4

Figure 1.26

Permission to use Figure 3 -- https://pubs.acs.org/doi/full/10.1021/ja2105653

PERMISSION:
Your permission requested is granted and there is no fee for this reuse. In your planned reuse, you must cite the ACS article as the source, add this direct link https://pubs.acs.org/doi/full/10.1021/ja2105653, and include a notice to readers that further permissions related to the material excerpted should be directed to the ACS.

If you need further assistance, please let me know.

Sincerely,

Raquel Picar-Simpson
ACS Publications Support
Customer Services & Information
Website: https://help.acs.org/

Figure 1.27(a)

License Number	4837171178672
License date	May 27, 2020
Licensed Content Publisher	Elsevier
Licensed Content Publication	Biosensors and Bioelectronics
Licensed Content Title	Reversible thrombin detection by aptamer functionalized STING sensors
Licensed Content Author	Paolo Actis,Adam Rogers,Jeff Nivala,Boaz Vilozny,R. Adam Seger,Olufisayo Jejelowo,Nader Pourmand
Licensed Content Date	Jul 15, 2011
Licensed Content Volume	26
Licensed Content Issue	11
Licensed Content Pages	5
Type of Use	reuse in a thesis/dissertation
Portion	figures/tables/illustrations
Number of figures/tables/illustrations	2
Format	both print and electronic
Are you the author of this Elsevier article?	No
Will you be translating?	No
Title	The detection of protein biomarkers using aptamer-based nanopores
Institution name	Imperial College
Expected presentation date	Jul 2020
Portions	Figure 2 Figure 3

Figure 1.27(b)



ACS Publications
Most Trusted. Most Cited. Most Read.

Capturing Single Molecules of Immunoglobulin and Ricin with an Aptamer-Encoded Glass Nanopore

Author: Shu Ding, Changlu Gao, Li-Qun Gu
Publication: Analytical Chemistry
Publisher: American Chemical Society
Date: Aug 1, 2009

Copyright © 2009, American Chemical Society

PERMISSION/LICENSE IS GRANTED FOR YOUR ORDER AT NO CHARGE

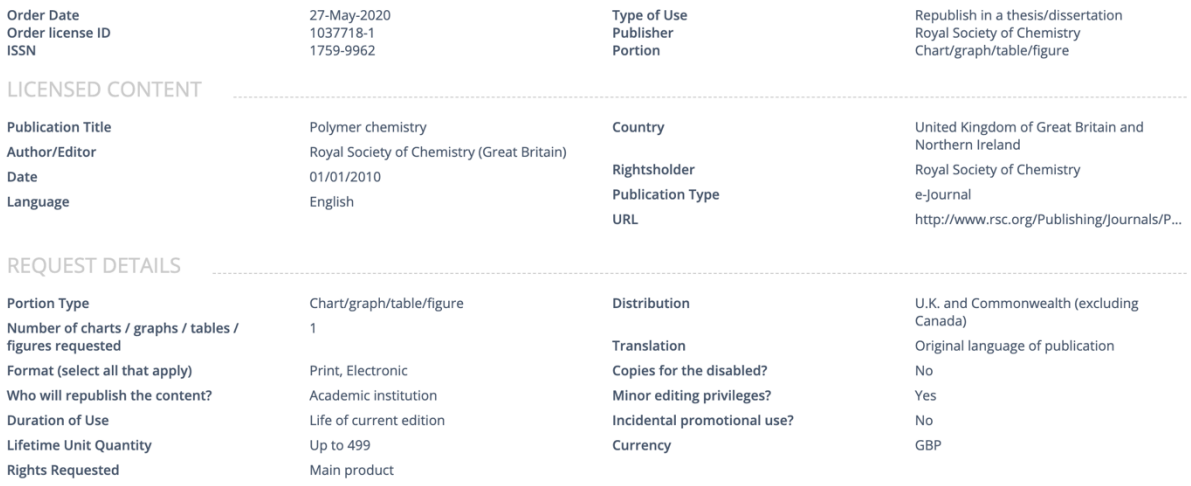
This type of permission/license, instead of the standard Terms & Conditions, is sent to you because no fee is being charged for your order. Please note the following:

- Permission is granted for your request in both print and electronic formats, and translations.
- If figures and/or tables were requested, they may be adapted or used in part.
- Please print this page for your records and send a copy of it to your publisher/graduate school.
- Appropriate credit for the requested material should be given as follows: "Reprinted (adapted) with permission from (COMPLETE REFERENCE CITATION). Copyright (YEAR) American Chemical Society." Insert appropriate information in place of the capitalized words.
- One-time permission is granted only for the use specified in your request. No additional uses are granted (such as derivative works or other editions). For any other uses, please submit a new request.

If credit is given to another source for the material you requested, permission must be obtained from that source.

BACK CLOSE WINDOW

Figure 3.15: Investigation into thiol-(meth)acrylate Michael addition reactions using amine and phosphine catalysts



Order Date	27-May-2020	Type of Use	Republish in a thesis/dissertation
Order license ID	1037718-1	Publisher	Royal Society of Chemistry
ISSN	1759-9962	Portion	Chart/graph/table/figure

LICENSED CONTENT

Publication Title	Polymer chemistry	Country	United Kingdom of Great Britain and Northern Ireland
Author/Editor	Royal Society of Chemistry (Great Britain)	Rightsholder	Royal Society of Chemistry
Date	01/01/2010	Publication Type	e-Journal
Language	English	URL	http://www.rsc.org/Publishing/Journals/P...

REQUEST DETAILS

Portion Type	Chart/graph/table/figure	Distribution	U.K. and Commonwealth (excluding Canada)
Number of charts / graphs / tables / figures requested	1	Translation	Original language of publication
Format (select all that apply)	Print, Electronic	Copies for the disabled?	No
Who will republish the content?	Academic institution	Minor editing privileges?	Yes
Duration of Use	Life of current edition	Incidental promotional use?	No
Lifetime Unit Quantity	Up to 499	Currency	GBP
Rights Requested	Main product		

Figure 4.4

License Number	4837190452408
License date	May 27, 2020
Licensed Content Publisher	Springer Nature
Licensed Content Publication	Nature Reviews Neuroscience
Licensed Content Title	Fibrinogen in neurological diseases: mechanisms, imaging and therapeutics
Licensed Content Author	Mark A. Petersen et al
Licensed Content Date	Apr 5, 2018
Type of Use	Thesis/Dissertation
Requestor type	non-commercial (non-profit)
Format	print and electronic
Portion	figures/tables/illustrations
Number of figures/tables/illustrations	1
High-res required	no
Will you be translating?	no
Circulation/distribution	1 - 29
Author of this Springer Nature content	no
Title	The highly sensitive and selective detection of protein biomarkers using aptamer-based nanopores
Institution name	Imperial College
Expected presentation date	Jul 2020
Portions	Figure 2

Figure 4.5

License Number	4837190855994
License date	May 27, 2020
Licensed Content Publisher	John Wiley and Sons
Licensed Content Publication	Angewandte Chemie International Edition
Licensed Content Title	Label-Free Electronic Detection of Thrombin in Blood Serum by Using an Aptamer-Based Sensor
Licensed Content Author	Kevin W. Plaxco, Alan J. Heeger, Arica A. Lubin, et al
Licensed Content Date	Aug 22, 2005
Licensed Content Volume	44
Licensed Content Issue	34
Licensed Content Pages	4
Type of Use	Dissertation/Thesis
Requestor type	University/Academic
Format	Print and electronic
Portion	Figure/table
Number of figures/tables	3
Will you be translating?	No
Title	The highly sensitive and selective detection of protein biomarkers using aptamer-based nanopores
Institution name	Imperial College
Expected presentation date	Jul 2020
Portions	Figure 1 Figure 3 Figure 4

Figure 4.6

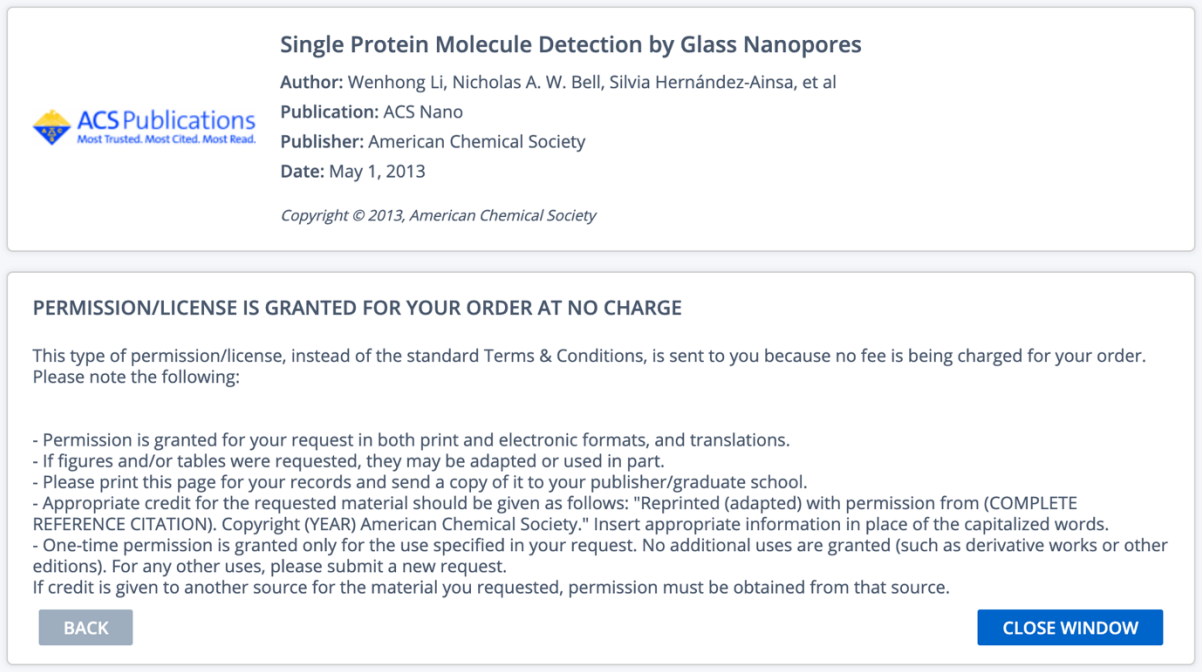
JOHN WILEY AND SONS LICENSE
TERMS AND CONDITIONS

May 28, 2020

This Agreement between Ben Edwards ("You") and John Wiley and Sons ("John Wiley and Sons") consists of your license details and the terms and conditions provided by John Wiley and Sons and Copyright Clearance Center.

License Number	4837840464168
License date	May 28, 2020
Licensed Content Publisher	John Wiley and Sons
Licensed Content Publication	Annals of Neurology
Licensed Content Title	Early detection of thrombin activity in neuroinflammatory disease
Licensed Content Author	Dimitrios Davalos, Kim M. Baeten, Michael A. Whitney, et al
Licensed Content Date	Feb 24, 2014
Licensed Content Volume	75
Licensed Content Issue	2
Licensed Content Pages	6
Type of use	Dissertation/Thesis
Requestor type	University/Academic
Format	Print and electronic
Portion	Figure/table
Number of figures/tables	2
Will you be translating?	No
Title	The highly sensitive and selective detection of protein biomarkers using aptamer-based nanopores
Institution name	Imperial College
Expected presentation date	Jul 2020
Portions	Figure 1 Figure 2

Figure 4.24



Single Protein Molecule Detection by Glass Nanopores

Author: Wenhong Li, Nicholas A. W. Bell, Silvia Hernández-Ainsa, et al

Publication: ACS Nano

Publisher: American Chemical Society

Date: May 1, 2013

Copyright © 2013, American Chemical Society

PERMISSION/LICENSE IS GRANTED FOR YOUR ORDER AT NO CHARGE

This type of permission/license, instead of the standard Terms & Conditions, is sent to you because no fee is being charged for your order. Please note the following:

- Permission is granted for your request in both print and electronic formats, and translations.
- If figures and/or tables were requested, they may be adapted or used in part.
- Please print this page for your records and send a copy of it to your publisher/graduate school.
- Appropriate credit for the requested material should be given as follows: "Reprinted (adapted) with permission from (COMPLETE REFERENCE CITATION). Copyright (YEAR) American Chemical Society." Insert appropriate information in place of the capitalized words.
- One-time permission is granted only for the use specified in your request. No additional uses are granted (such as derivative works or other editions). For any other uses, please submit a new request.

If credit is given to another source for the material you requested, permission must be obtained from that source.

BACK CLOSE WINDOW

Figure 5.3

SPRINGER NATURE LICENSE
TERMS AND CONDITIONS

May 28, 2020

This Agreement between Ben Edwards ("You") and Springer Nature ("Springer Nature") consists of your license details and the terms and conditions provided by Springer Nature and Copyright Clearance Center.

License Number	4837230900094
License date	May 27, 2020
Licensed Content Publisher	Springer Nature
Licensed Content Publication	Nature Reviews Neuroscience
Licensed Content Title	The many faces of α-synuclein: from structure and toxicity to therapeutic target
Licensed Content Author	Hilal A. Lashuel et al
Licensed Content Date	Dec 20, 2012
Type of Use	Thesis/Dissertation
Requestor type	academic/university or research institute
Format	print and electronic
Portion	figures/tables/illustrations
Number of figures/tables/illustrations	1
High-res required	no
Will you be translating?	no
Circulation/distribution	1 - 29
Author of this Springer Nature content	no
Title	The highly sensitive and selective detection of protein biomarkers using aptamer-based nanopores
Institution name	Imperial College
Expected presentation date	Jul 2020
Portions	Figure 1

Figure 5.5

JOHN WILEY AND SONS LICENSE
TERMS AND CONDITIONS

May 28, 2020

This Agreement between Ben Edwards ("You") and John Wiley and Sons ("John Wiley and Sons") consists of your license details and the terms and conditions provided by John Wiley and Sons and Copyright Clearance Center.

License Number	4837231253403
License date	May 27, 2020
Licensed Content Publisher	John Wiley and Sons
Licensed Content Publication	Annals of Neurology
Licensed Content Title	α-Synuclein oligomers and clinical implications for Parkinson disease
Licensed Content Author	Anthony E. Lang, Andres M. Lozano, Pamela J. McLean, et al
Licensed Content Date	Dec 7, 2012
Licensed Content Volume	73
Licensed Content Issue	2
Licensed Content Pages	15
Type of use	Dissertation/Thesis
Requestor type	University/Academic
Format	Print and electronic
Portion	Figure/table
Number of figures/tables	1
Will you be translating?	No
Title	The highly sensitive and selective detection of protein biomarkers using aptamer-based nanopores
Institution name	Imperial College
Expected presentation date	Jul 2020
Portions	Figure 1

Figure 5.6/7

Order Date	27-May-2020	**Type of Use**	Republish in a thesis/dissertation
Order license ID	1037760-1	**Publisher**	RSC Pub
ISSN	2040-3372	**Portion**	Chart/graph/table/figure

LICENSED CONTENT

Publication Title	Nanoscale	**Country**	United Kingdom of Great Britain and Northern Ireland
Author/Editor	National Center for Nanoscience and Technology., Royal Society of Chemistry (Great Britain)	**Rightsholder**	Royal Society of Chemistry
		Publication Type	e-Journal
Date	01/01/2009	**URL**	http://www.rsc.org/Publishing/Journals/N...
Language	English		

REQUEST DETAILS

Portion Type	Chart/graph/table/figure	**Distribution**	U.K. and Commonwealth (excluding Canada)
Number of charts / graphs / tables / figures requested	2	**Translation**	Original language of publication
Format (select all that apply)	Print, Electronic	**Copies for the disabled?**	No
Who will republish the content?	Academic institution	**Minor editing privileges?**	Yes
Duration of Use	Life of current edition	**Incidental promotional use?**	No
Lifetime Unit Quantity	Up to 499	**Currency**	GBP
Rights Requested	Main product		

Figure 5.8

ACS Publications
Most Trusted. Most Cited. Most Read.

Analysis of a Single α-Synuclein Fibrillation by the Interaction with a Protein Nanopore

Author: Hai-Yan Wang, Zhen Gu, Chan Cao, et al
Publication: Analytical Chemistry
Publisher: American Chemical Society
Date: Sep 1, 2013

Copyright © 2013, American Chemical Society

PERMISSION/LICENSE IS GRANTED FOR YOUR ORDER AT NO CHARGE

This type of permission/license, instead of the standard Terms & Conditions, is sent to you because no fee is being charged for your order. Please note the following:

- Permission is granted for your request in both print and electronic formats, and translations.
- If figures and/or tables were requested, they may be adapted or used in part.
- Please print this page for your records and send a copy of it to your publisher/graduate school.
- Appropriate credit for the requested material should be given as follows: "Reprinted (adapted) with permission from (COMPLETE REFERENCE CITATION). Copyright (YEAR) American Chemical Society." Insert appropriate information in place of the capitalized words.
- One-time permission is granted only for the use specified in your request. No additional uses are granted (such as derivative works or other editions). For any other uses, please submit a new request.

If credit is given to another source for the material you requested, permission must be obtained from that source.

BACK CLOSE WINDOW